Xiaofeng Peng

Micro Transport Phenomena During Boiling

TSINGHUA UNIVERSITY PRESS

Springer

Xiaofeng Peng

Micro Transport Phenomena During Boiling

Xiaofeng Peng

Micro Transport Phenomena During Boiling

With 210 figures

TSINGHUA UNIVERSITY PRESS

Springer

Author
Prof. Xiaofeng Peng (1961–2009)
Department of Thermal Science and Engineering
Tsinghua University, 100084, Beijing, China

ISBN 978-7-302-22355-9
Tsinghua University Press, Beijing

ISBN 978-3-642-13453-1 e-ISBN 978-3-642-13454-8
Springer Heidelberg Dordrecht London New York

Library of Congress Control Number: 2010927590

Cover design: Frido Steinen-Broo, EStudio Calamar, Spain

Printed on acid-free paper

Springer is a part of Springer Science+Business Media (www.springer.com)

Prof. Xiaofeng Peng making a speech on heat transfer at Tsinghua Univ. on Oct. 2008.


Prof. Peng with his students July, 2006.

About Author

Dr. X. F. Peng (Xiao-Feng Peng, May 6, 1961—September 10, 2009) was a renowned scholar and professor of the Thermal Engineering Department at Tsinghua University. He received his B.S. and Ph.D degrees from Tsinghua University in 1983 and 1987, respectively. He worked at Tsinghua University all through his career, as Lecturer (1987 – 1991), Associate Professor (1991 – 1995) and Professor (1995 – 2009). He served as Department Head from 1997 to 2002 and received the Cheung Kong Endowed Chair in 2001. He held multiple visiting professorships, and engaged in active collaborations with numerous research institutions in China, USA, France and Korea. His research activities cover the fundamentals of phase-change heat transfer and two-phase flows, interfacial transport phenomena, convective flow boiling, heat and mass transport in porous media, microscale heat transfer, heat transfer under microgravity conditions, cooling technology for thermal management, and micro energy systems. His outstanding research accomplishments won him many prestigious national honors, such as the Science and Technology Research Award (1989), National Natural Science Award (1990), Award for Research Achievement (1996), and the First Prize Award for Natural Scientific Research Achievement (2005). Also Professor Peng was invited to deliver plenary presentations at many international conferences, including the 10th and 11th International Heat Transfer Conferences (1994, 1998) and the 18th International Symposium on Transport Phenomena (2007). He had over 600 publications and presented papers and several contributions to different English books. He also served on the editorial boards of various international and regional scientific journals, including the International Journal of Heat and Mass Transfer and International Communications in Heat and Mass Transfer, International Journal of Transport Phenomena, Experimental Heat Transfer, Heat Transfer Asian Research, and a number of Chinese journals including the Chinese Journal of Engineering Thermophysics. He also served on numerous Chinese and international technical committees.

Preface

This book is based on the excellent fundamental research of Prof. X. F. Peng. Many unique micro transport phenomena during boiling with their corresponding mechanisms have been investigated. This will serve as a special reference for researchers interested in the field of microscale boiling.

Boiling exists widely in the natural world, with boiling heat transfer has been employed in many practical applications. However, due to the highly nonequilibrium and coupled driven effects of the various physical potential, boiling heat and mass transfer is extremely complicated and many interesting phenomena are triggered under different specified conditions. Nowadays, the rapid development of practical engineering applications of boiling in cooling of electronic devices, thermal management of aerospace and micro energy systems, and micro-manufacturing, promote a strong demand for better understanding of microscale transport phenomena and create a notable shift of thermal science and heat transfer research from macroscale to microscale. Consequently, in recent decades, more and more investigations have been conducted to explore the micro transport phenomena during boiling. This book reviews and summarizes the new achievements and contributions of recent investigations, including the outstanding fundamental research conducted by the writer and his co-authors. The fundamentals for conducting investigations on micro boiling, microscale boiling and transport phenomena, boiling characteristics at microscale, and some important applications of micro boiling transport phenomena are introduced and discussed.

Chapter 1 introduces the background and industrial applications, as well as the research history of boiling, and then, the critical concept of "micro boiling" is described. In Chapter 2, some important thermal physics concepts and principles involved in boiling phenomena, such as phase and phase equilibrium, phase transition, interfacial aspects, contact angle and dynamical contact behavior, and cluster dynamics are described in detail. Chapter 3 introduces new understandings of boiling nucleation and achievements in the latest 20 years. Cluster theory is used to analyze the dynamic characteristics of nucleus formation, with theories

for the characteristics of liquid-to-vapor phase change heterogeneous nucleation, and bubble evolution. In Chapter 4, the phase change and interfacial behavior of subcooled pool boiling on ultrathin wires are investigated experimentally and numerically, and a series of interesting phenomena is observed visually and analyzed. In Chapter 5, the complex subcooled boiling phenomena on fine wires is investigated under weakened gravity, and a bubble dynamics equation incorporating the thermocapillary effect is proposed to investigate various kinds of bubble motion such as slippage, separation, collision, oscillation and leaping, indicating that the thermocapillary effect on the bubble interface is very important for the bubble motion. Chapter 6 describes experimental investigations on phase-change transition, bubble nucleation, and bubble dynamics in microchannels conducted by the author and co-workers, including the new concepts of "evaporating space" and "fictitious boiling". Furthermore, the nucleation criterion in microchannels is derived by utilizing thermodynamics and cluster dynamics. Chapter 7 describes experimental investigations conducted to visualize the boiling phenomena, covering nucleate, transition and film boiling regimes and for individual water droplets on the heating surfaces. The oscillation of sessile droplets is investigated experimentally and numerically. Chapter 8 describes the boiling phenomena in micro structures and porous media; the dynamic behavior of bubble interfaces in a confined space, replenishment of liquid during boiling, interfacial heat and mass transfer in pores and occurrence of dryout are analyzed further. Chapter 9 presents visualizations of explosive boiling nucleation phenomena in micro capillary tubes, and liquid exploding emissions, with a correlation for the critical heat flux derived from a scaling analysis.

Prof. Xiaofeng Peng passed away suddenly on Sept. 10^{th}, 2009. As the supervisor of his Ph. D work before 1987 and his research co-worker for a long time, I write this preface with great sadness as a permanent memory to him. I hope this book is helpful and provides inspiration for many researchers and students.

I want to express my appreciation to my colleagues, particularly Prof. Qiang Yao and Prof. Yuanyuan Duan, for their great support and many helpful suggestions. I also thank his research group for their help in preparing the manuscript for publication.

Bu-Xuan Wang
Tsinghua University, Dec., 2009

Contents

1 Introduction

Abstract This chapter describes the importance of boiling research and its applications in modern industry. The history and trends of boiling are also reviewed, and then the scope and definition of "micro boiling", which is the key topic in this book, are described in detail.

Keywords boiling dynamics, micro boiling

1.1 Critical Technology

Boiling phenomena and the associated heat transfer, characterized by small temperature differences and high heat fluxes, are encountered in various energy conversion and utilization systems. The boiling process has been widely employed to improve the heat transfer performance of heating and cooling devices and to meet the increasing demand of high heat removal in various practical applications covering thermal and nuclear power engineering, space, aviation, cryogenic, refrigeration, chemical, food and bioengineering, and other technologies. In the latest 20 years, high-technology applications, such as spacecraft thermal control, aerospace systems, electronic devices and light emitting diodes (LED) cooling systems, micro-electro-mechanical systems (MEMS), and biological and medical systems, have further promoted more comprehensive investigations into boiling and other phase change phenomena.

Recent trends in science and technology have indicated an increasing emphasis on miniaturization of engineering systems with/without extremely fast processes and study of micro- and nano-scale phenomena [1 – 3]. Actually modern technologies and industrial developments have brought a drastic reduction in size of computers, electronic chips/components, laser devices, micro energy systems, compact heat exchangers and employed in various kinds of the micro-sensors and micro-actuators. In these systems and devices having characteristic lengths of several microns to 500 microns, mass and energy transport are always important and play critical roles in their performance and/or their safe operation. Apparently, the reduced characteristic size strongly affects the thermal fluid flow and transport processes, particularly suppressing boiling nucleation, vapor bubble formation, phase distribution and two phase flow development, and associated boiling heat

X. Peng, *Micro Transport Phenomena During Boiling*

transfer for micro boiling systems. As one important topic for microscale transport phenomena, the micro boiling has attracted great attention of investigators all over the world [2, 4 – 10].

Of the variety of innovative and high performance micro cooling technologies, the highly potential one is microchanneled sink technology of metal and silicone substrates in which flow boiling and two phase flow heat transfer occurs, and it is widely recognized that this kind of heat sinks can reach a high heat removal rate of 300 W/cm^2 [11]. Actually, various micro boiling and evaporation phenomena are critical transport processes encountered in many innovative technologies and practical applications, such as micro heat pipes, fuel cells, impinging and spreading cooling devices, ultra-compact heat exchangers, micro bio-systems/devices, micro mixers and separators, micro reactors, and other micro thermal devices/systems.

1.2 History and Trends of Boiling

As a normal recognition, the earliest work of boiling is the Leidenfrost's experiment in which the Leidenfrost phenomenon was observed and described [12], while the practical application where boiling was first encountered can be traced back to the alchemy [13]. However, boiling was recognized as a way having enormous potential for transferring heat at low temperature differences only in the 1930s, and this time has been known as the beginning of modern boiling research. In 1934 Nukiyama firstly described the basic characteristics of pool boiling on a wire, particularly the boiling regimes and associated heat transfer modes, normally termed as the boiling curve. Later, many researchers focused their research on understanding macroscopic phenomena and determining heat transfer performance, such as boiling nucleation, different boiling modes and transition, boiling heat transfer and associated heat transfer enhancement [3 – 4]. In more recent literature, the attention has shifted to explore new phenomena associated with microscale effects, micro gravity effects, electromagnetism effects, and so on [5 – 7]. Some high technological applications of boiling phenomena, like thermal ink jet printer and MEMS, bubble and nucleation driving or propulsion, have made researchers pay more attention to understand bubble dynamical behavior [8].

The boiling investigation mainly includes nucleation theory, bubble dynamics, and boiling mode and associated heat transfer characteristics [9]. In the boiling systems, the bubbles occur through a nucleation process. The nucleation is usually a nanoscale/microscale process, and it can be described by statistical mechanics and kinetic theory. The bubble dynamics is one of the critical problems in boiling research [10], and it directly affects the boiling heat transfer performance. The bubbling phenomena are very complex, because there are various forces and

special structures in the boiling fluid systems. The boiling usually has three modes: nucleate boiling, transition boiling, and film boiling. The heat transfer performance of different modes is critical important to the equipments with boiling processes, so various empirical correlations and physical models have been proposed to describe and predict the boiling heat transfer.

In general, two main reasons including practical and scientific requirements continuously improve the boiling investigation. Firstly, boiling is a very efficient mode of heat transfer and is employed in various energy systems and other practical applications. Secondly, boiling is a very complex process and understanding its physical nature is a very challenging work closely associated with many fundamental disciplines, or interdisciplinary nature is a critical aspect in the research. Since fewer studiers have focused on the physics of the boiling systems, it focused on the boiling physical nature especially its dynamics. The nucleation process was mainly investigated in three aspects: inception phenomena, evolution process, and microscale effect. Experimental investigation, theoretical analyses, and numerical method were conducted to study the dynamics of immobile and moving bubble during the subcooled boiling of water on heating wires. Additionally, the heat transfer performance of different boiling modes during the abrupt cooling was described, and the boiling stability was also theoretically analyzed.

A brief review of the boiling dynamics and an introduction to current studies were presented in this chapter. Because of the practical and scientific requirements, the boiling investigation is a very challenging work, and it can be mainly divided into three sections: nucleation theory, bubble dynamics, and boiling mode. Available literature is cited to introduce the boiling dynamics and associated research, and some problems are further pointed out. The boiling physical nature especially various dynamic behaviors are focused on, and its objective and content are also described in detail.

1.3 Micro Boiling

So far, the available investigations of micro boiling have almost been conducted in microchannels, especially the evaporation in microchannels. Although the great number of publications and research work was contributed to understand microscale thermal-fluid science and transport phenomena, mostly in microchannels, there is still no generally accepted definition of the word, “microscale”. As a simple and generally used word, it means that the hydraulic diameter of a microchannel is in the micrometer range, or the very large size range of 1 – 1000 μm. However, it is expected that the definition will be significantly different for boiling in microchannels due to the process of nucleation or bubble formation. For example,

boling and two phase flow in channels having hydraulic diameters up to several millimeters can not be described using classical theories [6]. Thome et al. [14] discussed these different definitions appeared in the literature under different situations. They suggested that a threshold is chosen to define bubble flow as the criterion of microchannel size, below which macroscale theories become unreliable for predicting flow boiling heat transfer coefficients, two phase flow pattern transitions, two phase pressure drops and critical heat flux (CHF).

In this book, the similar considerations are adapted. The term of the micro boiling dedicates that the boiling characteristics are significantly influenced by and/or dependent of the size at which boiling occurs, or greatly deviated from the classical boiling theory. This is to say, an emphasis is addressed on the boiling phenomena closely associated with size effects, rather than trying to reach a general conclusion on a popularly accepted definition of the micro boiling. For a more comprehensive consideration not only in micro-tubes/channnels, attention is also paid to explore new micro boiling phenomena in microstructure (or porous pores) and during any practical boiling processes, and re-recognize classical boiling phenomena and theories at microscale level.

Complexity of boiling phenomenon is connected with combination of phase conversion and turbulence in an area with irregular internal structure.

References

[1] C. L. Tien et al. Microscale Energy transport. NewYork: Taylor and Francis, 1998.

[2] G. P. Celata. Heat Transfer and Fluid Flow in Microchannels. New York: Begell House Inc., 2004.

[3] T. L. Bergman, A. Faghri, R. Viskanta. Frontiers in transport phenomena research and education: Energy systems, biological systems, security, information technology and nanotechnology. Int. J. Heat Mass Transfer, 51: 4599 – 4613, 5033 – 5044, 2008.

[4] X. F. Peng, B. X. Wang. Nucleation and thermodynamic nonequilibrium for boiling in microchannels and microstructures. In: Tien C. L. eds. Annual Review of Heat Transfer. New York: Begell house Inc., 307 – 350, 2000.

[5] J. R. Thome. Boiling in microchannels: a review of experiment and theory. Int. J. Heat Fluid Flow, 25(2): 128 – 139, 2004.

[6] B. Palm. Heat transfer in microchannels. Microscale Thermophysical Engineering, 5(3): 155 – 175, 2001.

[7] S. G. Kandlikar. Two-phase flow patterns, pressure drop, and heat transfer during boiling in minichannel flow passages of compact evaporators. Heat Transfer Engineering, 23(1): 5 – 23, 2002.

[8] A. E. Bergles, J. H. Lienhard, G. E. Kendall. Boiling and evaporation in small diameter channels. Heat Transfer Engineering, 24(1): 18 – 40, 2003.

[9] S. V. Garimella, C. B. Sobhan. Transport in microchannels-a critical review. In: Tien C. L. eds. Annual Review of Heat Transfer. New York: Begell House Inc., 2003.

[10] P. Cheng, H. Y. Wu. Mesoscale and microscale phase-change heat transfer. Adv. Heat Transfer, 39: 461 – 563, 2006.

[11] B. Agostini, M. Fabbri, J. E. Park, et al. State of the art of high heat flux cooling technologies. Heat Transfer Engineering, 28(4): 258 – 281, 2007.

[12] J. G. Leidenfrost, De Aquea. Communis nonnullis qualitatibus tractatus. Duisburg, 1756; Trans. By C. Wares, Int. J. Heat Mass Transfer, 9: 1153, 1966.

[13] J. H. Lienhard. Snares of pool boiling research: putting our history to use. Heat Transfer, 1: 361 – 376, 1994.

2 Thermal Physical Fundamentals

Abstract This chapter discusses mainly about five important physical concepts in liquid and gas systems, which are phase equilibrium, phase transition, interface, contact angle, and cluster. Phase refers to the physically distinctive form of a substance. From the view of thermodynamics, the states and conditions for phase equilibrium are described and some fundamentals for phase transition are introduced. A liquid-vapor interface is considered to be a very thin region having rapid changes in fluid or material properties from the bulk liquid to bulk vapor. Using surface excess quantity, the thermodynamic analysis can be conducted to explore the interfacial effects. Interface tension and Young-Laplace equation are discussed here. The contact angle, which is used to quantify the wettability of liquid, is defined as the angle between the liquid-vapor interface and the solid surface at the contact line. Contact angle equilibrium, hysteresis and dynamic are discussed. Clusters consisting of tens and hundred of atoms or molecules are a new class of compounds called atomic or molecular clusters. The number balance equation is formulated for activated molecules in clusters, with a comprehensive investigation of the dynamics of clusters formed with internal or external perturbations.

Keywords phase equilibrium, phase transition, interface, contact angle, cluster

2.1 Phase and Phase Equilibrium

As is well-known, substances, including both pure substances and mixtures, exist in different phases, and under different conditions each one may appear in different phases. Even though there are three principal phases—solid, liquid, and gas (vapor)—a substance may have several phases within a principal phase, each with a different molecular structure. Here we are only concerned with liquid and gas (in this book normally called vapor) phase and their transition or systems containing both liquid and vapor. From the view of thermodynamics, when a system or a portion of a system undergoes a phase change, the process is necessarily relative to a departure from equilibrium, and is moving towards a new equilibrium state. The equilibrium state (or phase equilibrium) and its conditions are of considerable practical importance.

X. Peng, *Micro Transport Phenomena During Boiling*

For a mixture of simple compressible substances in a thermally insulated, rigid container, the constraints imposed by the container with only work are

$$\mathrm{d}V = 0, \quad \mathrm{d}U = 0, \quad \delta W = p\mathrm{d}V \tag{2.1}$$

where, V, p, U, W are volume, pressure, internal energy and work of system, respectively. Combining the first and second laws of thermodynamics, spontaneous changes can occur only if

$$\mathrm{d}S \geqslant 0 \tag{2.2}$$

where S is entropy of system. Consequently, all spontaneous changes increase the entropy of the system and the equilibrium for a mixture of simple compressible substances held at constant volume and internal energy corresponds to conditions that maximize the entropy within the system constrains.

Alternate statements of the second law extremum condition can be similarly obtained for systems with different imposed constrains. Several of these are summarized as the following.

$$\text{constant } T,V \qquad \mathrm{d}F \leqslant 0 \tag{2.3}$$

$$\text{constant } p,T \qquad \mathrm{d}G \leqslant 0 \tag{2.4}$$

$$\text{constant } S,V \qquad \mathrm{d}U \leqslant 0 \tag{2.5}$$

where, T, F, and G denote temperature, Helmholtz function (or Helmholtz free energy) and Gibbs function (or Gibbs free energy), respectively.

For a system with a mixture of simple compressible substances the second law requires that the equilibrium state is one that maximizes S or minimizes U, F, or G, depending on the imposed system constrains. Figure 2.1 illustrates a series of samples that demonstrate how these considerations come into play for a system containing only pure water with both liquid and vapor phases. In these drawings x is quality denoting the ratio of mass of water vapor to the total system mass. Obviously, in this system the amount of water liquid and vapor present (i.e., the quality) at equilibrium will be that which maximizes the entropy of the system over all the possible x values, consistent with conservation of mass and specified V and U, while minimizing the Helmholtz free energy, internal energy of the system for specified T and V, and S and V, respectively. For cases except Fig. 2.1(c) the discussion of Fig. 2.1(c) can be found in the books of classical thermodynamics [1 – 3].

To explore properties at equilibrium, a close system shown in Fig. 2.2(a) is considered, containing two phases Ⅰ and Ⅱ of a mixture of n_c pure simple compressible substances. The system is constrained so that the overall entropy and volume remain constant regardless of internal changes, or S and V are constant, which corresponds to the equilibrium state having conditions to minimize the

internal energy over the range of conditions accessible to the system, as illustrated in Fig. 2.2(b). For this system all spontaneous processes must satisfy Eq. (2.5), i.e., they must cause a decrease in U.

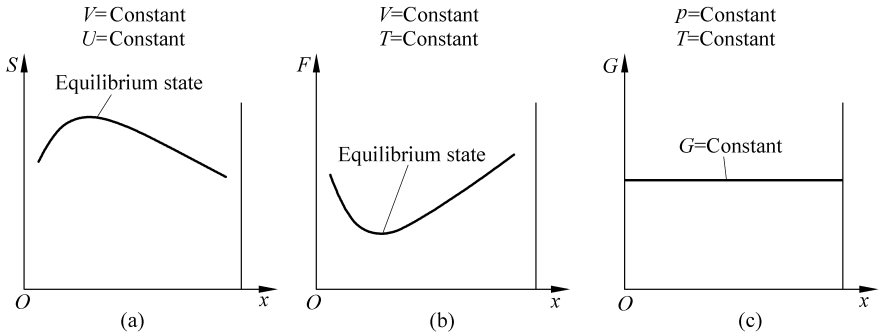

Figure 2.1 Equilibrium-state conditions for systems with different constrains

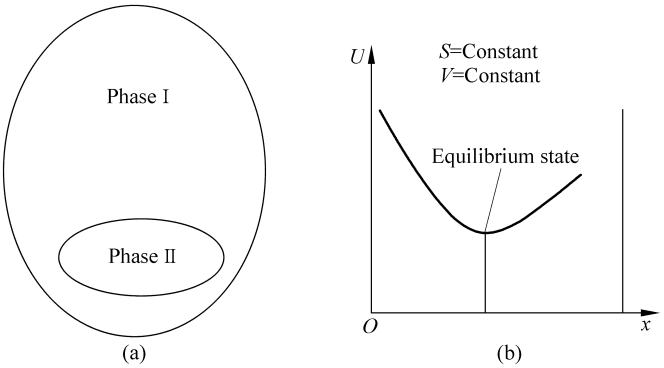

Figure 2.2 Equilibrium conditions in a two phase system at specified S and V

The overall internal energy is equal to the sum of the contributions from the two phases, and at equilibrium, any differential change in U is given by

$$\mathrm{d}U = \mathrm{d}U^{\mathrm{I}} + \mathrm{d}U^{\mathrm{II}} = 0 \tag{2.6}$$

Using thermodynamic relationships and expanding U in a Taylor series for each of the two phases, then substituting the resulting first-order relations for $\mathrm{d}U^{\mathrm{I}}$ and $\mathrm{d}U^{\mathrm{II}}$ into Eq. (2.6) yields

$$U_V^{\mathrm{I}}\mathrm{d}V^{\mathrm{I}} + U_S^{\mathrm{I}}\mathrm{d}S + \sum_{i=1}^{n_c} U_{N_i}^{\mathrm{I}}\,\mathrm{d}N_i^{\mathrm{I}} + U_v^{\mathrm{II}}\mathrm{d}V^{\mathrm{II}} + U_S^{\mathrm{II}}\mathrm{d}S^{\mathrm{II}} + \sum_{i=1}^{n_c} U_{N_i}^{\mathrm{II}}\,\mathrm{d}N_i^{\mathrm{II}} = 0 \tag{2.7}$$

in addition

$$\mathrm{d}V = \mathrm{d}V^{\mathrm{I}} + \mathrm{d}V^{\mathrm{II}} = 0 \tag{2.8}$$

$$\mathrm{d}S = \mathrm{d}S^{\mathrm{I}} + \mathrm{d}S^{\mathrm{II}} = 0 \tag{2.9}$$

$$\mathrm{d}N_i = \sum_{i=1}^{n_c} \mathrm{d}N_i^{\mathrm{I}} + \sum_{i=1}^{n_c} \mathrm{d}N_i^{\mathrm{II}} = 0 \tag{2.10}$$

Substituting Eqs. (2.8) – (2.10) into Eq. (2.7) yields

$$\left(U_V^{\mathrm{I}} - U_V^{\mathrm{II}}\right)\mathrm{d}V^{\mathrm{I}} + \left(U_S^{\mathrm{I}} - U_S^{\mathrm{II}}\right)\mathrm{d}S^{\mathrm{I}} + \sum_{i=1}^{n_c}\left(U_{N_i}^{\mathrm{I}} - U_{N_i}^{\mathrm{II}}\right)\mathrm{d}N_i^{\mathrm{I}} = 0 \tag{2.11}$$

Apparently, Eq. (2.11) holds for all possible perturbations in V, S, and N_i only if

$$U_V^{\mathrm{I}} = U_V^{\mathrm{II}}, \quad U_S^{\mathrm{I}} = U_S^{\mathrm{II}}, \quad U_{N_i}^{\mathrm{I}} = U_{N_i}^{\mathrm{II}} \tag{2.12}$$

Using the Maxwell relations

$$\begin{aligned} U_V &= \left(\frac{\partial U}{\partial V}\right)_{S,N_i} = -p \\ U_S &= \left(\frac{\partial U}{\partial S}\right)_{V,N_i} = T \\ U_{N_i} &= \left(\frac{\partial U}{\partial N_i}\right)_{S,V} = \tilde{\mu}_i \end{aligned} \tag{2.13}$$

So, at equilibrium

$$T^{\mathrm{I}} = T^{\mathrm{II}} \tag{2.14}$$

$$p^{\mathrm{I}} = p^{\mathrm{II}} \tag{2.15}$$

$$\overline{\mu}_i^{\mathrm{I}} = \overline{\mu}_i^{\mathrm{II}} \quad \text{or} \quad \mu_i^{\mathrm{I}} = \mu_i^{\mathrm{II}} \tag{2.16}$$

where $\overline{\mu}$ and μ are molar and mass-based specified chemical potentials, respectively. Very clearly, necessary conditions for equilibrium are that the temperature, pressure and chemical potential of each component must be the same in both phases of each pure substance in a closed system. These conditions are the same for a system containing more than two phases at equilibrium.

2.2 Phase Transition

In classical thermodynamics, phase transitions are treated as if they are quasi-equilibrium processes at the equilibrium saturation conditions. As is well known, real phase transitions or phase changes usually occur under nonequilibrium

conditions. This section introduces some fundamentals related to micro boiling phenomena.

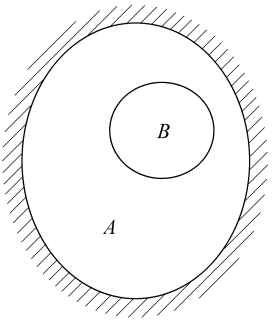

Figure 2.3 Phase stability analysis model

Phase transition corresponds to the instability of a phase, and consequently the stability of a system in thermodynamic nonequilibrium is important. For a closed system initially containing all phase Ⅰ of a pure substance, a small change in U is investigated for determining whether U is at a minimum using thermodynamics when a small portion of the substance is transition into phase Ⅱ, as shown in Fig. 2.3, and the critieria for equilibrium and stability are derived as,
Criterion of equilibrium:

$$\delta U = 0 \tag{2.17}$$

Criterion of stability:

$$\delta^m U > 0 \text{ for the smallest } m = 2,3,4,... \text{ at which } \delta^m U \neq 0 \tag{2.18}$$

Furthermore these criteria can be expressed as

$$\overline{c}_v > 0 \tag{2.19}$$

or molar specific heat at constant volume, $\overline{c}_v$, is always positive, and

$$\left(\frac{\partial p}{\partial V}\right)_T < 0 \quad \text{or} \quad \left(\frac{\partial p}{\partial v}\right)_T < 0 \tag{2.20}$$

Eq. (2.19) is referred to as the criterion of thermal stability. Eq. (2.20) is called the criterion for mechanical stability. Since $\overline{c}_v$ is greater than zero for virtually all substances, the criterion of thermal stability is satisfied and Eq. (2.20) is a necessary and sufficient condition for stability of a phase.

For the multicomponent systems phase stability can similarly be discussed [4]. In these cases Eqs. (2.19) and (2.20) are necessary but not sufficient conditions for stability. Taking a binary mixture as an example, the following inequality must

hold for the phase to be stable,

$$\left(\frac{\partial \mu_1}{\partial x_1}\right)_{T,p} \geqslant 0 \tag{2.21}$$

Where μ_1 and x_1 are the chemical potential and mass fraction of component 1 in the binary mixture, respectively. Eq. (2.21) is sometimes referred to the criterion of diffusional stability. If both thermal and mechanical stability inequalities are satisfied, Eq. (2.21) is a necessary and sufficient condition for phase stability of a binary mixture.

Generally, phase transition occurs under quasi- or non- equilibrium conditions, evaporation occurring above and condensation below the equilibrium saturation temperature. This means that both vapor supercooled below and liquid superheated above the equilibrium saturation temperature exist in a nonequilibrium condition and are referred to as metastable vapor and liquid, respectively. On a *p*-*v* diagram, metastable states for a pure substance can be visualized as lying on an isotherm that extends from the stable single-phase region into the vapor dome, as the dashed lines *BC* and *EF* illustrated in Fig. 2.4.

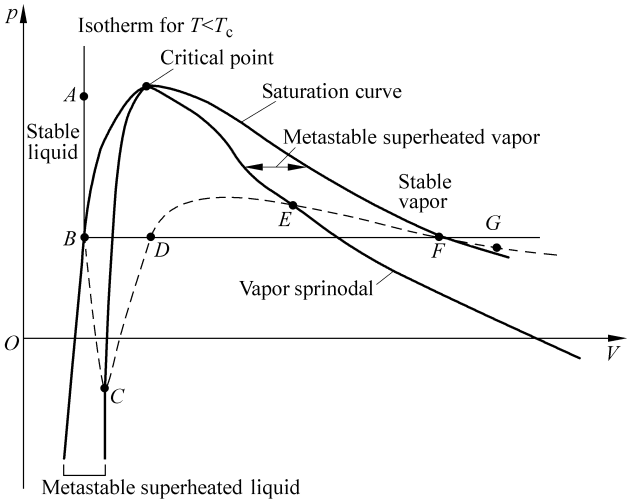

Figure 2.4 Stable and metastable regions on a *p*-*v* diagram

Actually, the van der Waals equation,

$$p = \frac{\left(\bar{R}/\bar{M}\right)T}{v-b} - \frac{a}{v^2} \tag{2.22}$$

can predict the isotherm *ABCDEFG* very well as one possible approach, including stable single-phase liquid (*AB*) and vapor (*FG*), metastable liquid (*BC*) and vapor

(*EF*), and *CDE* sections. The section *CDE* is physically impossible because corresponding states violates the mechanical stability criterion of $\left(\frac{\partial p}{\partial v}\right)_T < 0$. The metastable limits or spinodal lines and two metastable regions of liquid and vapor can be determined using the van der Waals equation, as shown in Fig. 2.4.

By integrating the Gibbs-Duhem equation,

$$\mathrm{d}\mu = -S\mathrm{d}T + v\mathrm{d}p \tag{2.23}$$

From point *A* to an arbitrary location along the isotherm shown in Fig. 2.4 the variation of the chemical potential is obtained as

$$\mu = \mu_{\mathrm{A}} + \int_{p_{\mathrm{A}}}^{p} v\mathrm{d}p \tag{2.24}$$

Arbitrarily evaluating a value of μ at point *A* and using the van der Waals equation, a variation of μ with *p* is given in Fig. 2.5. Segments *AB* and *FG* of the curve correspond to stable liquid and stable vapor, while *BC* and *EF* to metastable liquid and vapor, respectively. The portion of the curve *CDE* corresponds to the region violating the mechanical stability criterion and the system cannot access states along this section of the curve. From the view of energy, on line *CDE* the system is in a state with highest energy which is an unstable state and impossible.

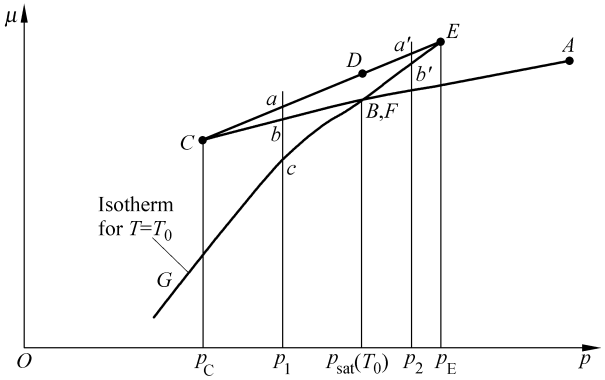

Figure 2.5 Variation of μ with *p* along an isotherm

2.3 Interfacial Aspects

From a microscopic point of view a liquid-vapor interface is a very thin region having rapid changes in fluid or material properties from the bulk liquid to bulk vapor, as illustrated in Fig. 2.6. For a theoretical description, the interfacial region is presumed to be bounded by two surfaces S_{I}^* and S_{II}^*, which are parallel

to the interface surface S^* but located in the corresponding bulk phases. All fluid and thermodynamic properties vary continuously across the interfacial region, as shown in Fig. 2.7, and a surface excess quantity is introduced to express interfacial properties and defined as

$$\Gamma_e^{S^*} = \int_{-y_I}^{y_{II}} \rho\gamma \mathrm{d}y - \rho_I\gamma_I y_I - \rho_{II}\gamma_{II} y_{II} \tag{2.25}$$

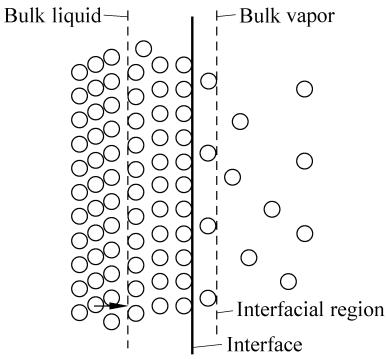

Figure 2.6 Molecular structure of interface

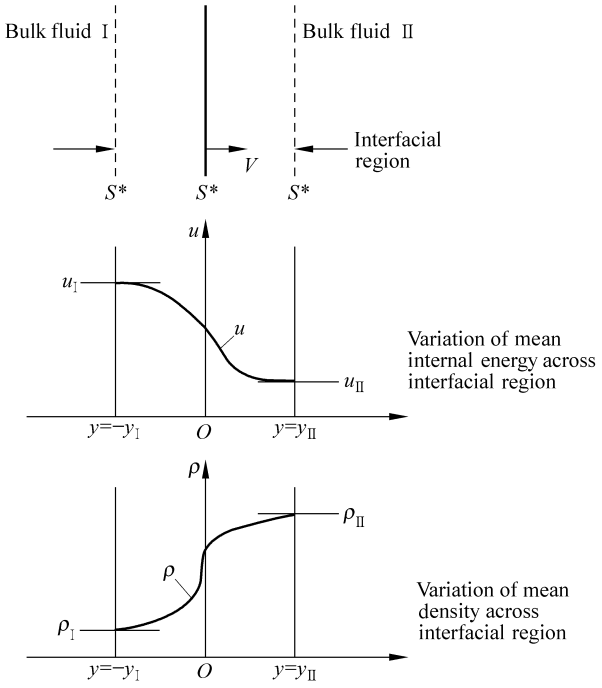

Figure 2.7 Interfacial properties in the interfacial region

where γ is any specific fluid property or energy, however, for surface excess mass, $\rho_e^{S^*}$, we have $\gamma = 1$. For example, the surface excess mass is given by

$$\rho_e^{S^*} = \int_{-y_I}^{y_{II}} \rho \mathrm{d}y - \rho_I y_I - \rho_{II} y_{II} \tag{2.26}$$

and the surface excess internal energy, $U_e^{S^*}$

$$U_e^{S^*} = \int_{-y_I}^{y_{II}} \rho u \mathrm{d}y - \rho_I u_I y_I - \rho_{II} u_{II} y_{II} \tag{2.27}$$

These quantities depend on the location of the surface S^*. A special location may make $\Gamma_e^{S^*}$ to be zero, but in general they may be positive or negative.

The surface excess quantity can be used in the thermodynamic analysis to explore the interfacial effects. Without losing generality, consider a system at equilibrium, as shown in Fig. 2.8, consisting of the interfacial region, bulk phase Ⅰ and phase Ⅱ. The energy change of the system can be used to relate the interfacial tension to the surface excess free energy,

$$\sigma = \left(\frac{\partial F_e^{S^*}}{\partial A_i} \right)_{N_e^{S^*}, T} \tag{2.28}$$

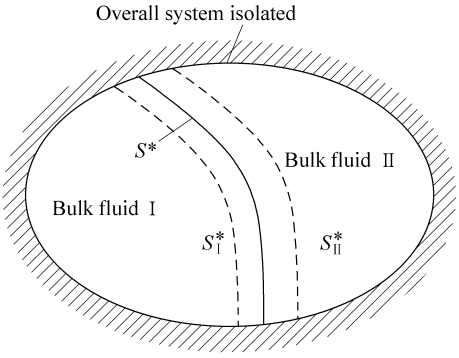

Figure 2.8 Analytical model of interface

Then, σ is equal to the change in surface excess free energy produced by a unit increase in interface area, A_i. Therefore, for an arbitrary interface in the system the force balance or pressure difference due to the existence of the interface is derived and expressed by

$$p_I - p_{II} = \sigma \left(\frac{1}{r_1} + \frac{1}{r_2} \right) \tag{2.29}$$

where r_1 and r_2 are two radii of curvature measured in two perpendicular planes

containing the local normal to S^*. Eq. (2.29) is normally termed the Laplace or the Young-Laplace equation, relating the pressure difference across the interface to the interfacial tension and the geometry of the interface at equilibrium.

The thermodynamic analysis of the interface as a thin region successfully relates the interfacial tension to the surface excess free energy, and this interfacial tension is further linked to the molecular properties that dictate the variation of the molecular spacing (density) and other properties across the interfacial region.

As an important application, the interfacial shape of a sessile bubble or droplet on a solid surface, as shown in Fig. 2.9, can be determined using the Young-Laplace equation [4]

$$\frac{\xi''}{\left[1+\left(\xi'\right)^2\right]^{3/2}}+\frac{\xi'}{\lambda\left[1+\left(\xi'\right)^2\right]^{1/2}}=2+Bo\,\xi \tag{2.30}$$

The two dimensionless variables are

$$\xi=\frac{z}{r_0},\quad \lambda=\frac{r}{r_0} \tag{2.31}$$

where r_0 is radius of curvature at point 0 in Fig. 2.9. And the dimensionless number, Bo, is defined as

$$Bo=\frac{g\left(\rho_{\mathrm{I}}-\rho_{\mathrm{II}}\right)r_0^2}{\sigma} \tag{2.32}$$

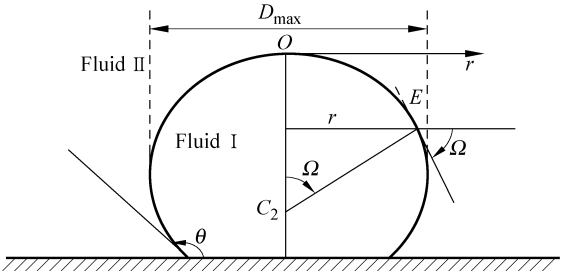

Figure 2.9 A sessile bubble or droplet on a flat surface

The boundary conditions of this second-order ordinary differential Eq. (2.30) are given as

$$\xi=0\quad\text{and}\quad\xi'=0\quad\text{at}\quad\lambda=0 \tag{2.33}$$

If the interfacial tension is a function of temperature [5],

$$\sigma=a+bT=\sigma_o(1-A\xi) \tag{2.34}$$

where a and b are constant empirical coefficients and are dependent on the specific fluid, and A is a coefficient describing temperature distribution in the liquid, Eq. (2.30) should be modified as

$$\frac{\xi''}{\left[1+\left(\xi'\right)^2\right]^{3/2}}+\frac{\xi'}{\lambda\left[1+\left(\xi'\right)^2\right]^{1/2}}=\frac{2+Bo\xi}{1-A\xi} \tag{2.35}$$

For mixtures, interface tension will be a function of both temperature and concentration, and similar modification should be made to account for their influence on determining the interfacial shape at equilibrium.

2.4 Contact Angle and Dynamical Contact Behavior

In almost all boiling and condensation systems, boiling and condensation phase change may first take place on solid surfaces, and vapor or liquid is frequently observed to contacts with the solid surfaces as a vapor bubble or liquid droplet, respectively. This is actually associated with the affinity of liquids for solids, referred as the wettability of the fluid.

2.4.1 Contact Angle at Equilibrium

The wettability of a liquid is quantified by the contact angle θ. This angle is defined as the angle between the liquid-vapor interface and the solid surface at the contact line formed by the intersection of the three solid-liquid-vapor phases, measured from the liquid side, as shown in Fig. 2.10. For a real axisymmetric drop or bubble there is a line common to all three phases (actually a circle line) which is the so-called contact line. A specified quantity of liquid spreads more over the surface as θ decreases. In the limit of $\theta \to 0$, the liquid spreads to form a thin film over the surface. In the another limit of $\theta \to 180^{\circ}$, the liquid constricts to a spherical drop contacting with the solid at a single point.

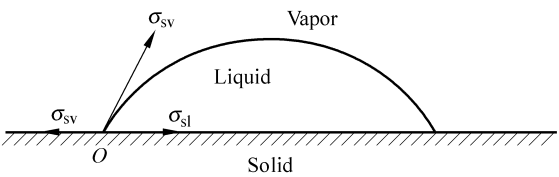

Figure 2.10 Contact angle and interfacial tensions

The system in Fig. 2.10 has three interfaces, liquid-vapor, solid-liquid and solid-vapor interfaces. The interfacial tensions on these interfaces correspond to

σ_{lv}, σ_{sl} and σ_{sv}, respectively. At equilibrium, a force balance at point O in the horizontal direction is expressed as

$$\sigma_{sv} = \sigma_{sl} + \sigma_{lv}\cos\theta \tag{2.36}$$

or

$$\cos\theta = \frac{\sigma_{sv} - \sigma_{sl}}{\sigma_{lv}} \tag{2.37}$$

Eq. (2.36) or Eq. (2.37) is often called Young's equation, and the contact angle is also termed as Young contact angle.

For rough horizontal surface, the contact angle was found to differ from the Young contact angle, and the deviation was considered as the result of surface roughness [6]. Introducing the ratio of actual solid surface area to its ideal smooth surface area or $\gamma = A_r / A_s$ to describe the surface roughness, Wenzel [6] modified Young's equation to

$$\cos\theta_W = \frac{\sigma_{sv} - \sigma_{sl}}{\sigma_{lv}}\gamma \tag{2.38}$$

and

$$\cos\theta_W = \gamma\cos\theta \tag{2.39}$$

Since γ is greater than 1, $\cos\theta_W > \cos\theta$, which means that the contact angle on a rough surface is always smaller than that on a smooth surface of the same material. It is worthy to note that the either Young's angle or Wenzel's angle is unique for a combination of a fluid and solid surface.

2.4.2 Contact Angle Hysteresis

In many real systems and almost all available experimental investigations conducted to understand liquid wetting and contact phenomena on a real solid surface, the contact line was observed to be at equilibrium as the contact angle changed in a range. This phenomenon is referred to contact angle hysteresis, or expressed as the difference of advancing and receding contact angle, $\Delta\theta = \theta_a - \theta_r$. The fundamentals of contact angle hysteresis are very well discussed by Carey [4] and Good [7].

As shown in Fig. 2.11, considering a liquid droplet with a constant volume on a rough solid surface, initially the droplet has a steady contact angle, θ, at equilibrium state "a". After a little bit of the liquid is added, the solid-liquid-gas contact line does not move at all while the contact angle changes to θ_2, or the droplet is at the equilibrium state "b". Conversely, if a little liquid is taken away out of the drop, the droplet remains at equilibrium state "c" and the contact angle

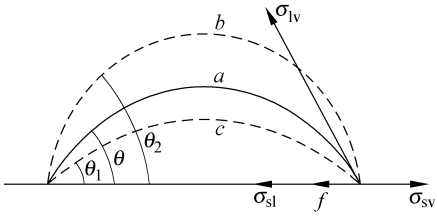

Figure 2.11 Contact angle hysteresis phenomenon

becomes θ_1 without contact line removal. If there are only three interfacial tensions on the contact line, from the equilibrium condition of mechanics the following expression would be derived for all cases as,

$$\cos\theta = \cos\theta_1 = \cos\theta_2 = \frac{\sigma_{sv} - \sigma_{sl}}{\sigma_{lv}} = \phi \tag{2.40}$$

This result of a unique contact angle, is in contradiction with experimental observations. Apparently, both Young's and Wenzel's theories are not able to characterize the experimental phenomena on rough solid surfaces, conceivably resulting in some confusing conclusions. There must be a new force existing at the contact line to obstruct droplet from spreading or contracting on a rough surface as the contact angle varies.

Wang et al. [8] introduced the hysteresis tension to represent the effect of surface roughness and proposed a simplified model to interpret the contact angle hysteresis on solid surfaces. This hysteresis tension, denoted as f representing force per unit contact line, always blocks the moving of the contact line, acting like a static resistance of a body having a moving trend, and changes its direction depending on liquid droplet spreading or contracting. For convenience, f is given as an algebraic constant depending on surface roughness, and $f > 0$ when f and σ_{sl} have a consistent direction, while $f < 0$ when the direction of f and σ_{sv} is consistent with each other. The equilibrium condition of mechanics is expressed as,

$$\sigma_{sv} = \sigma_{lv}\cos\theta + \sigma_{sl} + f \tag{2.41}$$

or

$$\cos\theta = \frac{\sigma_{sv} - \sigma_{sl}}{\sigma_{lv}} - \frac{f}{\sigma_{lv}} = \cos\theta_Y - \frac{f}{\sigma_{lv}} \tag{2.42}$$

And the advancing and receding contact angles are

$$\begin{aligned} \cos\theta_a &= \cos\theta - \frac{f_{max}}{\sigma_{lv}} \\ \cos\theta_r &= \cos\theta - \frac{f_{min}}{\sigma_{lv}} \end{aligned} \tag{2.43}$$

For a given droplet system, ϕ specified as a constant, the free energy-contact area curves would change as a function of roughness of surfaces, as illustrated in Fig. 2.12. The curves *a*, *b*, *c*, *d*, *e*, ⋯ , correspond to different rough surfaces, and the loci of advancing and receding contact angles are represented by the dash-line. There are three regions, an equilibrium region between the two loci and two non-equilibrium regions out side of the two loci. In the two non-equilibrium regions, since free energy is higher than the minimum, droplets tend to contract or spread minimizing free energy and move to their equilibrium states, while droplets are invariably at equilibrium in the middle region. It can be seen that the region of minimum free energy is enlarged as the surface becomes more irregular or rougher. This increase in the total system energy leads to that the system would exhibit less stability. Curve *a* is the free energy variation on an ideal smooth surface. The advancing contact angle is exactly same as the receding one, and there does not exist the contact angle hysteresis. As the surface becomes rougher, the advancing contact angle enlarges and the receding contact angle decreases, which means that the surface roughness enlarges the difference between advancing and receding contact angles. A surface with higher irregularity displays a lower ability to be wetted (larger advancing contact angle) and to be dried (smaller receding contact angle). These observations lead to the conclusion that the wettability of a solid surface includes two distinct physical natures, wetting and drying characteristics, which can be characterized by advancing and receding contact angles, respectively, as noted in most available literature.

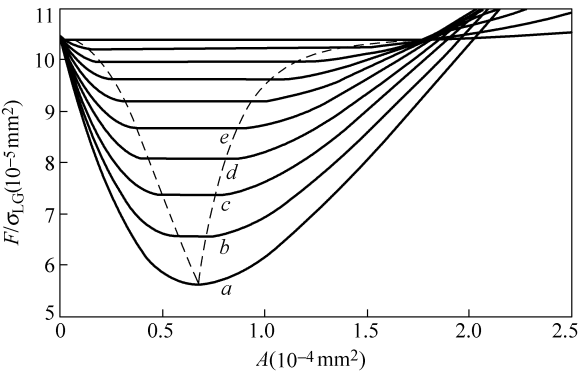

Figure 2.12 Change of free energy with surface roughness

2.4.3 Dynamical Contact Angle

In any boiling systems, dynamical contact angle, or contact angle in wetting dynamical processes and/or contact line movement, plays much more important role in understanding and describing boiling phenomena. The dynamical contact

angle is significantly different from static (equilibrium) contact angle and closely dependent of the velocity of the contact line, and the typical experimental results [9] are illustrated in Fig. 2.13. Very clearly, the static advancing and receding contact angles (θ_a and θ_r) are smaller or larger than those (θ'_a and θ'_r) obtained from extending the experimental results, respectively.

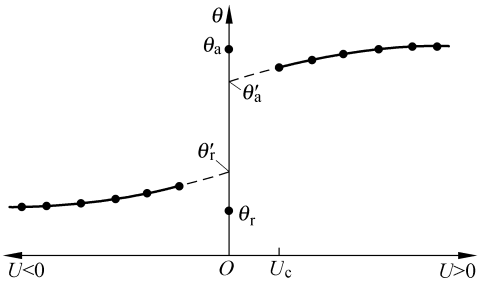

Figure 2.13 Dynamic contact angle changing with contact line velocity [9]

The movement of the contact line alters physical conditions in the immediate vicinity of the contact line and destroys mechanical equilibrium in the Young's equation. The unimaginable problem in the analysis of dynamic contact angle is the stress singularity in the immediate vicinity of contact line, as schematically shown in Fig. 2.14, which means that classical no-slip condition makes viscous stress infinite in the immediate vicinity of the contact line and is non-practical. Wang et al. conducted a series of investigations to experimentally and theoretically discuss the fundamentals of the dynamical contact angle characteristics [10 – 12]. Using their proposed hysteresis tension concept and associated theory, Wang et al. [13] theoretically demonstrated the following relationship of advancing and receding contact angles between static and extended from the dynamical measurements, or

$$\begin{aligned} \theta_a &> \theta'_a \\ \theta_r &< \theta'_r \end{aligned} \tag{2.44}$$

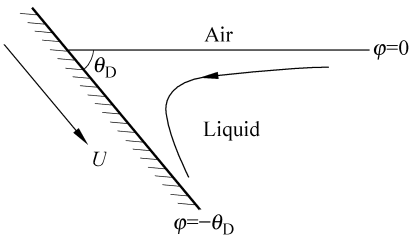

Figure 2.14 Flow in a contact line wedge corner

2.5 Cluster Dynamics

2.5.1 Clusters

Clusters consisting of tens and hundreds of atoms or molecules are a new class of compounds called atomic or molecular clusters [14]. These clusters are expected to have very interesting chemical and physical properties that span the range from molecular size to bulk. Small clusters have been very useful in the investigating intermolecular forces as well physical and chemical dynamics of molecular collisions and energy transfer, while large clusters have been widely employed in understanding the early stages of nucleation and condensation, chemical catalysis, and transition phenomena between molecular and condensed bulk materials. In studying boiling and condensation, "clusters" normally mean the ensembles of atoms or molecules having high energy that are bound without electronic coupling [14 – 17].

Focusing on understanding bubble nucleation in microscale boiling systems, Peng et al. [18] investigated molecular clusters of superheated liquids and the role of perturbations on the dynamics of clusters. Particularly, the number balance equation was formulated for activated molecules in clusters, and then a comprehensive discussion was conducted to investigate the dynamics of clusters formed with internal or external perturbations.

2.5.2 Number Balance of Activated Molecules in a Cluster

Consider a liquid system at ambient pressure, p_∞, and temperature, T, higher the corresponding boiling point temperature T_s at p_∞'. Apparently, the liquid is at a meta-stable state. Figure 2.15 schematically depicts the cluster association and/or dissociation processes.

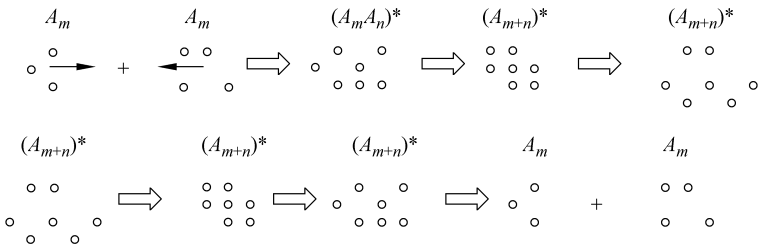

Figure 2.15 Association and dissociation of clusters

Consider an ensemble containing N_0 molecules, including n activated molecules in the cluster, N activated molecules in the bulk liquid, and the remaining N'

molecules (see Fig. 2.16), or, $N_0 = n + N + N'$. Then, the number balance of activated molecules in the cluster is:

$$\frac{\mathrm{d}n}{\mathrm{d}t} = \text{gain} - \text{loss} \tag{2.45}$$

The increase in n comes from the collision between activated molecules in cluster and the activated molecules in the bulk liquid. That is,

$$\text{gain} = \lambda N \times n \tag{2.46}$$

where λ is collision adsorption coefficient and could be expressed as a function of liquid superheat [19]:

$$\lambda = \nu(T - T_s) \tag{2.47}$$

Conventional nucleation theory states that

$$N = N_0 \exp\left(-\frac{\Delta G}{KT}\right) \tag{2.48}$$

where ΔG is the free energy of nucleation and could be approximated as:

$$\Delta G = \zeta(T - T_s)n \tag{2.49}$$

Then a first-order Taylor expansion of N in Eq. (2.48) gives:

$$N = N_0\left[1 - \frac{\zeta}{KT}(T - T_s)n\right]n \tag{2.50}$$

Substituting Eqs. (2.48) – (2.50) into Eq. (2.46) yields the following expression for the gain:

$$\text{gain} = \lambda N_0\left[1 - \frac{\zeta}{KT}(T - T_s)n\right]n \tag{2.51}$$

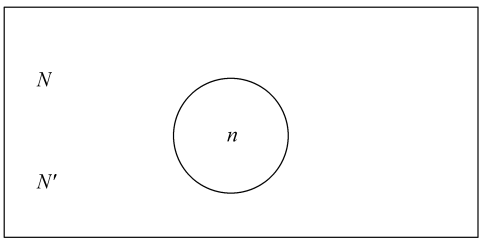

Figure 2.16 Number balance model

Each activated molecule in the cluster might become deactivated that is controlled by the difference between its chemical potential and that in the bulk liquid. Restated,

$$\text{loss} = kn \tag{2.52}$$

where k is the deactivation coefficient. The chemical potential $\mathrm{d}\mu = V\mathrm{d}p$, denoting the property difference between molecules under meta-stable state and those in the bulk liquid [20]. Restated, $k \propto |\, p_\infty - p_v \,|$.

Consequently, the number balance of activated molecules in a cluster could be stated as the follows:

$$\frac{\mathrm{d}n}{\mathrm{d}t} = k_1 n - k_2 n^2 \tag{2.53}$$

where

$$k_1 = \lambda N_0 - k \tag{2.54a}$$

$$k_2 = \lambda N_0 \frac{\xi}{k}\left(1 - \frac{T_\mathrm{s}}{T}\right) \tag{2.54b}$$

For a superheated liquid considered herein, $T > T_\mathrm{s}$, thereby $k_2 > 0$. On the other hand, k_1 could be positive or negative, depending upon the relative significance between association and dissociation processes.

A particular solution of Eq. (2.53) is:

$$n(t) = \frac{k_1}{2k_2} - \frac{|k_1|}{2k_2}\frac{C\exp\left(-|k_1|t\right) - 1}{C\exp\left(-|k_1|t\right) + 1} \tag{2.55}$$

where

$$C = \frac{\left|\dfrac{k_1}{k_2}\right| + \dfrac{k_1}{k_2} - 2n_0}{\left|\dfrac{k_1}{k_2}\right| + \dfrac{k_1}{k_2} + 2n_0} \tag{2.56}$$

and n_0 is the initial condition for n. Notably, $n(\infty) = 0$ for $k_1 \leqslant 0$; and $n(\infty) = k_1 / k_2$ for $k_1 > 0$. $k_1 = 0$ thereby denotes the critical point of the transcritical bifurcation.

For a non-positive k_1, the n_0 activated molecules in the cluster would finally die out. The inequality $k_1 = \lambda N_0 - k \leqslant 0$ can be rearranged as:

$$\Delta T = T - T_\mathrm{s} \leqslant \frac{k}{\nu N_0} \tag{2.57}$$

The physical interpretation of Eq. (2.57) is that if liquid superheat is less than

$k/\nu N_0$ and there is no external or internal perturbations, all clusters would collapse and the final steady state is $n=0$. Otherwise, the cluster would form that contain k_1/k_2 activated molecules.

2.5.3 Cluster Evolution with Internal Perturbations

Consider the number balance of n, Eq. (2.53), evolving with a white-noise perturbation, $\Gamma(t)$. The white noise is originated from the inhomogeneity self-generated in the superheated liquid, which satisfies the following two terms: $\Gamma(t)=0$ (zero-mean), and $\langle \Gamma(t)\Gamma(t')\rangle = 2D\delta(t-t')=0$ (independent actions). D denotes the strength of white-noise perturbation and δ is the delta function. The corresponding Fokker-Planck equation for the probability density function, $\rho(n,t)$, for the stochastic variable n at time t, is:

$$\frac{\mathrm{d}\rho(n,t)}{\mathrm{d}t} = -\frac{\partial}{\partial n}\left[\left(k_1 n - k_2 n^2\right)\rho(n,t)\right] + D\frac{\partial^2 \rho(n,t)}{\partial n^2} \tag{2.58}$$

The initial condition is $\rho(n,0)=\delta(n)$.

Define characteristic time $\tau = \sqrt{\frac{D}{k_1}}\,\mathrm{e}^{k_1 t}$. Let $\tau \ll 1$, that is, the very beginning of cluster evolution. Since the initial probability distribution is very close to $n=0$, $|n^2| \ll |n|$, and Eq. (2.58) has an analytical solution:

$$\rho(n,t) = \sqrt{\frac{k_1}{2\pi D(\mathrm{e}^{2k_1 t}-1)}}\exp\left[-\frac{k_1 n^2}{2D(\mathrm{e}^{2k_1 t}-1)}\right] \tag{2.59}$$

If $\sqrt{D} \ll \tau \ll 1$, Eq. (2.59) is simplified as:

$$\rho(n,t) = \frac{1}{\sqrt{2\pi\tau}}\exp\left\{-\frac{n^2}{2\tau^2}\right\} \tag{2.60}$$

Eq. (2.60) represents a Gaussian distribution around $n=0$.

In accord with Eq. (2.59), the time for the initial stage of relaxation process, t_s, is identified as $D^{-1} \gg \exp(2k_1 t_s) \gg 1$.

At the other extreme of $\tau \gg 1$, at the final steady state, the solution of Eq. (2.58) is:

$$\rho(n,\infty) = \sqrt{\frac{k_1}{4\pi D}}\exp\left[-\frac{k_1\left(n-\frac{k_1}{k_2}\right)^2}{D}\right] \tag{2.61}$$

Eq. (2.61) also represents a Gaussian-distribution with a mean value of $n = k_1 / k_2$.

Figure 2.17 schematically depicts the time evolution of a probability density function of a random variable *n*. The presence of large internal perturbation would introduce a Gaussian-distribution with a large variance however its mean value is the same as that with no perturbation (see Eq. (2.55)).

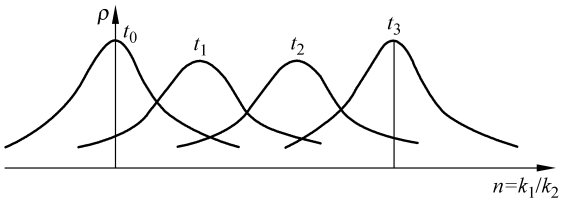

Figure 2.17 Probability density function with internal perturbation

2.5.4 Cluster Evolution with External Perturbations

For the cluster dynamics with the existence of external perturbations was considered, which are originated from sources other than the system self-generated fluctuations, the external perturbations could stochastically affect the values of system parameters, like k_1 (Notably, as stated above, $k \propto | p_\infty - p_v |$. Consequently, any external perturbations that would yield a change in system pressure would influence the parameter k_1). A form is assumed for the external perturbation as:

$$k_1^* = k_1 + \Gamma(t) \tag{2.62}$$

where $\Gamma(t)$ has the white-noise characteristics and $k_1 = \lambda N_0 - k$. The corresponding Fokker-Planck equation of the probability density function for the stochastic variable *n* at time *t*, is expressed as:

$$\frac{\mathrm{d}\rho(n,t)}{\mathrm{d}t} = -\frac{\partial}{\partial n}\left[(k_1 n - k_2 n^2)\rho(n,t) + Dn\rho(n,t) \right] + D\frac{\partial^2 n^2 \rho(n,t)}{\partial n^2} \tag{2.63}$$

The initial condition is $\rho(n,0) = \delta(n)$. The steady-state solution for Eq. (2.63) is obtained as:

$$\rho(n,\infty) = \delta(n) \quad \text{for} \quad k_1 \leqslant 0 \tag{2.64a}$$

$$\rho(n,\infty) = Cn^{\frac{k_1}{D}-1} \mathrm{e}^{-\frac{k_2 n}{D}} \quad \text{for} \quad k_1 > 0 \tag{2.64b}$$

The parameter *C* in Eq. (2.64b) is an integer constant.

Defining the potential function U_{FP} as $U_{\mathrm{FP}} = -D\ln\rho(n,t)$, we have the following

expressions:

$$U_{\mathrm{FP}} = \ln \delta(n) \quad \text{for} \quad k_1 \leqslant 0 \tag{2.65a}$$

$$U_{\mathrm{FP}}(n) = k_2 n - k_1 n + D \ln n - D \ln N \quad \text{for} \quad k_1 > 0 \tag{2.65b}$$

Notably, there are two qualitative changes in ρ-distribution occurring at $k_1 = D$ and 0. Figure 2.18 schematically illustrates such an occurrence. For $k_1 > D$, a maximum probability for cluster exists at a size of $n = (k_1 - D)/k_2$. For $0 < k_1 < D$, the maximum probability point is at $n = 0$, denoting that most molecules are not in the associated state (cluster). However, there is still possibility to have some clusters at a greater size in the system. For $k_1 < 0$, $n = 0$ behaves as the only attractor in the system. Regardless of the size of the initial clusters, eventually they will all dissociate into individual molecules. Imposing external perturbations would have a different influence to cluster dynamics than internal perturbations. Restated, external perturbation causing collapse of clusters.

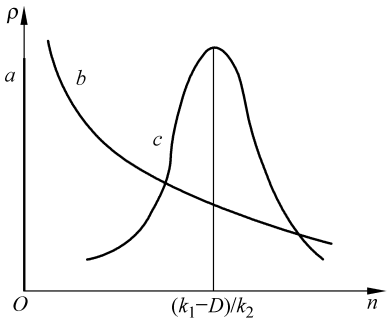

Figure 2.18 Probability density function with external perturbation

For the criterion of $k_1 < D$ with most activated molecules in a dissociated state, the liquid superheat could be found as:

$$\Delta T = T - T_{\mathrm{s}} \leqslant \frac{k + D}{\nu N_0} \tag{2.66}$$

Apparently, when compared with Eq. (2.57), the external perturbation would require a greater liquid superheat to form stable clusters of the smaller size $(k_1 - D)/k_2$.

References

[1] G. Van Wylen，R. E. Sonntag. Introduction to Thermodynamics—Classical and Statistical (2nd ed.). New York: John Wiley & Sons Inc., 1982.

[2] J. R. Howell, R. O. Buckius. Fundamentals of Engineering Thermodynamics. New York: McGraw-Hill Companies Inc., 1987.

[3] M. Modell, R. C. Reid. Thermodynamics and Its Applications(2nd ed.). Englewood Cliffs: Prentice-Hall, 1983.
[4] V. P. Carey. Liquid-Vapor Phase-Change Phenomena. Washington D. C.: Hemisphere Pub. Co., 1992.
[5] X. F. Peng. Interface shape and Marangoni effect around a bubble within the thermal boundary layer. 1996 National Heat Transfer Conference, AIAA 96-3974, Houston, Texas, August 3 – 6, 1996.
[6] R. N. Wenzel. Resistance of solid surfaces to wetting by water. Industrial Engineering Chemistry, 28: 988 – 994, 1936.
[7] R. J. Good. Contact angle, wetting, and adhesion: a critical review. in: K. L. Mittal (Ed.). Contact Angle, Wetting and Adhesion. VSP, Utrecht, The Netherlands, 3 – 36, 1993.
[8] X. D. Wang, X. F. Peng, B. X. Wang. Contact angle hysteresis and hysteresis tension on rough solid surfaces. Chinese Journal of Chemical Engineering, 12(5): 615 – 621, 2004.
[9] G. E. P. Elliott, A. C. Riddiford. Dynamic contact angles, Part 1. The effect of impressed motion. Journal of Colloid and Interface Science, 23: 389 – 398, 1967.
[10] X. D. Wang, X. F. Peng, J. F. Lu, et al. Contact angle hysteresis on rough solid surfaces.. Heat Transfer—Asian Research, 33(4): 201 – 210, 2004.
[11] X. D. Wang, X. F. Peng, B. X. Wang. Effect of solid surface properties on dynamic contact angles. Heat Transfer—Asian Research, 35(1): 1 – 12, 2006.
[12] X. D. Wang, X. F. Peng, Y. Y. Duan, et al. Dynamics of spreading of liquid on solid surface. Chinese Journal of Chemical Engineering, 15(5): 730 – 737, 2007.
[13] X. D. Wang, X. F. Peng, D. J. Lee. Description of dynamic contact angle on a rough solid surface. Proceedings of the 2003 ASME Summer Heat Transfer Conference, Vol.3: 283 – 288, Las Vegas, Nevada, USA, 2003.
[14] S. Kotake. Molecular clusters. In: C.L. Tien (Ed.). Microscale Energy Transport, 167 – 186, 1998.
[15] H. Y. Kwak, R. L. Panton. Tensile strength of simple liquids predicted by a molecular interaction model. J. Phys. D, 18: 647 – 659, 1985.
[16] H. Y. Kwak, S. Lee. Homogeneous bubble nucleation predicted by a molecular interaction model. ASME J. Heat Transfer, 113: 714 – 721, 1991.
[17] H. Y. Kwak, Y. W. Kim. Homogeneous nucleation and macroscopic growth of gas bubble in organic solutions. Int. J. Heat Mass Transfer, 41: 757 – 767, 1998.
[18] X. F. Peng, D. Liu, D. J. Lee. Cluster dynamics and fictitious boiling in microchannels. Int. J. Heat Mass Transfer, 43(23): 4259 – 4265, 2000.
[19] J. W. Westwater. Boiling of liquids. Adv. Chem. Engng., 2: 1 – 56, 1958.
[20] V. P. Skripov. Metastable Liquids (Chap. 2). New York: John Wiley & Sons Inc., 1974.

3 Boiling Nucleation

Abstract The nucleation process is investigated in terms of the nucleus formation, nucleus structure, inception nucleation phenomena, evolution process. The inception process of nucleation in a boiling system is studied by considering the surface adjoining effects. According to the supersaturation and chemical potential of the liquid near a flat surface, the stable layer, free energy peak and embryo bubble distribution would be further investigated. The evolution behavior of heterogeneous nucleation on a solid surface is analyzed in detail, and three main types of nucleation in ideal conical cavities are described as nucleation inside cavity, nucleation outside a cavity, and twice nucleation inside and outside a cavity.

Keywords nucleus, interface, stable layer, twice nucleation

Nucleation is a basic part of phase transformations, which plays an important role in understanding and describing any phase change processes. For a boiling process, nucleation appears in the initial stage, and directly affects bubble formation and boiling intensity.

According to the heterophase fluctuations which induce phase transition, the phase change has two main types. Classically, phase change caused by the fluctuation with large range and small region is named phase change of nucleation, for example as normal boiling process. The phase change caused by the fluctuation with little range and large region is named continuous phase change. In terms of the bulk phase and boundary conditions, nucleation has two main types as homogeneous nucleation and heterogeneous nucleation.

The discussion of normal boiling nucleation and systematic nucleation theory is beyond the scope of this book, and readers can refer to some classical books and textbooks [1, 2]. This chapter introduces some new understanding of boiling nucleation and achievements in the latest 20 years, particularly associated with author's research group.

X. Peng, *Micro Transport Phenomena During Boiling*

3.1 Nucleus Formation

3.1.1 Mean Free Path

Cluster theory [3, 4] states that there are generally a number of active molecules inside the bulk phase during phase transition process. Active molecules with higher energy have longer free pathes in the liquid. According to the molecular collision theory, the mean free path of a molecule in a single-component fluid is expressed as

$$l = \frac{1}{\sqrt{2}\pi n a_0^2} = \frac{0.707}{\pi n a_0^2} \tag{3.1}$$

where l is the mean free path, a_0 the effective molecule diameter, n the number density obtained from a state equation. At a specified state the number of the molecules whose free path ranges from x to $x + \mathrm{d}x$ is obtained from Eq. (3.1)

$$\left|\mathrm{d}n\right| = \frac{1}{l} n_0 \exp\left(-\frac{x}{l}\right)\mathrm{d}x \tag{3.2}$$

If the mean free path at saturation, l^s, is selected as the criterion for distinguishing active molecules from inactive molecules, all of the molecules whose mean free pathes are greater than l^s are active molecules. However, the real number of active molecules is less than expected. Therefore a positive constant η(<1) is introduced as a modification, which is dependent on the critical aggregation concentration (CAC). The concentration of the active molecules is expressed as

$$\frac{N_\mathrm{a}}{N_0} = \eta \exp\left(-\frac{l^s}{l}\right) \tag{3.3}$$

3.1.2 Self-Aggregation

With an increase of the temperature or a decrease of the pressure, the mean molecular free path and number of active molecules increases, and molecular energy distribution becomes heterogeneous in bulk phase. Generally, not all active molecules exist in the form of the monomers, some associating with each other to form an aggregate. Unlike solid particles or rigid macromolecules, aggregates have soft interfaces and their interaction forces are van der Waals and other microscopic forces.

Active molecules can be regarded as solute, while bulk phase molecules as

solvent. The number of active molecules is very small compared with bulk phase molecules. From Raoult's law, the chemical potential of active molecules is

$$\mu_N = \mu_N^0 + k_B T \ln \frac{X_N}{N} \qquad N = 1, 2, 3, \cdots \tag{3.4}$$

where μ_N and μ_N^0 are mean and standard chemical potential of an N-aggregate, respectively, and X_N / N is concentration. k_B is Boltzmann constant. The chemical potential of a molecule in an N-aggregate is

$$\overline{\mu_N} = \overline{\mu_N^0} + \frac{k_B T}{N} \ln \frac{X_N}{N} \qquad N = 1, 2, 3, \cdots \tag{3.5}$$

where $\overline{\mu_N^0} = \mu_N^0 / N$ is standard molecular mean chemical potential. When the bulk phase is at equilibrium, $\overline{\mu_N} = \mu_N / N$ is independent of aggregation number, N, and

$$\begin{aligned} \overline{\mu} &= \overline{\mu_1^0} + k_B T \ln X_1 = \overline{\mu_2^0} + \frac{k_B T}{2} \ln \frac{X_2}{2} \\ &= \cdots = \overline{\mu_N^0} + k_B T \ln \frac{X_N}{N} \quad N = 1, 2, 3, \cdots \end{aligned} \tag{3.6}$$

There exist dynamic processes in which monomers associate and aggregates disassociate in bulk phase (see Fig. 3.1). Regarded as a generalized chemical reaction, association rate and the disassociation rate are, respectively

$$r_a = k_1 X_1^N, \qquad r_d = k_N \frac{X_N}{N} \tag{3.7}$$

where k_1 and k_N are proportional constants. At equilibrium the association rate is equal to disassociation rate,

$$K = \frac{k_1}{k_N} = \exp\left[-\frac{N\left(\overline{\mu_N^0} - \overline{\mu_1^0}\right)}{kT} \right] \tag{3.8}$$

Combining Eq. (3.7) with Eq. (3.8) yields

$$X_N = N \left\{ X_1 \exp\left[\frac{\left(\overline{\mu_1^0} - \overline{\mu_N^0}\right)}{kT} \right] \right\}^N \tag{3.9}$$

and the total concentration of active molecules is

$$c = X_1 + X_2 + X_3 + \cdots = \sum_{N=1}^{\infty} X_N \tag{3.10}$$

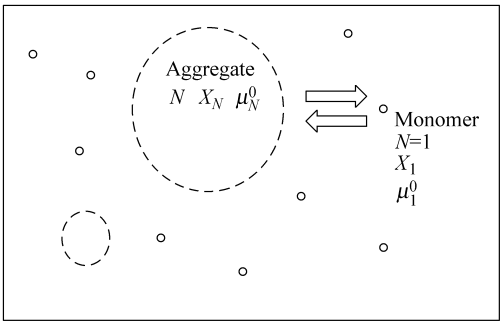

Figure 3.1 Association-disassociation of an aggregate with active molecules

Eqs. (3.9) and (3.10) constitute the fundamental equations of self-aggregation thermodynamics. It should be noted that Eq. (3.4) holds only for dilute solutions, where interactions between the aggregates is neglected.

3.1.3 Aggregate Formation

Assuming molecules in different sized aggregates all experience the same interaction with their surroundings, the value of the standard mean chemical potential in an *n*-aggregate is constant, or $\overline{\mu_1^0} = \overline{\mu_2^0} = \cdots = \overline{\mu_N^0}$. So, Eq. (3.9) evolves to

$$X_N = NX_1^N \tag{3.11}$$

Since $X_1<1$, then $X_N \ll X_1$. Apparently, almost all active molecules exist in monomer. $\overline{\mu_N^0}$ increases with N, active molecules become more difficult to form aggregates. Therefore, the necessary condition of aggregate formation is $\overline{\mu_N^0} < \overline{\mu_1^0}$ for some number values of N.

As first order approximation, the relation between $\overline{\mu_N^0}$ and N can simply be determined from aggregate geometry. Considering a one dimensional aggregate, as shown in Fig. 3.2(a), letting αkT be the bonding energy between monomers in an aggregate, and α a characteristic parameter describing the interaction between monomers or a monomer and solvent, total free energy of an N-aggregate is obtained as,

$$N\overline{\mu_N^0} = -(N-1)\alpha k_B T \tag{3.12}$$

$$\overline{\mu_N^0} = -\left(1-\frac{1}{N}\right)\alpha k_B T = \overline{\mu_\infty^0} + \frac{\alpha k_B T}{N} \tag{3.13}$$

As N increases, $\overline{\mu_N^0}$ decreases gradually up to $\overline{\mu_\infty^0} = -\alpha k_B T$.

A 2D aggregate of the active molecule is shown in Fig. 3.2(b). Because N (total molecular number of a disc) is proportional to the area or πR^2, and the molecule number located at the periphery of the disc is proportional to the perimeter of $2\pi R$ or $N^{1/2}$, the mean standard free energy of an active molecule is

$$\overline{\mu_N^0} = \overline{\mu_\infty^0} + \frac{\alpha k_B T}{N^{1/2}} \tag{3.14}$$

A 3D aggregate of radius R is given in Fig. 3.2(c). Because N is proportional to the volume of the sphere, $4\pi R^3/3$, and molecular number located at the sphere surface is proportional to the sphere area, $4\pi R^2$, or, $N^{2/3}$, the mean standard free energy of an active molecule is

$$\overline{\mu_N^0} = \overline{\mu_\infty^0} + \frac{\alpha k_B T}{N^{1/3}} \tag{3.15}$$

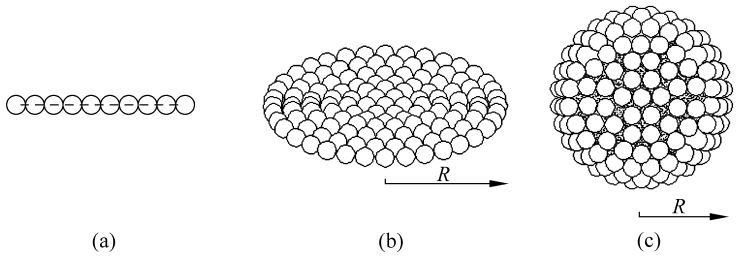

Figure 3.2 Simple patterns of aggregates
(a) 1D aggregate; (b) 2D aggregate; (c) 3D aggregate

Assuming v_0 is the mean volume of a molecule, total number of the molecules is $N = 4\pi R^3/3v_0$. The standard free energy of a spherical aggregate is the sum of volume and surface energy. Letting γ be Gibbs free energy per interface, or interfacial tension, the mean standard free energy of an active molecule in an N-aggregate is

$$\overline{\mu_N^0} = \overline{\mu_\infty^0} + \frac{4\pi R^2\gamma}{N} = \overline{\mu_\infty^0} + \frac{4\pi\gamma\left(\frac{3v_0}{4\pi}\right)^{2/3}}{N^{1/3}} = \overline{\mu_\infty^0} + \frac{\alpha k_B T}{N^{1/3}} \tag{3.16}$$

and

$$\alpha = \frac{4\pi\gamma\left(\frac{3v_0}{4\pi}\right)^{2/3}}{k_B T} = \frac{4\pi r^2\gamma}{k_B T} \tag{3.17}$$

where r is the effective radius of active molecules. For an N-aggregate of simple

geometry structure, the standard free energy of an active molecule can be expressed as

$$\overline{\mu_N^0} = \overline{\mu_\infty^0} + \frac{\alpha k_B T}{N^P} \tag{3.18}$$

where P is a dimensional or geometric factor. Eq. (3.18) means that all $\overline{\mu_N^0}$ of different dimensional aggregates monotonically decrease with the increase of N, which is the necessary condition for the formation of aggregates.

3.1.4 Critical Aggregation Concentration

Substituting Eq. (3.18) into Eqs. (3.9) and (3.10) yields,

$$X_N = N\left\{\exp\left[\frac{\left(\overline{\mu_1^0} - \overline{\mu_N^0}\right)}{k_B T}\right]\right\}^N = N\left\{X_1 \exp\left[\alpha\left(1 - \frac{1}{N^P}\right)\right]\right\}^N \approx N\left(X_1 \mathrm{e}^{\alpha}\right)^N \tag{3.19}$$

For a sufficiently low value of X_1, $X_1 \exp\left[\frac{\left(\overline{\mu_1^0} - \overline{\mu_N^0}\right)}{k_B T}\right]$ or $X_1 \mathrm{e}^{\alpha}$ is much less than unity, and it is apparent that $X_1 > X_2 > X_3 > \cdots$ At lower concentration almost all of the active molecules exist as monomers, i.e. $X_1 \approx \text{const}$. Since X_N can not exceed unity, clearly, X_1 ceases to increase once it approaches $\exp\left[-\frac{\left(\overline{\mu_1^0} - \overline{\mu_N^0}\right)}{k_B T}\right]$ or $\mathrm{e}^{-\alpha}$. Accordingly, this monomer concentration is referred to as the critical aggregation concentration of active molecules,

$$\left(X_1\right)_c = \mathrm{CAC} \approx \exp\left[-\frac{\left(\overline{\mu_1^0} - \overline{\mu_N^0}\right)}{k_B T}\right] \approx \mathrm{e}^{-\alpha} \tag{3.20}$$

Evidently, when the monomer concentration is lower than CAC, almost all active molecules exist as monomers and the aggregate concentration approximates to zero, and then $X_1 \approx c$. Line *Oa* in Fig. 3.3 describes the change of monomer concentration, and *Ob* denotes the change of total concentration. When monomer concentration approaches CAC and maintains invariable (*acd*) or $X_1 \equiv \mathrm{CAC}$, active molecules aggregate suddenly, and the concentration of aggregates rapidly increases along with the increase of the total concentration (*bce*).

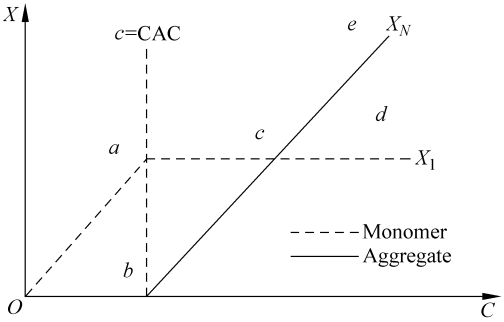

Figure 3.3 Monomer and aggregate concentration variation

3.1.5 Infinite Aggregation Formation

For disc-like and spherical aggregates, Eq. (3.9) becomes

$$\begin{cases} X_N = N\left[X_1 \mathrm{e}^{\alpha}\right]^N \mathrm{e}^{-\alpha N^{1/2}} & \text{1D} \\ X_N = N\left[X_1 \mathrm{e}^{\alpha}\right]^N \mathrm{e}^{-\alpha N^{2/3}} & \text{2D} \end{cases} \tag{3.21}$$

When monomer concentration approaches CAC, $X_1 \mathrm{e}^{\alpha} = 1$, Eq. (3.21) may be approximate to $X_N = N\exp(-\alpha N^{1/2})$ and $X_N = N\exp(-\alpha N^{2/3})$. For any reasonable positive values of α (>1), there will be few aggregates with $N > 5$, except for a few dimmers, trimer, etc. In other words, even if the total concentration of active molecules is higher than CAC, the concentration of aggregates is still very low. Because these active molecules do not exist steadily in the bulk phase, they have to be separated from bulk phase and form a nucleus, consequently phase transition happens. This process can also be regarded as the process of the formation of an infinite aggregate ($N \to \infty$).

Figure 3.4 shows a family of isotherms on a p-v diagram given by the van der Waals equation. According to thermodynamic theory the destruction of the stability implies occurrence of the phase transition. The spontaneous phase transition process of an ideal pure liquid or vapor must occur at the critical superheated point g or the critical supercooled point j without any external perturbations. Obviously, CAC1 and CAC2 correspond to the critical superheated point g and the critical supercooled point j, respectively. The parameter η in Eq. (3.3) can be identified as

$$\eta \approx \mathrm{CAC} \exp\left(\frac{\overline{\lambda}^s}{\overline{\lambda}_{\mathrm{sup,limit}}} \right) \tag{3.22}$$

3.1.6 Physical Configuration of Nucleus Formation

For boiling phenomenon, as a typical example, initial state of bulk phase stays at any point on *de* (referring to Fig. 3.4), temperature T_l = constant and the pressure greater than the saturated pressure p_s. Nearly, all active molecules exist as monomers since the concentration is much less than CAC. As the pressure decreases, the concentration of active molecules gradually increases. Secondly, when the pressure reaches and becomes lower than the saturated pressure p_s, the concentration is still less than CAC. However, if there are not any perturbations, for example, the local fluctuation or dust particles as nuclei, the liquid is at metastable superheated state and active molecules still exist as monomers. Finally, the pressure continuously decreases down to the critical superheated point *g*, active molecule concentration approaches CAC. At this time the monomer concentration keeps constant and then aggregation occurs. Since only a few of active molecule aggregates, for example, dimers, trimers, etc., is able to steadily exist in the bulk phase, a lot of active molecules has to spontaneously separate from the bulk phase which results in an infinite aggregation if the pressure keeps decreasing. Accordingly, nucleus or tiny new phase forms. On *efg* a perturbation, like a local fluctuation, can bring about a rapid increase in local monomer concentration, and this concentration locally reaches CAC, forming a nucleus. As observed in many experiments, boiling of metastable liquid will be abruptly produced when the tiny impurity is added, though the liquid is already at very high superheated temperature, but lower than the critical superheated temperature (the point *g*). This can be explained by that local perturbation or tiny impurity destroys the local balance of active molecule concentration and the concentration locally exceeds CAC.

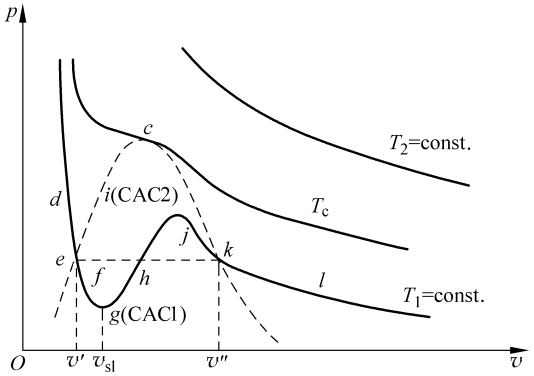

Figure 3.4 van der Waals isotherms

3.2 Interfacial Effects on Nucleation

3.2.1 Nucleus Structure Evolution

Obviously, active molecules first aggregate in a central region to form an initial nucleus, and then the nucleus gradually absorbs more active molecules and grows up. This model describes the physical nature of a nucleus formation, however, the liquid-vapor interface is still treated as a normal geometrically shaped interface without accounting for the effect of nucleus inner structure and evolution process. Practically, the homogeneous structure of a nucleus is only the final state of nucleus evolution.

With consideration of afore-mentioned formation process of a nucleus, a two-region structure model was proposed to describe the evolution of a nucleus [3], namely a central region and a transition region, as shown in Fig. 3.5. The inner structure is assumed to be a spherical zone having radius r_2 and consisting of two regions. The inner central region has radius r_1 and can be regarded as a pure vapor region with density ρ_v. The transition region surrounds the central region, and its density continually varies from the density of the central region, ρ_v, at r_1, to the density of the bulk liquid phase, ρ_l, at r_2. The active molecules first aggregate and aggregates grow in the transition region. Those close to the boundary of the central region convert into vapor phase and get into the inside of central region. As a result, the central region gradually enlarges, while the transition region continually expands outward and decreases its dimension during the whole evolution process of a nucleus. When the transition region approximately decreases to a thickness of several molecules, i.e. normal geometrical liquid-vapor interface forms, the revolution of a nucleus completes and a vapor bubble generates with stable liquid-vapor interface.

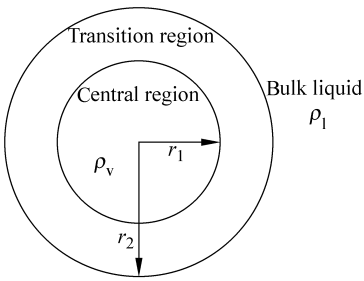

Figure 3.5 Structure of a nucleus

3.2.2 Interfacial Tension of a Nucleus

Walton et al. [5] suggested that the interfacial density was approximately proportional to the distance normal to the interface. It is reasonable to assume that in transition region the density distribution is linear (refer to Fig. 3.6). If transition region is divided into m layers with thickness $(r_2 - r_1)/m$ and uniform density, the density in layer j is $\rho_v + j(\rho_l - \rho_v)/m$. Assuming that the interfacial energy is proportional to the density differences between both side of a layer, the interfacial energy per unit area (interfacial tension) of layer j can be expressed as

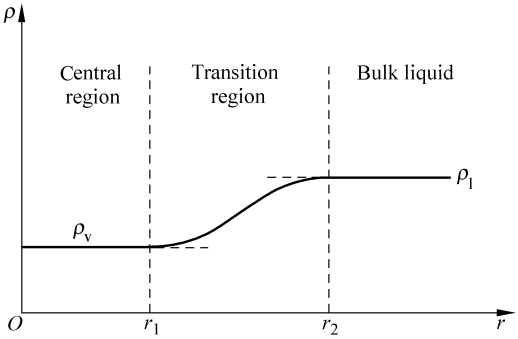

Figure 3.6 Density in transition region

$$\sigma_j = \frac{\sigma}{\rho_l - \rho_v}\frac{\rho_l - \rho_v}{m} = \frac{\sigma}{m} \tag{3.23}$$

where σ is the interfacial tension of normal liquid-vapor interface. The radius of layer j is

$$r_j = r_1 + \frac{r_2 - r_1}{m} j \tag{3.24}$$

and the area of layer j is

$$A_j = 4\pi r_j^2 = 4\pi\left(r_1 + \frac{r_2 - r_1}{m} j\right)^2 \tag{3.25}$$

The total interfacial energy of layer j is

$$F_j = \sigma_j A_j = \frac{4\pi\sigma}{m}\left(r_1 + \frac{r_2 - r_1}{m} j\right) \tag{3.26}$$

Consequently, total interfacial energy of the transition region is expressed as

$$F^m = \sum_j F_j = \frac{4\pi\sigma}{m}\sum_j\left(r_1 + \frac{r_2 - r_1}{m}j\right)^2$$
$$= \frac{4\pi\sigma}{m^3}\left[m^3 r_1 + \frac{m^3 + m^2}{m^3}r_1\left(r_2 - r_1\right) + \frac{m\left(m+1\right)\left(2m+1\right)}{6}\left(r_2 - r_1\right)^2\right] \quad (3.27)$$

As $m\to\infty$, the total interfacial energy of transition region tends to a constant, or

$$F = \lim_{m\to\infty} F^m = 4\pi\sigma\left[r_1^2 + r_1\left(r_2 - r_1\right) + \frac{1}{3}\left(r_2 - r_1\right)^2\right] \quad (3.28)$$

Interfacial tension per unit area (interfacial tension) of a nucleus can be expressed as

$$\gamma = \frac{F}{4\pi r_2^2} = \frac{r_1^2 + r_1\left(r_2 - r_1\right) + \frac{1}{3}\left(r_2 - r_1\right)^2}{r_2^2}\sigma \quad (3.29)$$

Figure 3.7 illustrates the variation of the interfacial tension with r_2 keeping a constant of 1 μm. Apparently, the interface evolves to normal macroscopic one as the transition region entirely converts into vapor phase. This model also exhibits that both interface and interfacial tension gradually generate during phase evolution.

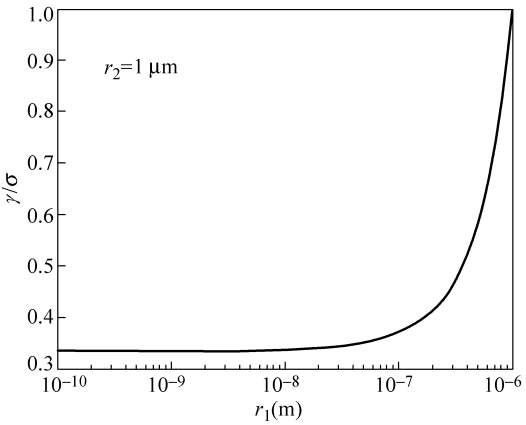

Figure 3.7 Interfacial tension variation

3.2.3 Modification of Nucleation Rate

If the Gibbs surface tension is adopted, the interfacial tension between bulk liquid phase and a nucleus is the same as macroscopic liquid-vapor interface. From classical nucleation theory, the nucleation rate is expressed as

$$J = n\frac{k_B T_l}{h}\exp\left(-\frac{4\pi r_c^2 \sigma}{3k_B T_l}\right) \tag{3.30}$$

where n denotes number density of molecules, h the Planck constant, T_l temperature of bulk liquid phase, r_c critical nucleus radius. From Eq. (3.30) the order of the nucleation rate at the critical superheated state is evaluated only 10^6 cm^{-3}/s, whereas the actual nucleation rate was experimentally determined as 10^{22} cm^{-3}/s. Apparently, the interfacial tension between bulk liquid phase and a nucleus plays a critical role in predicting J, and the interfacial tension should account for the effect of nucleus structure and molecular interaction in modifying the interfacial tension with γ rather than handling as an ideal interface [3 – 5].

Nucleation rate is assumed to happen at the instant earliest vapor phase generating at the center of an aggregate or a nucleus with a structure, particularly with density gradients from the center to bulk liquid phase. This is to say, the interfacial tension between the bulk liquid phase and a nucleus is approximately,

$$\gamma \approx \frac{1}{3}\sigma \tag{3.31}$$

Substituting Eq. (3.31) into (3.30) to replace σ with γ yields the nucleation rate as $J \approx 10^{21}$ cm^{-3} /s. This value is quite close to the experimental result. Very clearly, when the central region or r_l approaches zero, the interfacial tension between bulk liquid phase and a nucleus satisfies Eq. (3.31). When the transition region completely converts into vapor phase, the macroscopic liquid-vapor interface and an embryo bubble forms, and associated interfacial tension approaches to the normal value.

In addition to improving the prediction of the nucleation rate, the present analysis indicates that the model or structure of a nucleus clearly describes the physical nature. The nucleation is the evolution of a nucleus, particularly matter structure of a nucleus. And the definition of the nucleation rate implies the generation of nuclei having the appearance of pure vapor in the inner central region.

3.3 Microscope Activation near a Flat Surface

3.3.1 Liquid Behavior near a Heated Wall

For a heterogeneous boiling system, the classical theory states that a vapor embryo bubble is easily generated on a heated surface due to its higher surface energy [1]. On the other hand, an ultrathin film forms underneath a bubble during boiling, and it can strongly enhance the heat and mass transfer in nucleate boiling

[1, 6 – 8]. Apparently, these two conclusions are different opinions. The long distance intermolecular force near the wall was used to describe the fundamental behavior of these phenomena [9, 10], with a theoretical investigation conducted to determine where nucleation is most likely to occur [11].

The forces between the solid and liquid are either attractive or repulsive. For liquid very close to the surface, only the attractive force plays an important role as shown in Fig. 3.8. The Hamaker formula is usually applied to describe the interaction potential between liquid phase and solid surface, or expressed as,

$$\Pi(h) = -\frac{A_{\mathrm{slv}}}{6\pi h^3} \tag{3.32}$$

where A_{slv} is Hamaker constant, and $\Pi(h)$ is the attractive potential per unit liquid area at a distance from the wall, h. The liquid pressure change caused by the attractive force is

$$p_{\mathrm{att}}(h) = \int_h^\infty -\frac{\partial \Pi}{\partial h}\mathrm{d}h = -\frac{A_{\mathrm{slv}}}{6\pi h^3}\bigg|_h^\infty = \frac{A_{\mathrm{slv}}}{6\pi h^3} \tag{3.33}$$

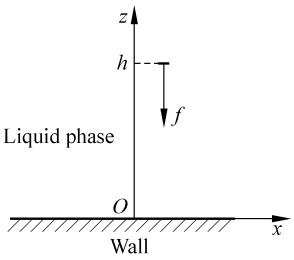

Figure 3.8 Attractive force between liquid near the wall and the solid wall

Consequently, the local pressure is

$$p(h) = p_0 + \frac{A_{\mathrm{slv}}}{6\pi h^3} \tag{3.34}$$

p_0 denotes the liquid pressure without the long-range force interaction effect. $p(h)$ sharply rises close to the wall due to the very strong long-range force interaction.

For a saturated vapor-liquid system, the pressure is a function of liquid saturation temperature described by the Clausius-Clapeyron as,

$$\left(\frac{\mathrm{d}p}{\mathrm{d}T}\right)_{\mathrm{sat}} = \frac{h_{\mathrm{lv}}}{T\left(v_{\mathrm{l}} - v_{\mathrm{v}}\right)} \tag{3.35}$$

For a small temperature rise at the saturation line, as shown in Fig. 3.9, the change in saturation pressure can be approximated from Eq. (3.35) as

$$\Delta p = \frac{h_{\mathrm{lv}}}{T_{0,\mathrm{sat}}\left(v_{\mathrm{l}} - v_{\mathrm{v}}\right)}\Delta T = \frac{h_{\mathrm{lv}}\Delta T}{T_{0,\mathrm{sat}}\Delta v} \tag{3.36}$$

where $T_{0,\mathrm{sat}} = T_{\mathrm{sat}}(p_0)$ is the saturation temperature corresponding to p_0. And the saturation pressure corresponding to the local temperature approximates to

$$p_{\mathrm{sat}}(T) = p_0 + \frac{h_{\mathrm{lv}}\Delta T_{\mathrm{sup}}}{T_{0,\mathrm{sat}}\Delta v} \tag{3.37}$$

where $\Delta T_{\mathrm{sup}} = T - T_{0,\mathrm{sat}}$ is the superheat on the wall corresponding to the saturation temperature $T_{0,\mathrm{sat}}$. For the liquid near the wall within a thermal boundary layer, the temperature changes very little over a very short distance.

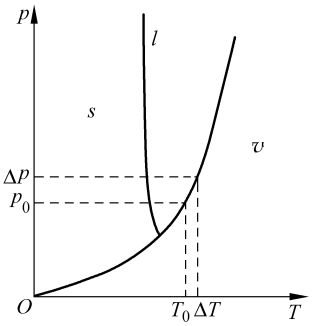

Figure 3.9 Phase diagram of water

The liquid close to the wall is superheated and metastable state corresponding to the bulk liquid pressure. Since in this region the local pressure rises sharply due to the long-range interaction effects, while the saturation pressure increases slowly as the liquid temperature rises in the thermal boundary, there exists a region near the wall where the saturation pressure is lower than the local liquid pressure, and consequently the liquid phase is subcooled and stable immediately next to the wall as a stable liquid sublayer. It is reasonably expected that nucleation would not be able to occur in the sublayer and exactly on the wall.

In this stable sublayer, the pressure is $p(h) \geqslant p_{\mathrm{sat}}(T)$. Comparing Eqs. (3.34) and (3.37) yields

$$\frac{A_{\mathrm{slv}}}{6\pi h^3} \geqslant \frac{h_{\mathrm{lv}}\Delta T_{\mathrm{sup}}}{T_{0,\mathrm{sat}}\Delta v} \tag{3.38}$$

At exactly close to the wall, $\Delta T_{\mathrm{sup}} \approx \Delta T_{\mathrm{w,sup}}$, where $T_{\mathrm{w,sup}}$ is the wall superheat, and then the thickness of stable sublayer is derived as,

$$h_{\mathrm{c}} = \sqrt[3]{\frac{A_{\mathrm{slv}}\Delta v T_{0,\mathrm{sat}}}{6\pi h_{\mathrm{vl}}\Delta T_{\mathrm{w,sup}}}} \tag{3.39}$$

Obviously, the thickness of the stable sublayer decreases with the superheat rising. For saturated water at $p_0 = 10^5$ Pa, $T_{0,\mathrm{sat}} = 373$ K, the associated parameters and thermal properties are $h_{\mathrm{vl}} \approx 2.257 \times 10^6$ J/kg, $\Delta v = 1.681$ m^3/kg, $A_{\mathrm{slv}} \approx 10^{-20}$ J, and in a normal situation, $\Delta T_{\mathrm{w,sup}} = 10$ K. Both local pressure and saturation pressure near the wall is illustrated in Fig. 3.10 for this case. The thickness of the stable sublayer is $h_{\mathrm{c}} = 2.45 \times 10^{-9}$ m, which is much smaller than the critical radius of an embryo bubble.

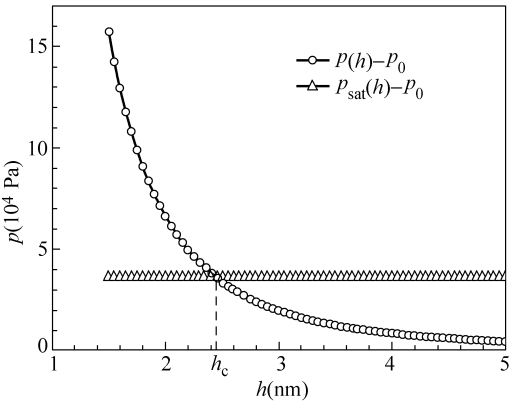

Figure 3.10 Pressure variation near a wall

In this liquid film sublayer, the liquid phase is subcooled and stable, and the embryo bubble is difficult to form. As a result, nucleation mostly occurs beyond this sublayer, and the sublayer is probably the initial structure of the ultrathin film below a bubble.

3.3.2 Nucleation Position

In classical thermodynamics, the supersaturation, s, is usually used to describe the phase stability and defined as

$$s = p_{\mathrm{sat}} - p \tag{3.40}$$

From Eqs. (3.34) and (3.37) liquid supersaturation near a heated wall is derived as

$$s(h) = p_{\mathrm{sat}}(h) - p(h) = \frac{h_{\mathrm{lv}} \Delta T_{\mathrm{sup}}}{T_{0,\mathrm{sat}} \Delta v} - \frac{A_{\mathrm{slv}}}{6\pi h^3} \tag{3.41}$$

In a very small wall region, the liquid temperature varies approximately linearly with the distance as

$$T = T_{0,\mathrm{sat}} + \Delta T_{\mathrm{w,sup}} - \alpha h \tag{3.42}$$

or $\Delta T_{\text{sup}}(h) = \Delta T_{\text{w,sup}} - \alpha h$ and simply $\Delta T(h) = \Delta T_{\text{w}} - \alpha h$. So,

$$s(h) = \frac{h_{\text{lv}} \Delta T_{\text{w,sup}}}{T_{0,\text{sat}} \Delta v} - \frac{h_{\text{lv}} \alpha h}{T_{0,\text{sat}} \Delta v} - \frac{A_{\text{slv}}}{6\pi h^3} \tag{3.43}$$

By setting $\partial s / \partial h$ to zero, the critical distance is derived as

$$h_{\text{p}} = \sqrt[4]{\frac{A_{\text{slv}} T_{0,\text{sat}} \Delta v}{2\pi \alpha h_{\text{lv}}}} \tag{3.44}$$

At the critical distance h_{p}, the liquid with maximum supersaturation would be the most unstable and easiest to form an embryo bubble. On the other hand, the liquid within the sublayer $h < h_{\text{c}}$ is still subcooled and is hardly to nucleate. For water and $\alpha \approx 10^4$ K / m, the supersaturation variation is illustrated in Fig. 3.11, and the critical distance is obtained as $h_{\text{p}} \approx 8.16 \times 10^{-8}$ m. Apparently, h_{p} is normally greater than h_{c}, so nucleation should occur above the sublayer.

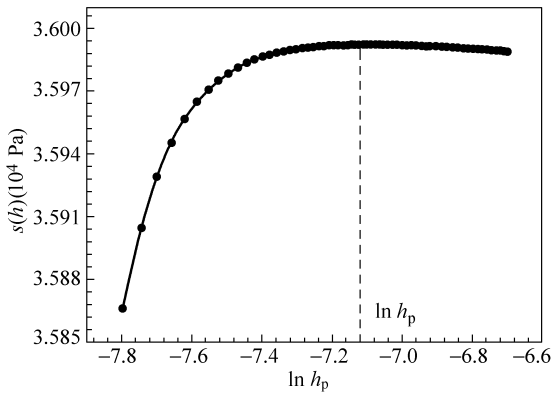

Figure 3.11 Supersaturation variation near the wall

From Eq. (3.35), $\Delta T = \Delta p \Delta T_{0,\text{sat}} \Delta v / \Delta v_{\text{lv}}$, and the saturation temperature at the local position from Eq. (3.34) is

$$T_{\text{sat}}(p) = T_{0,\text{sat}} + \frac{T_{0,\text{sat}} \Delta v}{h_{\text{lv}}} p_{\text{att}} = T_{0,\text{sat}} + \frac{T_{0,\text{sat}} \Delta v}{h_{\text{lv}}} \frac{A_{\text{slv}}}{6\pi h^3} \tag{3.45}$$

From Eqs. (3.42) and (3.45), the local superheat is

$$\Delta T_{\text{l,sup}}(h) = \Delta T_{\text{w,sup}} - \alpha h - \frac{T_{0,\text{sat}} \Delta v}{h_{\text{lv}}} \frac{A_{\text{slv}}}{6\pi h^3} \tag{3.46}$$

Comparing Eq. (3.45) with Eq. (3.42) yields

$$\Delta T_{\mathrm{l,sup}}(h) = s(h)\frac{T_{0,\mathrm{sat}}\Delta v}{h_{\mathrm{lv}}} \tag{3.47}$$

The superheat in Eq. (3.47) is linearly related with the supersaturation, implying that the maximum superheat also occurs at the same position as the maximum supersaturation. Substituting Eq. (3.44) into Eq. (3.46) yields

$$\Delta T_{\mathrm{l,sup,max}}(h) = \Delta T_{\mathrm{w,sup}} - \alpha h_{\mathrm{p}} - \frac{T_{0,\mathrm{sat}}\Delta v}{h_{\mathrm{lv}}}\frac{A_{\mathrm{slv}}}{6\pi h_{\mathrm{p}}^3} \tag{3.48}$$

And the maximum superheat or Eq. (3.48) is re-written as

$$\Delta T_{\mathrm{l,sup,max}}(h) = \Delta T_{\mathrm{w,sup}} - \Delta T_{\mathrm{D}} \tag{3.49}$$

where $\Delta T_{\mathrm{D}} = \alpha h_{\mathrm{p}} + \frac{T_{0,\mathrm{sat}}\Delta v}{h_{\mathrm{lv}}}\frac{A_{\mathrm{slv}}}{6\pi h_{\mathrm{p}}^3} = \frac{4}{3}\alpha^{3/4}A_{\mathrm{slv}}{}^{1/4}\left(\frac{T_{0,\mathrm{sat}}\Delta v}{2\pi h_{\mathrm{lv}}}\right)^{1/4}$ denotes the superheat decrement due to the effect of the disjoining force, and it increases with the temperature gradient rising. From Eq. (3.49), the wall superheat in a boiling system at least satisfies $\Delta T_{\mathrm{w,sup}} > \Delta T_{\mathrm{D}}$.

3.3.3 Embryo Bubble Evolution

As noted in Chapter 2, the chemical potential difference usually describes the phase change evolution process. The vapor chemical potential difference relative to the saturation state is

$$\mu_{\mathrm{v}} = RT\ln(p/p_{\mathrm{sat}}) \tag{3.50}$$

where R is the ideal gas constant. Eq. (3.50) can be linearized as

$$\begin{aligned}\mu_{\mathrm{v}} &= RT\ln\{[p_{\mathrm{sat}} + (p - p_{\mathrm{sat}})]/p_{\mathrm{sat}}\} \\ &\approx (RT/p_{\mathrm{sat}})(p - p_{\mathrm{sat}}) = v_{\mathrm{v}}(p - p_{\mathrm{sat}})\end{aligned} \tag{3.51}$$

where v_{v} is vapor specific volume. The chemical potential difference of liquid relative to its saturation state is

$$\mu_{\mathrm{l}} = v_{\mathrm{l}}(p - p_{\mathrm{sat}}) \tag{3.52}$$

where v_{l} is liquid specific volume.

For the case of $R = 461.89\ \mathrm{J/(K\cdot kg)}$, $T_{\mathrm{w,sup}} = 10\ \mathrm{K}$, $p_{\mathrm{sat}} = 1.43\times10^5\ \mathrm{Pa}$, $v_{\mathrm{v}} = 1.572\ \mathrm{m^3/kg}$, the chemical potentials of the liquid and vapor near saturation are shown in Fig. 3.12.

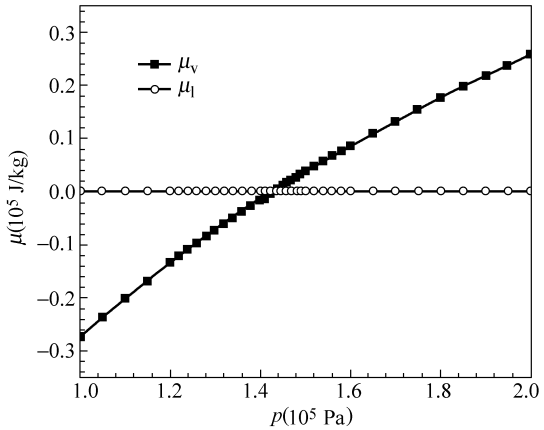

Figure 3.12 Chemical potential for vapor and liquid phase

The chemical potential difference at the local temperature and pressure is

$$\Delta\mu(h) = \mu_v(h) - \mu_l(h) \tag{3.53}$$

Substituting Eqs. (3.51) and (3.52) into Eq. (3.53) yields

$$\Delta\mu(h) = (v_v - v_l)(p - p_{sat}) = -(v_v - v_l)s(h) \tag{3.54}$$

The chemical potential difference corresponding to Fig. 3.11 is illustrated in Fig. 3.13, where $v_v - v_l \approx 1.571\ \mathrm{m^3/kg}$. Obviously, the position of the maximum supersaturation also has the maximum chemical potential difference. Consequently, the nucleation is mostly like to occur at the critical distance.

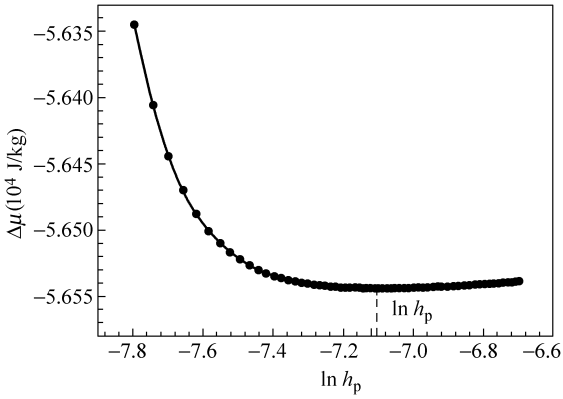

Figure 3.13 Chemical potential difference

An embryo bubble or new phase is induced by free energy fluctuation. The whole excess free energy of an embryo bubble is expressed as [12]

$$\Delta G(r) = \frac{4}{3}\pi r^3 \rho_v \Delta\mu + 4\pi\sigma r^2 \tag{3.55}$$

For simplification, the formation of an embryo bubble is considered in the bulk phase with high thermal conductivity. Therefore, the nucleation process is isothermal at temperature T, and the equilibrium distribution of heterophase fluctuation or clusters is

$$n = N\exp\left[-\frac{\Delta G(r)}{k_B T}\right] \tag{3.56}$$

Substituting Eq. (3.55) into Eq. (3.56) yields

$$n(r) = N\exp\left[-\frac{4\pi\sigma r^2}{k_B T} - \frac{4\pi r^3}{3k_B T v_v}\Delta\mu\right] \tag{3.57}$$

Apparently, as the liquid is just close to the surface, an embryo bubble is difficult to form, and it probably occurs away from the surface. And large embryo bubbles generate more far away than small embryo bubbles.

In the whole formation process of embryo bubbles and bubbles, the disjoining force maintains a stable sublayer adjacent to the surface, and the heterogeneous fluctuation mainly occurs beyond this sublayer at the initial time. As an embryo bubble grows, the region between embryo bubble and surface or the stable sublayer is just the preliminary structure of ultrathin film.

3.4 Bubble Evolution from a Cavity

3.4.1 Description of Heterogeneous Nucleation

The dynamical evolution of a heterogeneous nucleation is evidently dependent upon many factors as cavity structure, cluster structure and thermodynamic conditions. For heterogeneous nucleation occurring in an ideal conical cavity with cavity radius R, conical angle β and contact angle $\theta = 90^\circ$, as shown in Fig. 3.14, the growth process of a cluster can be divided into three stages: growing within the cavity, growing at the edge of the cavity, and growing outside the cavity. Correspondingly, the change of the free energy is expressed as,

$$\Delta G(r) = \Delta\mu_d V + \sigma_{lv} S_{lv} - \sigma_{sl} S_{sl} + \sigma_{sv} S_{sv} \tag{3.58}$$

where S_{lv} and S_{sv} are the area of interface between new and bulk phase and the contact area between new phase and solid surface, respectively, S_{sl} contact area between bulk liquid and solid surface.

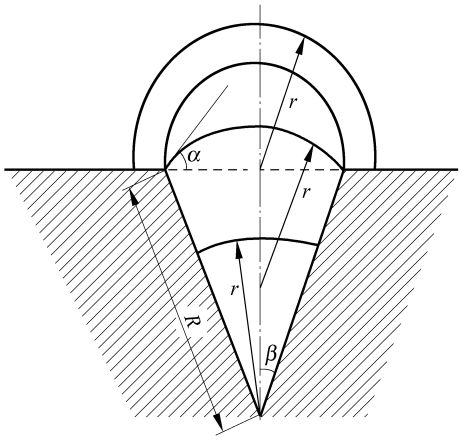

Figure 3.14 Evolution of a cluster in a cavity

For $\theta = 90^\circ$ and $\sigma_{sl} - \sigma_{sv} = \sigma_{lv}\cos\theta$, Eq. (3.57) can be simplified to

$$\Delta G(r) = \Delta\mu_d V + \sigma_{lv} S_{lv} \tag{3.59}$$

At very early beginning when phase fluctuation occurs a cluster forms in a cavity, as shown in Fig. 3.14, and geometrical parameters of the cluster are $r < R$ and

$$S_{lv} = 2\pi r^2(1-\cos\beta) \tag{3.60a}$$

$$V = S_{sv} r/3 = \frac{2}{3}\pi r^3(1-\cos\beta) \tag{3.60b}$$

$$S_{sv} = \pi r^2 \sin\beta \tag{3.60c}$$

Substituting Eq. (3.60) into Eq. (3.59) yields

$$\Delta G(r) = \left(\frac{4}{3}\pi r^3 \Delta\mu_d + 4\pi\sigma_{lv} S_{lv}\right)\frac{1-\cos\beta}{2} \tag{3.61}$$

As the contact line slips to the cavity edge, the angle α varies from β to 90°, and the radius of the cluster is

$$r = \frac{\sin\beta}{\sin\alpha} R \tag{3.62}$$

The geometric parameters of the cluster at the edge for $\beta \leqslant \alpha \leqslant 90^\circ$ are

$$S_{lv} = 2\pi r^2(1-\cos\alpha) \tag{3.63a}$$

$$V = \frac{1}{3}\pi R^3 \sin^2\beta\cos\beta + \frac{1}{3}(1-\cos\alpha)^2(2+\cos\alpha)\pi r^3 \tag{3.63b}$$

Substituting Eqs. (3.62) and (3.63) into Eq. (3.59) yields

$$\Delta G(r) = \Delta\mu_{\mathrm{d}}\left[\frac{1}{3}\pi R^3 \sin^2\beta\cos\beta + \frac{1}{3}\pi r^3(1-\cos\alpha)^2(2+\cos\alpha)\right] + \sigma_{\mathrm{lv}} 2\pi r^2(1-\cos\alpha) \tag{3.64}$$

When the cluster grows outside the cavity, the geometric parameters of the cluster for $r > R\sin\beta$ are

$$S_{\mathrm{lv}} = 2\pi r^2 \tag{3.65a}$$

$$V = \frac{1}{3}\pi R^3 \sin^2\beta\cos\beta + \frac{2}{3}\pi r^3 \tag{3.65b}$$

Substituting Eq. (3.65) into Eq. (3.59) yields

$$\Delta G(r) = \left(\frac{1}{3}\pi R^3 \sin^2\beta\cos\beta + \frac{2}{3}\pi r^3\right)\Delta\mu_{\mathrm{d}} + 2\sigma_{\mathrm{lv}}\pi r^2 \tag{3.66}$$

The radius of a cluster generated from a cavity, predicted by Eqs. (3.60b), (3.63b) and (3.65b), exhibits the variation with the volume shown in Fig. 3.15, where $V_{\mathrm{r}} = \pi R^3/3$. The radius of the cluster firstly increases to R from zero within the cavity, then decreases to $R\sin\beta$ at the cavity edge, and finally increases again as it crosses over the edge. As a result, the nucleation process is reasonably expected to have different characteristics in different conical cavity structures.

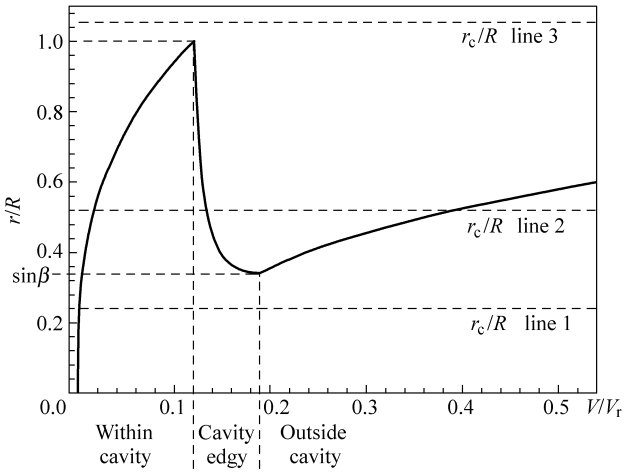

Figure 3.15 Radius variation of a cluster ($\beta = 20^\circ$)

According to cluster dynamical evolution in Fig. 3.15, there are three main types of heterogeneous nucleation. For $r_c / R \leqslant \sin\beta$, corresponding to line 1, the radius of a cluster is possible to reach the critical radius within the cavity, or the minimum radius of cluster at edge is larger than the critical radius. This is to say, if a cluster grows and reaches the critical radius within the cavity, it is going to spontaneously grow and finally evolve into a mature bubble. For $r_c / R > 1$, line 3, the radius of a cluster can reach its critical radius only outside the cavity. Apparently, the cluster would not evolve into a mature bubble within the cavity. For $\sin\beta < r_c / R < 1$, line 2, a cluster will experience the critical radius three times as it generates and grows up within the cavity, on the cavity edge and outside the cavity, and this kind of nucleation is reasonably expected to have some special behavior not fully understood and probably very different from normal classical nucleation.

The equilibrium distribution of clusters (new phase) in a system is [12]

$$n_i = N_0 \exp(-\Delta G(i) / kT) \tag{3.67}$$

where N_0 denotes molecule number per volume. Apparently, the equilibrium distribution of clusters is mainly dependent upon the change of free energy.

For nucleation on an ideal flat surface (surface without any cavities), the number of molecules immediately adjacent to the surface per unit of surface area can be taken as $N = N_0^{2/3}$, and the equilibrium distribution of the clusters is expressed as [1]

$$n_i = N_0^{2/3} \exp\left[-\frac{\Delta G(i)}{k_B T}\right] \tag{3.68}$$

For nucleation on a surface with ideal conical cavities or cavities having very regular configurations as shown in Fig. 3.14, the number of molecules adjacent to this type of cavities per unit surface area is determined by the number of these cavities per unit of area N_{ca} and the number of adjacent molecules for one cavity n_{ca}. Similar to Eqs. (3.67) and (3.68), the equilibrium distribution of the clusters in this type of cavities is expressed as [10]

$$n_i = N_{nc} n_{ca} \exp\left[-\frac{\Delta G(i)}{k_B T}\right] = N \exp\left[-\frac{\Delta G(i)}{k_B T}\right] \tag{3.69}$$

where $N = N_{nc} n_{ca}$. As a general expression, the equilibrium distribution of clusters all is stated as $n_i = N \exp\left[-\frac{\Delta G(i)}{k_B T}\right]$, and N is determined by different nucleation conditions.

As generally assumed in classical nucleation theory, the clusters only aggregate or dissipate a single particle, and the kinetic equation has the standard form [1]

$$\frac{\partial f_i}{\partial t} = w^+_{i-1,i} f_{i-1} - w^-_{i+1,i-1} f_i + w^-_{i+1,i} f_{i+1} - w^+_{i,i+1} f_i \tag{3.70}$$

where f_i is the distribution of a new cluster containing i single particles, $w^+_{i-1,i}$ the probability that a cluster absorbs a particle per unit time and the number of particles in a cluster is increased from $i-1$ to i, $w^-_{i+1,i}$ the probability for a cluster to release one particle per unit time and transfer to the state with i particles. The cluster volume $V = i\omega$, here ω means the volume per particle. The net flow J_i is described as,

$$J_i = w^+_{i,i+1} f_i - w^-_{i+1,i} f_{i+1} \tag{3.71}$$

where $w^+_{i,i+1} = s_i \alpha_i$, $w^-_{i,i-1} = s_i \beta_i$, and α_i, β_i denotes evaporation and condensation coefficient, or the number of molecule that evaporate and condensate per area, respectively. Under equilibrium condition, the condensation or evaporation is equal, or $J_i = w^+_{i,i+1} n_i - w^-_{i+1,i} n_{i+1} = 0$, and then the equilibrium condition is

$$\frac{w^+_{i,i+1}}{w^-_{i+1,i}} = \frac{n_{i+1}}{n_i} \tag{3.72}$$

So, the nucleation rate is expressed as [12]

$$J^{-1} = \int_1^M \frac{\mathrm{d}x}{w^+_{x,x+1} n_x} \tag{3.73}$$

where $w^+_{x,x+1} = s_x \alpha_x = 4\pi r_x^2 \alpha_x$, and α_x denotes evaporation rate of a cluster who has x molecule, and the cluster volume $V = \omega x$.

3.4.2 Nucleation with One Barrier

For nucleation with one free energy barrier, integrating Eq. (3.72) yields,

$$J = Z D_{n_c} N \exp\left[-\frac{\Delta G(n_c)}{k_B T} \right] = Z D_{n_c} n_{n_c} \tag{3.74}$$

where $Z = -\dfrac{1}{2\pi k_B T} \left(\dfrac{\partial^2 \Delta G}{\partial i^2} \right)_{i=n_c}$ is Zeldovich non-equilibrium factor, $D_{n_c} = w^+_{n_c,n_c+1}$ $= 4\pi r_c^2 \alpha$, rate of molecules striking on the surface of a critical cluster, α, evaporation rate at the critical radius.

For a cavity large enough and $r_c / R \leqslant \sin\beta$, the change of free energy is predicted as the curve in Fig. 3.16, and the cluster has one free energy barrier within the

cavity, where $\Delta G_r = -\Delta\mu_d \pi R^3/3$. Apparently, if a perturbation can induce a cluster to overcome the free energy barrier within the cavity, it spontaneously grows across the edge of cavity with the free energy reduction. This means the nucleation process occurs totally within the cavity.

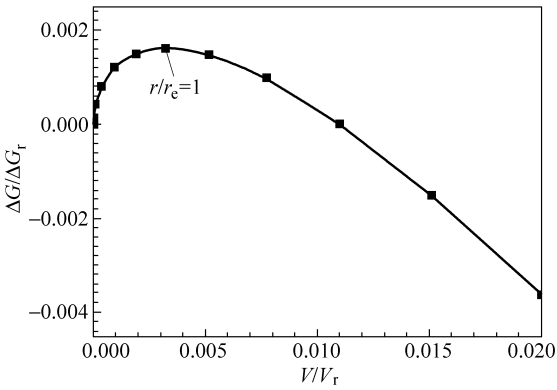

Figure 3.16 Free energy change of a cluster ($\beta = 20^\circ$, $r_c/R = 0.3 < \sin\beta$)

From Eqs. (3.53) and (3.54), the kinetic characteristics for a critical cluster within a conical cavity is described as

$$\Delta G(r_c) = \left[\frac{4}{3}\pi r_c^3 \Delta\mu_d + 4\pi\sigma_{lv} r_c^2\right]\frac{1-\cos\beta}{2} = \chi\Delta G_0 \tag{3.75a}$$

$$D = s_{n_c}\alpha = 2\pi r_c^2(1-\cos\beta)\alpha = \chi D_0 \tag{3.75b}$$

$$Z = -\frac{1}{2\pi k_B T}\left[\frac{\partial^2 \Delta G(i)}{\partial i}\right]_{i=n_c'} = -\frac{1}{2\pi k_B T}\left[\frac{\partial^2 \chi\Delta G(i_0)}{\left(\partial\chi i_0\right)^2}\right]_{i_0=n_c} = \chi^{-1} Z_0 \tag{3.75c}$$

where $\chi = \left(1-\cos\beta\right)/2$, $\Delta G_0 = 4\pi r_c^3 \Delta\mu_d/3 + 4\pi\sigma r_c^2$, $D_0 = 4\pi r_c^2\alpha$, and i is the molecule number of a heterogeneous cluster, i_0 the molecule number of the homogeneous cluster with an identical radius as the heterogeneous cluster with i molecules, and Zeldovich non-equilibrium factor for homogeneous nucleation $Z_0 = -\frac{1}{2\pi k_B T}\left[\frac{\partial^2 \Delta G(i_0)}{\partial i_0^{\,2}}\right]_{i_0=n_c}$.

Substituting Eq. (3.75) into Eq. (3.74) yields

$$J = D_0 Z_0 N \exp\left[-\chi\frac{\Delta G_0}{k_B T}\right] \tag{3.76}$$

For the nucleation within cavities, the free energy barrier quickly becomes small as the cavity angle decreases, and the nucleation rate rises sharply, as shown in Fig. 3.17.

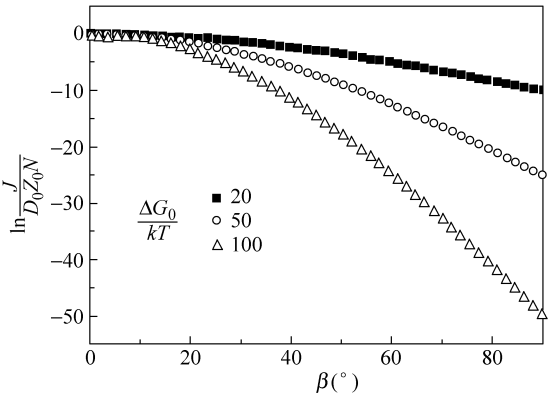

Figure 3.17 Nucleation rate varying with radius and cavity angle

For an idea surface, $\beta = 90^{\circ}$, $\chi = 1/2$, $J_i = D_0 Z_0 N \exp\left[-\dfrac{\Delta G_0}{2k_{\mathrm{B}}T}\right]$, while for surface with cavity, $\beta < 90^{\circ}$, $\chi < 1/2$. $J > J_i$. Generally, a cavity can significantly increase the nucleation rate by decreasing the conical angle, as predicted by Eq. (3.76). In order to form nucleation within a cavity at high nucleation rate, the cavity should have a radius large enough, or $r_{\mathrm{c}} / R \leqslant \sin\beta$, and/or a small conical angle.

For a cavity small enough or $r_{\mathrm{c}} / R > 1$, the free energy change of a cluster generating from a cavity is illustrated in Fig. 3.18, and the cluster has only one

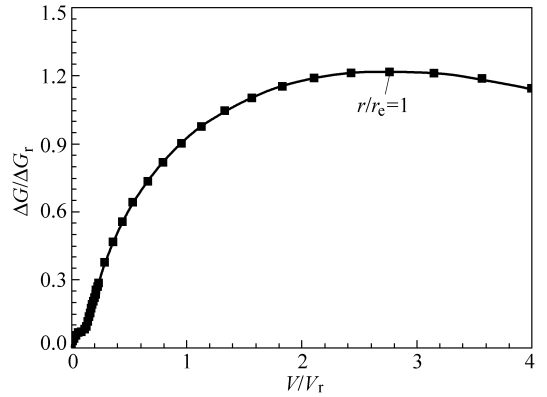

Figure 3.18 Free energy change of a cluster in a small cavity ($\beta = 20^{\circ}$, $r_{\mathrm{c}} / R = 1.1$)

free energy barrier existing outside rather than inside the cavity. In this case, clusters within cavities are unstable and will collapse, or nucleation would not occur within the cavity for weak fluctuations. If there are any strong fluctuations, the cluster would be able to evolve out of the cavity and overcome the energy barrier and induce nucleation outside the cavity. Comparing Fig. 3.18 with Fig. 3.16, the free energy barrier outside a cavity is much higher than that inside a cavity. Consequently, much stronger perturbation or fluctuation is necessary for nucleation.

From Eqs. (3.65) and (3.66), the associated parameters for a critical cluster are obtained as

$$\Delta G(r_c) = \Delta\mu_d \pi R^3 \sin^2\beta\cos\beta/3 + \Delta G_0/2 = \Delta G' + \Delta G_0/2 \tag{3.77a}$$

$$D = 2\pi r_c^2 \alpha = D_0/2 \tag{3.77b}$$

$$\begin{aligned} Z &= -\frac{1}{2\pi k_B T}\left[\frac{\partial^2 \Delta G(i)}{\partial i}\right]_{i=n_c} \\ &= -\frac{1}{2\pi k_B T}\left[\frac{\partial^2 \left(\Delta G(i_0)/2 + \Delta G'\right)}{\partial\left(i_{0i} + i_0/2\right)^2}\right]_{i_0 = n_{c0}} = 2Z_0 \end{aligned} \tag{3.77c}$$

where $\Delta G' = \Delta\mu_d \pi R^3 \sin^2\beta\cos\beta/3$, and i_{0i} is the number of molecules in a cluster within the cavity. Substituting Eq. (3.77) into Eq. (3.74) yields,

$$J = Z_0 D_0 N \exp\left[-\frac{\Delta G_0}{2k_B T}\right]\exp\left[-\frac{\Delta G'}{k_B T}\right] \tag{3.78}$$

As $R \to 0$ or $\beta \to 90^\circ$, $\Delta G' \to 0$, $J \to Z_0 D_0 N \exp\left[-\frac{\Delta G_0}{2k_B T}\right]$, is the rate of heterogeneous nucleation on an ideal surface, and it is identical to the result for a flat plane with $\gamma = 90^\circ$. Defining a function

$$\ln\frac{J}{J_i} = \left(\frac{R}{R_0}\right)^3 \sin^2\beta\cos\beta = \frac{R\sin\beta}{R_0}\cot\beta \tag{3.79}$$

where $R_0 = \left[\frac{-\Delta\mu_d \pi}{3k_B T}\right]^{-1/3}$, and $J_i = Z_0 D_0 N \exp\left[-\frac{\Delta G_0}{2k_B T}\right]$ denotes nucleation rate on an ideal surface.

Compared the free energy of a cluster outside of a cavity, $\Delta G'$, reduced from Eqs. (3.77) and (3.78) with that of a cluster on a flat surface, ΔG_0, the nucleate

rate significantly increases. For a constant R, the nucleation rate, as illustrated in Fig. 3.19(a), increases quickly as cavity radius decreases, and reaches its maximum value at a special cavity angle of $\beta_c = \arcsin\sqrt{2/3}$. For constant $R\sin\beta$, the nucleation rate, as illustrated in Fig. 3.19(b), rises quickly as $R\sin\beta$ increases, while it evidently decreases with β. It is noted that this conclusion is only based on independent cavities without any interaction with each other. The complicated interaction and nucleation competition between adjacent cavities on a surface possibly impress practical nucleation rate.

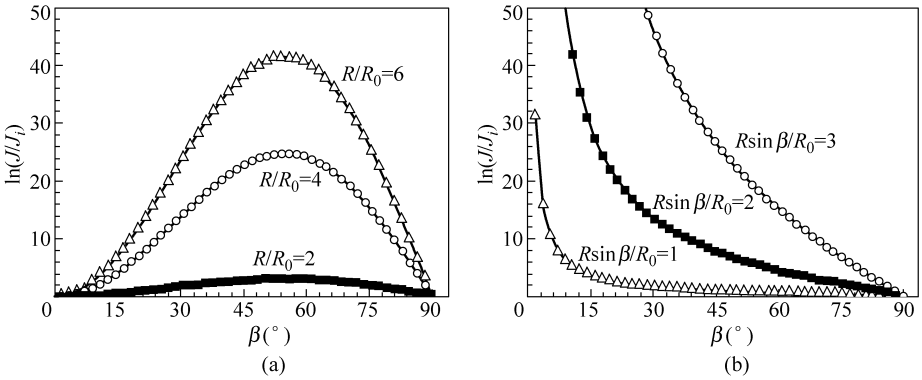

Figure 3.19 Nucleation rate varying with cavity radius and angle
(a) Cavity with constant R; (b) Cavity with constant $R\sin\beta$

From Eq. (3.77a), the free energy of a critical cluster outside the cavity is affected by the chemical potential and cavity volume, with the nucleation rate in Eq. (3.78) much lower than that for nucleation within a cavity, but higher than that on an ideal flat surface.

3.4.3 Heterogeneous Nucleation with Two Barriers

For the radius of a cavity being moderate or $R\sin\beta < r_c < R$, the change of free energy is described as the curves shown in Fig. 3.20, and a cluster has two free energy barriers existing within and outside the cavity, respectively. In this case, a cluster will first cross an energy barrier within the cavity, and then spontaneously grows up to the edge of cavity. Because of the confine of the cavity size, the cluster can not spontaneously grow across the edge. This means the nucleation is not complete inside the cavity and the cluster needs stronger fluctuation to promote its growing across the cavity edge. Outside the cavity the cluster would meet the second barrier as it grows up and then evolve to a mature bubble. Very clearly, a cluster in this type of cavities should cross two free energy barriers, and this evolution process was denoted as twice nucleation [10].

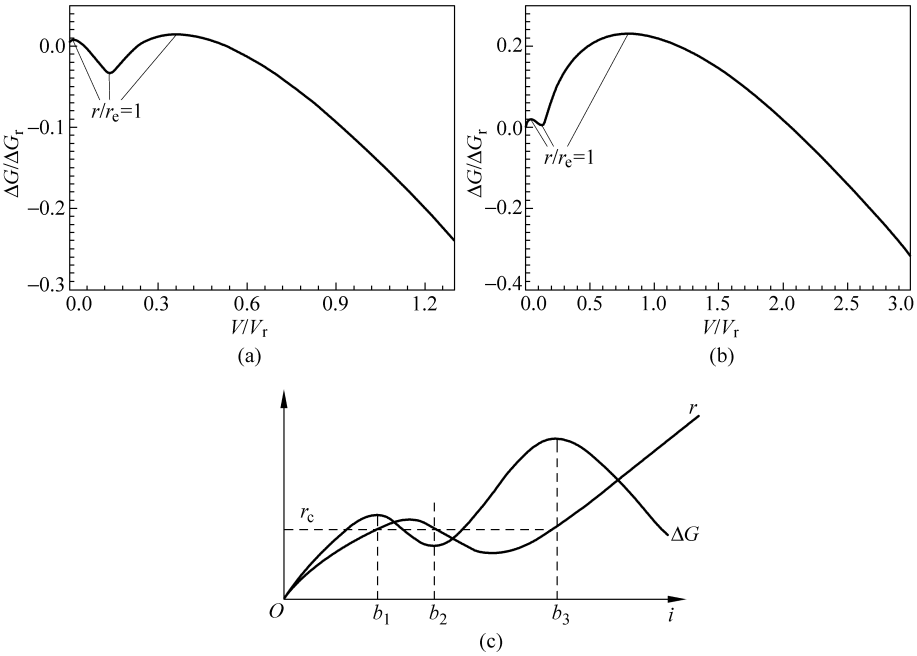

Figure 3.20 Free energy change of a cluster with two energy barriers (a) $r_c / R = 0.5$ ($\sin\beta < r_c / R < 1$), $\beta = 20^\circ$; (b) $r_c / R = 0.7$ ($\sin\beta < r_c / R < 1$), $\beta = 20^\circ$; (c) Typical variation of free energy and radius

For a cluster with i molecules as in Fig. 3.20(c), if $b_1 < i < b_2$, cluster radius is larger than the critical radius, and the cluster will grow to the state b_2 as the free energy decreasing. If $b_2 < i < b_3$, the radius is less than the critical radius, and it collapses to the state b_2 as decreasing the free energy. So, state b_2 is a metastable state between two free energy barriers during the nucleation process.

If the free energy of the metastable state $\Delta G(r_{b_2}) \leqslant 0$, as shown in Fig. 3.20(a), the equilibrium distribution of clusters at the metastable state is $n_{b_2} = N\exp\left[-\dfrac{\Delta G(r_{b_2})}{k_B T}\right] > N$. It is impossible since the cluster has more molecules than the initial molecule number. Apparently, this kinetic process can not be described by Eq. (3.73). On another hand, if the free energy of the metastable state $\Delta G(r_{b_2}) > 0$, as shown in Fig. 3.20(b), the equilibrium distribution of clusters at the metastable state $N\exp\left[-\dfrac{\Delta G(r_{b_2})}{k_B T}\right] < N$. This process can still be described by Eq. (3.73).

For $\Delta G(r_{b_2}) \geqslant 0$, a cluster will first cross the free energy barrier b_1 within the

cavity induced by any fluctuation. After that, the cluster can spontaneously evolve to the state b_2 which is more unstable than the bulk phase and is easy to change to other states if any fluctuation occurs. Any clusters near the metastable stable b_2 aggregating enough molecules will easily cross the second free energy barrier b_3 and evolve into the second region of free energy reduction. These clusters would spontaneously grow and become mature bubbles.

From Eq. (3.73) and Fig. 3.20, the nucleation rate is mainly determined by the cluster distribution near two free energy barriers [10], or

$$J^{-1} \approx \int_{x\approx b_1} \frac{\mathrm{d}x}{w^+_{x,x+1} n_x} + \int_{x\approx b_3} \frac{\mathrm{d}x}{w^+_{x,x+1} n_x} \tag{3.80}$$

Introducing $w^+_{x,x+1}\Big|_{x\approx b_1} = D_{b_1}$, $w^+_{x,x+1}\Big|_{x\approx b_3} = D_{b_3}$, $\int_{x\approx b_1} \frac{\mathrm{d}x}{n_x} = \frac{1}{Z_{b_1} n_{b_1}}$, $\int_{x=b_3} \frac{\mathrm{d}x}{n_x} = \frac{1}{Z_{b_3} n_{b_3}}$ (Ref. [12]), two integrations in Eq. (3.80) are approximately obtained as

$$\int_{x\approx b_1} \frac{\mathrm{d}x}{w^+_{x,x+1} n_x} = \frac{1}{D_{b_1} Z_{b_1} n_{b_1}} \tag{3.81a}$$

$$\int_{x=b_3} \frac{\mathrm{d}x}{w^+_{x,x+1} n_x} = \frac{1}{D_{b_3} Z_{b_3} n_{b_3}} \tag{3.81b}$$

From Eqs. (3.75) and (3.77), $Z_{b_1} D_{b_1} = Z_{b_3} D_{b_3} = Z_0 D_0$. Substituting Eq. (3.81) into Eq. (3.80) yields

$$J^{-1} = \frac{1}{Z_0 D_0} \left(\frac{1}{n_{b_1}} + \frac{1}{n_{b_3}} \right) \tag{3.82}$$

And substituting Eq. (3.69) into Eq. (3.82) yields

$$J = N Z_0 D_0 \left\{ \exp\left[\frac{\Delta G(r_{b_1})}{k_\mathrm{B} T} \right] + \exp\left[\frac{\Delta G(r_{b_3})}{k_\mathrm{B} T} \right] \right\}^{-1} \tag{3.83}$$

From the classical theory, the nucleation rate is determined by the highest energy barrier, or

$$J_\mathrm{c} = N Z_0 D_0 \exp\left[-\frac{\max\left[\Delta G(r_{b_3}), \quad \Delta G(r_{b_3}) \right]}{k_\mathrm{B} T} \right] \tag{3.84}$$

The difference between Eq. (3.83) and Eq. (3.84) is expressed as

$$\frac{\Delta J}{J}=\frac{J_{\mathrm{c}}-J}{J}=\frac{\min[1,\exp(-l)]-(1+\exp l)^{-1}}{(1+\exp l)^{-1}} \tag{3.85}$$

where $l=\dfrac{\Delta G(r_{b_3})-\Delta G(r_{b_1})}{k_{\mathrm{B}}T}$, which denotes the free energy difference between two energy barriers, and the difference caused by twice-nucleation in Eq. (3.85) is illustrated in Fig. 3.21. When $l>4.6$, the nucleation rate is mainly dependent upon the highest free energy barrier, and the difference is below 1%. On the other hand, both of the two free energy barriers should be considered for $l<4.6$.

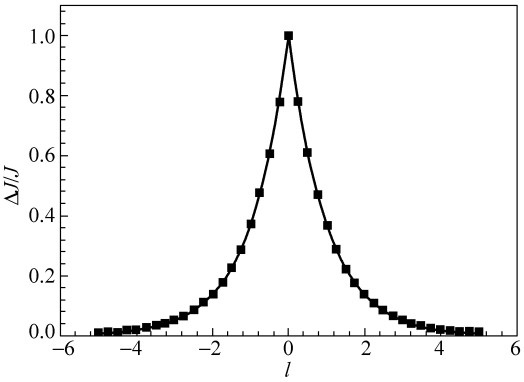

Figure 3.21 Nucleation rate difference caused by twice-nucleation

The distribution of clusters at the metastable state b_2 satisfies [12]

$$\frac{f_{b_2}}{n_{b_2}}=J\int_{b_2}^{M}\frac{\mathrm{d}x}{w_{x,x+1}^{+}n_x}\approx J\int_{x\approx b_3}\frac{\mathrm{d}x}{w_{x,x+1}^{+}n_x} \tag{3.86}$$

Substituting Eq. (3.68) into Eq. (3.85) yields

$$\begin{aligned}\frac{f_{b_2}}{n_{b_2}}=\frac{n_{b_1}}{n_{b_1}+n_{b_3}}&=\frac{\exp\left[-\dfrac{\Delta G(r_{b_1})}{k_{\mathrm{B}}T}\right]}{\exp\left[-\dfrac{\Delta G(r_{b_1})}{k_{\mathrm{B}}T}\right]+\exp\left[-\dfrac{\Delta G(r_{b_3})}{k_{\mathrm{B}}T}\right]}\\&=\frac{1}{1+\exp(-l)}\end{aligned} \tag{3.87}$$

The distribution of clusters at the metastable state is illustrated in Fig. 3.22, and is also highly dependent upon the relation of two free energy barriers. When the free energy barrier b_1 is much higher as $l\ll -1$ or $\Delta G(r_{b_1})-\Delta G(r_{b_3})\gg k_{\mathrm{B}}T$, $f_{b_2}/n_{b_2}\to 0$, so the distribution of clusters at the metastable state is

approximately zero. On the other hand, when the free energy barrier b_3 is much higher as $l \gg 1$ or $\Delta G(r_{b_3}) - \Delta G(r_{b_1}) \gg k_B T$, $f_{b_2} / n_{b_2} \to 1$, the distribution of clusters at the metastable state b_2 is almost equal to its equilibrium distribution.

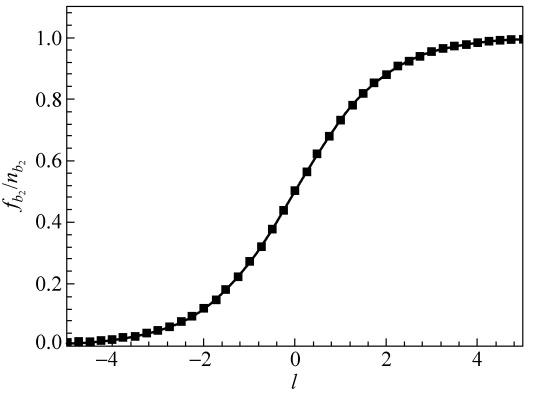

Figure 3.22 Distribution of clusters at metastable state

For nucleation with $\Delta G(r_{b_2}) \leqslant 0$ as shown in Fig. 3.20(a), the evolution process is quite different from that with $\Delta G(r_{b_2}) > 0$. A cluster first crosses the free energy barrier b_1 within the cavity and evolves to the state b_2 as the free energy decreases. Since $\Delta G(r_{b_2}) \leqslant 0$, the metastable state b_2 is more stable than the bulk phase, and then the cluster across the first free energy barrier will tend to aggregate to the states near the metastable state b_2. For the second nucleation process across b_3, the metastable cluster b_2 is considered as a new initial state for final nucleation of the liquid on this solid surface. After the first nucleation process across b_1, the distribution of clusters at the metastable state b_2 is approximately

$$f_{b_2} = J\, t = N Z_0 D_0 \exp\left[-\frac{\Delta G(r_{b_1})}{k_B T} \right] t \tag{3.88}$$

For the second nucleation process, the initial state is the metastable state with distribution f_{b_2}, and the energy barrier is

$$\Delta G = \Delta G(r_{b_3}) - \Delta G(r_{b_2}) \tag{3.89}$$

Similar to Eq. (3.74) and from Eqs. (3.88) and (3.89), the nucleation rate is

$$\begin{aligned} J &= f_{b_2} Z_0 D_0 \exp\left[-\frac{\Delta G(r_{b_3}) - \Delta G(r_{b_2})}{k_B T} \right] \\ &= N (Z_0 D_0)^2 \exp\left[\frac{\Delta G(r_{b_2}) - \Delta G(r_{b_1}) - \Delta G(r_{b_3})}{k_B T} \right] t \end{aligned} \tag{3.90}$$

From Eq. (3.90), the nucleation rate will increase with time and is also dependent upon the free energy of the metastable state. In conclusion, the nucleation rate under these conditions is not only dependent on the energy barriers but also on the metastable state and the evolution time. These conclusions are different from the classical theory.

References

[1] V. P. Carey. Liquid-vapor phase-change phenomena: an introduction to the thermophysics of vaporization and condensation processes in heat transfer equipment. Hemisphere Pub. Corp., 1992.

[2] J. P. Holman. Heat Transfer (9th Ed.). McGraw-Hill Education—Europe, 2002.

[3] X. D Wang, X. F. Peng, Y. Tian, et al. Formation, structure, and evolution of boiling nucleus and interfacial tension between bulk liquid phase and nucleus. Heat and Mass Transfer, 41: 651 – 658, 2005.

[4] X. D Wang, X. F. Peng, Y. Tian. Self-aggregation of vapor-liquid phase transition. Progress in Natural Science, 13: 451 – 456, 2003.

[5] J. P. R. B. Walton, D. J. Tildesley, J. S. Rowlinson. The pressure tensor at the planar surface of a liquid. Molecular Physics, 48: 1357 – 1368, 1983.

[6] P. Stephan, J. Hammer. A new model for nucleate boiling heat transfer. Int. J. Heat and Mass Transfer, 30: 119 – 125, 1994.

[7] J. G. Truong, P. C. Wayner. Effects of capillary and van de Walls dispersion forces on the equilibrium profile of a wetting liquid: theory and experiment. J. Chem. Phys, 87: 4180 – 4188, 1987.

[8] K. Stephan. Influence of dispersion forces on phase equilibria between thin liquid films and their vapour. Int. J. Heat and Mass Transfer, 24: 4715 – 4725, 2002.

[9] J. F. Lu, X. F. Peng. Microscopic activation phenomena in heterogeneous nucleation. US ASME National Heat Transfer Conference, 655 – 661, 2003.

[10] J. F. Lu, X. F. Peng. Dynamical evolution of heterogeneous nucleation on surfaces with ideal cavities. Heat and Mass Transfer, 43: 659 – 667, 2007.

[11] J. F. Lu, X. F. Peng. Microscope activation near a wall during heterogeneous boiling. Heat and Mass Transfer, 44(7): 889 – 894, 2008.

[12] Y. I. Frenkel. Kinetic Theory of Liquids. Oxford: Oxford University Press, 1946.

4 Jet Flow Phenomena

Abstract Various forms of jet flows were observed in boiling experiments conducted on fine wires. The jet flows broke forth from nucleation sites like volcano erupting, or issued from stationary bubbles like tails. The jet flows were quite different from typical bubbles and brought distinct insight to boiling heat transfer mechanisms. A series of theoretical work was conducted to reveal the nature of the various forms of jet flows. Some of them, bubble-top jet flow and multi-jet flow, were successfully modeled.

Keywords jet flow, nucleation jet, bubble-top jet, multi-jet flow, Marangoni thermocapillary effect, evaporation, condensation

In the last 20 years, the development of digitally enhanced measurement and visualization techniques and the urgent demand for very efficient high heat flux removing technologies in unconventional environments, especially microscale and microgravity environments, have promoted more comprehensive investigations of boiling processes. Some interesting phenomena and dynamic processes were observed in the open literature. Lin et al. [1, 2] observed microscale homogeneous nucleation. Glod et al. [3] investigated the explosive vaporization of water close to its superheat limit at the microscale level. Peng and Wang [4] experimentally observed and theoretically investigated many quite new boiling phenomena occurring at micro scale level. Even though Shekriladze [5, 6] and some other investigators considered some flows around a bubble as "pump effects" many years ago, various nucleation and bubble jet flows, and strange bubble dynamics on micro wires were visually observed and found to have some unique characteristics in a sequence of experiments [7 – 16]. Particularly, the PIV technique was employed to visually observe flow fields around micro bubbles with intensive jet flows [10, 15]. These studies also proposed a number of models to describe the phenomena and investigated various possible physical mechanisms, having providing an additional insight into the fundamental mechanisms controlling the boiling process and the complexity of nucleate boiling.

Nucleation jet flows, bubble-top jet flows, jet-like flows from the bubble top surface into the bulk liquid, are interesting phenomena observed in many experimental investigations [7 – 16]. These jet flows represents important mechanisms in more accurate boiling heat transfer models, especially by clarifying

X. Peng, *Micro Transport Phenomena During Boiling*

the balance between microlayer evaporation and heat removal by the liquid phase, which both are widely recognized as key boiling heat transfer mechanisms. Many investigations sought to observe these phenomena and provide more experimental and theoretical evidences for better understanding the physical nature of bubble-top jet flows. Various investigators suggested that the interfacial mass flux due to evaporation and condensation, Marangoni effect induced by the surface tension gradient and the surface pressure gradient resulting from evaporation all contribute to the jet flows.

4.1 Experimental Phenomena

4.1.1 Boiling on a Plate Heater

Employing the experimental setup illustrated in Fig. 4.1, which included a liquid vessel, test module, HP data acquisition system, CCD camera, and computer, Peng et al. [7] visually observed the boiling characteristics of subcooled liquids on a heating surface facing downward. In the test system, the bottom plate was manufactured as a mini heat exchanger that serves as the cooler to maintain the temperature of the working liquid in the vessel. The MatoxMeter image analyzer was employed to the photo acquisition system for image processing. A helium-neon laser was employed as sheet light source for visual observation and image measurement. A pressure gauge and a thermocouple were installed for pressure and liquid temperature measurement. The heater is shown in Fig. 4.2.

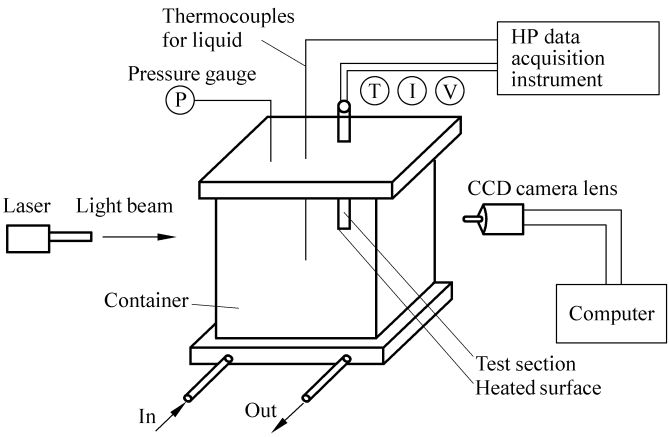

Figure 4.1 Test setup of boiling observation

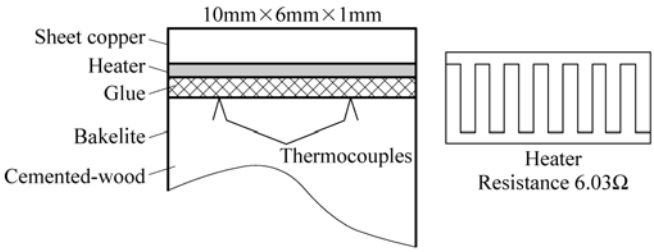

Figure 4.2 Heater module

Figure 4.3 illustrates several photographs of the methanol as it was heated at a bulk temperature of 19℃ or a subcooling of 45℃. In Fig. 4.3(a), the liquid bulk remained quiet and stable with a lighter region near the heating surface which is the thermal boundary layer at a low applied heat flux. As shown in Fig. 4.3(a), the thermal boundary layer was about 2 mm thick at a heat flux of $q'' = 13.8$ kW/m^2. As the heat flux was further increased, the surface temperature increased and the thermal boundary layer became wavy. When the applied heat flux was about 31.1 kW/m^2, a small bubble formed in the thermal boundary layer, and meanwhile a jet-like superheated liquid flow emerged from the bubble top and penetrated into the bulk liquid against the direction of gravity. The jet flow momentum was exhausted after traveling some distance from the bubble due to the resistance of the flow and buoyancy. The bubble broke when its size grew to larger than 3 mm.

At higher heat fluxes, $q'' = 55.3$ kW/m^2 and $q'' = 86.4$ kW/m^2 (illustrated in Fig. 4.3(c),(d), respectively), the bubbles grew fast and the jet-like flows from the tops of the bubbles penetrated deeper into the bulk liquid than that in Fig. 4.3(b), indicating stronger jet flows with higher jet velocities. More bubbles, particularly smaller ones were generated on the heated surface, which induced more violent flow in the bulk liquid.

In saturated liquid boiling the jet flow behavior became almost invisible. Closer observation reveals that for saturation condition the bubbles were greater in size with the jet flow still produced from the region near the bubble top. The bulk liquid subcooling intensified the strength of the jet flow. At very high liquid subcoolings, the bubbles decreased in size with very strong jet flow developing over most of the bubble interface. Therefore, more bulk liquid around the bubble was driven outwards from the heated surface, compared with the saturated boiling case. It is more obvious the jet flow phenomenon is highly dependent on the liquid subcooling. The thickness of thermal boundary layer was decreased a little bit rather than increasing as bubble jet flow happened, as observed and compared the images in Fig. 4.3. This means that the heat transfer should be enhanced by the jet flow.

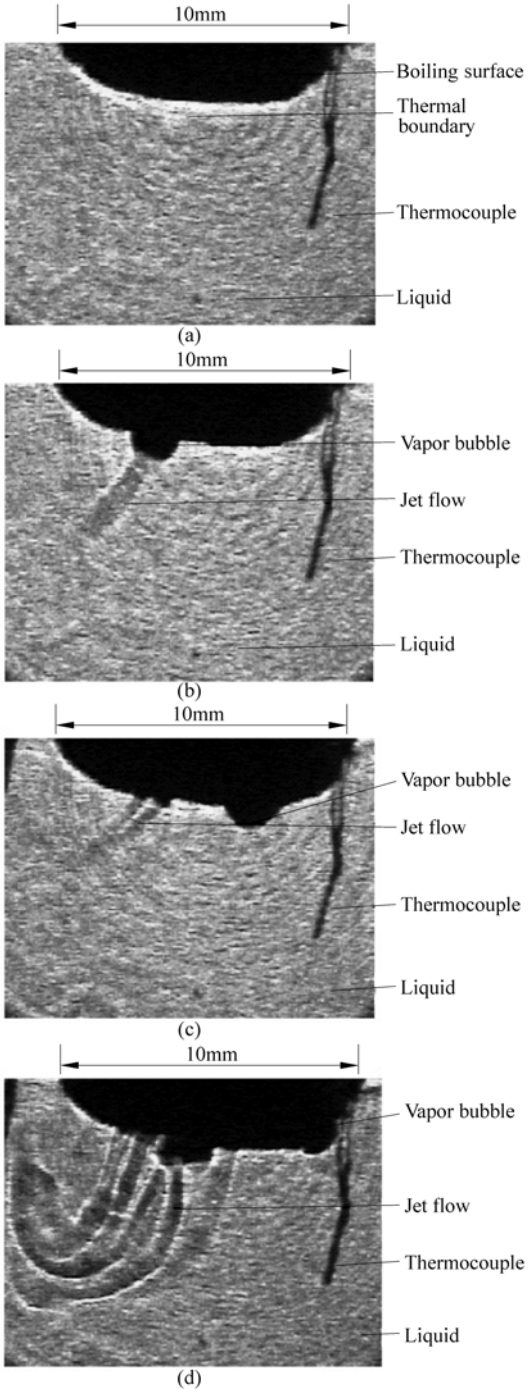

Figure 4.3 Boiling jet flow on a plate heater
(a) q''=13.8 kW/m^2; (b) q''=31.1 kW/m^2; (c) q''=55.3 kW/m^2; (d) q''=86.4 kW/m^2

4.1.2 Boiling on Small Wires

Wang et al. [8 – 16], Lu and Peng [16] conducted a sequence of experimental investigations to visually observe boiling phenomena of subcooled liquids on very small wires, employing the experimental facility shown in Fig. 4.4. Several modes of jet flows were explored and described during the nucleate boiling on the wires.

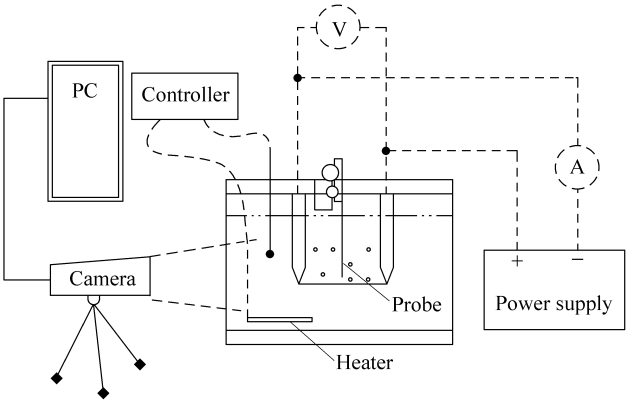

Figure 4.4 Test system of subcooled boiling on small wires

(1) High Energy Liquid Jet Flow

Figure 4.5 shows a kind of jet flows for liquid alcohol at temperature 23℃ and atmospheric pressure. This was observed before nucleate boiling occurred or the wire did not reach the boiling conditions. The observed jet flows generated from, or more accurately, from nucleate sites of the wire and sprayed into the bulk liquid. Though there was no bubble generated from these nucleation sites, the applied heat fluxes were enough to reach some critical values for activating these nucleation sites. These jets could be clearly distinguished from their ambient

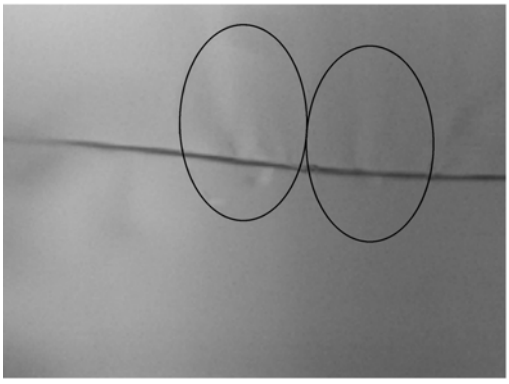

Figure 4.5 High-energy liquid jet flows

liquid. Since the momentum of the jet flows was weak, they disappeared completely after the departure from the wire for some short distance (usually 1 – 3 mm). It is reasonable to assume this kind of jet flows consisting of liquid that had absorbed much local energy and did not reached the energy level for nucleation. So, this kind of jet flows was termed as “high-energy liquid jet flow”.

(2) Fog-Like Jet Flow

For liquid alcohol at 45℃ and atmospheric pressure, the fog-like jets were observed on the heating wire appeared in the bulk liquid, as shown in Fig. 4.6. These fog-like jets generated from active nucleation sites on the wire and sprayed in all directions. The direction of jet flows ought to be relative with the special structure and characteristics of each site. The fog-like jets would disappear gradually after leaving away from the wire for a distance. The distance might be even as long as 7 mm. These jet flows could not very well be identified by naked eyes even with much carefulness, at first glance very similar to normal natural convection. By means of zoom lens, the jet flows were clearly observed and differed from the liquid. Their appearance was totally different from natural convection.

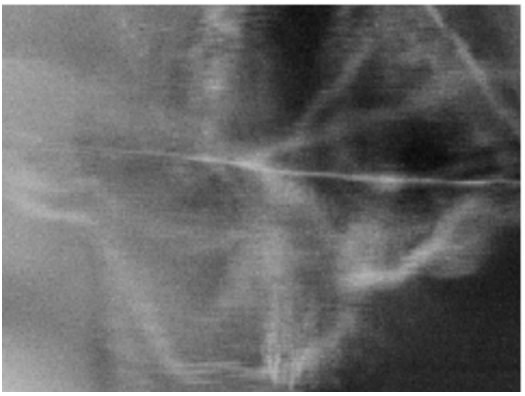

Figure 4.6 Fog-like jet flows

The formation of these fog-like jet flows may attribute to high heat flux and high subcooling of working fluids. The liquid immediately close to the wire absorbed much heat but not enough to cause nucleation and formation of bubbles. The local heated liquid carried energy, especially at the active sites and sprayed from the wire surface into the bulk liquid. They might be vapor-liquid mixture in the sprayed jet flows and cooled by subcooled liquid around, like the condensation of vapor in the jet flows, and so they displayed the fog-like behavior.

(3) Cluster Bunch Jet Flow

As the liquid around the heating wire almost reached saturation the jet flows became clearer and more regular. Though common bubbles were not observed, it

was obvious that jet flows consisted of bunches of small liquid masses, so-called "cluster bunch jet flows", as shown in Fig. 4.7. The cluster bunch jet flows are expected mainly consisting of liquid masses and have characteristics of the liquid that absorbed much amount of heat energy but have not nucleated yet. In Fig. 4.5, especially in Fig. 4.6, the high subcooling liquid made high-energy clusters "condensed" and collapsed. On the contrary, in saturated bulk liquid, bulk liquid would not impose "condensation" effect on high-energy liquid masses or clusters spraying away from the wire. So clusters kept their order and form strong cluster bunch jet flows in the bulk liquid.

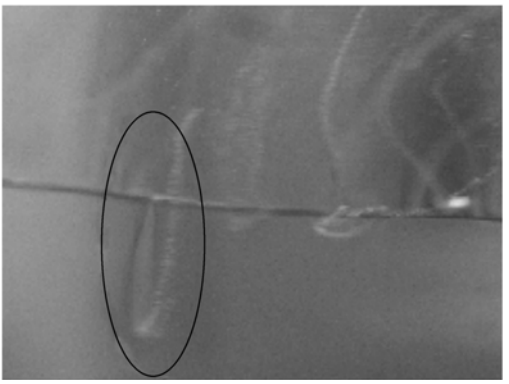

Figure 4.7 Cluster-like jet flows

(4) Nucleation Jet Flow

When the thermofluid conditions reached the part of nucleation or nucleate boiling, vapor bubbles formed, grew and departed from the heating wire. At this time, some jet flows were observed to be generated from nucleation sites without any bubbles and evolved to miniature bubbles even common bubbles as the jet flows flowed away from the wire, as shown in Fig. 4.8. Some bubble generated at the end of jet flows, some in middle of the jet flow evolving process, some occurred in the whole process of jet flow spraying, but not at the nucleation sites. This type of jet flow likely shows the process of bubble formation, and as a result, is termed "nucleation jet flow".

(5) Bubble Bunch Jet Flow

Figure 4.9 shows another jet flow phenomenon, bubble bunch jet flow. This phenomenon can also be observed in some local regions of the heating wire in Fig. 4.8. Bubble bunch appeared when the bulk liquid was saturated and heat flux was higher and approaching the critical value for nucleate boiling. The jet flows highly looked like they consisted of vapor bubbles. However, these were not either exactly like the normal bubbles or the liquid clusters as that in cluster-bunch jet

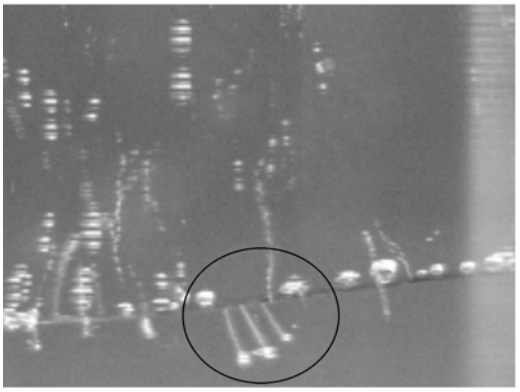

Figure 4.8 Nucleation jet flows

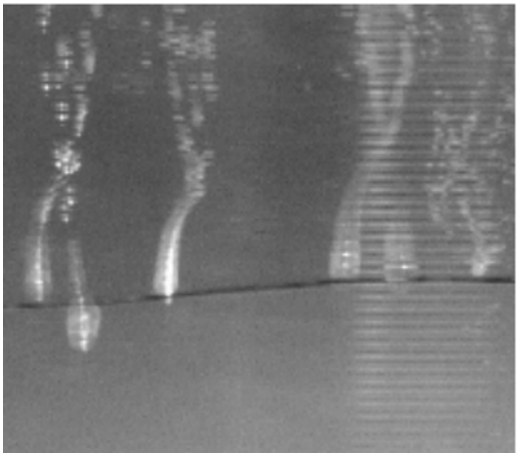

Figure 4.9 Bubble bunch jet flows

flows in Fig. 4.7. The bubbles stably and continuously generated and flowed from active nucleation sites on the heating wire to form jet flows in the liquid. They behaved as a bunch and formed a tail like a "gas channel".

The cluster bunch jet flows, nucleation jet and bubble jets all concern with liquid nucleation. These phenomena indicate that diversity of nucleation in boiling is extremely complex and interesting.

(6) Bubble-Top Jet

As mentioned above, the jet flows were generated on the wire and sprayed directly into the bulk liquid from active nucleation sites of the heating wire. But in some cases, some jet flows came from the tops of bubbles, as shown in Fig. 4.10. Figures 4.11 and 4.12 illustrate another type of bubble-top jet, which will be discussed in detail in section 4.2.

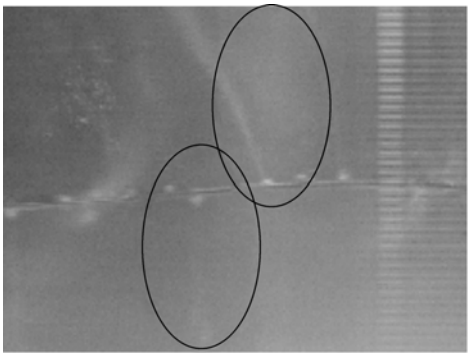

Figure 4.10 Bubble-top jet flows

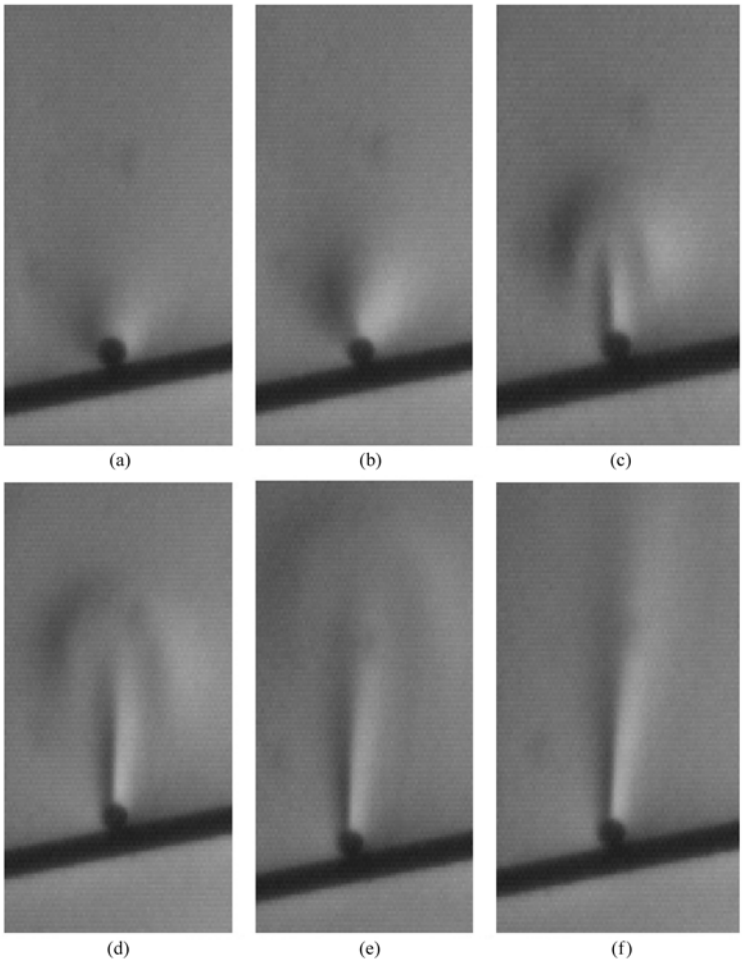

Figure 4.11 Formation of a bubble-top jet flow
(a) $t = 0$ s; (b) $t = 0.046$ s; (c) $t = 0.058$ s; (d) $t = 0.076$ s; (e) $t = 0.098$ s; (f) $t = 0.138$ s

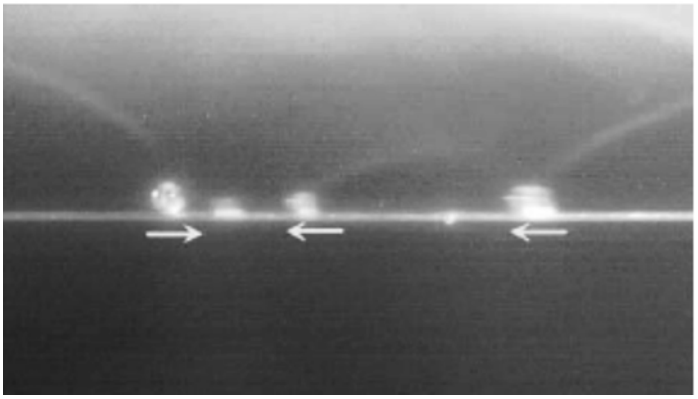

Figure 4.12 Bubble-top jet flows from moving bubbles

The downward jet flows changed their direction upward gradually with the impact of the buoyancy, no matter what kind of jet flows was. This behavior indicates that jet flow has apparent density difference from the ambient liquid. Preliminary measurements show that the heat transfer associated with jet flows is much higher than the free convection and even higher than the normal nucleate boiling heat transfer. The actual composition of jet flows, what mechanisms, driving the jet flows from the wire, the diversity of jet flows, and many other questions need to be answered in future investigations.

4.2 Bubble-Top Jet Flow Structure

4.2.1 General Features

Of all different jet flows bubble-top jet flow was the most popular and important during subcooled boiling on very fine wires. It had a stable structure and intensity which pumped liquid into the bulk region. Normally smaller bubbles usually had more concentrated and stronger jet flows than larger bubbles. The magnitude of jet flow velocity is one of important parameters representing its intensity, which normally ranged from 10 mm/s to about 140 mm/s in the conducted experiments [10]. A higher heat flux and high wire temperature could enhance jet flow intensity. However, bubbles were hard to maintain on the wire surface at very high heat flux which promoted bubble departure and eliminated jet flows.

Gravity had little effect on the jet flow velocities. Figure 4.13 shows that the downward facing bubbles had strong jet flows from their top as the upward facing bubbles.

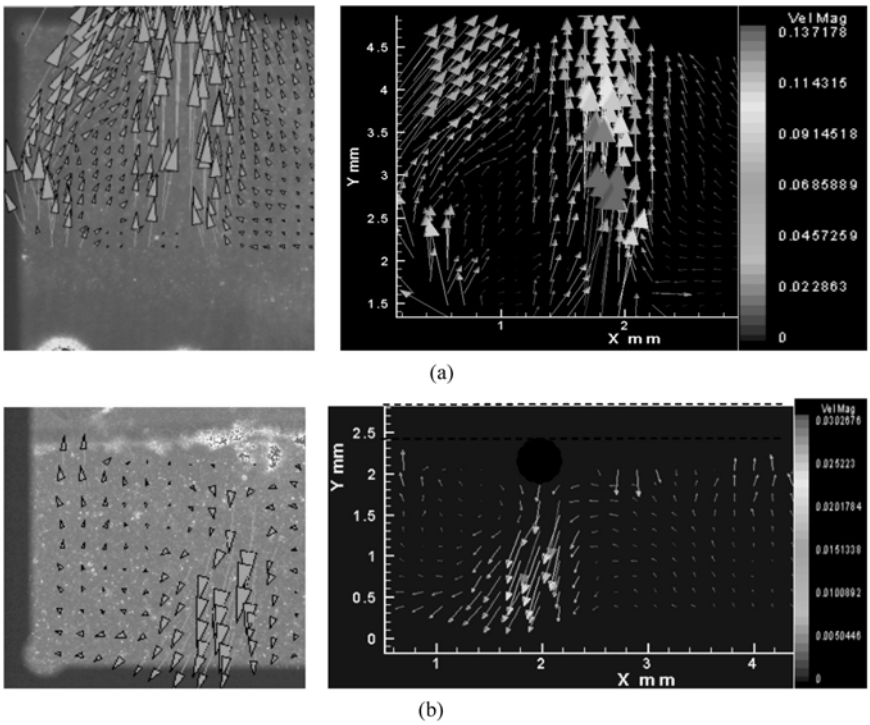

Figure 4.13 PIV measurements of upward and downward bubble jet flows (a) Upward bubbles; (b) Downward bubbles

4.2.2 Jet Structure

Typically, a developed bubble-top jet flow can be divided into four parts shown in Fig. 4.14, body region, neck region, pumping region and wake region. It is expected that the fluid in jet body region has different density from subcooled bulk liquid. The neck region under the body region is just at the top of the bubble and is considered as the root of a jet flow. The joint of the neck region and body region is jet flow neck where the pumped liquid will concentrate to form a strong flow having the highest velocity in the whole jet flow. Around the bubble is the pumping region, where the hot liquid around the wire is pumped up along the surface of the bubble and then get the neck region to form a jet flow. The Pumping region strongly influences the heat transfer performance of the jet flow and the bubble. The end of the jet flow is the wake region, the transition zone from jet flow to steady bulk liquid. Figure 4.14 shows there is no distinct boundary between a jet flow and bulk liquid, and the top surface of the bubble is intact.

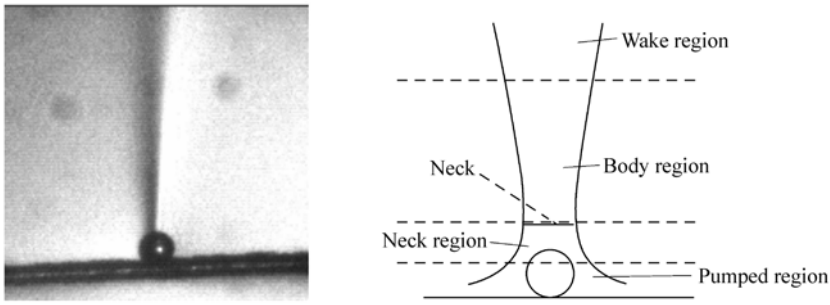

Figure 4.14 Structure of a bubble-top jet flow

Figure 4.15 illustrates the track of a particle moving with bubble jet flow to show the flow streamlines and geometrical configuration of a bubble-top jet flow around a bubble. This clearly demonstrates the jet flow structure. The PIV images in Fig. 4.13 also support this structure.

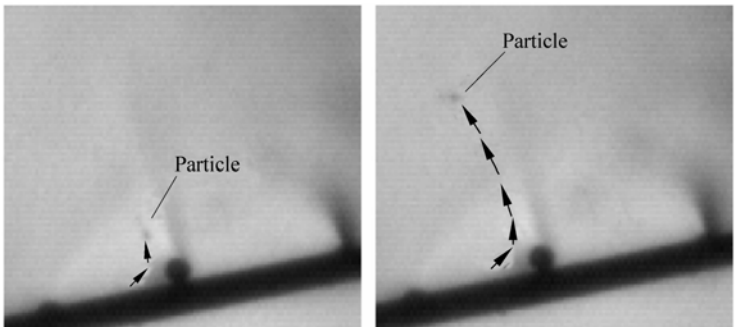

Figure 4.15 Bubble-top jet flow tracing

4.2.3 Multi Bubble-Top Jet Flow

In several experiments, some jet flows were observed quite different from typical scheme of a bubble-top jet flow shown in Fig. 4.14, and Fig. 4.15. One bubble might own more than one jet flow. The geometry of the wire and bubble were supposed as important factors influencing this kind of multi-jet flow phenomena. Normally, small bubbles had only a single and distinct jet flow. The bubble on the downward plane wall had also only a single jet flow [5, 7].

The larger bubble size relative to the wire might increase complexity of the temperature distribution condition on bubble surface. When a bubble has big size (normally bigger than the wire diameter), not only its top, but also its side surface formed side jet flows on a bubble, as illustrated in Fig. 4.16.

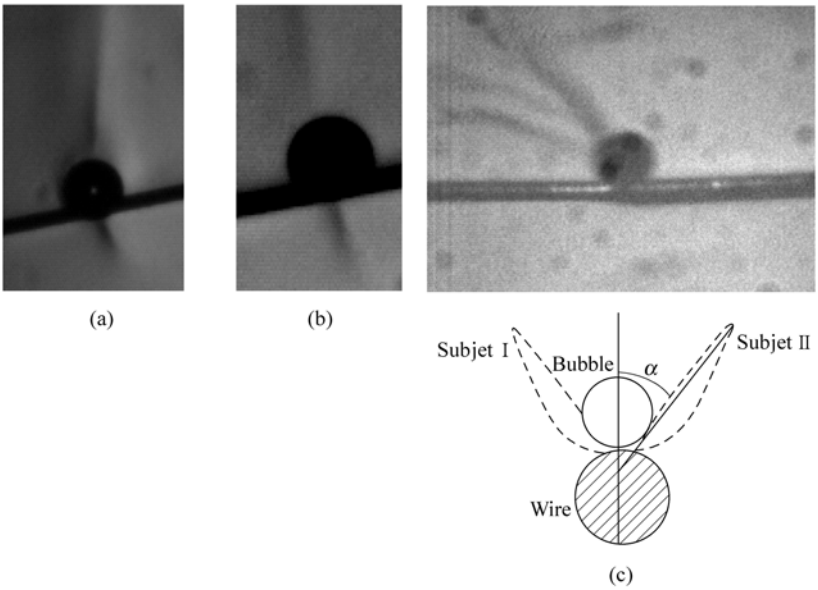

Figure 4.16 Multi bubble-top jet flows
(a) Stable bubble; (b) Moving bubble; (c) Ideal structure

4.3 Dynamical Behavior of Bubble-Top Jet Flows

4.3.1 Jet Flow Evolution

Bubble-top jet flow usually formed when the bubble was very small, and its formation process lasts about 0.020 – 0.200 s. After its formation, a bubble jet flow continued growing up until the bubble lost its stability due to departure or collision with bulk liquid. During the bubble jet formation process, the bubble radius was usually in the range of about 0.01 – 0.04 mm.

Figure 4.17 shows the formation process of a bubble jet flow during subcooled boiling on a tungsten wire having diameter of 200 μm at bulk liquid temperature of 36℃ and heat flux of 0.60×10^6 W/m^2. At the beginning, a small bubble formed on the wire, and a high temperature region correspondingly appeared just near the bubble interface. At 0.040 s, the high temperature region still had no obvious change. After about 0.050 s, the high temperature region began to develop quickly, and a mushroom-like cloud formed around the bubble as the initial bubble-top jet flow at 0.060 s. In the next 0.020 s, the cloud quickly evolved and gradually converged to an embryo jet flow. At 0.110 s, the head of the jet flow began to diffuse into the bulk liquid. After that, the mushroom-like cloud would finally evolve and converge into a fully-developed bubble-top jet flow extending into the bulk liquid. During the formation process, the bubble size had no

significant change, and its radius was about 0.035 mm. Generally, a bubble jet flow formation process can mainly be described as three stages, bubble generation, formation of mushroom-like cloud and pre jet flow, finally inducing a mature jet flow. These phenomena were observed in various subcooled boiling on different thin wires of diameter 0.1 – 0.24 mm, while the radius of the bubble was always observed to have only unobvious variation.

Typically, the mushroom-like cloud during the burst stage can be divided into two main regions: mushroom stem and mushroom head, as schematically shown in Fig. 4.18. The mushroom stem was an intense jet flow with strong intensity just above the bubble, and it kept stable during the developing stage. The mushroom

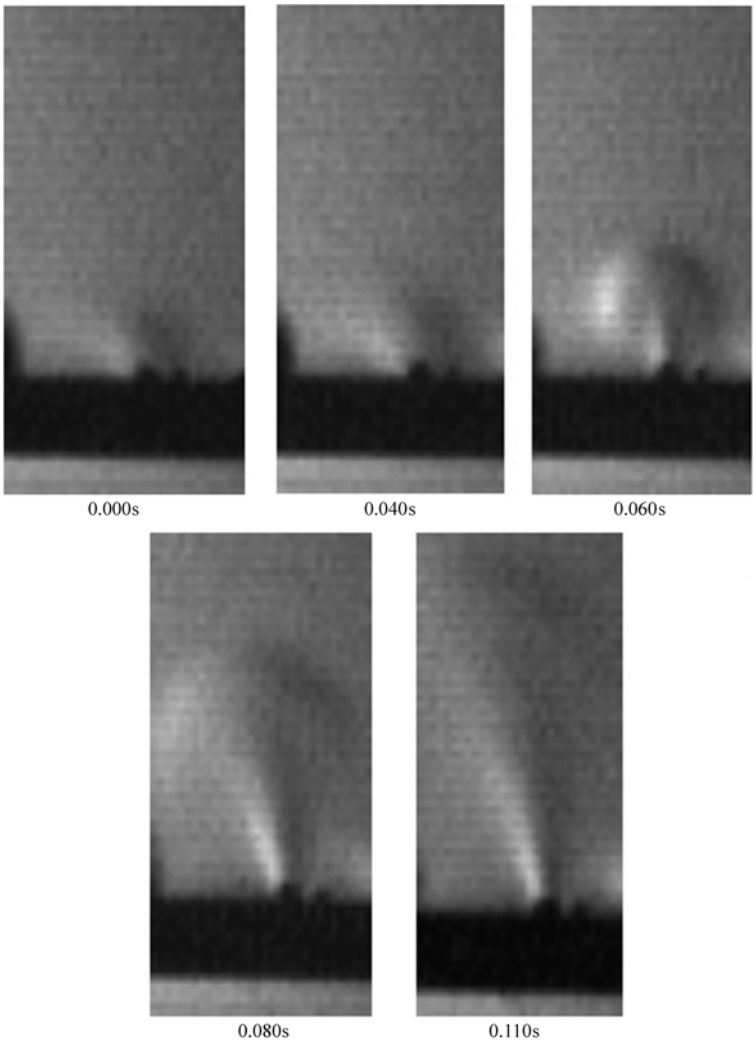

Figure 4.17 Bubble-top jet flow formation ($T_w = 36℃$, $q''_w = 0.60 \times 10^6$ W/m^2)

head was the front of the jet flow, and it would merge into the bulk liquid to form a fully-developed jet flow. For a quantitatively investigation, a jet flow is described with its geometrical parameters of height, H, and width, D. The dynamical behavior of the bubble jet flow in Fig. 4.17 is illustrated in Fig. 4.19, where $u_H = dH/dt$, $u_D = dD/dt$. In the waiting period of 0.000s – 0.050 s, the jet flow front or parameter H varied only from 0.17 mm to 0.26 mm, and the expansion velocity along the height was lower than 4 mm/s. During 0.050 s – 0.080 s, the jet flow burst and the height rapidly varied from 0.26 mm to 0.71 mm. It approached its maximum vertical expansion velocity of 22 mm/s at 0.7 mm away from the wire. After 0.080 s, the jet flow front reached a constant velocity of about 8 mm/s, and the front merged into the bulk liquid. The jet flow expansion velocity had a jump at about 0.050 s, and this was identified as the transition time from the waiting stage to burst stage.

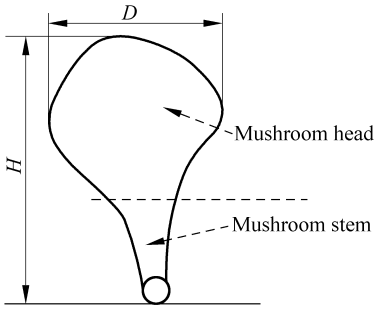

Figure 4.18 Earlier structure of a bubble jet

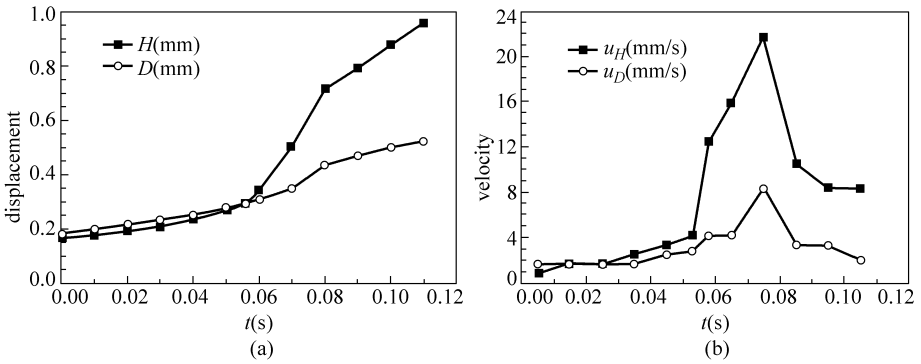

Figure 4.19 Dynamical behavior of a jet flow formation
(a) Jet flow geometry; (b) Expansion velocity

During the dynamical process, the width of a jet flow expanded more slowly than its height, indicating that the upward flow dominated the jet flow. Since the basic jet flow configuration was similar during the short burst stage, the velocity along the height and width reached the maximum values at almost the same time.

4.3.2 Competition and Self-Organization of Jet Flows

It was frequently observed that there existed strong competition between neighboring bubble-top jet flows, especially the pumping effect in the pumping region. This competition and pumping effect could suppress some bubble-top jet flows or form a stronger jet flow coalescing with several jet flows. Inside a group of bubbles, the jet flows from neighbor bubbles usually coalesced into a stronger, bigger and more stable one, here termed as "jet column", which shows a typical self-organization of jet flows when they exist very close to each other with strong interaction. A jet column commonly included three to five individual jet flows. When there were groups of bubbles attaching on the wire, the interaction and self-organization among the columns occurred, and finally formed a regular and steady flow pattern in boiling system. In Fig. 4.20, the weak columns changed direction to follow, or get close to, and/or join the stronger column flow field.

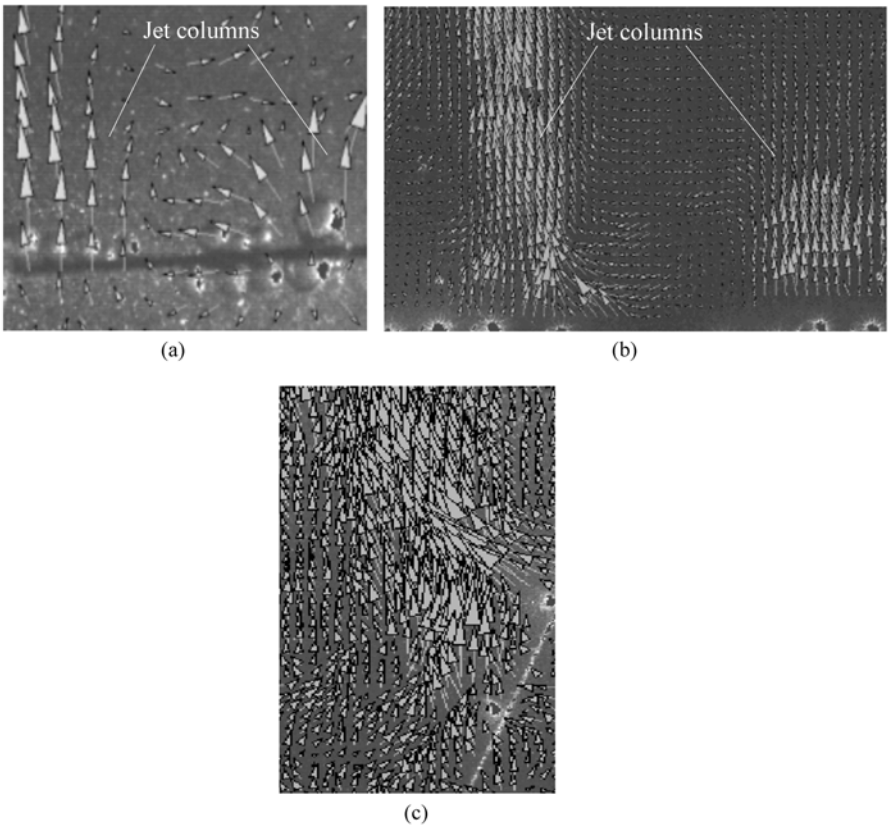

Figure 4.20 Jet flow columns
(a) On a horizontal wire; (b) Co-existing jet flow columns; (c) On an inclined wire

In addition to bubble-top jets, some liquid jet flows were observed to be directly generating from the nucleation sites and to be greatly affected by neighbor bubble jet flows. Figures 4.21(a) and (b) illustrate the interaction between a bubble-top jet flow and a liquid jet flow from a nucleation site. Figure 4.21(c) and (d) present a PIV image and vector field for this kind of interaction, respectively.

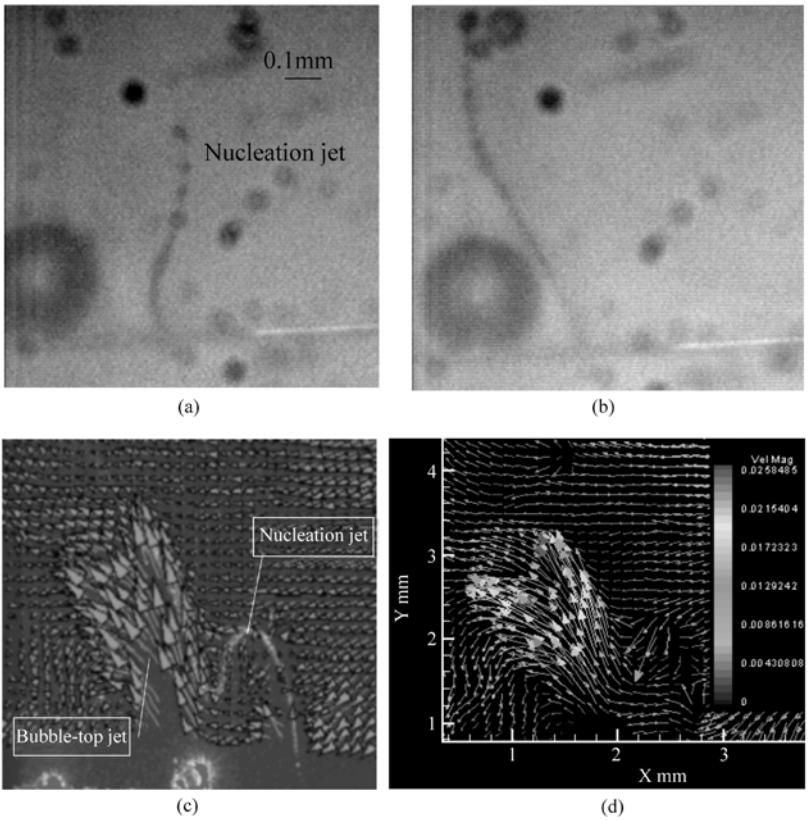

Figure 4.21 Interaction between bubble-top and nucleate jet flows
(a) $t = 0.000$ s; (b) $t = 0.088$ s; (c) Photo image by PIV; (d) Vector field

In the experiments, a jet flow could remain on a bubble until the bubble departed. However, the direction of the jet flow could be influenced by the surrounding conditions. Figure 4.22 presents a bubble jet flow changing its flow direction as a nearby bubble departing during the boiling on the tungsten wire of 200 μm in diameter at bulk liquid temperature 36℃ and heat flux 0.64×10^6 W/m^2. At the initial time, a large bubble stood on the wire, and three jet flows in the left zone trended to the large bubble. At 0.018 s, the large bubble departed. In this stage, the jet flows were slightly affected by the bubble departure and had no

significant variation. During the next 0.024 s, the root of the jet flows became to have the trend to the left side, and the whole flow field of the jet flows was accordingly changed. After 0.196 s, the jet flows and whole flow field became stable.

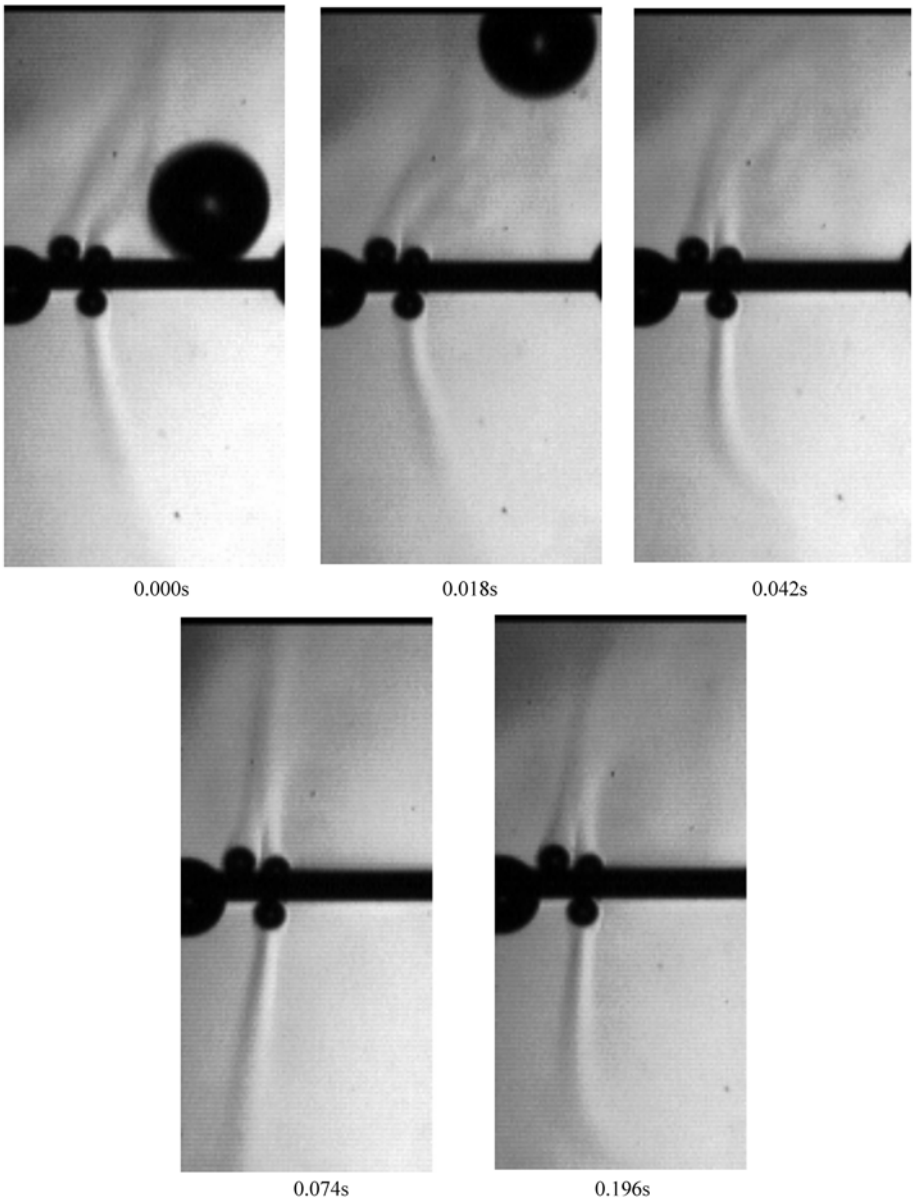

Figure 4.22 Effect of bubble departure on bubble jet flows

4.4 Models of Bubble-Top Jet Flow

4.4.1 Governing Equations

The experimental observations showed that a fully developed bubble jet flow can be stable, so a 3-dimensional steady laminar model was used to describe the fluid flow and heat transfer in the liquid region around a heating wire and a spherical bubble on the wire, as illustrated in Fig. 4.23. The governing equations are given as:

$$\nabla \cdot (\rho \boldsymbol{V}) = 0 \tag{4.1}$$

$$\boldsymbol{V} \cdot \nabla \boldsymbol{V} = \nu \nabla^2 \boldsymbol{V} - \frac{\nabla p}{\rho} - g \cdot \boldsymbol{j} \tag{4.2}$$

$$\boldsymbol{V} \cdot \nabla (c_{\mathrm{p}} T) = \frac{1}{\rho} \lambda \nabla^2 T \tag{4.3}$$

The natural convection was modeled using the Boussinesq approximation, or

$$\rho = \rho_{\mathrm{ref}} \beta (T - T_{\mathrm{ref}}) \tag{4.4}$$

where β is the thermal expansion coefficient of water.

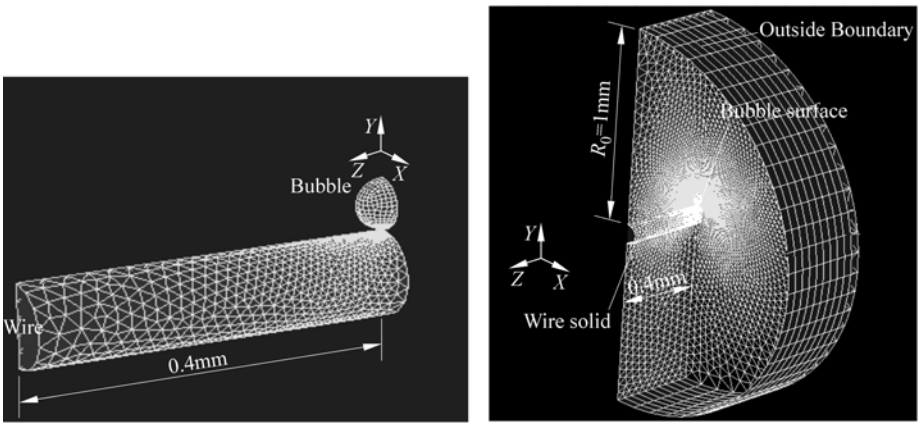

Figure 4.23 Model and mesh for numerical simulations
(a) Bubble and wire; (b) Ideal domain

4.4.2 Fundamental Considerations

1. Phase Change Heat Transfer at Bubble Interface

The vapor temperature inside a spherical bubble is obtained from the Laplace and Clausius-Clapeyron equations [13, 15] as,

$$T_{\mathrm{v}} = T_{\mathrm{s}} + \frac{2\sigma T_{\mathrm{s}}}{h_{\mathrm{fg}}\rho_{\mathrm{v}} R_{\mathrm{b}}} \tag{4.5a}$$

or accurately from Rayleigh equation and Clausius-Clapeyron equation [16] as

$$T_{\mathrm{v}} = T(P_{\mathrm{v}}) = T_{\mathrm{sat}}(p_0) + \frac{2\sigma\, T_{\mathrm{sat}}}{h_{\mathrm{fg}}\rho_{\mathrm{v}} r_{\mathrm{b}}} + \frac{T_{\mathrm{sat}}\rho_{\mathrm{l}}}{h_{\mathrm{fg}}\rho_{\mathrm{v}}}\left[r_{\mathrm{b}}\frac{\mathrm{d}^2 r_{\mathrm{b}}}{\mathrm{d}t^2} + \frac{3}{2}\left(\frac{\mathrm{d}r_{\mathrm{b}}}{\mathrm{d}t}\right)^2 \right] \tag{4.5b}$$

The heat transfer between the vapor inside the bubble and the interface is

$$q''_{\mathrm{i}} = h_{\mathrm{i}}(T_{\mathrm{v}} - T_{\mathrm{i}}) \tag{4.6}$$

where the interfacial heat transfer coefficient due to evaporation or condensation is:

$$h_{\mathrm{i}} = \frac{2\hat{\sigma}}{2-\hat{\sigma}}\frac{h_{\mathrm{fg}}^2\rho_{\mathrm{v}}}{T_{\mathrm{v}}}\left(\frac{\bar{M}}{2\pi\bar{R}T_{\mathrm{v}}}\right)^{1/2}\left[1 - \frac{p_{\mathrm{v}}}{2h_{\mathrm{fg}}\rho_{\mathrm{v}}}\right] \tag{4.7}$$

Accommodation coefficient, $\hat{\sigma}$, is assumed to be 0.03.

When the local interfacial temperature $T_{\mathrm{i}} > T_{\mathrm{v}}$, $q''_{\mathrm{i}} < 0$, liquid evaporates from the surface into the bubble and the bubble absorbs heat. When $T_{\mathrm{i}} < T_{\mathrm{v}}$, $q''_{\mathrm{i}} > 0$, condensation occurs at the surface, and the bubble on the wire surface absorbs energy from the bubble bottom ($T_{\mathrm{i}} > T_{\mathrm{v}}$) and releases energy from its top ($T_{\mathrm{i}} < T_{\mathrm{v}}$). Eqs. (4.5) – (4.7) are used as the internal boundary conditions at the bubble surface to calculate the heat transfer along the bubble surface. The interfacial temperature T_{i} along the bubble surface is part of the unknown temperature distribution determined by the solution of the governing Eqs. (4.1) – (4.3).

2. Marangoni Flow at the Bubble Interface

The interfacial temperature along the bubble surface results in a decreasing temperature gradient along the bubble surface from the bottom to the top of the bubble. The temperature gradient causes a surface tension gradient which causes the Marangoni flow along the bubble interface [1]. As noted in many previous

investigations [4, 7 – 16], thermocapillary or Marangoni flow driven by an interfacial tension gradient is expected to play a principal role in bubble-top jet flow phenomena. This interfacial flow induces a shear force in the liquid phase, $\tau_{R\theta}$, and in the vapor phase, $\tau'_{R\theta}$, at the interface. These shear forces are balanced by the surface tension gradient for a steady flow:

$$\tau_{R\theta} + \frac{1}{R}\frac{d\sigma}{dT}\frac{\partial T}{\partial \theta} + \tau'_{R\theta} = 0 \tag{4.8}$$

Because the vapor viscosity is very small, $\tau'_{R\theta} \approx 0$, the boundary condition corresponding to the interfacial effect is

$$\mu\left[r\frac{\partial}{\partial r}\left(\frac{u_\theta}{r}\right)\right]_{r=R} + \frac{1}{R}\frac{d\sigma}{dT}\frac{\partial T}{\partial \theta} = 0 \tag{4.9}$$

In addition to the tangential flow along the interface caused by the surface tension gradient, a mass flux normal to the bubble surface occurs due to the evaporation and condensation. The heat transfer in the microlayer under the bubble is mainly conduction and the maximum heat flux is:

$$q''_i \approx \frac{T_w - T_i}{\delta}\lambda_l < \frac{T_w - T_v}{\delta}\lambda_l \tag{4.10}$$

4.5 Characteristics of Bubble-Top Jet Flow

4.5.1 Jet Flow Driving Force and Pumping Effect

The typical numerical results [13, 15] shown in Fig. 4.24 illustrate the flow field and flow structure for a static bubble having diameter of 0.03 mm at wire superheat of 7 K and a bulk liquid subcooling of 43 K, showing very good agreement with the experimental measurements. In Fig. 4.24(b), the flow at the bubble top is very slow because the temperature distribution is quite uniform there with very weak Marangoni effect compared to the region close to the wire. The PIV measurements in Fig. 4.13 show that the fastest flow was not at the bubble top, but some distance away from the top surface, in the “neck” of the jet flow in Fig. 4.14. The slow region observed experimentally verifies that the bubble-top jet flow is not induced by the mass flux from condensation or breaking out of vapor inside the bubble.

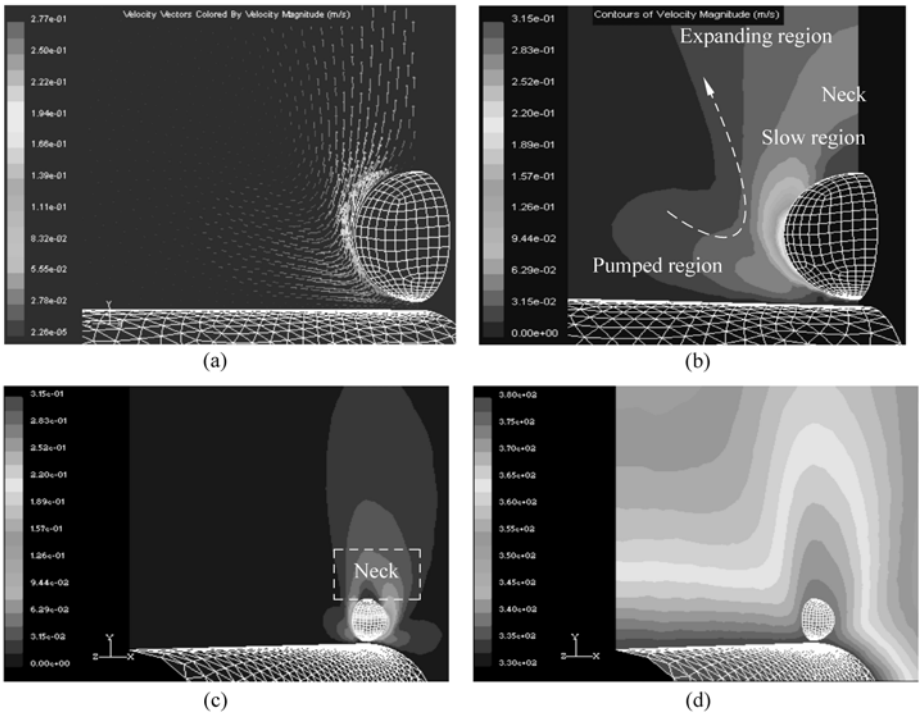

Figure 4.24 Simulation results for the bubble-top jet flow
(a) Velocity vectors on *Y-Z* plane; (b) Velocity contours on *Y-Z* plane; (c) Velocity contours in *X-Y* and *Y-Z* planes; (d) Temperature contours in *X-Y* and *Y-Z* planes

Figure 4.24(c) shows that the Marangoni flows form around the lower half of the bubble. The flows from all sides concentrate above the top of the bubble to form the observed bubble-top jet flow phenomenon. Hot liquid is sucked from the pumping region and pumped into the expanding region, where there is a significant temperature difference between the jet flow and the surrounding liquid, as shown in Fig. 4.24(d). The density difference allowed the jet flow to be observed by light refraction in the CCD photographs. The pumping effect of the jet flow is the key heat transfer mechanism.

The numerical results shown in Fig. 4.25 are the velocity and temperature fields when gravity is reversed. The velocity distributions are almost identical with the results in Fig. 4.24. This is coincident with the experimental observations that the gravity had little effect on the jet flows. The temperature distribution in Fig. 4.25(b) is also similar to that in Fig. 4.24(d), only with the hot liquid layer somewhat thinner around the bubble because the natural convection is reversed. If the simulation is conducted with only natural convection and without Marangoni flow, the jet flow does not form, as shown in Fig. 4.26.

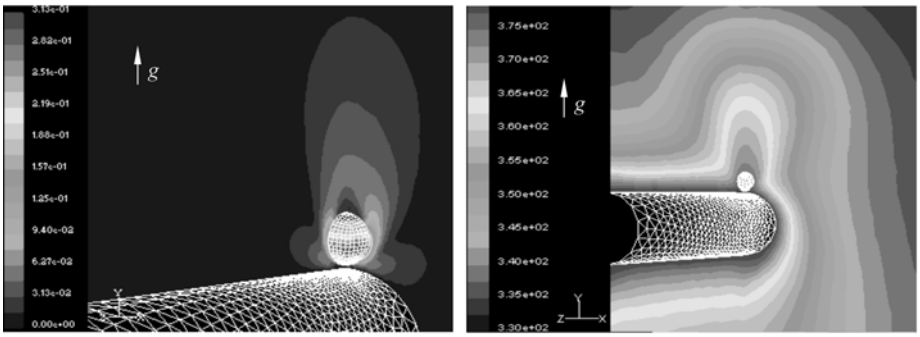

Figure 4.25 Gravitational effect on the jet flow
(a) Velocity contours in *X-Y* and *Y-Z* planes; (b) Temperature contours in *X-Y* and *Y-Z* planes

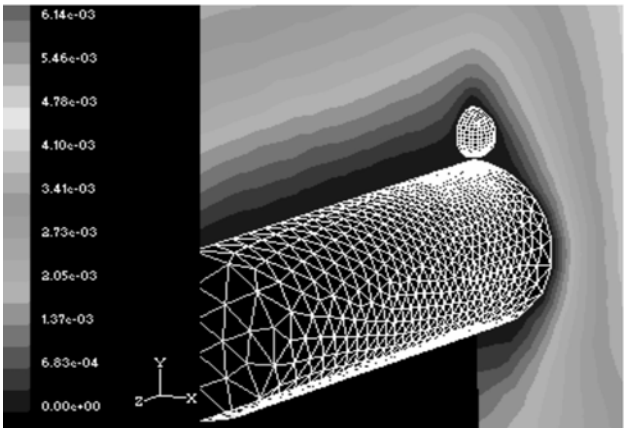

Figure 4.26 Natural convection flow field without Marangoni flow

4.5.2 Jet Flow Bifurcation Phenomenon

The predicted flow structure for a bubble having a diameter of 0.06 mm is shown in Fig. 4.27 at the same superheat and subcooling conditions as in Fig. 4.24. The flow in the central plane parallel to the wire axis is shown in Fig. 4.27(a). The shape is similar to the bubble-top jet flow around the 0.03 mm bubble (see Fig. 4.24(b)), however, the velocities accordingly are much smaller. The velocity at the neck in Fig. 4.24(b) is about 50 mm/s, but only 20 mm/s in Fig. 4.27(a). This is consistent with the experimental observations that smaller bubbles had stronger jet flows than larger bubbles.

The flow in the *X-Y* plane perpendicular to the wire axis exhibits a butterfly-like flow structure, as seen in Fig. 4.27(b), with two symmetrical sub jets around

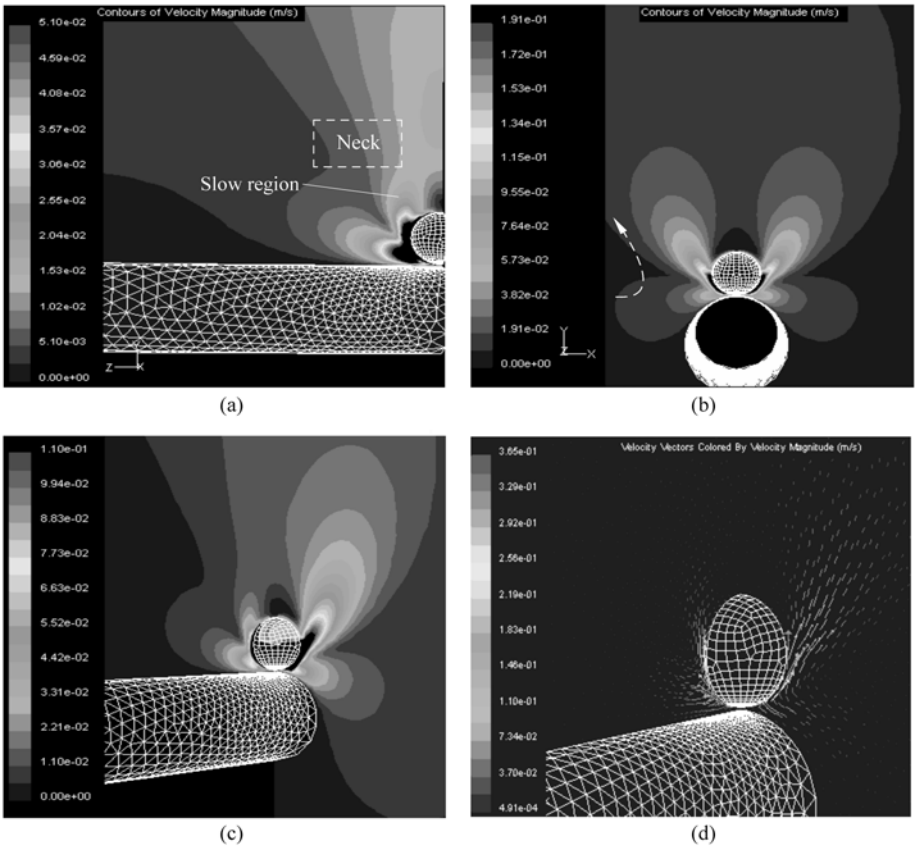

Figure 4.27 Velocity magnitudes for a multi-jet flow
(a) Central plane parallel to wire: top jet flow; (b) *X*-*Y* plane perpendicular to wire: multi jet flow; (c) Velocity field in *X*-*Y* and *Y*-*Z* planes; (d) Velocity vectors in *X*-*Y* and *Y*-*Z* planes

the wire and bubble, which is consistent with the multi-jet flows observed in the experiments. The highest flow velocities are not above the bubble because the two sub jet flows do not coalesce there, but occur on the two sides of the bubble where the sub jet flows are driven by the Marangoni effect. Figures 4.27(c) and (d) illustrate the very complex multi-jet flow structure around a bubble. The pumping effect of the multi-jet flows spreads the high temperature fluid over a larger region than a single bubble-top jet flow. Comparison of the flow in Fig. 4.24 with that in Fig. 4.27 shows that the bubble size significantly affects the jet flow structure.

Actually, the flow structure was noted to be a function of both the bubble size and the ratio of the bubble diameter (0.03 mm or 0.06 mm) to the wire diameter (0.1 mm) in the experiments. A smaller bubble was not able to extend far into the subcooled liquid on either side of the wire, while a larger bubble extended farther into the subcooled liquid resulting in a more non-uniform temperature distribution on the bubble. The ratio of the bubble diameter to the wire diameter also affected

the flow structure. The smaller bubble was smaller than the wire so that the obstruction due to the wire was more uniform. The larger bubble diameter was similar to that of the wire, so the flow in the two regions beside the wire moving up past the bubble was less obstructed than the flow directly above the wire.

The temperature distribution on the bubble surface helps explain the multi-jet flow phenomenon. Since a smaller bubble ($d = 0.03$ mm) is mostly within hot liquid layer where exists great temperature gradient, the temperature distribution on its surface decreases fairly uniformly from the bottom to the top, as shown in Fig. 4.28(a). For a larger bubble ($d = 0.06$ mm), the top and much area of the two sides stretch into the cold bulk liquid. Both the bubble-top jet and side jet flows pump the hot liquid up past the bubble. Since the flow is relatively slow and there are vortices above the bubble (see Fig. 4.29), the fluid above the bubble is not cooled by the incoming subcooled liquid, while condensation along upper surface of the bubble releases energy to heat the liquid (see Fig. 4.30). Furthermore, since the larger bubble extends farther out into the around liquid region, the flow passes the bubble along the lower half of the bubble and the colder liquid cools the interface, which creates a higher heat transfer rate there, and hence lower temperature. Therefore, the coldest parts of the 0.06 mm bubble are the two sides stretching into the cold bulk liquid, as shown in Fig. 4.28(b). The specific location of the coldest regions is closely relative to the bubble and wire sizes, the hot liquid layer thickness, temperature of the wire, bulk liquid subcooling and condensation and evaporation taking place on the bubble surface.

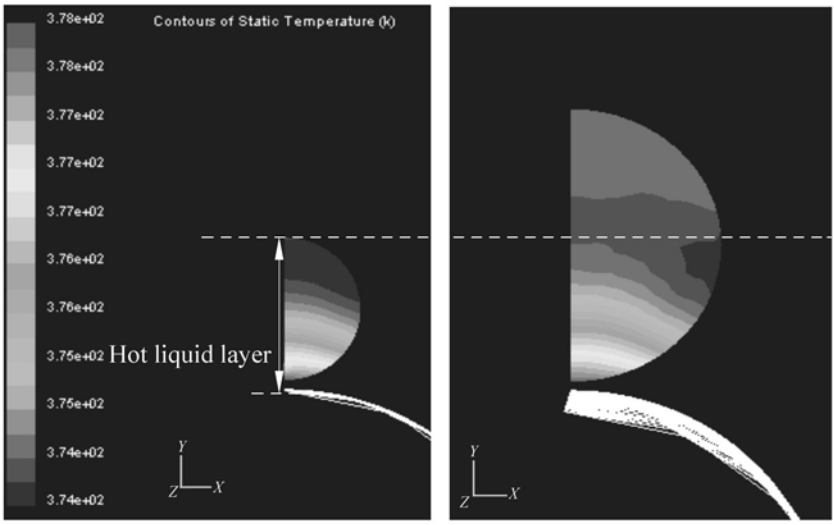

Figure 4.28 Temperature field on the bubble surface
(a) 0.03 mm bubble; (b) 0.06 mm bubble

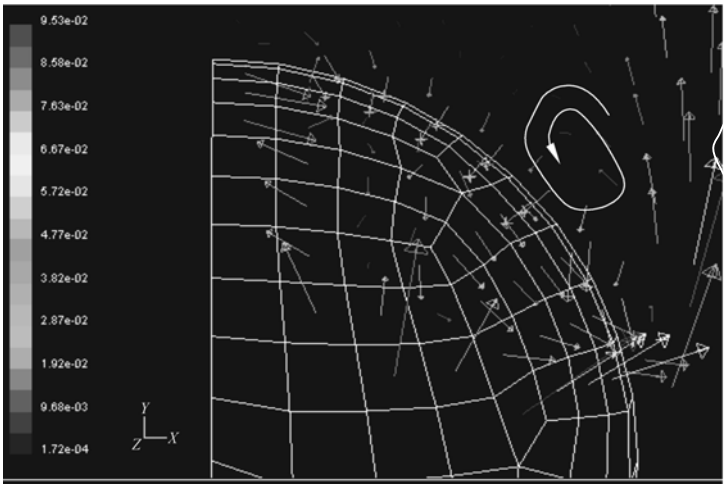

Figure 4.29 Vortices above a 0.06 mm bubble

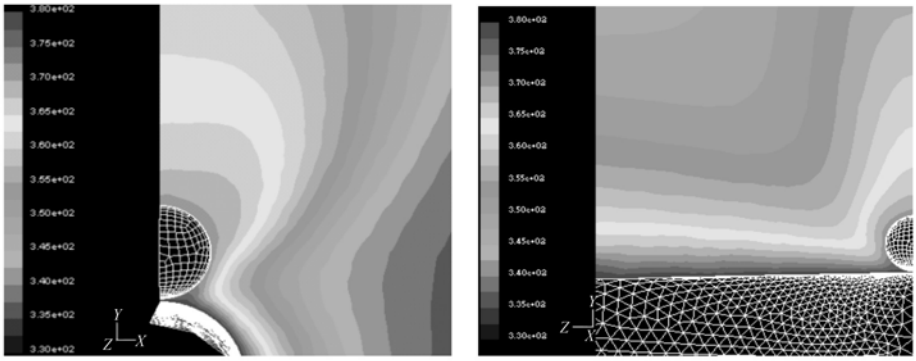

Figure 4.30 Temperature field around 0.06 mm bubble
(a) *X*-*Y* plane; (b) *Y*-*Z* plane

4.6 Formation of Bubble-Top Jet Flow

4.6.1 Temperature Evolution

Lu and Peng [16] further investigate the flow around a single bubble attached to a heating wire during the formation process of a bubble jet flow. Figure 4.31 illustrates the temperature variation around a bubble during bubble jet flow formation at bulk liquid temperature 303 K and wire temperature 380 K. The bubble is 0.07 mm in diameter and the wire is 0.2 mm in diameter.

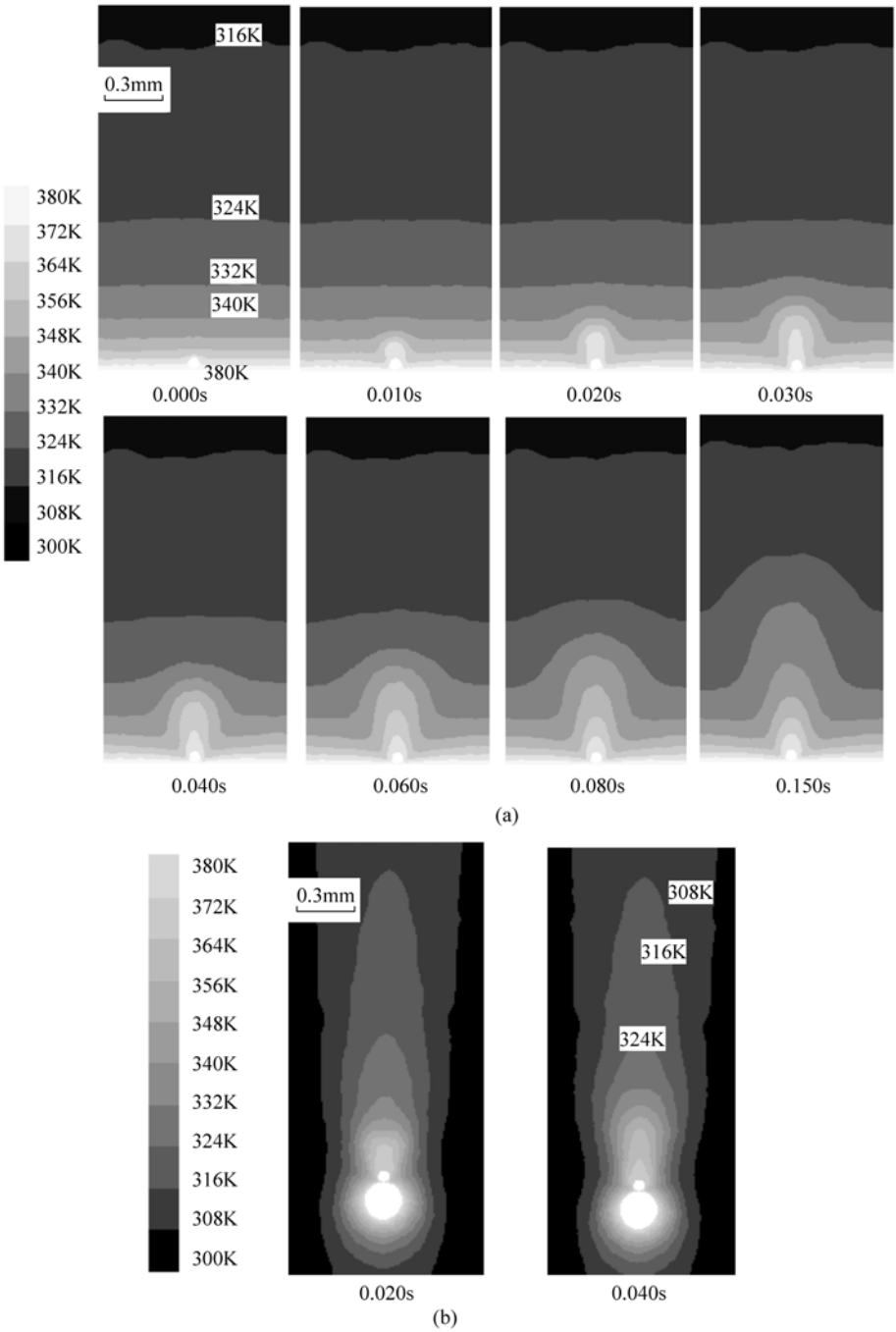

Figure 4.31 Temperature evolution during jet flow formation
(a) Vertical plane across the wire axis ($z = 0$ mm); (b) Vertical plane normal to the wire ($x = 0.5$ mm)

During the waiting stage at $t = 0.000$ s, the thermal boundary layer near the wire has a thickness of 0.3 mm, and a high temperature region, a very thin layer is observed around the bubble. Before 0.010 s, the high temperature region is still within the thermal boundary layer, and bubble jet flow is not obvious. After 0.010 s, the high temperature region pushes the thermal boundary layer into the cold liquid, and the bubble jet begins to develop. In a short time, the jet flow with high temperature quickly bursts, and both the center and boundary rapidly extend. As seen in the experimental images shown in Fig. 4.17, both mushroom head and stem extended and penetrated far away within 0.040 s (from 0.040 s to 0.080 s). After 0.060 s, the stem of the jet flow became stable, while the top of the jet flow still continued to extend into the bulk liquid. Comparing Fig. 4.17 with Fig. 4.31(a), it can be found that the simulation results in the vertical plane across the wire are in a quite reasonable agreement with the experimental observations, clearly showing three main stages in the bubble jet flow evolution described in Section 4.4.1. In the vertical plane normal to the wire as shown in Fig. 4.31(b), the temperature decreases to the bulk liquid temperature quickly from the jet flow region.

Figure 4.32 illustrates the temperature profiles at different heights above the

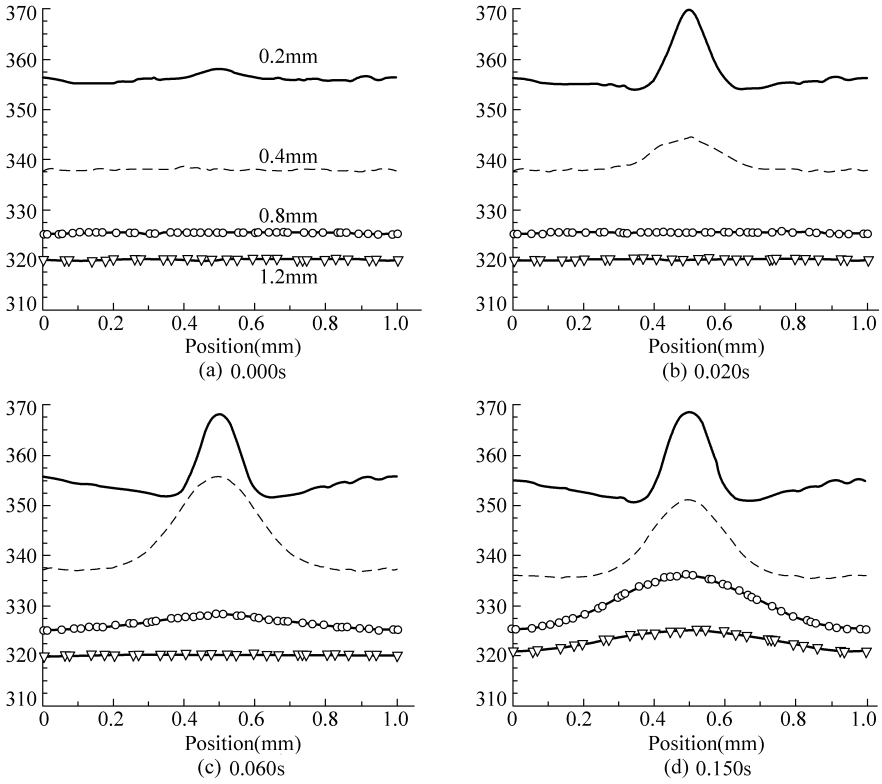

Figure 4.32 Temperature field above wire

wire ($y = 0.2$ mm, 0.4 m, 0.8 mm, 1.2 mm). During the waiting stage or at 0.000 s, only the temperature profile at $y = 0.2$ mm has a small peak around the bubble. At 0.020 s, the temperature profiles at both $y = 0.2$, 0.4 mm have a peak, and the jet flow with high temperature above the bubble extends quickly. At 0.060 s, the temperature profile at $y = 0.8$ mm forms a peak. From 0.060 s to 0.150 s, the temperature profiles of the mushroom stem at $y = 0.2$, 0.4 mm have little change, while the profiles of mushroom head at $y = 0.8$, 1.2 mm have very significant changes. Additionally, the mushroom head of the jet flow is going to disappear into the bulk liquid as the jet flow develops, because the temperature difference decreases at its head.

4.6.2 Temperature Evolution on Bubble Interface

The temperature on the spherical bubble surface is illustrated in Fig. 4.33. At initial time, the temperature increases along the interface approaching to the wire, and there is a cold spot just on the top of bubble. This steady temperature distribution without thermocapillary force occurs in the waiting stage. During 0.000 – 0.010 s, the jet flow changes rapidly from waiting stage to bursting stage. After the transition or the initial stage, the thermocapillary convection flow quickly makes the temperature in the upper region of the bubble interface uniform, only the temperature at the bubble interface near the wire still changes obviously, and this is quite different from that in the waiting stage.

After 0.010 s, two cold areas appear near the middle region of the bubble interface on the two sides symmetrical about the wire axis, respectively, and they expand up to 0.030 s. From 0.030 s to 0.060 s, the cold area shrinks, and the temperature in the upper region on the bubble becomes uniform again. After 0.060 s, the temperature profile on the bubble interface changes very little.

From the temperature evolution on the bubble interface, two special phenomena can be identified clearly. The cold region on the bubble interface occurs in the middle region of the bubble during burst and fully developed stages, and a lowest surface temperature in the cold region appears during the burst stage. These phenomena are mainly caused by the coupling effects of the jet flow and temperature field. Because of the spatial limit, the pumping and cooling effect in the region exactly above the wire is weaker than that in the two bubble side regions symmetrical about the wire, and then two side regions emerge two cold patches. Furthermore, since the velocity of jet flow formation reaches its maximum value during burst stage, as illustrated in Fig. 4.18, the thermal boundary layer near two sides of the bubble will reach a minimum value, and the lowest temperature of the cold region is reached accordingly.

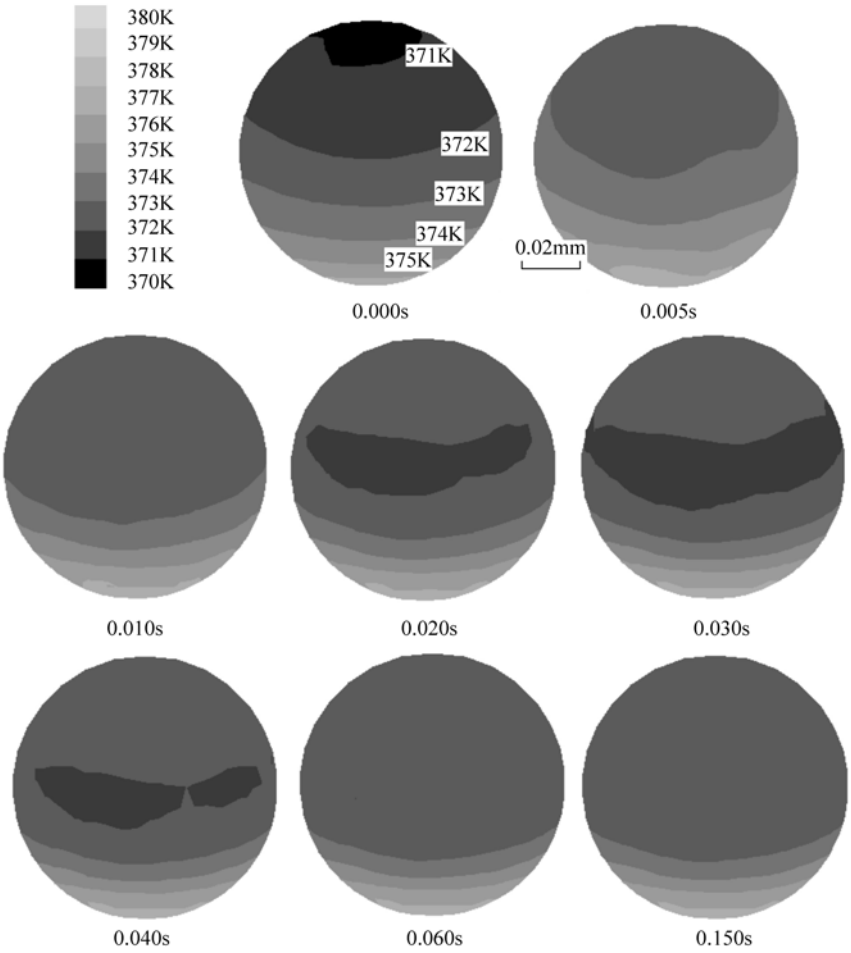

Figure 4.33 Temperature evolution on a bubble interface

4.6.3 Flow Evolution

The dynamical evolution of the flow field is presented in Fig. 4.34. At initial time or during waiting stage, natural convection contributes to the flow as a principle mechanism, and the jet flow around the bubble has little effect on the bulk liquid. After the waiting stage, the interfacial thermocapillary force becomes to drive the liquid, but the jet flow is still within the thermal boundary layer in the first 0.010 s.

During 0.010 – 0.030 s, two cold areas appear near the middle region on both sides of the bubble surfaces which symmetrically distributes along the wire axis, respectively, referring to Fig. 4.33, and this would cause special flow field because the interfacial thermocapillary force drives the liquid from the hot region to the

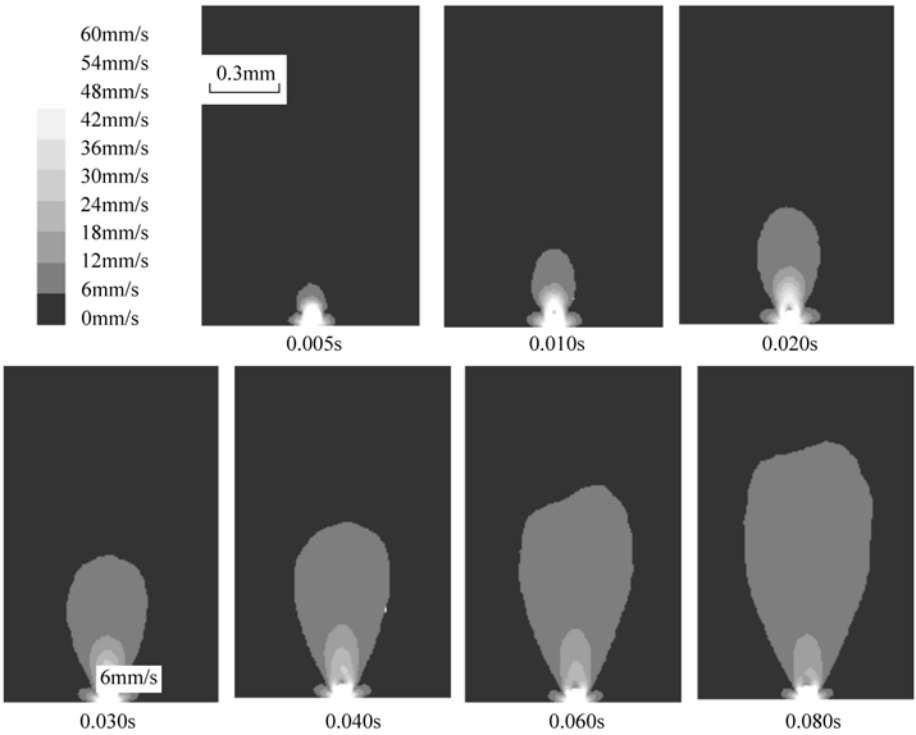

Figure 4.34 Flow evolution around a bubble

cold region. In the vertical plane across the wire axis, the liquid at the bubble top is driven downwards to the cold region, while the liquid at the bubble bottom is pumped upwards. As a result, the jet flow disperses above the bubble, and that is just like a mushroom cloud as in Fig. 4.17. From 0.030 to 0.060 s, two cold areas shrink, and the temperature in the upper region on the bubble becomes uniform. Apparently, the flow from the bubble top to middle region would decrease quickly, and the mushroom correspondingly evolves and converges to a strong jet flow.

After 0.060 s, the structure of interface temperature distribution is almost invariable. As a result, the mushroom stem also keeps its shape. On the other hand, the mushroom head penetrates into the bulk liquid and gradually mixes with the bulk liquid. Finally, a fully-developed jet flow forms. In this stage, both jet flow and its temperature profile evolve stably and can last a long time.

During the bubble jet flow formation, the temperature gradient at the bubble interface first causes thermocapillary flow near the bubble, and then the flow extends above the bubble. Because of the hot liquid flow from the region near the bubble or wire, the temperature of the liquid above the bubble increases significantly. As a result, both flow field and temperature profile are coupled with each other. Apparently, the bubble jet flow plays an important role in boiling heat transfer due to liquid pumped from the hot region to the cold region.

References

[1] L. W. Lin. Microscale thermal bubble formation-thermal physical phenomena and applications. Microscale Thermophysical Engineering, 2 (2): 71, 1998.

[2] L. W. Lin, A. P. Pisano, V. P. Carey. Thermal bubble formation on polysilicon micro resistors. Journal of Heat Transfer: Transactions of the ASME, 120 (3): 735, 1998.

[3] S. Glod, D. Poulikakos, Z. Zhao, et al. An investigation of microscale explosive vaporization of water on an ultrathin Pt wire. Int. J. Heat and Mass Transfer, 45(2): 367 – 379, 2002.

[4] X. F. Peng, B. X. Wang. Nucleation and thermodynamic non-equilibrium for boiling in microchannels & microstructures. Annual Review of Heat Transfer, XI: 307 – 350, 2000.

[5] I. G. Shekriladze. On the role of the "pumping effect" of a vapor bubble growing at the wall during nucleate boiling. In: Voprosy Konvektivnogo Teploobmena I Chistoty Vodianogo Para. Metsniereba Press, Tbilisi, in Russian, 90 – 97, 1970.

[6] I. G. Shekriladze. Mechanisms of heat removal in the process of developed boiling. Heat Transfer-Soviet Research, 22 (4): 445 – 463, 1990.

[7] X. F. Peng, Y. J. Huang, D. J. Lee. Transport phenomenon of a vapor bubble attached to a downward surface. International Journal of Thermal Sciences, 40(9): 797 – 803, 2001.

[8] H. Wang, X. F. Peng, B. X. Wang et al. Jet flow phenomena during nucleate boiling. Int. J. Heat and Mass Transfer, 45 (6): 1359 – 1363, 2002.

[9] H. Wang, X. F. Peng, B. X. Wang et al. Bubble sweeping and jet flows during nucleate boiling of subcooled liquids. Int. J. Heat and Mass Transfer, 46 (5): 863 – 869, 2003.

[10] H. Wang, X. F. Peng, C. Pan et al. Bubble-top jet flow on micro wires. Int. J. Heat and Mass Transfer, 47 (14): 2891 – 2900, 2004.

[11] H. Wang, X. F. Peng, D. M. Christopher et al. Jet flows around microbubbles in subcooled boiling. ASME Journal of Heat Transfer, 127 (8): 802 – 804, 2005.

[12] D. M. Christopher, H. Wang, X. F. Peng. Dynamics of bubble motion and bubble top jet flows from moving vapor bubbles on microwires. ASME Journal of Heat Transfer, 127 (11): 1260 – 1268, 2005.

[13] H. Wang, D. M. Christopher, X. F. Peng et al. Jet flows from a bubble during subcooled pool boiling on microwires. Science in China (Series E), 48 (4): 385 – 402, 2005.

[14] H. Wang, X. F. Peng, D. M. Christopher et al. Flow structures around micro-bubbles during subcooled nucleate boiling. Chinese Physics Letters, 22 (1): 154 – 157, 2005.

[15] H. Wang, X. F. Peng, D. M. Christopher et al. Investigation of bubble-top jet flow during subcooled boiling on wires. Int. J. Heat and Fluid Flow, 26(3): 485 – 494, 2005.

[16] J. F. Lu, X. F. Peng. Bubble jet flow formation during boiling of subcooled water on fine wires. Int. J. Heat and Mass Transfer, 51 (17 – 18): 4461 – 4469, 2007.

5 Bubble Dynamics on Fine Wires

Abstract Experimental investigations were conducted to observe bubble motion during subcooled boiling of water on heating wires, and theoretical models were proposed to describe the associated dynamical phenomena and understand the physical significance. Various kinds of bubble motion, such as sweeping, separation, collision, oscillation during leaping were further studied by the bubble dynamics model. Both experimental and theoretical evidences indicated that interfacial thermocapillary force played an important role in many bubble motions. The thermocapillary force can be induced by the bubble motion, the interaction between neighbor bubbles or the heating surface. The theoretical predictions are compared with the experimental observations is presented and discussed. Bubble dynamics including nucleation, bubble growth and departure have been intensively investigated in past decades. For boiling on a fine wire, however, some micro bubbles were found to move along the wire, to sweep back and forth, and to return to the wire after departure. Analyses were conducted to probe into the mechanisms behind.

Keywords bubble dynamics, bubble sweeping, bubble return, bubble leap, Marangoni effect, evaporation, condensation

In classical boiling investigations, bubble dynamics were investigated comprehensively, such as nucleation, bubble growth and departure, and associated heat transfer enhancement [1 – 7]. Bubble moving along heating surfaces was well known in some boiling experiments, such as forced flow boiling, boiling on a vertical wall [5] and a downward wall [7]. In these cases, some bubbles might move along the wall surface instead of detaching from the wall, because of the force of fluid flow or gravity/buoyancy. These moving bubbles would not change their moving direction and just move in the direction of forced flow or buoyancy. This chapter describes some unique bubble dynamics occurring on very fine wires [8 – 16].

X. Peng, *Micro Transport Phenomena During Boiling*

5.1 Modes of Bubble Motion

5.1.1 Bubble Sweeping

In subcooled boiling on various wires, there was a plenty of bubble dynamical phenomena visually observed. Vapor bubbles were observed to move along the horizontal heating wire without forced flow, and they could change moving direction backward when encountering with another bubble. These bubbles came to induce forward and backward sweeping movement along the wire, different from general moving bubbles in forced flow, on a vertical wall or downward wall. Here it is simply termed as bubble slippage.

A series of photographs illustrated in Fig. 5.1 show a bubble sweeping on a heating wire, which was obtained from the boiling of water with a subcooling of 80℃ [8, 9, 15]. Figure 5.2 shows a forward and backward sweeping movement along a vertically placed wire and sweeping of a single bubble on a horizontal wire. The bubble sweeping phenomenon was observed when bubbles were generated separately at active nucleate sites at lower heat fluxes and in the case of subcooled boiling. The experiments apparently indicate that the bubble back-and-forth sweeping was not induced by inertial or buoyancy, and the interaction between bubbles might be an important factor. Moving bubbles always halt and reverse when encountering another larger bubble. Bubbles usually moved very fast, accelerating and decelerating within a very short time resulting in significant disturbance in vicinity area.

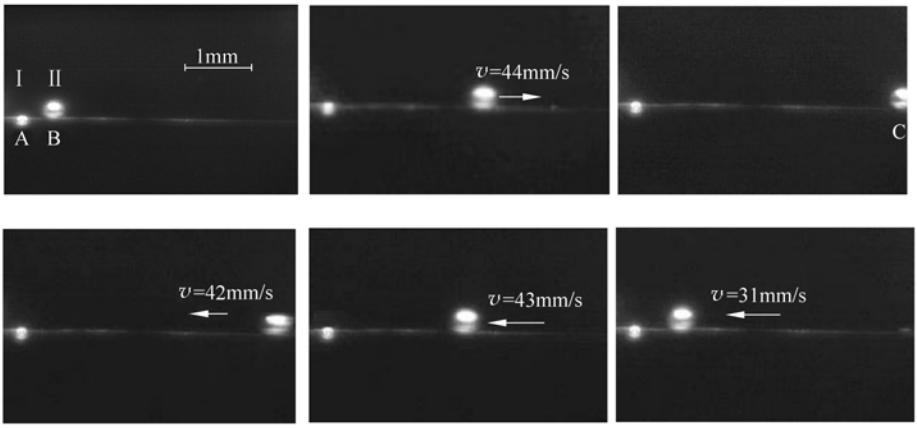

Figure 5.1 Bubble forward-and-backward motion on a heated wire

Under normal conditions, a bubble sweeping process began with a bubble acceleration process from its initial position [15], as illustrated in Fig. 5.3. Initially, the bubble stood on the wire with a bubble-top jet just above the bubble.

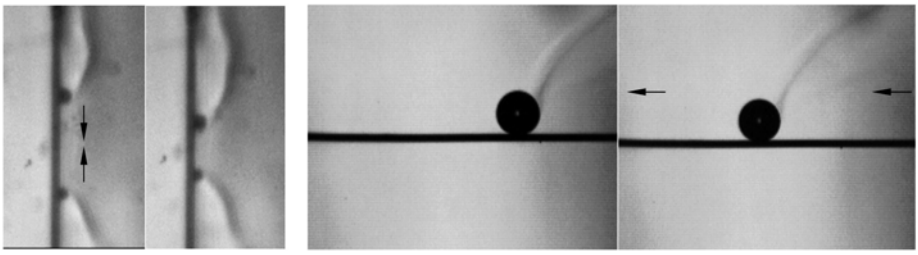

Figure 5.2 Bubble slippage on different wires
(a) On a vertical wire; (b) On a horizontal wire

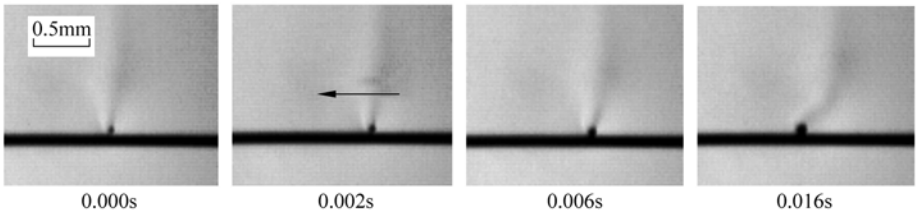

Figure 5.3 Bubble slipping startup (water at 30℃ and $q'' = 0.66 \times 10^6$ W/m^2)

In the next 0.030 s, the bubble began to move from the initial position, and the jet above the bubble trailed behind in the opposite direction of bubble motion. The bubble grew and absorbed heat from the wire during accelerating. The acceleration and velocity change of the moving bubble is depicted in Fig. 5.4. The bubble accelerated to a velocity of 20 mm/s within 0.16 s, and then moved at the constant velocity of 20 mm/s. During this period, the acceleration of the bubble decreased from about 2.5 m/s^2 to 0.

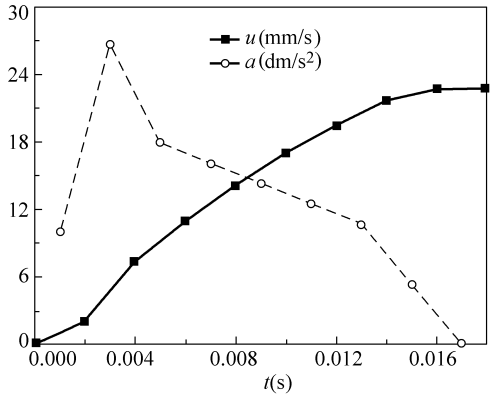

Figure 5.4 Acceleration and velocity changes during bubble sweeping startup

5.1.2 Bubble Interaction

As one of the bubble dynamical phenomena, bubble interaction [12] was frequently observed in various experiments of subcooled boiling on very fine wires, including several different bubble interactions with bubble separation, collision and coalescence.

1. Bubble Separation

Bubble separation phenomenon plays an important role during the period of initial bubble motion. A typical experimental phenomenon is presented in Fig. 5.5. A bubble began to separate from the left immobile bubble in the initial stage, and then accelerated along the wire within the distance of about 0.25 mm, as it grew.

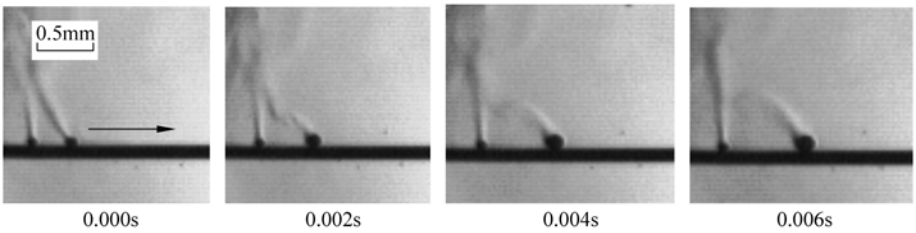

Figure 5.5 Separation from an immobile bubble

2. Bubble Collision

As illustrated in Fig. 5.6, a large bubble collided with an immobile bubble. Initially, the left bubble was at $x_0 = 0.95$ mm away from the immobile bubble and had a velocity of $u_0 = 40$ mm/s. After 0.024 s, the left bubble decelerated its velocity to zero as approaching to the right one, and then began to return and accelerate. This bubble collision process was just like an elastic collision. The experimental observations on the collision of two moving bubbles is illustrated in Fig. 5.7. Initially, two bubbles moved oppositely and approached to collide with each other. After colliding at about 0.014 s, they separated and moved away along two opposite directions.

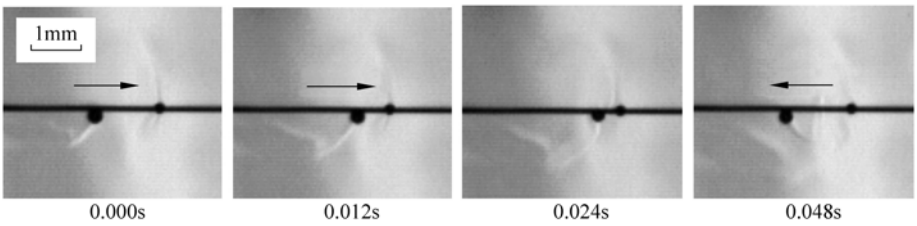

Figure 5.6 Bubble collision with an immobile bubble (water at 70℃ and $q'' = 0.6 \times 10^6$ W/m^2)

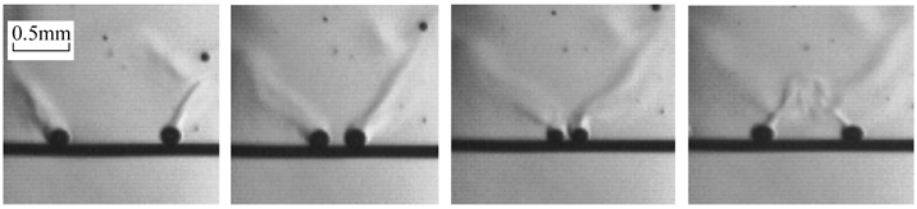

Figure 5.7 Collision of two moving bubbles

Figure 5.8 presents another special bubble collision process for water at a subcooling of 70℃ and heat flux of 1.30×10^6 W/m^2. At the beginning, the right bubble moved close to and tended to collide with the left bubble. At 0.004 s, the distance between these two bubbles reached the minimum, and the right bubble stops on the wire. A little bit later, the left bubble began to separate from the right bubble because of the interaction of these two bubbles, even though they did not really contact with each other. That is to say, the movement of the bubbles was exchanged through this collision without direct contact.

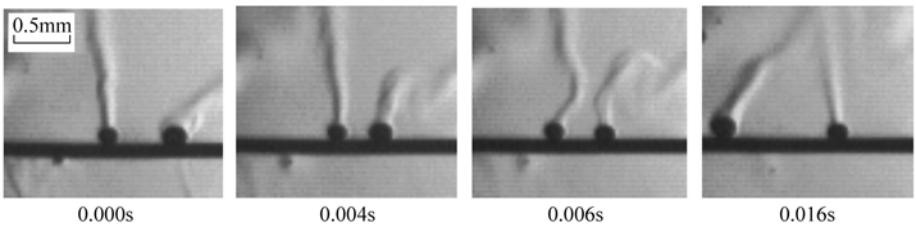

Figure 5.8 Bubble movement exchange through collision

3. Bubble Coalescence

Figure 5.9 shows a bubble coalescing process through bubble collision for water at a subcooling of 60℃ and heat flux 0.8×10^6 W/m^2. During $0.002-0.004$ s, the two bubbles finished colliding and formed a larger bubble. As this larger bubble swept to the right side, another collision occurred within the time period of $0.066-0.068$ s, and the right small bubble merged to the left big bubble. This type of collision made bubble growth much faster.

Apparently, the bubble motions can cause additional flow and greatly enhance heat transfer. The separation, collision and coalescence, enable sweeping bubbles to influence whole heating wires, and the heat flux would be re-distributed more uniformly. As a result, bubble separating, colliding and coalescing phenomena improve the heat transfer. These bubbles are also easier to depart from heating wires through bubble colliding and coalescing, of course, which is one of the important reasons significantly enhancing the heat transfer.

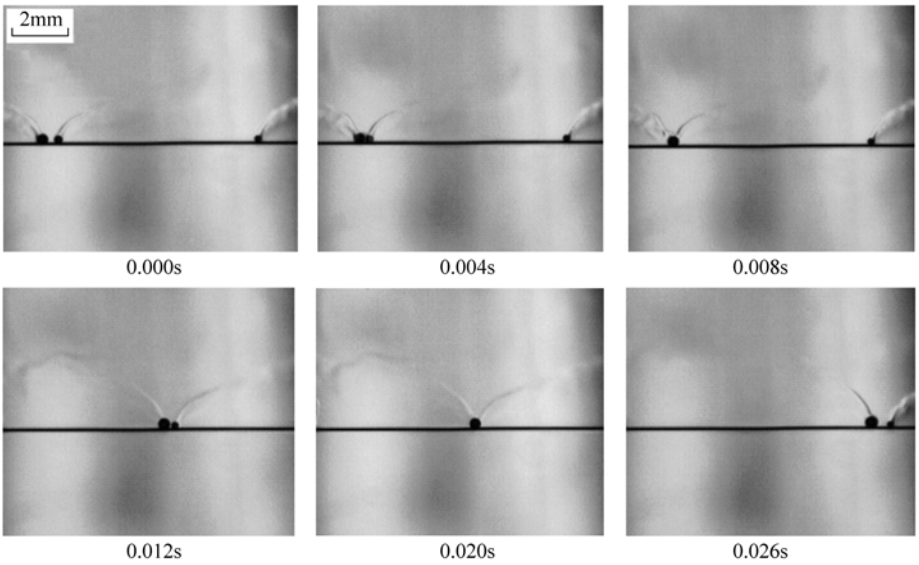

Figure 5.9 Bubble coalescing process

5.1.3 Bubble Oscillation Phenomena

In the experiments [8, 11, 12, 15], bubbles could oscillate between immobile bubbles or some ends on a wire, and single bubble oscillation usually occurred between two immobile bubbles regularly. Additionally, an oscillating bubble on a wire mostly moved at the maximum speed of 20 – 80 mm/s, and its spatial period was about 0.3 – 2 mm.

Figure 5.10 presents a typical process of a single bubble oscillation for boiling of water. Two large bubbles stood at their initial positions and a small bubble with the diameter of 0.10 mm oscillated between them. The small bubble oscillated with an average velocity of 20 – 30 mm/s, and it returned to the initial location after 0.026 s. Additionally, the oscillation period was about 0.026 s, and the spatial period was about 0.60 mm, which was about 6 times of the bubble diameter. Figure 5.11 presents two bubble oscillations nearby with a center immobile bubble separating these two oscillating bubbles. Two bubbles might oscillate between two immobile bubbles without any center bubbles, as shown in Fig. 5.12. This phenomenon is termed as coupling bubble oscillation.

A bubble oscillation process usually ended in two ways. If the oscillating bubble moved faster, it probably coalesced with an immobile bubble or made the immobile bubble unstable by collision, as the phenomenon in Fig. 5.13. If bubble oscillation slowed, the oscillating bubble usually halted near the center between the two immobile bubbles.

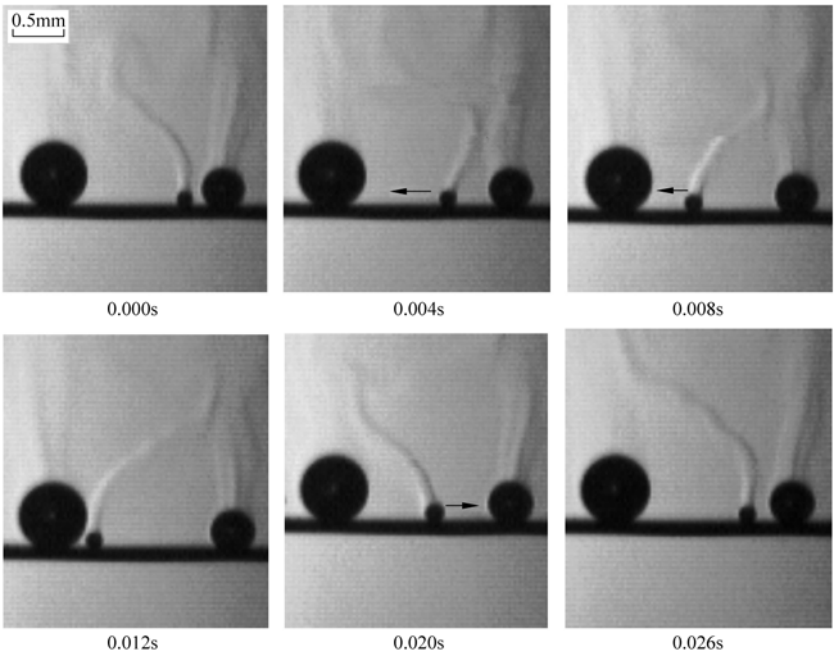

Figure 5.10 Single bubble oscillation
($T_{liq} = 30℃$, $q'' = 1.5 \times 10^6$ W/m^2, $T_w = 102℃$)

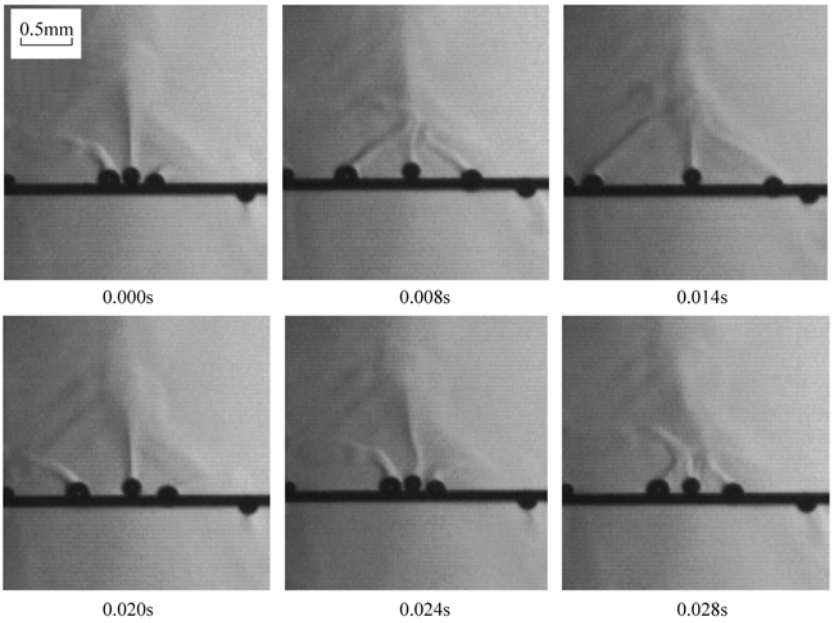

Figure 5.11 Two bubbles approaching an immobile bubble
($T_{liq} = 30℃$, $q'' = 1.6 \times 10^6$ W/m^2, $T_w = 105℃$)

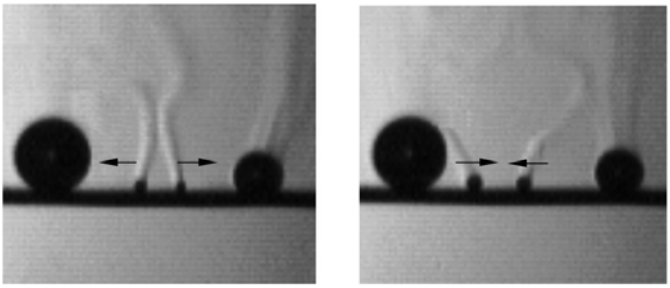

Figure 5.12 Coupling bubble oscillation
($T_{liq} = 30℃$, $q'' = 1.6 \times 10^6$ W/m^2, $T_w = 105℃$)

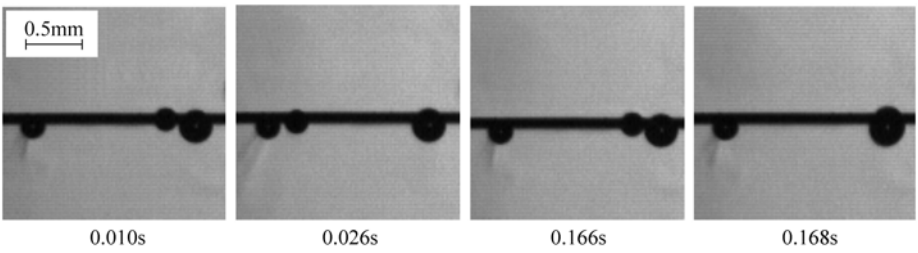

Figure 5.13 Bubble coalesce after oscillation
($T_{liq} = 30℃$, $q'' = 1.6 \times 10^6$ W/m^2, $T_w = 105℃$)

Generally, the bubble oscillation distance was 3 – 10 times diameter of the oscillating bubble, while the interaction range between immobile bubbles is usually less than 3 times of their diameter. Apparently, the oscillating bubble greatly extends the interaction distance of two bubbles and strengthens the intensity of bubble interaction. As a result, the bubble oscillation enhances the heat transport during boiling.

5.1.4 Bubble Leaping

1. Bubble Leaping at a Fixed Location

Bubble leaping at a fixed location [16] was observed at lower heat flux, and its radius was normally much smaller than the wire diameter. A leaping bubble would depart from and return to the wire without sweeping in the liquid close to the wire. Figure 5.14 shows a periodic leaping of a bubble on a heating wire at bulk water temperature of 30℃ and heat flux of 6.6×10^5 W/m^2. At 0.008 s, the bubble was on the wire, and then grew up and was ready to depart in the next 0.002 s. At 0.012 s, the bubble jumped away from the wire by about 0.12 mm. At 0.014 s, the bubble returned to the wire to finish a leaping period. At 0.020 s after the

second period, the bubble began to stay on the wire and then slipped away from the initial place. The leaping bubble actually experienced size changes during its leaping, as shown in Fig. 5.15.

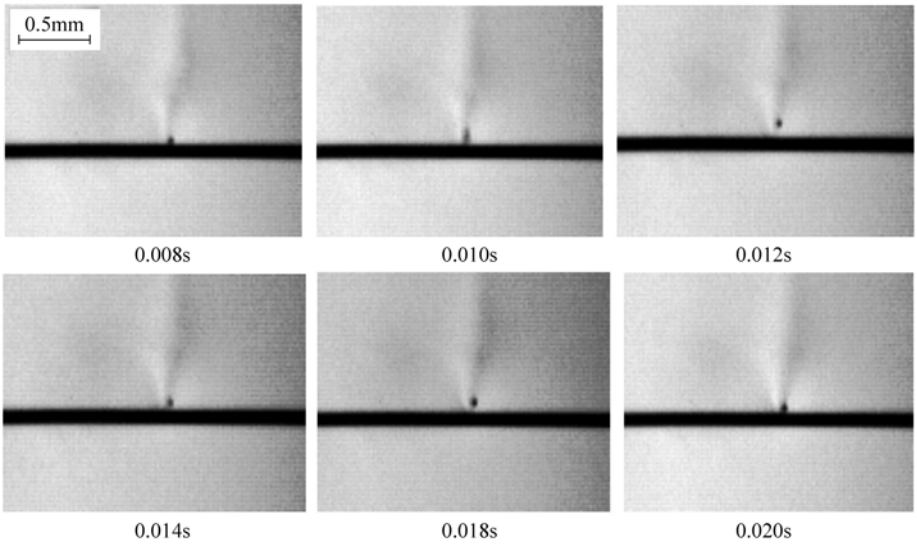

Figure 5.14 Bubble periodically leaping
($T_{liq} = 30℃$, $q'' = 6.6 \times 10^5$ W/m^2, $T_w = 101℃$)

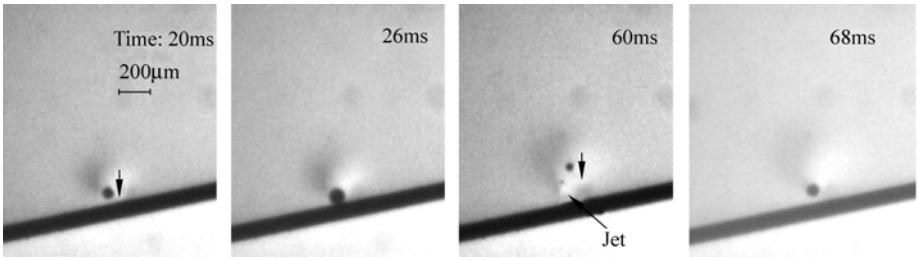

Figure 5.15 Bubble size changes during leaping

2. Bubble Leaping with Sweeping

The bubble leaping with sweeping at the same time was more stable and regular than that of bubble periodic leaping at a special position. A series of photographs is illustrated in Fig. 5.16 to show bubble leaping with slipping on a heating wire. At $t = 0$ s, a bubble with radius of 0.15 mm was on the middle of the wire. At 0.001 s, the bubble jumped off the wire and its size became smaller. In next 0.001 s, the bubble continued moving in the water along the wire for a distance of 0.037 mm. At 0.003 s, the bubble reattached to the wire and then swept along the wire much slowly. At 0.004 s, the bubble finished its leaping period, and it grew on

the wire just to the same size at the initial time. After $t = 0.004$ s, the bubble began the second leaping and sweeping period, jumping away from the wire, then sweeping and reattaching back to the wire, and growing up to the original size at 0.008 s. This bubble leaping with sweeping lasted for a long time until it met with another bubble or strong perturbation. The dynamical phenomenon of bubble leaping with sweeping was also observed on vertical wires, as shown in Fig. 5.17.

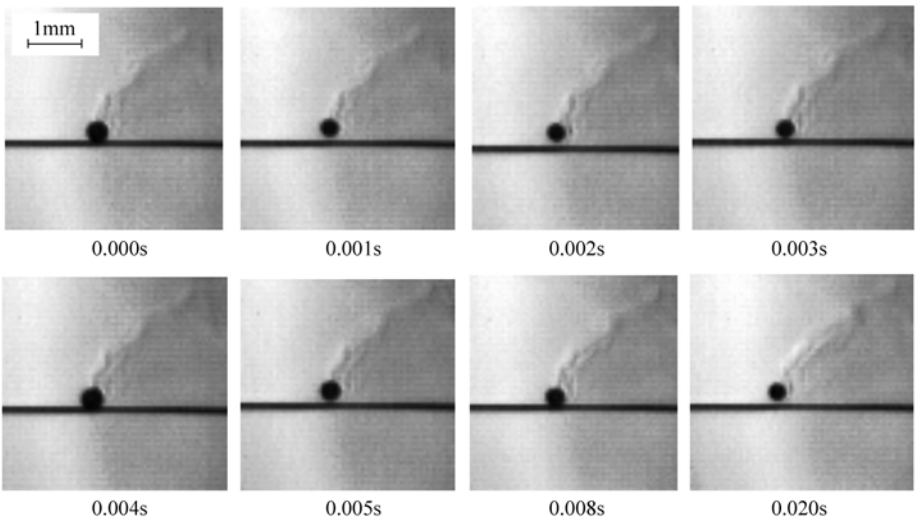

Figure 5.16 Bubble leaping with sweeping
($T_{liq} = 41$℃, $q'' = 8.8 \times 10^5$ W/m^2, $T_w = 103$℃)

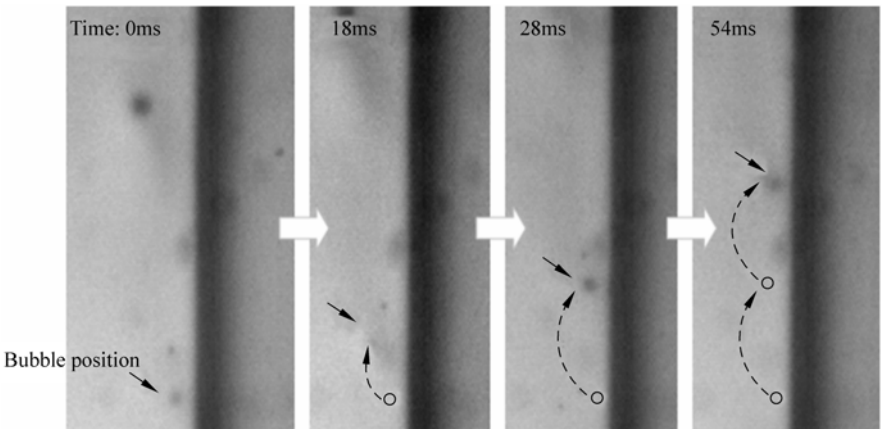

Figure 5.17 Bubble leaping with sweeping on a vertical wire

Generally, bubble leaping with sweeping has four main stages in one period [16], as illustrated in Fig. 5.18, jumping from 1 to 2, sweeping from 2 to 3, returning

from 3 to 4 and growing from 4 to 5, and each stage was nearly 0.001 s in Fig. 5.16. The simple leaping process at a special position is also similar to the process described in Fig. 5.18.

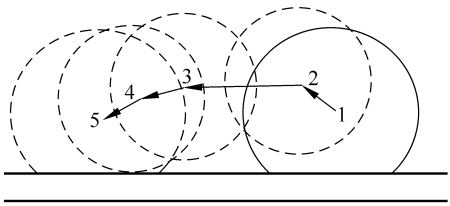

Figure 5.18 Stages of bubble leaping with sweeping

5.2 Fundamentals of Bubble Dynamics

Complex bubble motions are dependent upon the forces on the bubble induced by various effects. The buoyant force is important for a bubble in liquid. The interfacial tension and thermocapillary force also play important roles due to temperature difference along the bubble interface. If the bubble has a movement relative to the bulk liquid, the viscous force stunts the bubble moving, and as the bubble grows up, the force or inertial effect of the surrounded liquid would not be ignored.

5.2.1 Thermocapillary Force

In all of the boiling experiments, the diameters of heating wire and bubble were usually less than 1 mm, and consequently, both interfacial force and thermocapillary force are important for bubble dynamics. Actually, the interfacial effects were noted in different researches, but, they were not considered as important factors in many cases due to the existence of the buoyancy. However, these effects were widely recognized dominant in micro systems [4] and associated boiling systems [1]. For a single bubble generated from a surface or wire, the thermocapillary effect always causes liquid convection from high to low temperature region along the interface and generates the attraction force on the bubble towards the higher temperature surface. This may be expected to result in various bubble motions on a heating wire, as noted in the previous investigations [8 – 16]. Takahashi [4] found that the thermocapillary effect around a bubble was very strong and played an important role in driving liquid flow around a bubble and other microscale processes.

The forces applied on a moving bubble on a heated wire include the thermocapillary force induced by the bulk liquid temperature difference and

drag due to viscosity and bubble movement. Meanwhile, for bubble collision and oscillation phenomena, the inertia also plays an important role.

Consider a bubble submerged in an unbounded viscous Newtonian fluid having a 1D temperature profile, as shown in Fig. 5.19. The temperature difference between two sides of the bubble in the liquid could induce thermocapillary force. Apparently, the reverse force of the momentum transfer due to the Marangoni flow would push the bubble to move towards high temperature region, with the driving force in x direction expressed as [12, 15]

$$f_{\mathrm{d}} = -\int_0^{\pi} \frac{\partial \sigma(T_{\mathrm{i}})}{\partial T_{\mathrm{i}}} \frac{\mathrm{d}T_{\mathrm{i}}}{R\mathrm{d}\theta} 2\pi R \sin\theta \sin\theta R \mathrm{d}\theta \tag{5.1}$$

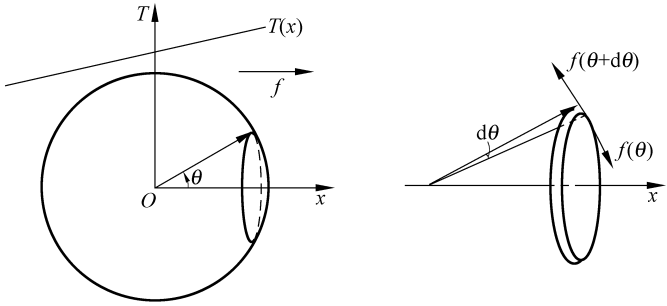

Figure 5.19 Analytical model for thermocapillary force on a bubble

The temperature gradient along the bubble interface would be

$$\frac{\mathrm{d}T_{\mathrm{i}}}{R\mathrm{d}\theta} = \frac{\mathrm{d}T_{\mathrm{i}}}{\mathrm{d}x}\frac{\mathrm{d}x}{R\mathrm{d}\theta} = \frac{\mathrm{d}T_{\mathrm{i}}}{\mathrm{d}x}\sin\theta \tag{5.2}$$

The relation between the interface temperature gradient $\mathrm{d}T_{\mathrm{i}}(x)/\mathrm{d}x$ and the bulk temperature gradient $\mathrm{d}T(x)/\mathrm{d}x$ is dependent upon the interfacial condition of $\left.\lambda_{\mathrm{l}}\frac{\mathrm{d}T}{\mathrm{d}r}\right|_{r=R} = h_{\mathrm{i}}(T_{\mathrm{i}} - T_{\mathrm{sat}}) = q''$ [1] and local heat transfer. As an approach, the temperature gradient along the interface of small bubbles is assumed to have a linear relation with the bulk temperature gradient as

$$\frac{\mathrm{d}T_{\mathrm{i}}(x)}{\mathrm{d}x} = \frac{\alpha \mathrm{d}T(x)}{\mathrm{d}x} \qquad 0 < \alpha < 1 \tag{5.3}$$

where α is a dimensionless coefficient.

The interfacial tension is expressed as a function of temperature

$$\sigma(T_{\mathrm{i}}) = \sigma(T_0) - B(T_{\mathrm{i}} - T_0) \tag{5.4}$$

where $\sigma(T_0)$ is the interfacial tension at temperature T_0, B a positive constant.

In a system with a small bubble on a thin wire, as illustrated in Fig. 5.19, the liquid temperature is assumed to be $T = T_0 + Dx + f(y)$, where T_0 being a reference temperature, and D temperature gradient in x direction. Substituting Eqs. (5.2) and (5.3) into Eq. (5.1) and integrating yields:

$$f_{\mathrm{d}} = \frac{8}{3}\pi\alpha DBR^2 \tag{5.5}$$

5.2.2 Force Caused by Bubble Motion

For a sliding bubble on a wire axis, the temperature of the liquid before the bubble is higher than that behind the bubble, the thermocapillary force induced by bubble motion itself would act as a drive force, which is opposite to the liquid viscous force.

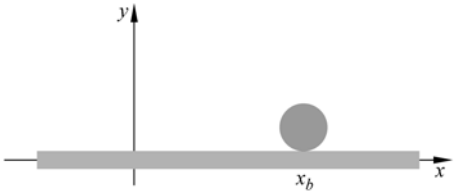

Figure 5.20 Temperature with a moving bubble sink

Consider a bubble at x_{b} as a heat sink, q_4, moving on a wire with cross-section area A and perimeter C, as illustrated in Fig. 5.20. The energy equation for the wire is

$$\rho cA\frac{\partial T}{\partial \tau} = \frac{\partial}{\partial x}\left[\lambda_{\mathrm{w}} A\frac{\partial T}{\partial x}\right] + q_3' - h\left(T_{\mathrm{w}} - T_{\mathrm{b}}\right)C \tag{5.6a}$$

$$-\lambda_{\mathrm{w}} A\left.\frac{\partial T}{\partial x}\right|_{x=x_{\mathrm{b}}^-} + \lambda_{\mathrm{w}} A\left.\frac{\partial T}{\partial x}\right|_{x=x_{\mathrm{b}}^+} = q_4 \tag{5.6b}$$

where q_3' is wire heat generation, T_{w}, T_{b}, temperatures of the wire surface and bulk liquid, respectively. Eq. (5.6) is rewritten as,

$$\frac{\partial \theta}{\partial \tau} = a\left(\frac{\partial^2 \theta}{\partial x^2} - b^2\theta\right) + \frac{q_3'''}{\rho c} \tag{5.7a}$$

$$-\left.\frac{\partial \theta}{\partial x}\right|_{x=x_{\mathrm{b}}^-} + \left.\frac{\partial \theta}{\partial x}\right|_{x=x_{\mathrm{b}}^+} = \frac{q_4}{\lambda_{\mathrm{w}} A} \tag{5.7b}$$

where $\theta = T_w - T_b$, $b = \sqrt{\dfrac{hC}{\lambda_w A}}$, $q_3''' = q_3'/A$, and $a = \dfrac{\lambda_w}{\rho c_p}$ is thermal diffusivity. As a preliminary approach, b is assumed to be constant.

Setting moving coordinate system attached to the bubble, and substituting $x' = x - u\tau, \tau' = \tau$ into Eq. (5.7) yields

$$\frac{\partial \theta}{\partial \tau'} - u\frac{\partial \theta}{\partial x'} = a\left(\frac{\partial^2 \theta}{\partial x'^2} - b^2\theta\right) + \frac{q_3'''}{\rho c} \tag{5.8a}$$

$$-\left.\frac{\partial \theta}{\partial x}\right|_{x'=0^-} + \left.\frac{\partial \theta}{\partial x}\right|_{x'=0^+} = \frac{q_4}{\lambda_w A} \tag{5.8b}$$

Considering the bubble moving steadily, or $\partial\theta/\partial\tau' = 0$, we have

$$-u\frac{\partial \theta}{\partial x'} = a\left(\frac{\partial^2 \theta}{\partial x'^2} - b^2\theta\right) + \frac{q_3'''}{\rho c} \tag{5.9}$$

Solving Eq. (5.9) yields

$$\begin{cases} \theta = \phi_{\max} \exp\left\{\left[\sqrt{\left(\dfrac{u}{2a}\right)^2 + b^2} - \dfrac{u}{2a}\right]x'\right\} + \dfrac{q_3''' A}{hC}, & \text{as } x' < 0 \\ \theta = \phi_{\max} \exp\left\{\left[-\sqrt{\left(\dfrac{u}{2a}\right)^2 + b^2} - \dfrac{u}{2a}\right]x'\right\} + \dfrac{q_3''' A}{hC}, & \text{as } x' > 0 \end{cases} \tag{5.10}$$

where $\phi_{\max} = \dfrac{-q_4}{2\lambda_w A\sqrt{\left(\dfrac{u}{2a}\right)^2 + b^2}}$.

In a zone around the small bubble, the temperature gradients for $x'<0$ and $x'>0$ caused by bubble motion are assumed to be uniform and taken as $\left.\dfrac{\partial \theta}{\partial x'}\right|_{x'\to 0^-}$ and $\left.\dfrac{\partial \theta}{\partial x'}\right|_{x'\to 0^+}$, respectively. From Eqs. (5.10) and (5.5), thermocapillary forces for these two zones are

$$f_{db1} = \frac{4}{3}\pi\alpha BR^2 \left.\frac{\partial \theta}{\partial x'}\right|_{x'\to 0^+} = \frac{4}{3}\pi\alpha BR^2 \phi_{\max}\left[-\sqrt{\left(\frac{u}{2a}\right)^2 + b^2} - \frac{u}{2a}\right], \quad x' > 0 \tag{5.11a}$$

$$f_{\mathrm{db2}} = \frac{4}{3}\pi\alpha BR^2 \left.\frac{\partial\theta}{\partial x'}\right|_{x'\to 0^-} = \frac{4}{3}\pi\alpha BR^2\phi_{\max}\left[\sqrt{\left(\frac{u}{2a}\right)^2 + b^2} - \frac{u}{2a}\right], \quad x' < 0 \quad (5.11b)$$

As a result, the total thermocapillary force caused by bubble motion is

$$f_{\mathrm{db}} = f_{\mathrm{db1}} + f_{\mathrm{db2}} = -\frac{4}{3}\pi\alpha BR^2\phi_{\max}\frac{u}{a} \quad (5.12a)$$

or

$$f_{\mathrm{db}} = \frac{4}{3}\pi\alpha BR^2 \frac{-q_4}{2\lambda_{\mathrm{w}} A\sqrt{\left(\frac{u}{2a}\right)^2 + b^2}}\frac{u}{a} \quad (5.12b)$$

Figure 5.21 presents the variation of the thermocapillary force with bubble velocity, where $u_0 = 2ab$, and $f_0 = -\frac{4}{3}\frac{\pi\alpha BR^2 q_4}{\lambda_{\mathrm{w}} A}$. For the experimental conditions of boiling on small wires [12, 15], the thermocapillary force caused by bubble motion has a good linear relation with the velocity, or can be expressed as,

$$f_{\mathrm{db}} \approx \frac{2}{3}\frac{\pi\alpha BR^2 q_4}{\lambda_{\mathrm{w}} Aab}u \quad (5.13)$$

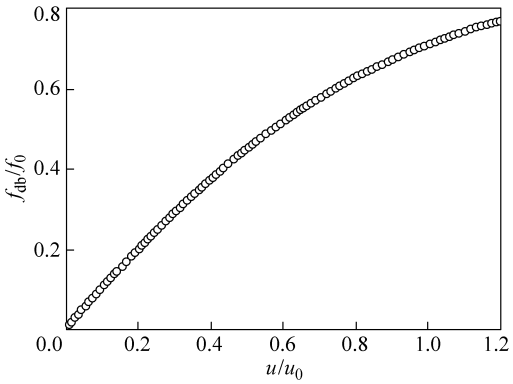

Figure 5.21 Thermocapillary force induced by bubble motion

For pure vapor bubbles, the viscous force is given by the Hadamard-Rybczynski law [20],

$$f_{\mathrm{vl}} = -4\pi\mu_{\mathrm{l}} Ru \quad (5.14)$$

where μ_{l} is the liquid viscosity. Finally, the viscous and thermocapillary effect

caused by bubble motion is:

$$f_{\mathrm{v}} = \left(-4\pi\mu_{\mathrm{l}} R + \frac{2}{3}\frac{\pi\alpha BR^2 q_4}{\lambda_{\mathrm{w}} Aab} \right) u \tag{5.15}$$

If the effects of bubble motion is considered as effectual viscosity and similar to Stokes' law, it can be expressed as

$$f_{\mathrm{v}} = -6\pi\mu Ru \tag{5.16}$$

where $\mu = \frac{2}{3}\mu_{\mathrm{l}} - \frac{\alpha BRq_4}{9\lambda_{\mathrm{w}} Aab}$ is the effectual viscosity.

5.2.3 Dynamic Equation

When a bubble accelerates or decelerates, the inertial effect acts on the bubble motion. For a sphere submerged in liquid, the equivalent inertial mass is [18]

$$m_{\mathrm{a}} = \frac{1}{2}\rho_{\mathrm{l}} V \tag{5.17}$$

and the total inertial mass is:

$$m = m_{\mathrm{a}} + \rho_{\mathrm{g}} V \tag{5.18}$$

For $\rho_{\mathrm{l}} \gg \rho_{\mathrm{g}}$, the inertia mass of the bubble in the liquid is

$$m = \frac{1}{2}\rho_{\mathrm{l}}\frac{4}{3}\pi R^3 = \frac{2}{3}\pi\rho_{\mathrm{l}} R^3 \tag{5.19}$$

From Eqs. (5.5), (5.16) and (5.19), the dynamical equation of a moving bubble on a heating wire is derived as [12, 15]:

$$ma = \frac{2}{3}\pi\rho_{\mathrm{l}} R^3 a = -6\pi\mu Ru + \frac{8}{3}\pi\alpha DBR^2 \tag{5.20a}$$

or

$$a = -ku + c \tag{5.20b}$$

where $k = \frac{9\mu}{\rho_{\mathrm{l}} R^2}$ is the relative effectual viscosity, $c = \frac{4\alpha BD}{\rho_{\mathrm{l}} R}$ acceleration caused by the thermocapillary force. Obviously, a bubble dynamic process is controlled by the effectual viscosity force and external thermocapillary force.

5.3 Bubble Sweeping Dynamics

5.3.1 Single Bubble Sweeping

For stable bubble sweeping without an external temperature gradient on a horizontal wire, $D = 0$, $c = 0$, and then

$$a = -ku \tag{5.21}$$

So

$$u = u_0 \exp(-kt) \tag{5.22}$$

Obviously, the effective viscosity μ or k governs the bubble sweeping. The sweeping distance is

$$l = \frac{u_0}{k}[1 - \exp(-kt)] = \frac{u_0}{k}\left(1 - \frac{u}{u_0}\right) \tag{5.23}$$

From Eq. (5.20), the dynamic characteristics were mainly dependent upon the effective viscosity and external conditions such as D. The effective viscosity in Eq. (5.16) is rewritten as

$$\mu = \frac{2}{3}\mu_1 - \frac{\alpha B}{9\pi\sqrt{2\lambda_w h a}}\frac{q_4}{R^{1/2}} \tag{5.24}$$

Obviously, the effective viscosity is dependent upon the heat sink intensity and bubble radius. Let $\mu = 0$, from Eq. (5.24) we can get

$$\frac{q_4}{R^{1/2}} = \frac{6\pi\sqrt{2\lambda_w h a}}{\alpha B}\mu_1 = k_0 \tag{5.25}$$

For the bubble slippage startup process shown in Fig. 5.3, the bubble had significant growth due to quickly absorbing heat, $q_4 R^{-1/2} > k_0$ or $\mu < 0$, and apparently the bubble would accelerate. As shown in Fig. 5.4, the startup process experienced two stages. In the first 0.003 s, the initial velocity was very small, however, the acceleration increased very fast. After that, the acceleration decreased and the velocity approached to a constant. At about 0.016 s, the acceleration was approximatey zero, and the bubble reached a stable sweeping speed, as described by Eq. (5.25).

For $q_4 R^{-1/2} < k_0$ or $\mu > 0$, the bubble velocity would tend to zero quickly according to Eq. (5.22), and the boiling system almost only has immobile bubbles. For $q_4 R^{-1/2} > k_0$ or $\mu < 0$, from Eq. (5.22) it is known that the bubble would quickly accelerate and violent collision would cause the bubbles unstable and departing

fast. As applied heat flux increases, the bubbles could not stay on the wire because of very high bubble density and acceleration.

Only for $q_4 R^{-1/2} \approx k_0$ or $\mu \approx 0$, the bubble velocity would not magnify or reduce significantly, and the bubble is mainly governed by various external conditions such as adjacent bubbles. In this case, the bubble moves along the wire stably and freely with small effectual viscosity, and complex and interesting bubble phenomena occur.

5.3.2 Bubble Separation from an Immobile Bubble

For subcooled boiling on thin wires, it is expected that the liquid temperature near a moving bubble is affected by adjacent bubbles due to their growth and heat absorbing. In a practical boiling system, temperature distribution is very complex, and heat transfer process includes conduction, single phase convection and phase change.

For a boiling system including a moving and an immobile bubble, as shown in Fig. 5.22, the wire serves as a line source, while the neighbor bubble acts as a cold source and affects the horizontal temperature gradient along x. For the moving bubble, the temperature gradient in the liquid is just induced by the line heater and the immobile bubble that is treated as a point heat source. Since the perpendicular temperature gradient has little effect on the horizontal motion [21], only the horizontal temperature gradient is considered. Setting up a coordinate system on the wire, it can be seen that the origin locates at the contact point of the immobile bubble. The heat transfer coefficient from the surrounding liquid and wire to the bubbles is described by a characteristic coefficient λ, which includes conductivity and convection. Since the temperature field in the surrounding liquid is only dependent upon a line source and a point sink, the steady temperature field is derived as [16],

$$T(x,y) = \frac{q_1'}{2\pi\lambda} \ln r - \frac{q_2}{4\pi\lambda \overline{OP}} + C_0 \tag{5.26}$$

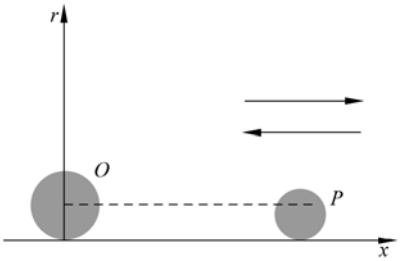

Figure 5.22 Analytical model for bubble separation

where q_1' denotes heat generation per unit length of line heater, q_2 heat generation of immobile bubble, and C_0 determined by boundary conditions. Since the temperature distribution for $x>0$ and $x<0$ is symmetric, only the distribution $x>0$ is discussed.

An arbitrary point P on the moving bubble is very close to the wire, and OP has a very small angle with the wire axis, then $\overline{OP} \approx x$, and the temperature in the liquid is expressed as

$$T = -\frac{q_2}{4\pi\lambda x} + c, \qquad x > 0 \tag{5.27}$$

where $c = \frac{q_1'}{2\pi\lambda}\ln(r_w + R_b) + c_0$, and r_w, R_b are radii of the wire and immobile bubble, respectively. For bubble movement along horizontal direction, only temperature profile along x is important. The liquid temperature gradient along x is:

$$D = \frac{\partial T}{\partial x} = \frac{q_2}{4\pi\lambda x^2}, \qquad x > 0 \tag{5.28}$$

The predicted temperature and its gradient are illustrated in Fig. 5.23, where dimensionless parameters $T_R = \frac{4\pi\lambda R_b}{q_2}(T-c)$, $D_R = \frac{4\pi\lambda R_b^2}{q_2}D$, $X = \frac{x}{R_b}$. Since the immobile bubble acts as a cold source, the temperature along horizontal direction increases away from the immobile bubble interface. In addition, the temperature gradient decreases quickly as the moving bubble moves away from immobile bubbles, mainly exhibiting two main regions. For the region near the immobile bubble or $X<4$, the temperature gradient decreases quickly and cause significant bubble velocity variation. For the region away from the immobile bubble or $X>4$, the temperature gradient decreases slowly and the bubble sweeping becomes stable.

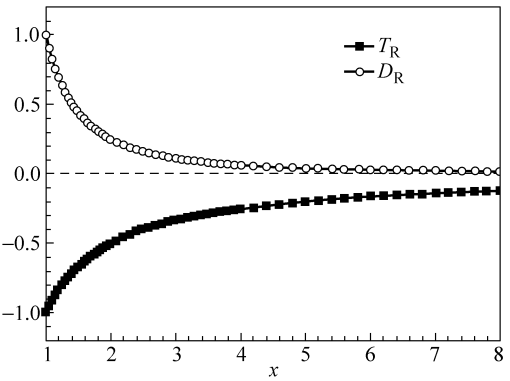

Figure 5.23 Temperature and its gradient along the wire

For bubble separation, the dynamical equation from Eq. (5.20b) is derived as

$$a = -ku + c \tag{5.29a}$$

$$x(0) = x_0 \tag{5.29b}$$

$$u(0) = 0 \tag{5.29c}$$

For $\mu<0$, a separating bubble accelerates quickly during the whole process and then become unstable.

For $\mu\approx0$, substituting Eq. (5.28) into Eq. (5.29) yields

$$a = \frac{\mathrm{d}^2 x}{\mathrm{d}t^2} = \frac{4B}{\rho_\mathrm{l} R_\mathrm{b}} \frac{\alpha q_2}{4\pi\lambda x^2} \tag{5.30}$$

Integrating Eq. (5.30) yields

$$u^2 = \frac{8B}{\rho_\mathrm{l} R_\mathrm{b}} \frac{\alpha q_2}{4\pi\lambda} \left(\frac{1}{x_0} - \frac{1}{x} \right) \tag{5.31}$$

where x_0 denotes bubble initial location. The bubble accelerates fast at initial time, and then it approaches to the limit velocity $u_\mathrm{m} = \left(\frac{8B}{\rho_\mathrm{l} R_\mathrm{b}} \frac{\alpha q_2}{4\pi\lambda} \frac{1}{x_0} \right)^{1/2}$ as $x \to \infty$. From Eq. (5.31), the separating velocity is greatly dependent upon the intensity of the heat source q_2.

In a practical system, a bubble sometimes grows or shrinks during separation or collision, and that makes its dynamics more complex. In Fig. 5.5, the left bubble was also a separating bubble from an immobile bubble after 0.004 s, and its volume varied not so much. For this situation, $\rho_\mathrm{l}\approx1000$ kg/m^3, $B = 1.7\times10^{-4}$ N/(m·K), $R_\mathrm{b} = 0.073$ mm, $x_0 = 0.37$ mm. As illustrated in Fig. 5.24, the predicted results from Eq. (5.31) with $\frac{\alpha q_2}{4\pi\lambda} = 1.42\times10^{-4}$ K·m are compared with the experimental results, showing a good agreement with each other.

Bubble separation with $\mu > 0$ has two main stages, accelerating and decelerating process. During the accelerating process, the thermocapillary force controls the motion. Since the thermocapillary force quickly decreases as increasing distance, the effectual viscosity caused by bubble motion plays a leading role after enough long time or distance moved away, and then the bubble would start the decelerating process. These two stages can be idealized as pure thermocapillary and effectual viscosity controlled processes, respectively.

In the thermocapillary controlled process, separating dynamics is just described by Eqs. (5.30) and (5.31) without the effective viscosity. The transition from

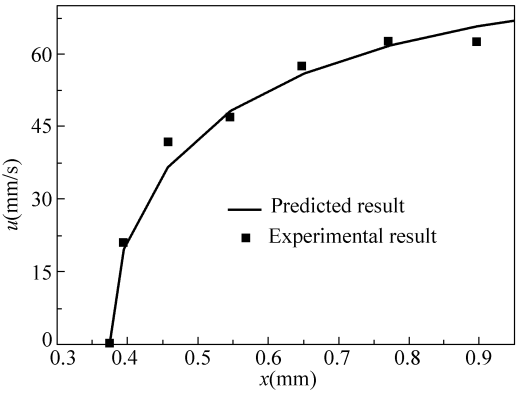

Figure 5.24 Comparison of bubble sweeping velocity

acceleration to deceleration appears when the thermocapillary force is equal to the viscous force. Setting Eq. (5.28) equal to zero, and the transition point is obtained as

$$\frac{9\mu}{\rho_l R_b^2} u = \frac{4B}{\rho_l R_b} \cdot \frac{\alpha q_2}{4\pi\lambda x_c^2} \tag{5.32}$$

Since the transition velocity is approximate to the highest limit u_{max}, the transition point is derived as

$$x_c = \left(\frac{4\alpha B R_b}{9\mu u_{max}} \cdot \frac{q_2}{4\pi\lambda} \right)^{1/2} \tag{5.33}$$

During decelerating process, the thermocapillary force is ignored, and Eq. (5.29) evolves to

$$a = -ku \tag{5.34a}$$

$$u(t_c) \approx u_{max} \quad \text{and} \quad x(t_c) \approx x_c \tag{5.34b}$$

and the bubble velocity is

$$u(t) = u_{max} \exp[-k(t - t_c)] \tag{5.35}$$

The moving distance after the transition is

$$l(t) = \int_{t_c}^{t} u \mathrm{d}t = u_{max} \left\{ 1 - \exp[-k(t - t_c)] \right\} / k \tag{5.36}$$

where $l = x - x_c$. As $t \to \infty$, $l_\infty = u_{max} / k$, and the velocity after the transition is

$$u(l) = u_{max} - kl = u_{max} - k(x - x_c) \tag{5.37}$$

The bubble separating velocity changes with the moving distance are predicted using the two stage model and exact calculation of Eq. (5.29), presented as lines 1 and 2 in Fig. 5.25, respectively. The associated change of distance and velocity with time are illustrated in Fig. 5.26. Apparently, the two stage model is a very good approximation.

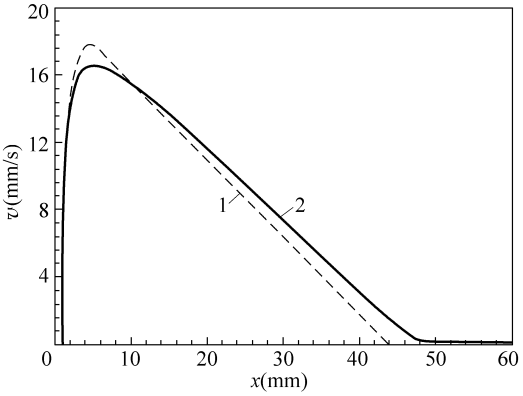

Figure 5.25 Separating velocity variation along x

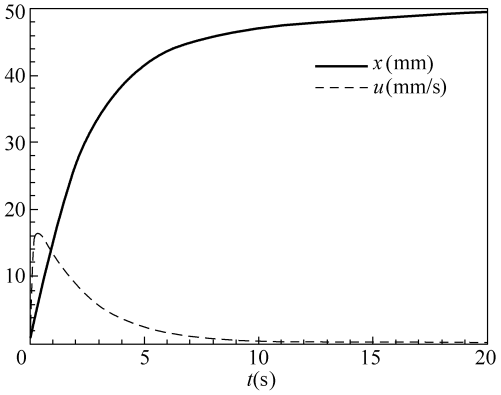

Figure 5.26 Variation of separation velocity and distance with time

5.3.3 Separation of Two Equivalent Moving Bubbles

For separation of two equivalent moving bubbles, having opposite moving direction, only the right bubble need be considered because of symmetry, and the system is shown in Fig. 5.27. For the right moving bubble at x, the local temperature gradient is dependent upon the line heat source and the point heat source at $-x$.

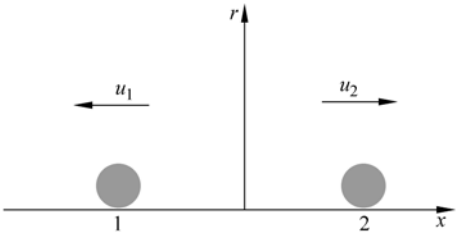

Figure 5.27 Separation of two bubbles

Similarly, the temperature gradient along x is

$$\frac{\partial T}{\partial x}=\frac{q_2}{4\pi\lambda(x+x)^2}=\frac{q_2/4}{4\pi\lambda x^2} \tag{5.38}$$

Ignoring effectual viscosity in the accelerating process and substituting Eq. (5.38) into Eq. (5.29) yields

$$\frac{\mathrm{d}^2x}{\mathrm{d}t^2}=\frac{1}{4}\frac{4\alpha B}{\rho_1 R}\cdot\frac{q_2}{4\pi\lambda x^2} \tag{5.39}$$

Accordingly, the separating velocity is

$$u=\frac{1}{2}\left(\frac{8B}{\rho_1 R}\frac{\alpha q_2}{4\pi\lambda}\right)^{1/2}\left(\frac{1}{x_0}-\frac{1}{x}\right)^{1/2} \tag{5.40}$$

This velocity is just a half of single bubble separation velocity in the accelerating region.

5.3.4 Separation of Two Non-Equivalent Bubbles

In usual cases, two moving bubbles have radii of R_1 and R_2, locate at $-x_1$ and x_2 with $u_{01}=u_{02}=0$, respectively, similar to those in Fig. 5.27. Ignoring the effective viscosity during the accelerating process and from Eq. (5.29), accelerations of two bubbles are derived as

$$a_1=\frac{\mathrm{d}^2x_1}{\mathrm{d}t^2}=\frac{4\alpha B}{\rho_1 R_1}\cdot\frac{q_{\mathrm{b}2}}{4\pi\lambda l^2} \tag{5.41a}$$

$$a_2=\frac{\mathrm{d}^2x_2}{\mathrm{d}t^2}=\frac{4\alpha B}{\rho_1 R_2}\cdot\frac{q_{\mathrm{b}1}}{4\pi\lambda l^2} \tag{5.41b}$$

where $l=x_1+x_2$. Since the ratio of these two accelerations is $\frac{a_1}{a_2}=\frac{\mathrm{d}^2x_1}{\mathrm{d}t^2}\Big/\frac{\mathrm{d}^2x_2}{\mathrm{d}t^2}=$

$\frac{R_2 q_{b2}}{R_1 q_{b1}} = \psi$, For simplification, select the origin to satisfy $x_{01}/x_{02} = \psi$, and then

$$x_1 / x_2 = \psi \tag{5.42a}$$

$$l = x_1(1+\psi)/\psi = x_2(1+\psi) \tag{5.42b}$$

Substituting Eq. (5.42) into Eq. (5.41) yields

$$\frac{\mathrm{d}^2 l}{\mathrm{d}t^2} = \frac{4\alpha B}{\rho_1} \cdot \frac{1}{4\pi\lambda l^2}\left(\frac{q_{b1}}{R_2} + \frac{q_{b2}}{R_1}\right) \tag{5.43}$$

Integrating Eq. (5.43),

$$u_1 = \left[\frac{8\alpha B}{\rho_1}\frac{1}{4\pi\lambda}\left(\frac{q_{b1}}{R_2} + \frac{q_{b2}}{R_1}\right)\left(\frac{1}{l_0} - \frac{1}{l_1}\right)\right]^{1/2} \tag{5.44}$$

If $\psi = 1$, $u_1 = \frac{1}{2}\left[\frac{8B}{\rho_1 R_2} \cdot \frac{\alpha q_{b1}}{4\pi\lambda}\left(\frac{1}{l_0/2} - \frac{1}{l/2}\right)\right]^{1/2} = \frac{1}{2}\left[\frac{8B}{\rho_1 R_1} \cdot \frac{\alpha q_{b2}}{4\pi\lambda}\left(\frac{1}{l_0/2} - \frac{1}{l/2}\right)\right]^{1/2}$,

which is consistent with Eq. (5.40). When $\psi \ll 1$, $u_1 = \left[\frac{8\alpha B}{\rho_1}\frac{q_{b1}}{4\pi\lambda R_2}\left(\frac{1}{l_0} - \frac{1}{l_1}\right)\right]^{1/2}$,

which is similar to the bubble separation away from an immobile bubble described by Eq. (5.31).

5.4 Bubble Collision Dynamics

5.4.1 Collision with an Immobile Bubble

For a bubble colliding with an immobile bubble, as illustrated in Fig. 5.22, the dynamical equation of the moving bubble is similar to separation phenomenon in a system in Fig. 5.22, or

$$\frac{2}{3}\pi\rho_1 R^3 a = -6\pi\mu R u + \frac{8}{3}\pi\alpha D B R_b^2 \tag{5.45a}$$

$$x(0) = x_0 \tag{5.45b}$$

$$u(0) = -u_0 < 0 \tag{5.45c}$$

The thermocapillary force acts as a resistance when the bubble moves close to the immobile bubble, and the main difference from separation dynamics is the initial conditions. As noted, the viscosity could be ignored for a short collision length, and the dynamic equation evolves to

$$u^2 = u_0^2 - \frac{8B}{\rho_1 R_b} \cdot \frac{\alpha q_2}{4\pi\lambda}\left(\frac{1}{x} - \frac{1}{x_0}\right) \tag{5.46}$$

Apparently, the collision process can be divided into two stages, approaching to the immobile bubble as a decelerating process and separating from the bubble as an accelerating process. Setting velocity $u \to 0$, the critical distance of these two bubbles is

$$x_c = \left[\frac{1}{x_0} + u_0^2\left(\frac{8B}{\rho_1 R_b} \cdot \frac{\alpha q_2}{4\pi\lambda}\right)^{-1}\right]^{-1} \tag{5.47}$$

As reaching to x_c, the bubble turns to separation from the immobile bubble and the thermocapillary force accelerates the bubble. The whole process is illustrated in Fig. 5.28, where $X = x/x_0$ and $u_{00} = \left(\frac{8B}{\rho_1 R_b} \cdot \frac{\alpha q_2}{4\pi\lambda x_0}\right)^{1/2}$ denote the dimensionless distance and characteristic velocity, respectively, and $\chi = u_0/u_{00}$ denotes the dimensionless initial velocity.

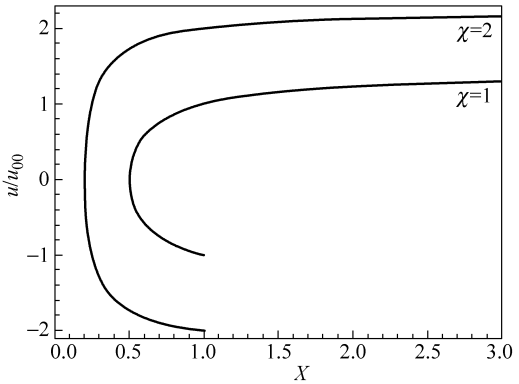

Figure 5.28 Bubble collision at different initial velocities

The collision characteristics are mainly dependent upon the dimensionless initial velocity χ. The bubble motion is almost symmetric about the critical point in the nearby zone, and the process is like an elastic collision. The dimensionless critical distance is smaller at large χ, and the two bubbles approach each other much closer. Also, a bubble with large χ reverses its

velocity very sharply near the critical point, while much smoothly for a bubble at little χ. The collision characteristics predicted by Eq. (5.22) for a case, as illustrated in Fig. 5.29, are compared with the experimental results in Fig. 5.29, showing a good agreement with each other.

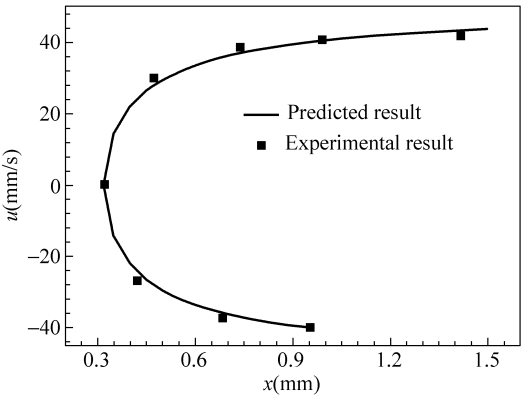

Figure 5.29 Comparison of bubble velocity for collision

5.4.2 Collision of Two Equivalent Bubbles

For the collision of two equivalent moving bubbles having initial velocity u_{01} and u_{02}, respectively, the thermocapillary forces is equal and opposite. From the momentum conservation, the bubble velocities satisfy $u_1 + u_2 = u_{01} + u_{02}$, and the velocity of the centre of two bubbles is $u_0 = (u_{01} + u_{02})/2$. Setting a moving coordinate system with the origin at the center of two bubbles, similar to that in Fig. 5.27, the relative initial velocity is $u'_{01} = (u_{01} - u_{02})/2$ and $u'_{02} = (u_{02} - u_{01})/2$, and the initial coordinates are $-x'_{01}$ and x'_{01}, respectively.

Because of symmetry, the motion of the right moving bubble is described by Eqs. (5.39) and (5.40), and the velocity is

$$u_2'^2 = u_{02}'^2 - \frac{2B}{\rho_1} \cdot \frac{q_2}{4\pi\lambda}\left(\frac{1}{x'_2} - \frac{1}{x'_{02}}\right) \tag{5.48}$$

When the bubble returns to $x'_2 = x'_{02}, u'_2 = u'_{02}$, its velocity is

$$u_2 = u'_2 + u_0 = u_{01} \tag{5.49}$$

This holds true for another bubble, or $u_1 = u_{02}$. This exactly implies that the two moving bubbles just exchange their velocity after the collision, as the experimental phenomenon shown in Fig. 5.7. Also, a special collision was observed in Fig. 5.8,

i.e., the left bubble gaining velocity while the right bubble halting after the collision.

Similar to Eq. (5.48), the two bubbles has minimum distance when the velocities of two bubbles are just as $u_1' = u_2' = 0,$ or

$$x_c = \left[\frac{1}{x_1'} + u_{01}'^2 \left(\frac{2B}{\rho_l} \cdot \frac{q_2}{4\pi\lambda} \right)^{-1} \right]^{-1} \tag{5.50}$$

Obviously, the minimum distance between two bubbles is $l_c = 2x_c$.

As noted above, the bubble collision is dependent upon relative velocity, relative distance and bubble radii. Since the thermocapillary forces induced by two different bubbles are usually not equal, the system with two bubbles does not satisfy the momentum conservation, and there is no symmetry coordinate to simplify collision process. As in normal cases, initial conditions are of critical important for collision behavior.

5.4.3 Bubble Coalescence

Usually, two bubbles would coalesce if the minimum distance between the two bubbles is smaller than the sum of the two bubble radii. For a moving bubble colliding with an immobile bubble, the coalescing condition from Eq. (5.47) is

$$x_c = \left[\frac{1}{x_0} + u_0^2 \left(\frac{8\alpha B}{\rho_l R_b} \cdot \frac{q_2}{4\pi\lambda} \right)^{-1} \right]^{-1} < R + R_b \tag{5.51}$$

When the initial distance x_0 is large enough, $\frac{q_2}{4\pi\lambda} < \frac{\rho_l (R + R_b) R_b u_0^2}{8B}$. Obviously, the moving bubble will coalesce with the immobile bubble if the cold source of the immobile bubble is not too large or the initial velocity of the moving bubble is high enough.

For two equivalent moving bubbles, the coalescing criteria from Eq. (5.50) is,

$$l_c = 2\left[\frac{1}{x_1'} + \left(\frac{u_{01} - u_{02}}{2} \right)^2 \left(\frac{2B}{\rho_l} \cdot \frac{q_2}{4\pi\lambda} \right)^{-1} \right]^{-1} < 2R \tag{5.52}$$

If x_1' is large enough, and $\frac{q_2}{4\pi\lambda} < \frac{2\rho_l R (u_{01} - u_{02})^2}{B}$, small cold source and/or higher relative velocity would promote the coalescence process.

Due to bubble coalescence, the bubbles would grow and depart fast, which should enhance the boiling heat transfer.

5.5 Bubble Oscillation

5.5.1 Temperature Profile of a Two Immobile Bubbles System

Consider a system containing two immobile bubbles on a heating wire horizontally installed, as shown in Fig. 5.30. The immobile bubbles are usually assumed equivalent, which does not affect the basic oscillation characteristics. The wire is treated as a line heat source with uniform heat generation. The two immobile bubbles, having the same radius R_b, serve as heat sinks locating at $-l$ and l, and a single bubble oscillates between these two immobile bubbles on the wire. So the steady temperature of the liquid is described as

$$T = -\frac{q_2}{4\pi\lambda\overline{O_1P}} - \frac{q_2}{4\pi\lambda\overline{O_2P}} + \frac{q_1'}{2\pi\lambda}\ln r + C_0 \tag{5.53}$$

where q_1' denotes heat generation per length of the wire, and q_2 denotes heat generation of the immobile bubbles, λ, heat transfer coefficient including both conductivity and convection. The first two items on the right side are due to the two heat sinks, respectively, and the third item is due to the line source, the last item C_0 a constant dependent upon the boiling conditions.

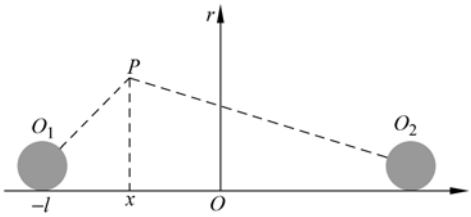

Figure 5.30 Analytical model for a system with two immobile bubbles

For a single small bubble oscillation between two immobile bubbles on the wire, an arbitrary point P along the bubble track is very close to the wire, and both O_1P and O_2P have small angle with the wire. Therefore, both $\overline{O_1P} \approx x + l$ and $\overline{O_2P} \approx l - x$ are acceptable approximations. The temperature of the liquid close to the wire between two bubbles is

$$T = -\frac{q_2}{4\pi\lambda(x+l)} - \frac{q_2}{4\pi\lambda(l-x)} + C \tag{5.54}$$

where $C = \frac{q_1'}{2\pi\lambda}\ln(r_w + r_b) + C_0$. The local temperature gradient is obtained as,

$$\frac{\partial T}{\partial x} = \frac{q_2}{4\pi\lambda l^2}\left[\frac{1}{(1+x/l)^2} - \frac{1}{(1-x/l)^2}\right] \tag{5.55}$$

Near to the center or $x \approx 0$, the temperature gradient linearly approximated to

$$\frac{\partial T}{\partial x} = -\frac{q_2 x}{\pi\lambda l^3} \tag{5.56}$$

There are three regions between the two immobile bubbles: linear region near to $x = 0$, two nonlinear regions near two immobile bubbles, as shown in Fig. 5.31.

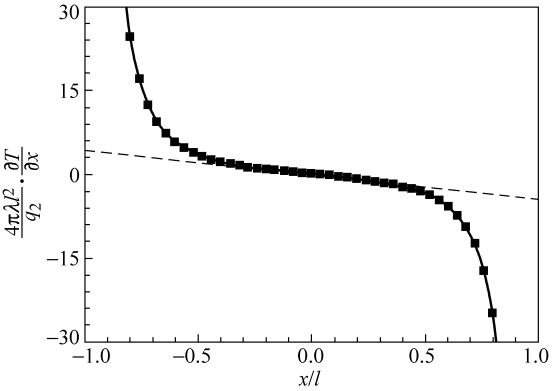

Figure 5.31 Temperature gradient distribution for a single bubble oscillation system

5.5.2 Bubble Oscillation Characteristics

For practical situations, the effective viscosity usually does not play an important role in one or half period, so the dynamic characteristics of oscillation in each half period are similar to each other. First, consider the oscillation with $\mu \approx 0$. Substituting Eq. (5.55) into Eq. (5.20) yields

$$\frac{\mathrm{d}^2 x}{\mathrm{d}t^2} = \frac{4\alpha B}{\rho_1 R_\mathrm{b}}\left[\frac{q_2}{4\pi\lambda(x+l)^2} - \frac{q_2}{4\pi\lambda(x-l)^2}\right] \tag{5.57}$$

Using initial condition $x_0 < 0$ as $u = 0$, integrating Eq. (5.57) yields

$$u^2 = \frac{8\alpha B}{\rho_1 R_\mathrm{b}} \cdot \frac{q_2}{4\pi\lambda}\left[\left(\frac{1}{x_0+l} - \frac{1}{x+l}\right) - \left(\frac{1}{x_0-l} - \frac{1}{x-l}\right)\right] \tag{5.58}$$

The bubble oscillates between x_0 and $-x_0$, and the oscillation process can continue for a long time. At $x = 0$, the oscillating bubble attains its maximum velocity as

$$u_{\max} = \left(\frac{8\alpha B}{\rho_1 R_b}\frac{q_2}{4\pi\lambda}\right)^{1/2}\left(\frac{1}{x_0 + l} - \frac{1}{x_0 - l}\right)^{1/2} \tag{5.59}$$

The bubble oscillating velocity in Fig. 5.10 is illustrated in Fig. 5.32, where $l = 0.56$ mm, $x_0 = -0.30$ mm, $x_0/l = -0.54$, $R = 0.5$ mm. The predicted results from Eqs. (5.58) – (5.59) with $\frac{\alpha q_2}{4\pi\lambda} = 3.37 \times 10^{-5}$ (K·m) are illustrated as the line in Fig. 5.32, showing the theoretical results agree well with experimental results.

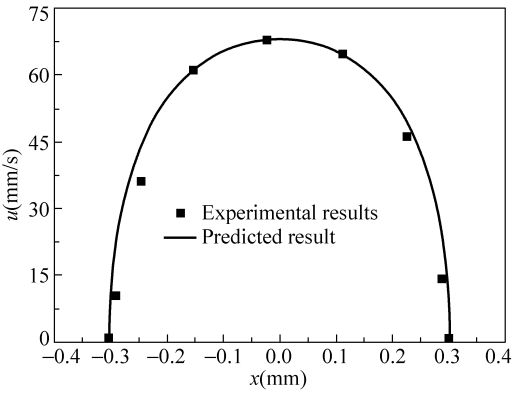

Figure 5.32 Experimental and theoretical oscillating velocity

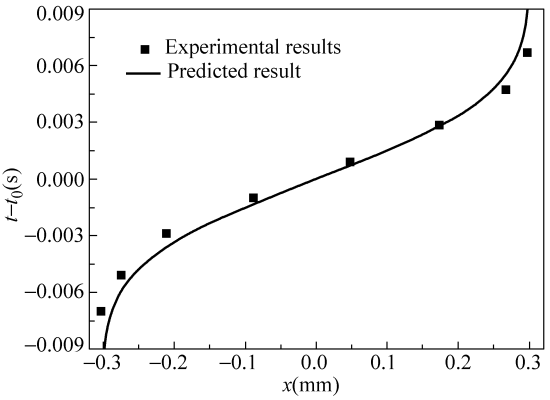

Figure 5.33 Theoretical and experimental oscillating time

In a half oscillation period, the predicted time from Eq. (5.59) can be integrated as

$$t(x) - t_0 = \int_0^x \mathrm{d}x / u \tag{5.60}$$

where t_0 means the time at the center or $x = 0$. Corresponding to the experimental

results in Fig. 5.10 and the conditions in Fig. 5.32, the oscillating time of experimental and predicted results are illustrated in Fig. 5.33. Obviously, the predicted results have a good agreement with the experimental results expect very a little bit large deviation in the two boundary regions.

5.5.3 Bubble Oscillations with Various Effective Viscosities

(1) Oscillation with Positive Effectual Viscosity

For $\mu \approx 0$, a bubble oscillation can continue for a long time, and dynamic characteristics are the same as that in a half period. However, oscillations usually stopped or were magnified within 0.1 – 2 s in the practical experiments, and mainly due to the non-zero effective viscosity. Substituting Eq. (5.55) into Eq. (5.20) yields

$$\frac{\mathrm{d}^2 x}{\mathrm{d}t^2} + \frac{9\mu}{\rho_\mathrm{l} R_\mathrm{b}^2}\frac{\mathrm{d}x}{\mathrm{d}t} - \frac{4\alpha B}{\rho_\mathrm{l} R_\mathrm{b}}\frac{q_2}{4\pi\lambda}\left[\frac{1}{(x+l)^2} - \frac{1}{(x-l)^2}\right] = 0 \tag{5.61a}$$

$$\frac{\mathrm{d}^2 (x/l)}{\mathrm{d}t^2} + \frac{9\mu}{\rho_\mathrm{l} R_\mathrm{b}^{\ 2}}\frac{\mathrm{d}(x/l)}{\mathrm{d}t} - \frac{4\alpha B}{\rho_\mathrm{l} R_\mathrm{b}}\frac{q_2}{4\pi\lambda l^3}\left[\frac{1}{(x/l+1)^2} - \frac{1}{(x/l-1)^2}\right] = 0 \tag{5.61b}$$

For $\mu > 0$, the oscillation weakens and the oscillating bubble will halt at a certain position at last. Corresponding to an oscillation system similar to that in Fig. 5.10, the whole oscillation process from Eq. (5.61) with $\mu \approx 4.6 \times 10^{-6}$ (N·s/m) and $\dfrac{\alpha q_2}{4\pi\lambda} = 4.5 \times 10^{-5}$ (K/m) is illustrated in Fig. 5.34 [13]. Obviously, the oscillation weakens as time going on, and the amplitude decreases to a half of its initial value within 0.3 s. The phase diagram has a stable sink where the oscillating bubble halts.

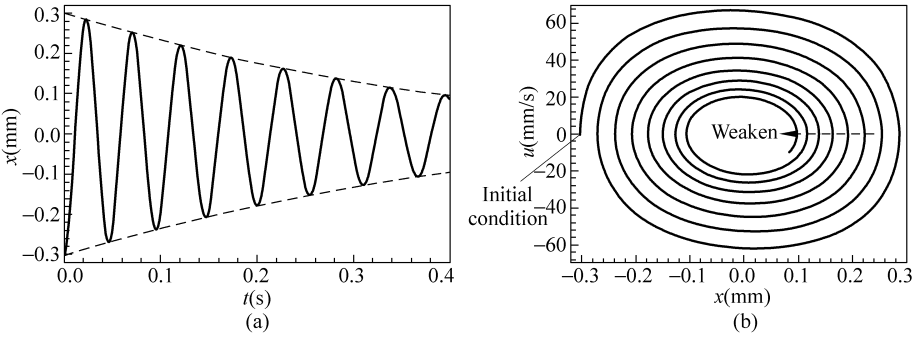

Figure 5.34 Oscillation with positive effectual viscosity
(a) Weakening process; (b) Phase diagram

When the oscillating bubble is very near the center, the thermocapillary effect is linearly approximated as Eq. (5.56), and Eq. (5.61) evolves to

$$\frac{\mathrm{d}^2x}{\mathrm{d}t^2}+\frac{9\mu}{\rho_1 R_\mathrm{b}^2}\frac{\mathrm{d}x}{\mathrm{d}t}+\frac{16\alpha B}{\rho_1 R_\mathrm{b}}\frac{q_2}{4\pi\lambda l^3}x=0 \tag{5.62}$$

The evolution with an effectual viscosity is simplified as [22]

$$x=A\exp(-kt)\cos[(\omega_0^2+k^2)^{1/2}t+\beta] \tag{5.63}$$

where A and β are the initial amplitude and phase angle, respectively, and the harmonic oscillation angle frequency $\omega_0=\left(\frac{16\alpha B}{\rho_1 R_\mathrm{b}}\frac{q_2}{4\pi\lambda l^3}\right)^{1/2}$. Considering the previous experimental case in Fig. 5.10 or Fig. 5.34, and the oscillation process near the origin is illustrated in Fig. 5.35, where $\beta=0$. Obviously, the oscillation weakens quickly near the origin, and then the bubble stops.

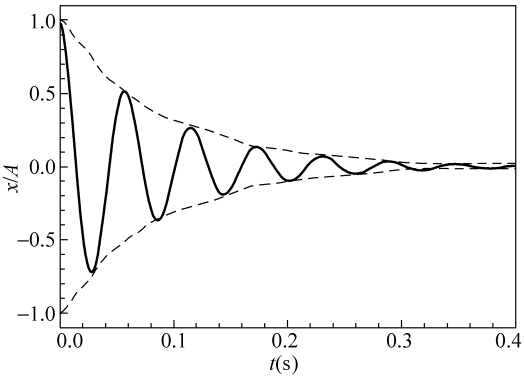

Figure 5.35 Attenuation of viscous oscillation

(2) Oscillation with Negative Effective Viscosity

For $\mu<0$, the oscillation magnifies and the oscillating bubble would collide with an immobile bubble or make the immobile bubble unstable. Corresponding to an oscillation similar to that shown in Fig. 5.34, the whole oscillation process from Eq. (5.61) with $\mu=-4.6\times10^{-6}$ (N·s/m) and $\frac{\alpha q_2}{4\pi\lambda}=4.5\times10^{-5}$(K/m) is illustrated in Fig. 5.36. Obviously, as oscillation magnifies, the oscillating bubble contacts with the immobile bubble when $|x|=l-R_\mathrm{b}=0.50$ mm, and the oscillation is unstable. A similar phenomenon was also observed in Fig. 5.13.

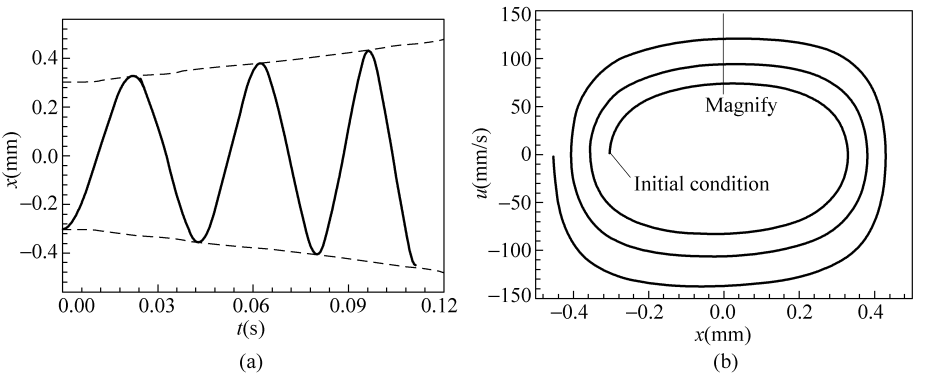

Figure 5.36 Oscillation with negative effectual viscosity
(a) Intensifying process; (b) Phase diagram

5.5.4 Coupling Bubble Oscillation

Two bubbles may continue oscillating by colliding each other between two immobile bubbles on the wires as illustrated in Fig. 5.12. To simplify the analyses, a symmetrical coupling oscillation is considered, and only two adjacent immobile bubbles and the wire are assumed to affect the external temperature field around the oscillating bubbles. Referring to Fig. 5.37, for an arbitrary symmetry double bubble oscillation system, the temperature gradient along x-axis is similar to Eq. (5.54) or

$$\frac{\partial T}{\partial x} = -\frac{q_2}{4\pi\lambda(2l-x)^2} + \frac{q_3}{4\pi\lambda \times 4x^2} \tag{5.64}$$

where q_2 denotes heat generation of the immobile bubble, and q_3 heat generation of the oscillating bubbles. The temperature gradient from Eq. (5.64) is just shown in Fig. 5.38, and $q_1 \approx q_2$ and $x_e \approx 0.6l$. There are three regions: linear region near the equilibrium point, two nonlinear regions far from the equilibrium point.

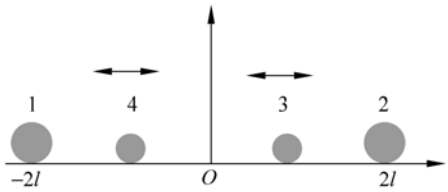

Figure 5.37 Coupling bubble oscillation model

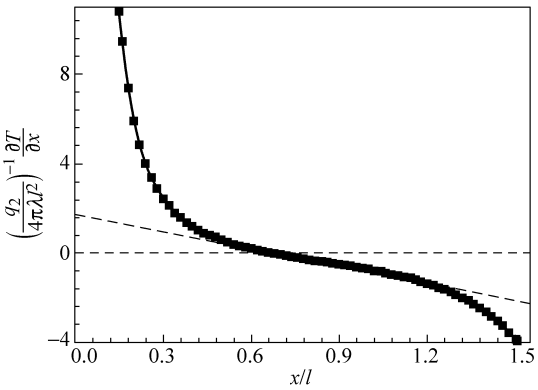

Figure 5.38 Temperature gradient for coupling bubble oscillation

Setting the right side of Eq. (5.64) to zero, the position with zero temperature gradient is obtained as,

$$x_e = 2l\left[1+(4q_1/q_2)^{1/2}\right]^{-1} \tag{5.65}$$

Substituting Eq. (5.64) into Eq. (5.20) yields

$$\frac{d^2x}{dt^2}+\frac{9\mu}{\rho_l R_b^2}\frac{dx}{dt}-\frac{4\alpha B}{\rho_l R_b}\left[-\frac{q_2}{4\pi\lambda(2l-x)^2}+\frac{q_3}{4\pi\lambda\times 4x^2}\right]=0 \tag{5.66}$$

By ignoring the effective viscosity in one period, gives

$$u^2=\frac{8\alpha B}{\rho_l R_b}\left[\frac{q_3}{16\pi\lambda}\left(\frac{1}{x_0}-\frac{1}{x}\right)+\frac{q_2}{4\pi\lambda}\left(\frac{1}{2l-x_0}-\frac{1}{2l-x}\right)\right] \tag{5.67}$$

Near the equilibrium position x_e, the temperature gradient is approximately

$$\frac{\partial T}{\partial x}=-\frac{1}{2\pi\lambda}\left[\frac{q_2}{(2l-x_e)^3}+\frac{q_3}{4x_e^3}\right](x-x_e),\quad x\approx x_e \tag{5.68}$$

Substituting Eq. (5.68) into Eq. (5.20) yields

$$\frac{d^2y}{dt^2}+\frac{27\mu}{4\rho_l R_b^2}\cdot\frac{dy}{dt}+\frac{8\alpha B}{\rho_l R_b}\frac{1}{4\pi\lambda}\left(\frac{q_2}{(2l-x_e)^3}+\frac{q_3}{4x_e^3}\right)y=0 \tag{5.69}$$

where $y=x-x_e$. Generally, the temperature gradient distribution of coupling bubble oscillation is similar to that of single bubble oscillation in Eq. (5.62), and the dynamical characteristics are also similar for both single and coupling bubble oscillation.

5.6 Bubble Leaping Dynamics

5.6.1 Dynamical Description

An analytical model, as shown in Fig. 5.39, is proposed to describe the dynamical process of bubble leaping with and without sweeping presented in Figs. 5.14 – 5.17, and meanwhile some geometrical parameters are specified, including bubble radius R, bubble center height H (the distance from the bubble center to wire surface), sweeping distance L. According to the experimental results, a bubble away from the wire is usually an ideal sphere as $R<H$, while it is a spherical crown on the wire as $R>H$.

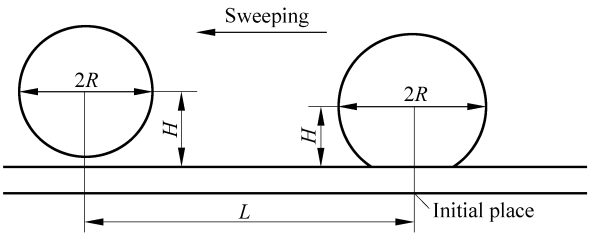

Figure 5.39 Analytical model for bubble leaping and sweeping

For the bubble periodic leaping process at a specified point, $L = 0$. Corresponding to the experimental observation in Fig. 5.14, the variations of the bubble radius and height are illustrated in Fig. 5.40. Obviously, the bubble radius increased as it approached to the wire, while the radius decreased as the bubble jumped away. During the leaping process, its period was 0.004 – 0.006 s, the leaping amplitude was 0.03 – 0.08 mm, and the leaping oscillation continued for about 0.020 s. Usually, the bubble leaping amplitude and radius were not very stable.

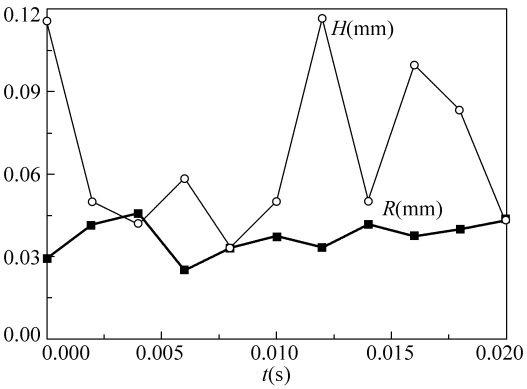

Figure 5.40 Variation of the height and bubble radius during the leaping process

Figure 5.41 presents the dynamic parameters for the bubble leaping with sweeping corresponding to the experiments shown in Fig. 5.16. The bubble had the radii ranging from 0.13 – 0.17 mm and swept along the wire with an average speed of 20 mm/s. The bubble height varied in the range of 0.13 – 0.21 mm. Very clearly, the bubble leaping with sweeping was very stable and regular.

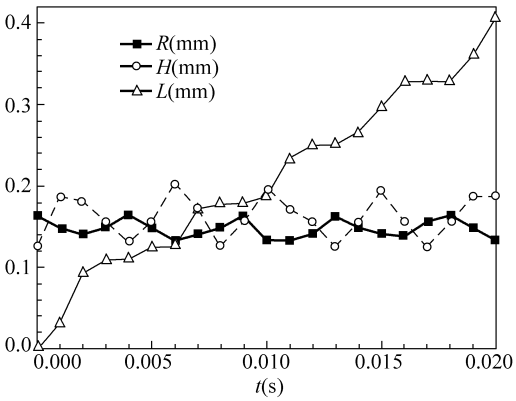

Figure 5.41 Parameter changes during leaping with sweeping

The relationship between the center height and bubble radius is illustrated in Fig. 5.42. Obviously, they were directly corresponding to each other. When jumping off, the bubble was surrounded with subcooled liquid and became smaller due to condensation at the bubble interface, and it would grow up to a large size for evaporation happening at the bubble interface on the wire.

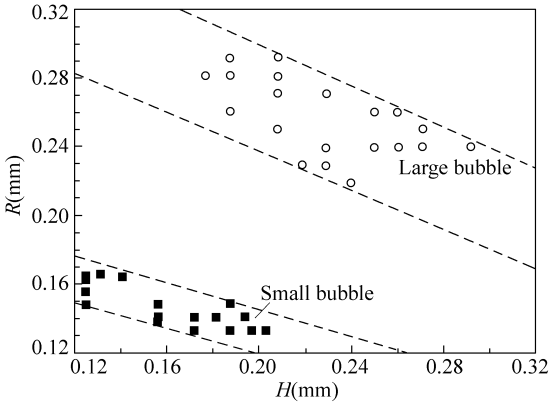

Figure 5.42 Bubble radius vs. center height during leaping with sweeping

Figure 5.43 shows the bubble center height changes with the sweeping distance. When the bubble was away from the wire, the sweeping was significant, while it

had little motion along the wire when attached to the wire. The average speed due to the sweeping in a 0.001 s period is illustrated in Fig. 5.44, about 60 mm/s and 45 mm/s for the large and small bubble away from the wire, respectively. On another hand, the speed could approximate to zero as the bubble attached on the wire. The spatial period of the large bubble was as about two times as that of the small bubble, and the large bubble also had higher average speed. The bubbles swept much faster away from the wire than on the wire, and it is expected there was higher resistance acting on bubbles when they attached to the wire.

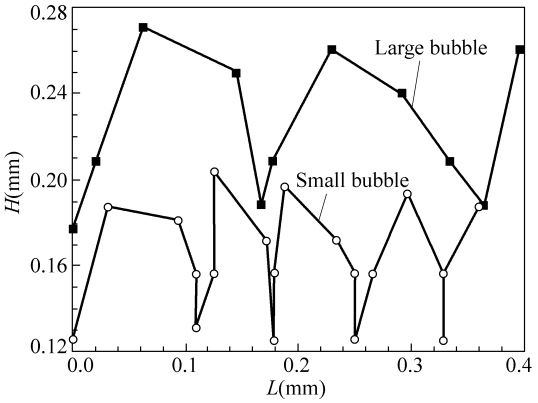

Figure 5.43 Variation of bubble center height with sweeping distance

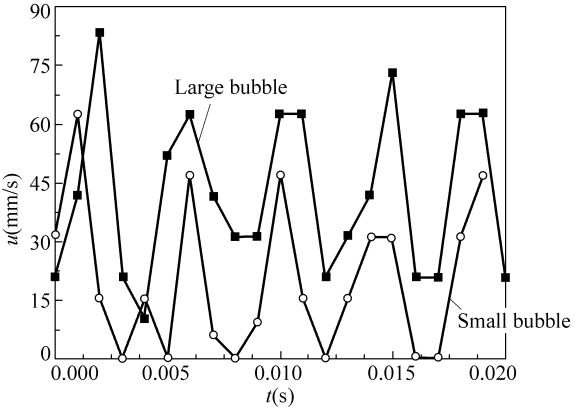

Figure 5.44 Average speed of bubble sweeping in 0.001 s

5.6.2 Simple Leaping Dynamics

The bubble leaping with sweeping includes two different dynamic processes, bubble

leaping and bubble sweeping. Comparing a normal simple sweeping with the coupled phenomenon of bubble leaping and sweeping, the speed of bubble leaping and sweeping would not keep constant, but it usually periodically varied with the companied leaping.

A periodic leaping process experiences two sub-stages, departing and returning. The departing or returning process also has two sub-processes, accelerating and decelerating. During the departing process, the bubble first leaves away from the wire, then accelerates to the maximum velocity, finally it decelerates to zero at the highest position. In the accelerating process, the escaping force is larger than the attraction force, while the attraction force should be larger than the escaping force in the decelerating process. As the bubble reaches the maximum velocity, the escaping force just balances the attraction force. The location at maximum velocity or zero acceleration is termed as equilibrium position. The dynamical characteristics of returning process are similar to departing.

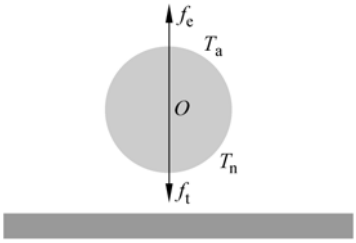

Figure 5.45 Forces acting on a bubble

A bubble is assumed to be an ideal sphere and the formation of oscillation or leaping is mainly considered in vertical direction, as shown in Fig. 5.45. The inertia force acting on the bubble is expressed as [16, 18]

$$M = \psi \rho_l 4\pi R^3 / 3 \tag{5.70}$$

where ψ is defined as a dimensionless inertia coefficient, determined by the local boiling conditions and normally $\psi > 1/2$ in the available investigations [18]. Apparently, the thermocapillary effects make the bubble to return to the wire. If average interfacial temperature gradient along vertical direction is assumed to be D_y, according to Eq. (5.5), the vertical thermocapillary force imposed on a bubble having radius R is

$$f_t = D_y B 8\pi R^2 / 3 \tag{5.71}$$

The corresponding gravity and buoyancy force imposed on the bubble are derived as, respectively,

$$f_g = -\rho_g g 4\pi R^3 / 3 \tag{5.72a}$$

$$f_b = \rho_l g 4\pi R^3 / 3 \tag{5.72b}$$

The induced buoyancy force is

$$f_e = (\rho_l g - \rho_g g) 4\pi R^3 / 3 \tag{5.73}$$

Correspondingly, the bubble leaping dynamical equation is

$$Ma = (\rho_l g - \rho_g g) 4\pi R^3 / 3 - D_y B 8\pi R^2 / 3 \tag{5.74}$$

Obviously, the bubble leaping dynamical characteristics are dependent upon the relation of buoyancy force f_e and returning force f_t. Re-arranging Eq. (5.74) yields dimensionless acceleration as [16]

$$\bar{a} = \bar{R}^3 - \bar{R}^2 \tag{5.75}$$

where $\bar{R} = \dfrac{R}{R_c}$, $R_c = \dfrac{2D_y B}{\rho_l g - \rho_g g}$, $\bar{a} = \dfrac{1}{MR_c^3} \dfrac{a}{\rho_l g - \rho_g g}$. Eq. (5.75) is illustrated in Fig. 5.46.

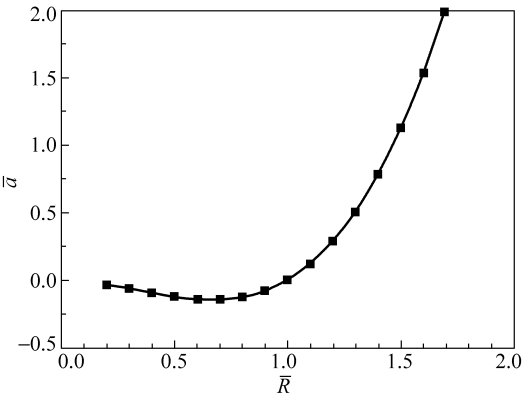

Figure 5.46 Bubble leaping characteristics

If $R > R_c$, the buoyancy force f_e is larger than the returning force f_t, and this causes an accelerating away from the wire as observed in the experiments. For $R_l < R_c$, the buoyancy force f_e decreases and is smaller than the returning force f_t, and the bubble will experience a decelerating process. Similar to the departing process, the bubble returning also experiences the accelerating and decelerating process. As bubble departing and returning continues, the bubble exhibits a periodic leaping phenomenon.

5.6.3 Heat Transfer Performance during Bubble Leaping and Sweeping

During bubble leaping with and without sweeping, the heat transport with periodic volume variation is very important. Two typical experimental measurements of heat transport with periodic volume variation during 0.001 s are presented in Fig. 5.47. The contribution of local heat flux by periodic volume variation is about $\frac{P}{\pi R^2} = 1.68 \times 10^5$ W/m^2 and $\frac{P}{\pi R^2} = 1.06 \times 10^5$ W/m^2, about equal to 18.3% and 12.1% of the wire heat fluxes for large and small bubbles, respectively.

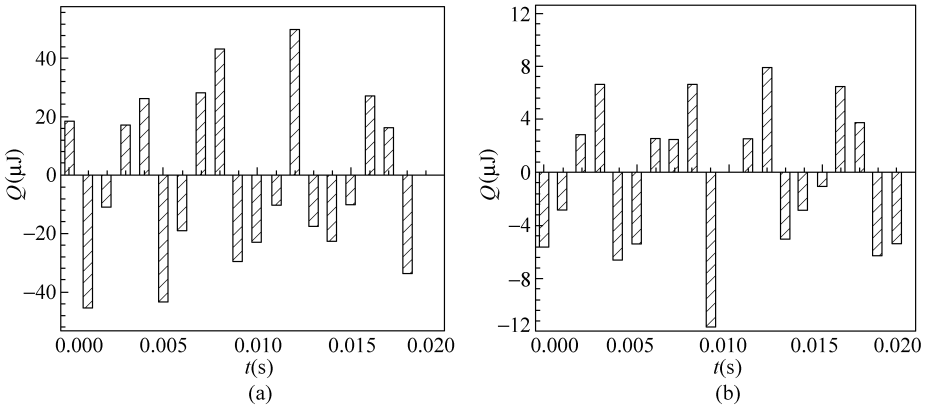

Figure 5.47 Heat transport for periodic volume variation
(a) Large bubble; (b) Small bubble

References

[1] V. P. Carey. Liquid-vapor phase-change phenomena: an introduction to the thermophysics of vaporization and condensation processes in heat transfer equipment. New York: Hemisphere Pub. Corp., 1992.

[2] H. K. Forster, N. Zuber. Dynamics of vapor bubble and boiling heat transfer. AIChE J., 1: 531 – 535, 1952.

[3] M. Shoji, J. Maeda, S. Fujii. Nonlinear bubble dynamics. In: Proc. of 32th National Heat Transfer Conference, 1: 257 – 258, 1995.

[4] K. Takahashi, J. G. Weng, C. L. Tien. Marangoni effect in microbubble systems. Microscale Themophysical Engineering, 3: 169 – 182, 1999.

[5] G. E. Thorncroft, J. F. Klausnera, R. Mei. An experimental investigation of bubble growth and detachment in vertical upflow and downflow boiling. Int. J. Heat Mass Transfer, 41: 3857 – 3871, 1998.

[6] K. Cornwell, I. A. Grant. Heat transfer to bubbles under horizontal tube. Int. J. Heat Mass Transfer, 41: 1189 – 1197, 1998.

[7] D. Qiu, V. K. Dhir. Experimental study of flow pattern and heat transfer associated with a bubble sliding on downward facing inclined surfaces. Experimental Thermal and Fluid Science, 26: 605 – 616, 2002.

[8] H. Wang, X. F. Peng, B. X. Wang, et al. Bubble sweeping and jet flows during nucleate boiling of subcooled liquids. Int. J. Heat and Mass Transfer, 46: 863 – 869, 2003.

[9] H. Wang, X. F. Peng, B. X. Wang, et al. Bubble-sweeping mechanisms. Science in China (Series E), 46: 225 – 233, 2003.

[10] H. Wang, X. F. Peng, D. M. Christopher. Dynamic bubble behavior during microscale subcooled boiling. Chinese Physics Letters, 22: 2881 – 2884, 2005.

[11] H. Wang, X. F. Peng, B. X. Wang, et al. Experimental observations of bubble dynamics on ultrathin wires. Experimental Heat Transfer, 18: 1 – 11, 2005.

[12] J. F. Lu, X. F. Peng. Bubble separation and collision on thin wires during subcooled boiling. Int. J. Heat and Mass Transfer, 48: 4726 – 4737, 2005.

[13] J. F. Lu, X. F. Peng. Bubble oscillation on thin wire during subcooled boiling. Int. J. Heat and Mass Transfer, 51: 4461 – 4469, 2008.

[14] D. M. Christopher, H. Wang, X. F. Peng. Dynamics of bubble motion and bubble top jet flows from moving vapor bubbles on microwires. ASME Journal of Heat Transfer, 127: 1260 – 1268, 2005.

[15] J. F. Lu, X. F. Peng. Bubble slippage on thin wires during subcooled boiling. Int. J. Heat and Mass Transfer, 49: 2337 – 2346, 2006.

[16] J. F. Lu, X. F. Peng. Bubble leaping and leaping slippage dynamics on thin wires during subcooled boiling. International Journal of Thermal science, 45: 908 – 916, 2006.

[17] M. Sultan, R. L. Judd. Interaction of the nucleation phenomena at adjacent sites in nucleate boiling. ASME J. Heat Transfer, 105: 3 – 11, 1983.

[18] T. E. Faber. Fluid Dynamic for Physicists. Cambridge: Cambridge University Press, 2001.

[19] G. E. Thorncroft, J. F. Klausner, R. Mei. Bubble forces and detachment. Multiphase Science and Technology, 13: 35 – 76, 2001.

[20] J. I. Romas. Lumped models of gas bubbles in thermal gradients. Applied Mathematical Modelling, 21: 371 – 386, 1997.

[21] H. Kasumi, Y. E. S. Solomentsev, A. Guelcher, et al. Thermocapillary flow and aggregation of bubbles on a solid wall. Journal of Colloid and Interface Science, 2000, 232: 111 – 120, 2000.

[22] A. H. Nayfeh, D. T. Mook. Nonlinear Oscillation. Wiley-Interscience Publication, 1979.

6 Boiling in Micrchannels

Abstract Microchannels play a critically important role in the development of modern science and technology, particularly micro/nano technology. Heat and mass transfer in microchannels has attracted worldwide researchers as one of frontiers in the energy and thermal fluid science discipline, showing great significance in both understanding fundamentals of transport phenomena at microscale and promoting development of new technologies such as micro energy systems, compact heat transfer devices/equipments, and cooling technology, etc. This chapter describes investigations of flow boiling and bubble formation, particularly the experimental investigations and theoretical analyses for boiling in microchannels by author and co-workers.

In a microchannel, the liquid temperature could be increased to much higher than the heterogeneous nucleation temperature of bubbles without detectable bubble formation or liquid motion. The geometrical size was experimentally demonstrated to have significant effect on the boiling, especially on the nucleation and bubble dynamics. The new proposed concepts of "evaporating space" and "fictitious boiling" were analyzed. Furthermore, nucleation criterion in microchannels was derived by utilizing thermodynamics and statistical mechanics. The derived nucleation criterion is reasonably coincident with the experimental measurements. Also, local interface competition and diversified bubble dynamics phenomena during flow boiling in microchannel were experimentally observed. At local heating condition, evaporation and condensation occurred at the upstream and downstream caps of an elongated bubble. Diversified phase-change modes showed dominant effect on the interface oscillation. Signal analysis depicted that the film-driven oscillations of both evaporating and condensing interfaces generally operated at higher frequencies than their counterparts driven by nucleation or dropwise condensation. The upper and lower caps of one elongated bubble oscillated at the same characteristic frequency.

Keywords microchannel, evaporating space, fictitious boiling, interface oscillation

The pioneering work of Tuckermann and Pease [1] indicates that the characteristics of fluid flow and heat transfer in microchannels are quite different from those in conventional-sized channels. Microscale boiling is also expected to be quite

X. Peng, *Micro Transport Phenomena During Boiling*

different. Bowers and Mudawar [2] investigated flow boiling of R113 in minichannel and microchannel. Lin et al. [3, 4] noted that it is extremely difficult to generate bubbles even at a very high heat flux from heater allocated in microchannels. Recently, many other investigators conducted a number of experimental and theoretical investigations to explore and understand various strange boiling phenomena and characteristics [5 – 14]. Peng and co-workers [15 – 28] conducted a series of experimental investigations on the flow boiling in microchannels. They noted the "bubble-extinction" behavior of microchannel boiling. That is, a high heat flux that is sufficient to induce vigorous nucleate boiling mode on a normal-sized heater or in normal-sized channels, one could hardly observe vapor bubble on a microchannel heater. Obviously, boiling in microchannels would display some unfamiliar aspects, especially for nucleation and bubble dynamics. This chapter does not attempt to make a complete description of the state-of-the-art of microscale boiling and heat transfer. The available investigations on the flow boiling and bubble formation, particularly the experimental investigations and theoretical analyses of boiling in microchannels by author and co-workers, are briefly reviewed, and some aspects of microscale boiling phenomena in microchannels are discussed. The emphases are laid on understanding the phase-change transition, bubble nucleation and bubble dynamics in microchannels, especially thermodynamic aspect and dynamic descriptions of the boiling.

6.1 Experimental Observations

6.1.1 General Behavior

In the earlier experimental observations of liquid flow boiling in rectangular microchannels [15 – 22], the heat transfer exhibited the characteristics of flow boiling at very low wall superheat, about 2℃. Boiling nucleation was likely initiated at much lower wall surface superheat than expected for normal situations. Although the liquid subcooling was as high as 65° to 90℃ for water and about 50℃ for methanol, the flow boiling quickly went to fully-developed nucleate boiling once it was initiated, with no apparent partial nucleate boiling region from the boiling curves. These observations suggest that the flow boiling is quite different from or even in contradiction with the observations of the boiling nucleation and bubble formation in microchannels by Lin et al. [3, 4], bubble formation temperature being as high as 80% to 90% of the liquid critical point temperature. However, no vapor bubbles were observed in the tested microchannels even as the heat transfer characteristics experimentally measured were actually in vigorous nucleate boiling region, as observed from the measured boiling curves.

So, actual bubble formation in the experiments of both Lin et al. [3, 4] and Peng and Wang [15, 16, 19] is very similar.

The visual observation for the flow boiling in triangular microchannels demonstrated the experimental evidence in rectangular microchannels, and also displayed some other features [20, 22, 23]. If there was a good seal between the glass cover and microchannel plate, no observable bubbles appeared and grew inside the channels even with heat flux greater than 10^6 W/m^2 or superheats greater than 100℃ for water at atmospheric pressure. At very high heat fluxes, a number of bubbles were generated in inlet plenum resulting in fluctuating liquid in the channels and rapid deterioration of the heat transfer. If the sealing was not good or there existed even some extremely narrow gaps between the glass cover and the plate, small bubbles which were much smaller than the channel size were observed at very low wall superheat and applied heat fluxes. Boiling nucleation or bubble formation similar to conventional vapor-bubble generation occurred at nucleation sites. The gaps, which were much smaller than the channel size, trap vapor when the section is heated and become active nucleation sites.

6.1.2 Nucleation Superheat

Figure 6.1 schematically depicts a further test setup for visual observation and measurement of nucleation in capillary tubes [27]. Three capillary tubes were employed, 1 mm, 0.5 mm, and 0.3 mm in diameter (D), respectively. Four working fluids were herein tested: water, methanol (CH_3OH), ethanol (C_2H_5OH), and carbon tetrachloride (CCl_4). In each test the capillary tube was first filled with saturated, degassed working fluid. Then the DC current through the Pt wire was increased very slowly. The electric voltage drop and the current data were continuously recorded until bubble nucleation occurred. A high-resolution CCD camera recorded the boiling dynamics.

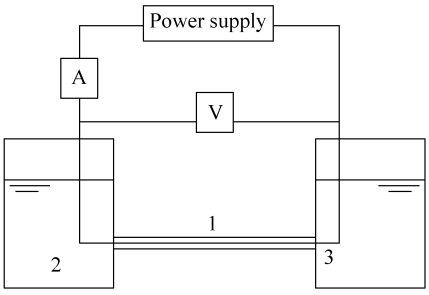

Figure 6.1 Microchannel boiling test setup
1–Microchannel; 2–Vessel; 3–Platininum wire

Table 6.1 lists the experimental results for the superheat required for bubble nucleation (T_{max}). As expected, although with certain data scattering, T_{max} markedly increases with decreasing capillary tube diameter for all four different liquids. Figure 6.2 presents these results as a function of tube diameter. A relatively faster decrease of nucleation superheat is noted for water tests, and the water test at 1.0 mm capillary tube reveals early boiling at 95℃, or a negative superheat of –5 K. Such a discrepancy has not been noted to the other three organic working fluids. Such an observation might be attributed to residual dissolved gas in the water.

Table 6.1 Superheat required for bubble nucleation

	$T_{max} - T_{sat}$ (K)			
Capillary tube (mm)	Water	Methanol	Ethanol	CCl_4
1.00	–5.0	9.7	10.0	5.3
0.50	23.1	35.2	19.7	21.0
0.30	67.3	55.7	51.1	69.2

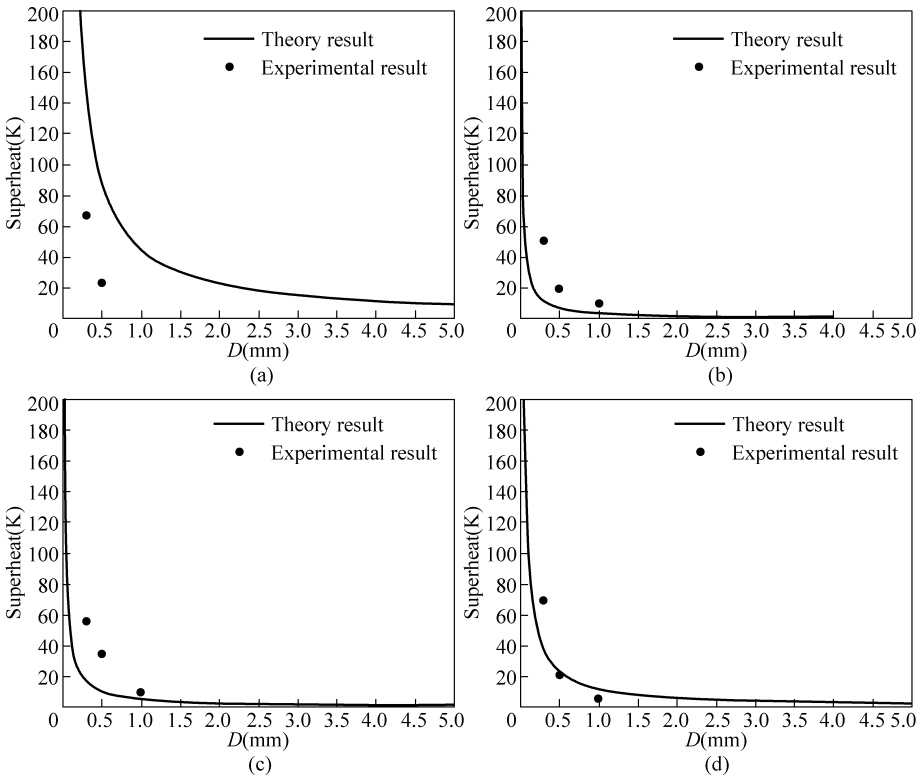

Figure 6.2 Nucleation superheat [20]
(a) Water; (b) Methanol; (c) Ethanol; (d) Carbon tetrachloride

6.1.3 Experimental Phenomena

Figure 6.3 represents some microphotographic observations to the boiling tests in 0.30 mm capillary tube. Figure 6.3(a) demonstrates the junction section between the capillary tube and the outside reservoir, in which water was subject to a superheat of 11 K. No bubbles are formed inside the capillary tube. However, large bubbles appeared at the junction port. Restated, the superheated liquid could not transform into vapor phase within the 0.3 mm capillary tube. However, once the superheated liquid was released to the un-confined space, normal bubble nucleation occurred. In Figs. 6.3(b) and 6.3(c), for boiling of methanol and ethanol at wire temperature close to their corresponding T_{max}, no visible bubbles could be detected. However, the liquid oscillated so vigorously that the heating Pt wire was masked and invisible. Figure 6.3(d) illustrates the phenomenon noted for CCl_4 boiled at superheat of 69 K on the Pt wire. Many small bubbles apparently appear around the wire in the capillary tube and vigorously oscillated along the axial direction in the tube.

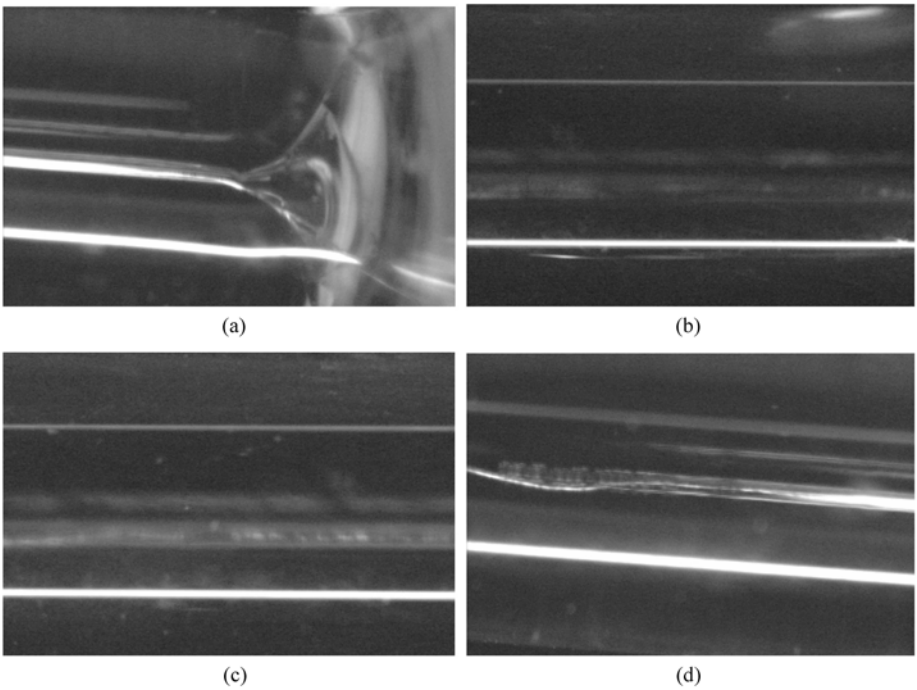

Figure 6.3 Boiling nucleation observation in a capillary tube
(a) Water; (b) Methanol; (c) Ethanol; (d) Carbon tetrachloride

Therefore, a physical picture could be summarized from the experimental observations with the four working fluids. In a microchannel, the liquid temperature

could be increased to much higher than the heterogeneous nucleation temperature for bubbles without detectable bubble formation or liquid motion. However, when the liquid temperature approaches T_{max}, chaotic vibrations of superheated liquid became visible. This might be attributed to the vigorous growth/collapse of bubble embryos in the superheated liquid. At T_{max}, vapor bubbles emerged from the whole body of the superheated liquid layer. If the microchannel is small enough and the cross flow liquid velocity is not strong enough to sweep out these bubbles, the heating wire dries out.

6.2 Physical Explanation

6.2.1 Evaporating Space and Fictitious Boiling

The geometrical size was experimentally demonstrated to have significant effect on the boiling, especially on the nucleation and bubble dynamics. Besides the usual necessary conditions, such as superheat and nuclei, the scale of the liquid bulk should be large enough for bubbles to exist and grow in the liquid, or there is a minimum liquid bulk size that allows internal evaporation to occur and bubble to grow within the liquid. This critical scale was referred to “evaporating space” by Peng and Wang [17]. Only when the liquid bulk size is larger than this necessary evaporating space will boiling or nucleation occur with bubble growth in liquid. Apparently, the evaporating space is affected by the thermal boundary conditions of the liquid or the boundaries surrounding the liquid. For example, at thin liquid film surface, evaporation usually takes place rather than nucleate boiling as it is heated. If the applied heat flux is sufficiently high, or the wall temperature approaches to Leidenfrost temperature, violent bursting evaporation happens and conventional nucleate boiling does not emerge. In microstructures and very small channels/tubes, bubble formation and bursting boiling occur at very high superheat because of liquid space restriction and the lack of effective active nuclei.

As noted in experiments, even though there was no bubble for flow boiling in microchannel, the heat transfer performance displayed true nucleate boiling characteristics, and the heat transfer was even much higher than that of flow boiling in conventional-sized channels. This “boiling” looks like single-phase convection, termed “fictitious boiling” [17]. This kind of boiling has two main aspects. First, the liquid has reached conventional nucleate boiling conditions, but internal evaporation and bubble growth have not yet occured or there might be countless unstable micro bubbles within the liquid that cannot be visualized by ordinary means. Second, the heated liquid will evaporate and generate bubbles as soon as it enters a space large enough for evaporating. For fictitious boiling,

the liquid would apparently be in an unstable thermodynamic non-equilibrium state.

The possible physical implications of this process would be described as the follows. First, the physical properties of the liquid in a non-equilibrium state could be quite different from those at any equilibrium state. For example, the specific heat might be much higher than that at equilibrium conditions, so that it is possible to absorb and store a large amount of heat without phase change. This would be the main reason for the process having very high heat transfer rates. Second, there might, in reality, be countless unstable micro embryo bubbles within the liquid, particularly on the heating surface, which cannot be observed by ordinary means. These bubbles would be too small to be stable, and are all likely to collapse according to the classical theory of nucleation [29]. The unstable micro embryo bubbles generate and collapse intermittently and frequently, and hence, cause the liquid to be in a high non-equilibrium state. A large amount of energy would be required to maintain the process having remarkably high frequency of micro embryo bubble generation and collapse. The ability for absorbing heat of this non-equilibrium liquid is greatly intensified, so that the heat transfer rate of the fictitious boiling could be evidently higher than that of usual nucleate boiling. The "evaporating space" and "fictitious boiling" may provide rational hypotheses to explain the extraordinary phase-change transport phenomena.

6.2.2 Thermodynamic Evidence

Consider an embryo bubble in a microchannel, which is normally comparable with channel size, as depicted in Fig. 6.4. The density fluctuations generated in a superheated liquid could form nuclei in a random manner. In doing so, a compressed pressure impulse would be imposed to the surrounding liquid regardless the nuclei are produced via homogeneous or heterogeneous nucleation mechanisms. In microchannels such a pressure impulse, δP, would propagate mainly along the axial direction.

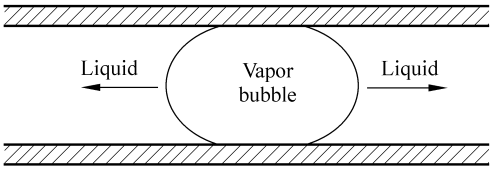

Figure 6.4 Embryo bubble in microchannels

The local dynamic characteristics in liquid should be consistent with that of the entire system. Thus, any local action in liquid, like the density fluctuation, would not markedly alter the system characteristics. Therefore, for microchannel

boiling, the following expression is satisfied:

$$\delta P \ll \Delta P \tag{6.1}$$

where ΔP denotes the characteristic pressure drop of liquid flow through the microchannel. The isothermal compressibility of liquid is defined as follows:

$$\beta = -\frac{1}{V}\left(\frac{\partial V}{\partial P}\right)_T \tag{6.2}$$

Hence, the pressure impulse is stated as follows:

$$\delta P = -\frac{\delta V}{\beta V} \tag{6.3}$$

Referring to Fig. 6.4, we have the following equation:

$$\frac{\delta V}{V} = -\frac{r_a^2}{r_h^2} \tag{6.4}$$

where $r_h = D_h / 2$ is microchannel hydraulic radius, and r_a is average radius of density fluctuation or bubble embryo.

Combining Eqs. (6.1), (6.3), and (6.4) yields

$$r_a \ll r_h \sqrt{\beta \Delta P} \tag{6.5}$$

For water at atmospheric pressure, β is about 50×10^{-6} m/bar. If taking $\Delta P \sim 1 \times 10^5$ Pa and $r_h \sim 10^{-3}$ m, then $r_a \ll 10^{-6}$ m, a value much less than r_h. That is to say, the mechanical condition requires that the density fluctuation or embryo should be much smaller than the channel scale.

Bubble embryo generated from density fluctuations could further develop only if $r_a > r_c$. r_c is on the order of 10^{-6} m for ordinary liquids. As a result, when a density fluctuation or bubble embryo is formed in a superheated liquid, it would be extremely difficult to grow beyond r_c, as illustrated in Fig. 6.5 [29]. As a result, the bubble embryos would generate and collapse continuously at an extra-high

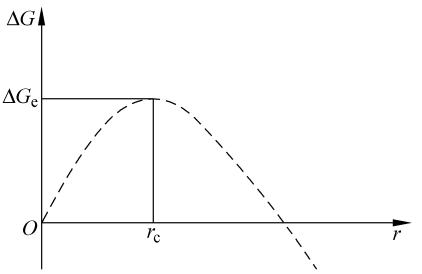

Figure 6.5 Free energy change with respect to bubble radius

frequency in microchannel/microstructure. The superheated liquid hence comprises many invisible, growing and collapsing micro-embryos and density fluctuations that absorb a great amount of energy to facilitate high heat flux convective heat transfer without apparent phase-change, or the fictitious boiling. If one expects mature nucleate boiling occurring in a microchannel or microstructure, much higher heat flux or higher superheat is necessary to be reached for sustaining the existence of stable and visible bubbles.

6.2.3 Cluster Dynamical Evidence

If the density fluctuation or a cluster is considered as an extremely large molecule or a Brownian particle, its movement is random and described by Brownian motion. As a result, we may clearly recognize and exactly describe the microscale nucleation and boiling phenomena from both the dynamic and kinematic characteristics of a cluster, discussed in Chapter 2.

Brownian particles, greatly larger than a molecule, suspend in bulk fluid and randomly move having collision with the around molecules and or particles. The forces applied to Brownian particles or density fluctuation clusters during boiling in microstructures/microchannels by the around particles and other factors in the bulk liquid, include damping and random force. The damping force is proportional to the particle velocity, and the random impact is transitory with random fluctuation and orientation. Langevin equation becomes

$$M\frac{\mathrm{d}u}{\mathrm{d}t} = F_{\mathrm{s}} - \alpha u + A_{\mathrm{s}}(t) \tag{6.6}$$

where F_{s} is applied force, $A_{\mathrm{s}}(t)$ random force and α damping coefficient. For the particles with the freedom of one-dimension, if F_{s} becomes zero Langivin equation Eq. (6.6) evolves to

$$\frac{\mathrm{d}u}{\mathrm{d}t} = -\frac{u}{\tau} + \frac{A_{\mathrm{s}}(t)}{M} \tag{6.7}$$

For a Brownian particle having radius, r, viscous friction is determined by Stokes' law as

$$-au = -6\pi r\eta u \tag{6.8}$$

Obviously, $\alpha = 6\pi r\eta$, and $\tau = M/\alpha$. Rearranging Eq. (6.6) yields

$$M\frac{\mathrm{d}^2x}{\mathrm{d}t^2} + \alpha\frac{\mathrm{d}x}{\mathrm{d}t} = A_{\mathrm{s}}(t) \tag{6.9}$$

It is easy to obtain the following relation,

$$x\frac{\mathrm{d}^2x}{\mathrm{d}t^2}=\frac{1}{2}\frac{\mathrm{d}^2x^2}{\mathrm{d}t^2}-u \tag{6.10}$$

Eq. (6.9) by x and combining with Eq. (6.10), gives

$$\frac{1}{2}M\frac{\mathrm{d}^2x^2}{\mathrm{d}t^2}-Mu^2+\frac{1}{2}\alpha\frac{\mathrm{d}x^2}{\mathrm{d}t}=xA_\mathrm{s}(t) \tag{6.11}$$

Averaging Eq. (6.11) and noting $\overline{xA_\mathrm{s}(t)}=0$, we have

$$\frac{1}{2}M\frac{\mathrm{d}^2\overline{x^2}}{\mathrm{d}t^2}-M\overline{u^2}+\frac{1}{2}\alpha\frac{\mathrm{d}\overline{x^2}}{\mathrm{d}t}=0 \tag{6.12}$$

If the Brownian particles are considered to be relevant to extremely large molecules, the theorem of equipartition of energy holds true or

$$M\overline{u^2}=kT \tag{6.13}$$

So, Eq. (10) becomes

$$\frac{\mathrm{d}^2\overline{x_2}}{\mathrm{d}t^2}+\frac{1}{\tau}\frac{\mathrm{d}\overline{x_2}}{\mathrm{d}t}-\frac{2kT}{M}=0 \tag{6.14}$$

The solution of Eq. (6.12) is given as

$$\overline{x^2}=\frac{2kT}{\alpha}t+C_1\mathrm{e}^{-t/\tau}+C_2 \tag{6.15}$$

where C_1 and C_2 are integral constants, and $C_1=0, C_2=x_0^2$.

Because of the following relation,

$$\overline{(x-x_0)^2}=\overline{x^2}+x_0^2-2\overline{xx_0}=\overline{x^2}-x_0^2 \tag{6.16}$$

As a result, the travelling distance of a Brownian particles is obtained,

$$\overline{(x-x_0)^2}=\frac{2kT}{\alpha}t \tag{6.17}$$

or the distance is a function of traveling time, the particle radius and fluid viscosity.

In the travel distance within the time from its original generation point to the place where it grows up to a nucleus, the cluster must absorb enough number activated molecules or coalesce with other clusters to make itself growing up. If it has collisions with other particles or walls and strongly disturbed by some thermal and fluid influences, the cluster might dissociate, disappear in superheated bulk liquid.

The experimental observations show that boiling nucleation occurs at longer time, or around thirty seconds, once the necessary superheat is reached. The travel distance is calculated using Eq. (6.17) for a cluster moving as a Brownian particle in this duration. For example, considering water at 120℃, $\eta = 0.001142$ kg/(m·s) and $k = 1.38 \times 10^{-23}$ J/K, the radius of a density fluctuation or cluster, r, is much less than the order of 10^{-6} m. If $r = 10^{-8}$, $t = 30$ s, the travel distance is

$$\overline{(x - x_0)^2} \approx 0.0672 \tag{6.18}$$

This implies that a cluster must obtain some activated molecules or coalesce with other clusters to develop a nucleus within 30 s and 0.0672 mm. When it collides with vessel or channel walls in its traveling and growing, the cluster may dissociate and not be possible to become a nucleus. If the scale of microstructures or microchannels is comparable with this travel distance, a large number of cluster having different sizes would collide with surrounding walls and dissociate or disappear. Apparently, the generation of nuclei would greatly depress and the boiling is very difficult to happen. The collision of a cluster with other clusters or Brownian particles around it and the walls of microstructures or microchannels greatly alter the dynamic characteristics of the cluster. This means that the generation of nuclei highly depends upon the dynamic process of clusters.

6.3 Nucleation Criterion

6.3.1 Thermodynamic Analysis

In microchannels having hydraulic diameters of same order as the bubble embryos, as shown in Fig. 6.4, bubble initiation is physically restricted by the surrounding walls and the inertia of the liquid on both ends of the bubble since the vapor bubble occupies almost whole cross-section of the channel once nucleation occurs. Or in microchannels the liquid must be removed by embryo bubble formed locally, due to great difference in density between liquid and its vapor.

From classical thermodynamics, the phase stability conditions for a pure substance are given by Eqs. (6.19) and (6.20). Because the thermal stability criterion, Eq. (6.19), is naturally satisfied, and Eq. (6.20) would be a necessary and sufficient condition for phase stability.

Using chain rule

$$\left(\frac{\partial p}{\partial V}\right)_T = \left(\frac{\partial p}{\partial V}\right)_S + \left(\frac{\partial p}{\partial S}\right)_V \left(\frac{\partial S}{\partial V}\right)_T \tag{6.19}$$

and the classical thermodynamic relationsassociated relations,

$$\left(\frac{\partial p}{\partial V}\right)_S = \left(\frac{\partial p}{\partial T}\right)_S \left(\frac{\partial T}{\partial V}\right)_S \tag{6.20}$$

$$\left(\frac{\partial p}{\partial S}\right)_V = -\left(\frac{\partial T}{\partial V}\right)_S \tag{6.21}$$

Eq. (6.20) is rearranged to give

$$\left(\frac{\partial p}{\partial V}\right)_T = \left(\frac{\partial p}{\partial T}\right)_S \left(\frac{\partial T}{\partial V}\right)_S - \left(\frac{\partial T}{\partial V}\right)_S \left(\frac{\partial S}{\partial V}\right)_T < 0 \tag{6.22}$$

Note that

$$\left(\frac{\partial T}{\partial V}\right)_S = -\left(\frac{\partial S}{\partial V}\right)_T \left(\frac{\partial T}{\partial S}\right)_V = -\left(\frac{\partial p}{\partial T}\right)_V \frac{T}{N\bar{C}_V} \tag{6.23}$$

Since $\left(\frac{\partial p}{\partial T}\right)_V > 0$, from Eq. (6.23), $\left(\frac{\partial T}{\partial V}\right)_S < 0$, Dividing Eq. (6.22) by $\left(\frac{\partial T}{\partial V}\right)_S$ gives

$$\left(\frac{\partial p}{\partial T}\right)_S - \left(\frac{\partial S}{\partial V}\right)_V > 0 \quad \text{or} \quad \left(\frac{\partial p}{\partial T}\right)_S > \left(\frac{\partial S}{\partial V}\right)_T \tag{6.24}$$

For a thermodynamic system in equilibrium at its saturation temperature, the pressure is only a function of temperature. Therefore, for a phase change system, with Clausius-Clapeyron equation

$$\left(\frac{\partial p}{\partial T}\right)_S = \frac{\mathrm{d}p}{\mathrm{d}T} = \frac{h_{\mathrm{lv}}}{T_{\mathrm{s}}(v'' - v')} \tag{6.25}$$

Considering the case of a saturated liquid in a microchannel heated at a specified constant heat flux, the entropy variation dS during time interval Δt in Eq. (6.24) can be approximated as

$$\Delta S = \frac{q'' \pi D_{\mathrm{h}} \Delta x}{T_{\mathrm{s}}} \Delta t \tag{6.26}$$

The volume change in Eq. (6.24) for bubble formation in the channel is

$$\Delta V = \frac{\pi}{4} D_{\mathrm{h}}^2 \Delta x \tag{6.27}$$

Combining Eqs. (6.26) and (6.27) yields

$$\left(\frac{\partial S}{\partial V}\right)_{T=T_{\mathrm{s}}} = \frac{4q'' \Delta t}{D_{\mathrm{h}} T_{\mathrm{s}}} \tag{6.28}$$

The heating time, Δt, can be determined for bubble growth, in which heat must diffuse throughout the cross-section once nucleation occurs. Thus,

$$\Delta t = c\frac{\pi D_{\mathrm{h}}^2}{4\alpha_{\mathrm{v}}} \tag{6.29}$$

where c is introduced as an empirical correction factor determined from experiment, and α_{v} is the thermal diffusivity of vapor. Combining Eqs. (6.26) – (6.29) yields

$$\left(\frac{\partial S}{\partial V}\right)_{T=T_{\mathrm{s}}} = \frac{cq''\pi D_{\mathrm{h}}}{\alpha_{\mathrm{v}} T_{\mathrm{s}}} \tag{6.30}$$

Substituting Eqs. (6.30) and (6.25) into Eq. (6.24) and rearranging, the phase stability condition is expressed by a dimensionless parameter

$$N_{\mathrm{mb}} = \frac{h_{\mathrm{lv}}\alpha_{\mathrm{v}}}{c\pi(v''-v')q''D_{\mathrm{h}}} \leqslant 1 \tag{6.31}$$

For convenience, the nucleation criterion is expressed by heat flux or superheat as [20, 23]

$$q'' \geqslant \frac{h_{\mathrm{lv}}\alpha_{\mathrm{v}}}{c\pi(v''-v')D_{\mathrm{h}}} \tag{6.32}$$

$$\Delta T_{\mathrm{sup}} \geqslant \frac{4AT_{\mathrm{s}}(v''-v')\sigma}{h_{\mathrm{lv}}D_{\mathrm{h}}} \tag{6.33}$$

where A is an empirical constant, being experimentally evaluated as $A \approx 280$ [20].

The predicted superheats by Eq. (6.32) with $c = 1$ are depicted in Fig. 6.2 for water, methanol, ethanol and carbon tetrachloride and compared with the experimental results, showing rationally consistent with each other.

6.3.2 Statistical Mechanics Approach

Consider a bubble embryo (cluster) as a canonical ensemble which comprises of a specified number of fluid molecules (N) and a specified fluid volume (V), and can exchange energy with a heat bath at constant temperature (T). The heat bath is so large that the bath energy is much larger than the energy of the embryo. Therefore, the energy levels of the bath could be regarded as continuous. A diathermal, rigid and impermeable boundary is assumed for dividing the embryo and the heat bath.

Only the potential clusters that might become a real vapor bubble are of interest. Therefore, only the ones that comprise a large number of molecules with size

close to r_c are considered. Schematically, a embryo is imagined to be comprised of many sub-systems that are of N_l fluid molecules, volume V_l, and energy ε_l, which are the eigenvalues of the Schrodinger's equation $H\psi_l = \varepsilon_l \psi_l$, where H is the Hamiltonian operating on the state vector ψ_l. Thus, we have the following identities for the embryo,

$$N = \sum_l N_l \tag{6.34}$$

$$V = \sum_l V_l \tag{6.35}$$

$$\varepsilon = \sum_l \varepsilon_l \tag{6.36}$$

Thermal equilibrium is achieved between the embryo and the heat bath. The number of states for the embryo with N, V and energy between ε_l and $\varepsilon_l + \mathrm{d}\varepsilon_l$ is derived as:

$$\Omega(\varepsilon)\mathrm{d}\varepsilon = 2\pi V \left(\frac{2m}{h^2}\right)^{3/2} \varepsilon_l^{1/2} \mathrm{d}\varepsilon_l \tag{6.37}$$

where m and h are the mass of fluid molecule and the Planck constant, respectively. Normally the growth (and collapse as well) of bubble embryo is so fast that the total system, the embryo and the heat bath, could be regarded as isolated. Hence the free energy of the system is expressed as

$$F = -NkT \ln Z \tag{6.38}$$

where k is the Boltzmann constant, and Z, the canonical partition function defined as

$$Z = \sum_l 2\pi V \left(\frac{2m}{h^2}\right)^{3/2} \varepsilon_l^{1/2} \exp\left(-\frac{\varepsilon_l}{kT}\right) \mathrm{d}\varepsilon_l \tag{6.39}$$

Many energy levels exist for micro particles in the embryo, the summation in Eq. (6.39) could be approximated by an integral. Hence, the free energy per unit volume of fluid is,

$$F_V = \frac{F}{V} = -\rho_N kT \ln\left[\int_0^\infty 2\pi V \left(\frac{2m}{h^2}\right)^{3/2} \varepsilon^{1/2} \exp\left(-\frac{\varepsilon_l}{kT}\right) \mathrm{d}\varepsilon\right] \tag{6.40}$$

Where ρ_N is the particle density ($= N/V$).

The particles having energy levels at the both extremes of integral are rare, while most of them could be allocated in the range $[\varepsilon_{l,\max}, \varepsilon_{l,\min}]$. According to mean-value theorem, there exists an energy level E_{ave} that belongs to this range which makes the following approximation hold:

$$F_V \approx -\rho_N kT \ln\left[2\pi V\left(\frac{2m}{h^2}\right)^{3/2} E_{\text{ave}}^{1/2} \exp\left(-\frac{E_{\text{ave}}}{kT}\right)(\varepsilon_{l,\max} - \varepsilon_{l,\min})\right] \quad (6.41)$$

At $T = T_{\max}$ where phase transition occurs, $F_V = F_{V,\max}$. The system temperature is obtained as

$$T_{\max} \approx \frac{E_{\text{ave}} - (F_{V,\max}/\rho_N)}{k \ln\left[2\pi V\left(\frac{2m}{h^2}\right)^{3/2} E_{\text{ave}}^{1/2}(\varepsilon_{l,\max} - \varepsilon_{l,\min})\right]} \quad (6.42)$$

The energy levels of all sub-systems or particles in the embryo change with temperature. Hence, the parameters F_V, E_{ave}, $\varepsilon_{l,\max}$, and $\varepsilon_{l,\min}$ increase with temperature T. Notably, the energy distribution is Gaussian-like if the numbers of fluid molecules and energy states in the embryo are both large. Hence, $\varepsilon_{l,\max} - \varepsilon_{l,\min} = c\sigma$, where σ is the standard deviation of the distribution and $\sigma^2 = kT^2(\partial E_{\text{ave}}/\partial T)_V$. c is a proportional constant. Therefore, the denominator of Eq. (6.42) is proportional to $\ln[T^2 E_{\text{ave}}(\partial E_{\text{ave}}/\partial T)_V]$, which changes slower than its numerator.

Both the numerator and denominator of Eq. (6.42) have to have the same sign for a physically relevant system. This is the case since at large V, $E_{\text{ave}} \gg F_{V,\max}/\rho_N$ and the logarithm of the denominator of Eq. (6.42) exceeds unity. On the contrary, at the $V \to 0$ limit, $E_{\text{ave}} \ll F_{V,\max}/\rho_N$ and the logarithm in the denominator changes sign as well.

Similar qualitative discussions are introduced to demonstrate the dependence of liquid superheat ($T_{\max} - T_{\text{sat}}$) required for bubble nucleation as a function of system volume, V. Figure 6.6 schematically depicts such a dependence. As the system volume decreases from a normal sized channel ($V \to \infty$), the required superheat increases accordingly, since in this case $E_{\text{ave}} \gg F_{V,\max}/\rho_N$, $T_{\max}$ inversely depends on InV. At another extreme ($V \to 0$), $E_{\text{ave}} \ll F_{V,\max}/\rho_N$, therefore both the numerator and denominator of Eq. (6.42) depend on ln$V$ and cancel each other. Note that $F_{V,\max}/\rho_N$ grows with ln$V$. $T_{\max}$ hence approaches a constant. For the case of extremely small confined space or comparable to particle size, the temperature decreases with the decrease of the volume, as shown in Fig. 6.6. This actually means that the phase change seems no significance. Apparently there exists a threshold system volume $V_{\max}$ where $T_{\max}$ reaches a peak value ($T_{\max,\max}$). Nevertheless, $T_{\max,\max}$ should not exceed the superheat limit for a specific working liquid. The dependence of $T_{\max}$ on system volume is dependent upon the range of the system volume. For normal fluids $V_{\max}$ is generally much smaller than the most practical situations. Hence, one would observe increased liquid superheat needed to trigger bubble nucleation when the size of microchannel heater went down.

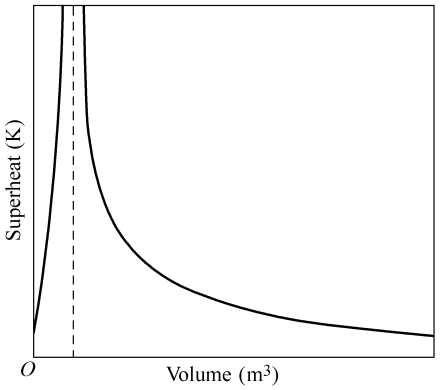

Figure 6.6 Effect of scale on boiling nucleation superheat

The predictions of Eq. (6.42) for liquids are presented in Fig. 6.7. These results are reasonably coincident with the experimental measurements [27] and in very good agreement with the thermodynamic nucleation criterion above discussed.

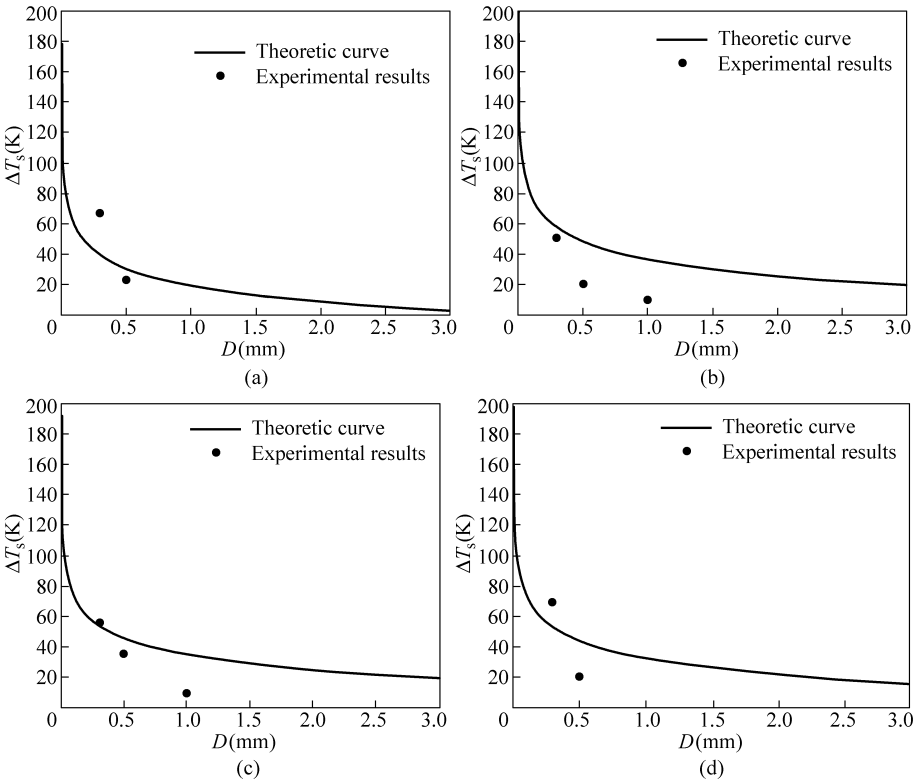

Figure 6.7 Comparison of predictions with the measurements
(a) Water; (b) Methanol; (c) Ethanol; (d) Carbon tetrachloride

6.3.3 Dynamic Model

In the above-mentioned discussions the action of external perturbation should mainly correspond to the bubble-extinction behavior or so-called fictitious boiling behavior observed in microchannel boiling. From cluster dynamical view, a pressure wave model was proposed to investigate the boiling nucleation in microchannels. This model states that a pressure wave generates accompanied with cluster formation, which is the source of external perturbations, and travels along all directions. The pressure wave might be meet microchannel walls and/or other waves and particles (including other clusters) and reflected and acting the wave producer.

Kwak et al. [30] estimated the pressure difference between that in the cluster and that in bulk liquid to be as high as 280 atm during the initial phase of cluster growth. Many clusters form and grow in the superheated liquid. The pressure waves would hence generated from many points and propagate themselves outwards in the liquid. For a normal-sized channel such a pressure wave would transmit outward from the cluster and rapidly dissipate. However, in a microchannel the wall may reflect the generated pressure waves back to the clusters, acting as random external perturbations imposed to the clusters, as shown in Fig. 6.8. Such an occurrence could stochastically affect the values of system parameters, like k_1 in Eq. (2.53). (Notably, as stated in Chapter 2, $k \propto | p_\infty - p_v |$. Consequently, any external perturbations that would yield a change in system pressure would influence the parameter k_1.)

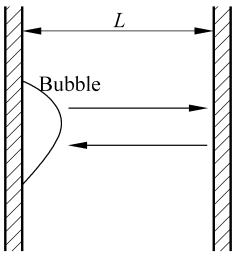

Figure 6.8 Pressure wave transmits in a microchannel

According to conventional nucleation theory, the nucleation rate per unit volume could be stated as follows:

$$J_n = N_0 D_n Z_\mathrm{f} \exp\left(-\frac{\Delta G}{kT}\right) \tag{6.43}$$

where D_n and Z_f are the collision frequency of liquid molecules with cluster surface, and the non-equilibrium factor, respectively. Notably, J_n is the product of the gain term in Eq. (2.46) and the concentration of clusters in a superheated

liquid (C_0); or $J_n = C_0 \times$ gain. Typically, $D_n Z_f = 10^7 \mathrm{s}^{-1}$ [31]. Hence, $\lambda C_0 = 10^7 \mathrm{s}^{-1}$.

Consider the radius of a cluster as r at time t. In an increment of time dt the cluster radius increases by dr, refering to Fig. 6.9. Then the number of activated molecules absorbed onto the cluster increases by $4\pi n J_n r^2 \mathrm{d}t$. Based on number balance of activated molecules, the change of radius with time is expressed as,

$$\frac{\mathrm{d}r}{\mathrm{d}t} = J_n n V_\mathrm{m} \tag{6.44}$$

where V_m is the volume of activated molecule. Take $r(0) = 0$, then the radius of cluster would increase linearly with time. The volume of cluster hence becomes,

$$\mathrm{d}V_\mathrm{c} = 4\pi (J_n n V_\mathrm{m})^3 t^2 \mathrm{d}t \tag{6.45}$$

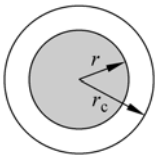

Figure 6.9 Growth model of a cluster

The change in bulk liquid volume would be $\mathrm{d}V = -\mathrm{d}V_\mathrm{c}$. Assume that the bulk liquid follows the van der Waal's equation of state:

$$\left(p + \frac{a}{V^2}\right)(V - b) = RT \tag{6.46}$$

Then the pressure fluctuation introduced by volume change dV could be simplified with the assistance of Eq. (6.46) as:

$$\mathrm{d}p = At^2 \mathrm{d}t \tag{6.47}$$

where

$$A = \left[-\frac{RT}{(V-b)^2} + \frac{2a}{V^3}\right]\frac{4\pi}{M}(J_n n V_\mathrm{m})^3 \tag{6.48}$$

Consequently, the pressure difference inside and outside the cluster could be estimated as:

$$p_\mathrm{v} - p_\infty = \frac{A}{3}t^3 \tag{6.49}$$

While the clustering process occurs in a short time scale, the pressure difference described in Eq. (6.49) could be taken as the magnitude of pressure wave generated.

The velocity of pressure wave propagation, c, is estimated as,

$$c = \sqrt{\left(\frac{\mathrm{d}p}{\mathrm{d}(1/V)}\right)_S} = \sqrt{\left(\frac{V}{V-b}\right)^2 RT - \frac{2a}{V}} \tag{6.50}$$

In a microchannel of size L (treated as characteristic length), the time for the pressure wave to be reflected by the wall back to the cluster (bubble embryo) is estimated as

$$t_{\mathrm{R}} \approx \frac{2L}{c} \tag{6.51}$$

The time required for a vapor embryo to develop during the initial phase (t_{c}) is approximately 10 μs [32]. As discussed in the preceding sections, the imposition of an external perturbation, like pressure wave discussed here, could markedly affect the parameter k_1, whence depress the development of clusters. Consequently, if t_{R} were less than the time for a cluster to form and grow, the pressure wave would have a chance to be reflected back and to depress its growth. The criterion for the occurrence of fictitious boiling is thereby expressed as,

$$L < \frac{1}{2} c t_{\mathrm{c}} \tag{6.52}$$

Take water at 120℃ and 1 MPa as an example. The corresponding pressure wave velocity c is estimated as 477 m/s. The critical scale of microchannel could be estimated on the basis of Eq. (6.52) as $L_{\mathrm{c}} = 2.4$ mm. Thus, if the channel size is less than approximately 2.4 mm, the fictitious boiling phenomenon would emerge.

6.4 Nucleation Kinetics

6.4.1 Bubble Evolution Dynamics near Critical Radius

Most researchers focused their attention on bubble behavior including evolution dynamics and interfacial phenomena for boiling in microchannels or microstructures, rather than considering the initial and microscopic process, which is expected to be quite different from those in normal-sized channels due to the size restriction.

In a boiling system, the bubble evolution is controlled by mass, momentum, and heat transport at the interface [29]. For a bubble near to its critical radius, the heat transfer is fast enough, and the growth rate is mainly governed by the momentum transfer or inertial effect. The total kinetic energy of moving liquid

surrounding a spherical bubble can be obtained as

$$K = \frac{\rho_1}{2}\int_{V_0} u^2 \mathrm{d}V \tag{6.53}$$

For an embryo bubble with length L and diameter D in the middle region, as shown in Fig. 6.10, the whole system can be divided into three regions, bubble within surface 1, bulk microchannel between surface 1 and 2, out of the microchannel or beyond surface 2. For the region near the bubble and beyond the microchannel, the flow is of spherical symmetry with velocity $u(R) = \frac{\mathrm{d}r}{\mathrm{d}t}\left(\frac{r}{R}\right)^2$, then

$$K_1 + K_2 = \frac{\rho_1}{2}\int_{r\leqslant D/2} u^2 \mathrm{d}V + \frac{\rho_1}{2}\int_{r>D/2} u^2 \mathrm{d}V = 2\pi\rho_1 r^3 \left(\frac{\mathrm{d}r}{\mathrm{d}t}\right)^2 \tag{6.54}$$

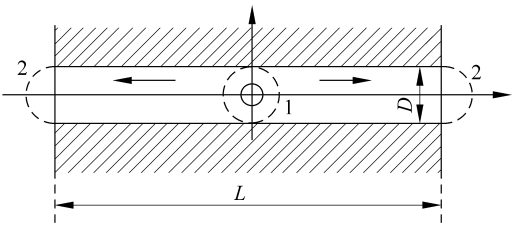

Figure 6.10 Bubble growing in a microchannel

For the flow in the bulk microchannel, the velocity in the channel is almost uniform, and mass transport equilibrium yields

$$2u\pi D^2/4 = \frac{\mathrm{d}r}{\mathrm{d}t} 4\pi r^2 \tag{6.55a}$$

$$u = \frac{\mathrm{d}r}{\mathrm{d}t} 8r^2/D^2 \tag{6.55b}$$

The kinetic energy in the bulk microchannel is

$$K_{12} = \frac{\rho_1}{2}\int_{V_0} u^2 \mathrm{d}V = 32\rho_1\pi r^4 D^{-2} L\left(\frac{\mathrm{d}r}{\mathrm{d}t}\right)^2 \tag{6.56}$$

So the kinetic energy of the liquid in microchannel is

$$K = K_1 + K_2 + K_{12} = 2\pi\rho_1 r^3\left(\frac{\mathrm{d}r}{\mathrm{d}t}\right)^2 + 32\rho_1\pi r^4 D^{-2} L\left(\frac{\mathrm{d}r}{\mathrm{d}t}\right)^2 = 2\rho_1\pi r^3\varphi\left(\frac{\mathrm{d}r}{\mathrm{d}t}\right)^2 \tag{6.57}$$

where $\varphi = 16rLD^{-2} + 1$. In free space, $r/D \to 0, L/D = O(1), \varphi = 1$. The net work done against the surrounding liquid is given as

$$W_1 = \int_0^r P_1 \cdot 4\pi R^2 \mathrm{d}R - \frac{4}{3}\pi P_\infty r^3 \tag{6.58}$$

Setting Eq. (6.57) equals to Eq. (6.58) yields

$$\rho_1 \pi r^3 \varphi \left(\frac{\mathrm{d}r}{\mathrm{d}t}\right)^2 = \int_0^r P_1 \cdot 4\pi R^2 \mathrm{d}r - \frac{4}{3}\pi P_\infty r^3 \tag{6.59}$$

Note R is related to the vapor pressure inside the bubble by the Young-Laplace equation,

$$p_1 = p_\mathrm{v} - 2\sigma / r \tag{6.60}$$

During nucleation process, the dynamics is mainly determined by the characteristics near the critical radius. Near the critical radius, differentiating Eq. (6.59) respect with t yields

$$r \cdot \ddot{r} + \frac{3}{2}\dot{r}^2 = \frac{1}{\rho_1 \varphi_\mathrm{c}}\left[p_\mathrm{v} - p_\infty - \frac{2\sigma}{r}\right] \tag{6.61}$$

At thermodynamic equilibrium for a critical bubble,

$$\dot{r} = 0 \qquad \text{at} \quad r = r_\mathrm{c} \tag{6.62}$$

From Eqs. (6.61) and (6.62), and $p_\mathrm{v} - p_\infty \approx 2\sigma / r_\mathrm{c}$, we have

$$p_\mathrm{v} - p_\infty - \frac{2\sigma}{r} = \frac{2\sigma}{r r_\mathrm{c}}(r - r_\mathrm{c}) \tag{6.63}$$

For this condition, for bubble evolution near critical radius, $\dot{r}^2 \ll r \cdot \ddot{r}$, and from Eq. (6.62),

$$\ddot{r} = \frac{\mathrm{d}r}{\mathrm{d}t} \cdot \frac{\mathrm{d}\dot{r}}{\mathrm{d}r} = \frac{1}{2}\frac{\mathrm{d}\dot{r}^2}{\mathrm{d}r} = \frac{2\sigma}{\rho_1 \varphi_\mathrm{c} r_\mathrm{c}} \cdot \frac{r - r_\mathrm{c}}{r^2} \tag{6.64}$$

Integrating Eq. (6.64) from r_c to r yields

$$\dot{r}^2 = \int_{r_\mathrm{c}}^r \frac{4\sigma}{\rho_1 \varphi_\mathrm{c} r_\mathrm{c}} \frac{r - r_\mathrm{c}}{r^2} \mathrm{d}r = \frac{2\sigma}{\rho_1 \varphi_\mathrm{c} r_\mathrm{c}^3}(r - r_\mathrm{c})^2 + O\left[(r - r_\mathrm{c})^2\right] \tag{6.65a}$$

$$\dot{r} = \sqrt{\frac{2\sigma}{\rho_1 \varphi_\mathrm{c} r_\mathrm{c}^3}}(r - r_\mathrm{c}) = K(r - r_\mathrm{c}) \tag{6.65b}$$

where $K = \sqrt{\dfrac{2\sigma}{\rho_l r_c^3 \varphi_c}}$, and the parameter φ_c dependent on the bubble evolution velocity. For a very long and small microchannel, $\varphi_c \approx 16 r_c L D^{-2} + 1 \to \infty$, and the velocity coefficient K decreases to zero.

6.4.2 Nucleation in Confined Space

For a nucleation process in a boiling system, the equilibrium distribution and dynamic characteristics of clusters are very different near the critical radius. A cluster, $i < i_c$, does not has a stable interface, and its equilibrium distribution is mainly dependent pon heterophase fluctuation. A cluster, $i > i_c$, has a stable interface, and its distribution is dependent of the surrounding conditions around the interface, particularly geometry and subcooling. As a result, the nucleation kinetic process is divided into two stages, or before and after its critical radius.

As a cluster $i < i_c$ fluctuates, the system almost keeps isotonic and isothermal, and the change of Gibbs function is expressed as

$$\Delta G(i) = i\Delta\mu_0 + 4\pi\sigma\left(\frac{3}{4\pi}\omega\right)^{2/3} i^{2/3} \tag{6.66a}$$

$$r(i) = \left(\frac{3}{4\pi}\omega\right)^{1/3} i^{1/3} \tag{6.66b}$$

where $\Delta\mu_0$ is the chemical potential difference of one single particle in the cluster and bulk liquid phase. Setting $\partial\Delta G/\partial n$ to zero, the critical particle number is derived as $i_c = -32\pi\sigma^3\omega^2/(3\Delta\mu_0^3)$.

For cluster $i < i_c$ near critical radius, we have

$$\begin{aligned}\Delta G(i) &= i\Delta\mu_0 + 4\pi\sigma\left(\frac{3}{4\pi}\omega\right)^{2/3} i^{2/3} \\ &= \Delta G(i_c) - \frac{4\pi\sigma}{9}\left(\frac{3}{4\pi}\omega\right)^{2/3} i_c^{-4/3}(i-i_c)^2 + O\left[(i-i_c)^2\right]\end{aligned} \tag{6.67a}$$

$$\frac{n_i}{n_c} \approx \exp\left[\frac{4\pi\sigma}{9kT}\left(\frac{3}{4\pi}\omega\right)^{2/3} i_c^{-4/3}(i-i_c)^2\right] = \exp\left[-\frac{q_0(i-i_c)^2}{2}\right] \tag{6.67b}$$

where $q_0 = -\dfrac{8\pi\sigma}{9kT}\left(\dfrac{3}{4\pi}\omega\right)^{2/3} i_c^{-4/3} = -\dfrac{\Delta\mu_0 i_c^{-1}}{3kT}$.

For a cluster of $i > i_c$, it forms stable interface and the liquid motion with bubble growth will cause significant effect especially in microstructure. From Eq. (3.72), the equilibrium distribution of cluster satisfies

$$\frac{n_i}{n_{i-1}} = \frac{w^+_{i-1,i}}{w^-_{i,i-1}} = \frac{s_{i-1}\beta_{i-1}}{s_i\alpha_i}, \quad i > i_c \tag{6.68}$$

where $s_i = 4\pi(3\omega/4\pi)^{2/3} i^{2/3}$ is surface area of a cluster. As a conclusion, distribution of the cluster $i > i_c$ is determined not only by interfacial area, but also by the phase change effects such as α_i, β_i.

In this case the interface velocity is expressed as

$$v = \dot{r} = (\alpha - \beta)/N \tag{6.69}$$

Since $\alpha = Nv_0/4$ [29], Eq. (6.69) evolves to

$$\frac{\beta}{\alpha} = \frac{Nv_0/4 - v/\omega}{Nv_0/4} = 1 - \frac{v}{v_0/4} \tag{6.70}$$

Substituting Eq. (6.65) into Eq. (6.70) yields

$$\frac{\beta}{\alpha_i} \approx 1 - \frac{4K(r - r_c)}{v_0} = 1 - \left(\frac{3}{4\pi}\omega\right)^{1/3} \frac{4K(i^{1/3} - i_c^{1/3})}{v_0} \tag{6.71}$$

For the bubble near critical radius $i - i_c \ll i_c$, $i^{1/3} - i_c^{1/3} = i_c^{1/3}[(i/i_c)^{1/3} - 1] \approx i_c^{1/3}[i/i_c - 1]/3$,

$$\frac{\beta}{\alpha_i} \approx 1 - q_2(i - i_c) \tag{6.72}$$

where the evolution coefficient $q_2 = K\left(\frac{3}{4\pi}\omega\right)^{1/3} \frac{i_c^{-2/3}}{12v_0} = \frac{i_c^{-2/3}}{12v_0}\left(\frac{3}{4\pi}\omega\right)^{1/3} \cdot \left(\frac{2\sigma}{\rho_l r_c^3}\right)^{1/2} \varphi_c^{-1/2}$, which is reduced in a microchannel for $\varphi_c \approx 16 r_c LD^{-2} + 1$. Substituting Eq. (6.72) into Eq. (6.68) yields

$$\frac{n_i}{n_{i-1}} = \frac{s_{i-1}}{s_i}[1 - q_2(i - i_c)], \quad i - n_c \ll n_c \tag{6.73}$$

and then

$$n_i = n_c \frac{s_{n_c}}{s_i} \prod_{i=n_c}^{i} [1 - q_2(i - i_c)] \tag{6.74}$$

As $q_2(i-i_c) \ll 1$, $1-q_2(i-n_c) \approx \exp[-q_2(i-i_c)]$, the equilibrium distribution approximates

$$n_i = n_c \frac{s_{n_c}}{s_i} \exp\left[-q_2 \sum_{i=i_c}^{i} (i-i_c)\right] \approx n_c \frac{s_{i_c}}{s_i} \exp\left[-q_2 (i-i_c)^2/2\right] \tag{6.75}$$

Near the critical radius, $s_i \approx s_{n_c}$, $n_i \approx n_c \exp[-q_2(i-i_c)^2/2]$. Apparently, the bubble evolution factor in a microchannel plays an important role for the equilibrium distribution near the critical radius.

From Eq. (3.73), boiling nucleation equation is derived for a cluster growing across its critical radius as

$$J^{-1} = \int_1^{n_c} \frac{\mathrm{d}x}{w^+_{x,x+1} n_x} + \int_{n_c}^{M} \frac{\mathrm{d}x}{w^+_{x,x+1} n^*_x} \tag{6.76}$$

where the first term on the right side is caused by clusters $i < i_c$, and the second term is caused by clusters $i > i_c$.

From Eq. (3.74), the nucleation rate in unbounded space is

$$Z = \left(-\frac{\Delta\mu_0 i_c^{-4/3}}{6\pi kT}\right)^{1/2} = \left(\frac{q_0}{2\pi}\right)^{1/2} \tag{6.77}$$

Many investigators found it was extremely difficult to generate bubbles even at a high heat flux from heater allocated in microchannels, which is usually called as "bubble-extinction" behavior of microchannel boiling. Since the whole boiling process has two stages including nucleation and bubble evolution, it is necessary to consider the special characteristics of nucleation process in microstructures.

Combining Eq. (6.67) with Eqs. (6.75), (6.77) evolves to

$$Z^{-1} = \frac{1}{2}\left(\frac{q_1}{2\pi}\right)^{-1/2} + \frac{1}{2}\left(\frac{q_2}{2\pi}\right)^{-1/2} \tag{6.78}$$

Very clearly, Zeldovich nonequilibrium factor will increase as q_2 increaes, as shown in Fig. 6.11. When nucleation and boiling occurs in a long and small microchannel, the evolution factor of bubble, q_2, is obviously reduced from Eq. (6.71), and then the nucleation rate also decreases. As $q_2 \to 0$, the nonequilibrium Zeldovich factor is

$$Z \approx (2q_2/\pi)^{1/2} \tag{6.79}$$

When the growth coefficient $q_2 \to 0$, $Z \to 0$, and from Eq. (3.73) $J = ZDn_{n_c} \to 0$. That is to say that the nucleation rate is approximately zero if the bubble evolution

is restrained strongly, and there seldom occur large bubbles as observed in the experiments [3, 4].

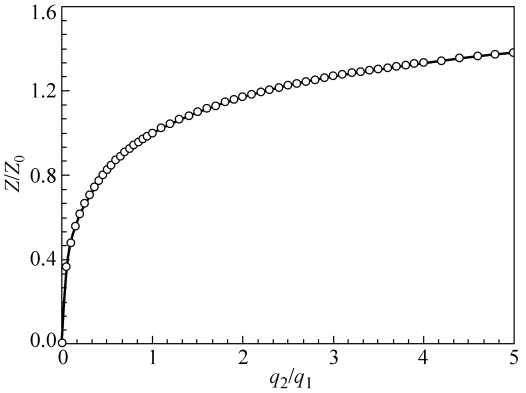

Figure 6.11 Zeldovich nonequilibrium factor

The distribution of critical clusters is [33]

$$\frac{f_c}{n_c} = J\int_{i_c}^{M}\frac{\mathrm{d}x}{w_{x,x+1}^{+}n_x} = \frac{1}{1+(q_2/q_1)^{1/2}} \tag{6.80}$$

as shown in Fig. 6.12. As $q_2 \to \infty$, the distribution of critical cluster $f_c/n_c \to 0$, and it is relatively very small because it evolves to a big bubble quickly. If the bubble evolution is restrained as $q_2 \to 0$, the distribution of critical cluster $f_c/n_c \to 1$, the relative distribution near the critical radius reaches its maximum, which means the embryo bubbles are very difficult to grow.

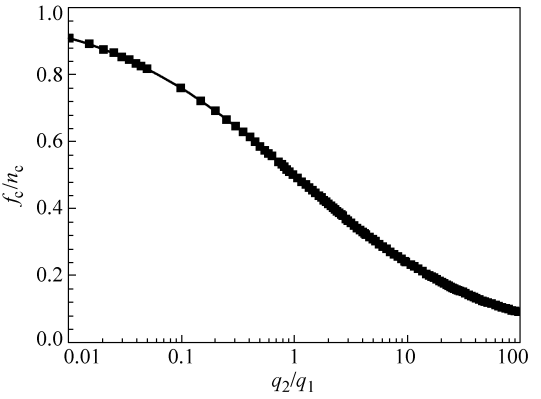

Figure 6.12 Distribution of the critical clusters

6.5 Bubble Dynamic Behavior with Local Heating

6.5.1 Experiments

The experimental apparatus and flow loop are shown in Fig. 6.13 for conducting local phase change tests with deionized water at ambient temperature (20 – 25℃) [28]. The design of the test section is shown in Fig. 6.14. 22 microchannels of 100 μm (W) × 100 μm (H) were fabricated into a silicon substrate in parallel at a

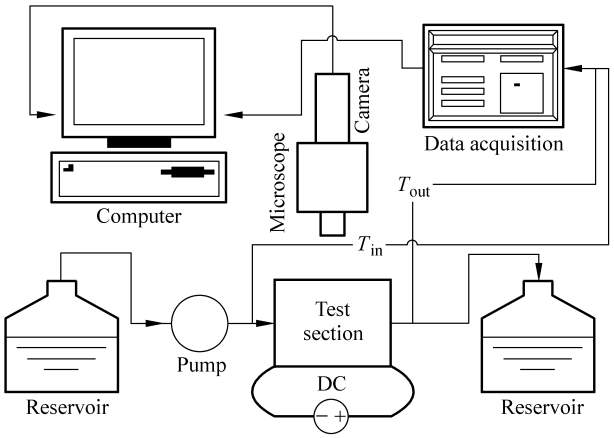

Figure 6.13 Experimental setup for local phase change study

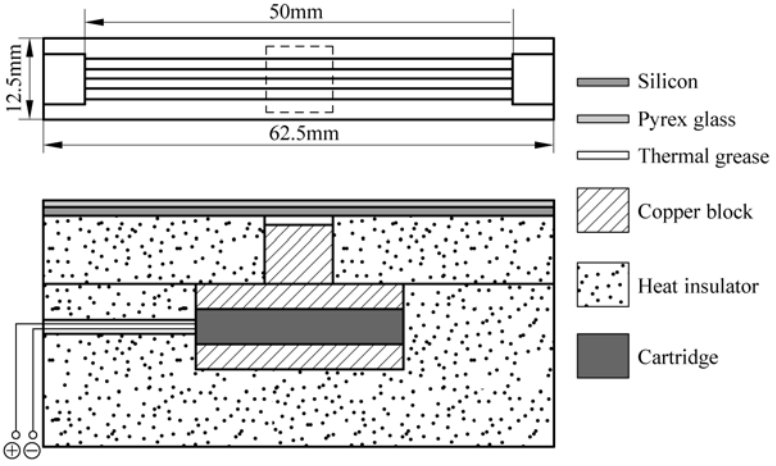

Figure 6.14 Test section layout

uniform spacing of 150 μm by means of plasma etching. The chip was 62.5 mm (L) × 12.5 mm (W) × 0.9 mm (H). The top of the channels was covered by a Pyrex glass layer by anodic bonding to insulate the liquid and allow visual observation. The heated area was located in the center region of the flow path within a restricted area of 10×10 mm^2.

6.5.2 Phase Change Behavior

A locally heated duct liquid flow usually has a fully-developed velocity profile and a developing thermal boundary, which could therefore be categorized as the thermal entrance problem, or the Graetz-type problem. [34] When heat flux within heated region increased to a value so that both fluid temperature and thermal layer thickness favored nucleation condition at some active locations, nucleate boiling began as shown in Fig. 6.15(a). From classical bubble dynamics theory, initial period of bubble growth should be inertia-controlled, shown bi-directional bubble growth along both the upstream and downstream direction to satisfy the pressure balance. Since the bubble was confined by small channel width, it was an elongated bubble or vapor column. The length of the elongated bubble increased until the pressure difference across the liquid-vapor phase interface reduced, and the interface movement decelerated. Then the bubble growth entered the heat transfer controlled period.

In heat transfer control period, the upstream cap of the elongated bubble evaporated due to continuous heating from the channel wall. And highly energetic vapor generation pushed both the upper and lower caps moving further upstream and downstream, respectively. As the upper interface moved upwards into upstream subcooled liquid and even out of heating region, the interfacial temperature or liquid superheat for inducing evaporation would decrease, and the evaporation rate slowed. Finally the upstream cap stopped moving, as depicted in Fig. 6.15(b). The downstream cap of the bubble, on the other hand, left the locally heated region during its movement downwards, and superheated vapor started to condense on the relatively low temperature surface of the upper channel wall, or the Pyrex glass layer bottom (see Fig. 6.15(c)). Condensation continued until vapor was entirely consumed, and liquid single phase flow recurred.

These experimental observations can be idealized as a concise and conceptual description of the steady phase change process in an individual microchannel at locally heated condition, which is schematically shown in Fig. 6.15(d). In a real operation, however, the phase change at both caps of the bubble was usually quite intensive, so that a stable phase interface was rarely realized. Contrarily, the movement of the interface always departed from the equilibrium point and showed a remarkable oscillating nature.

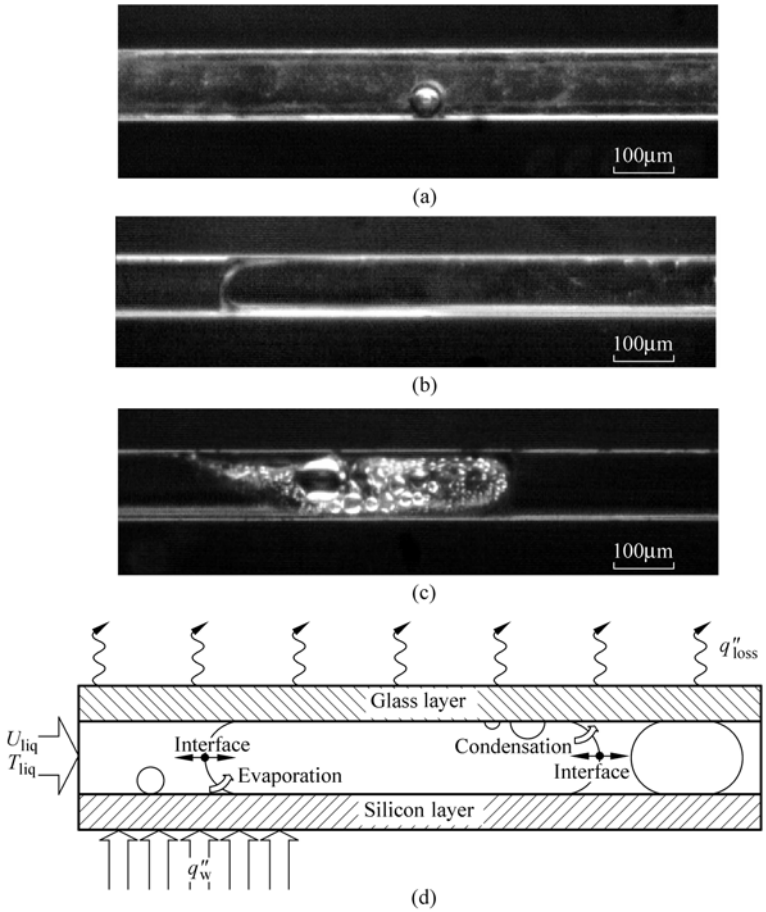

Figure 6.15 Phase change process under locally heated condition
(a) Single bubble; (b) Elongated bubble; (c) Condensation at downstream interface; (d) Analytical model

6.6 Interface Oscillation

6.6.1 Periodic Feature

Figure 6.16 illustrates the upstream cap of an elongated bubble in an individual channel. Visual observation indicates that the interface was oscillating at a period, which can be roughly calculated by counting the number of cycles within the recorded time. More in-dept information, e.g., the dominant factor of the oscillation, or the relationship between the interface oscillation and the periodic behavior of another physical phenomenon, is hardly provided by this method.

Generally speaking, every oscillating object can be treated as a form of wave, or a signal, being a superposition of many periodic components. The dominant component among them has a physical counterpart which has the greatest impact on the oscillating object. Therefore, a signal analysis method is employed in the present study to investigate the interface oscillation. The streamwise location of the phase interface at each instant is taken as the oscillating object, which is treated as the source signal to be analyzed in both time and frequency domains.

The oscillation process in Fig. 6.16 is taken as an example. The location of the vapor interface versus time chart is depicted in Fig. 6.17(a), showing very apparent periodic feature, which is consistent with visual observations. If a signal

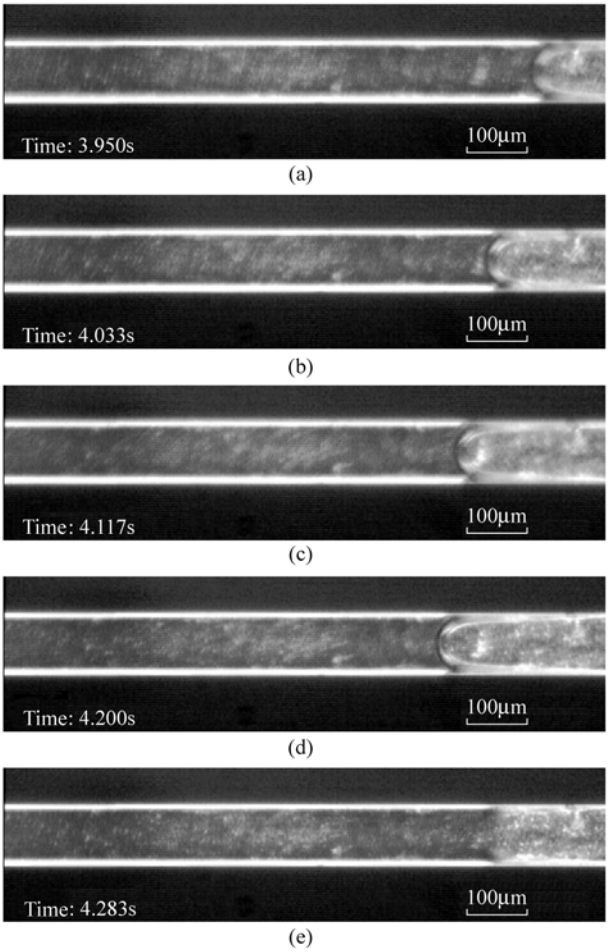

Figure 6.16 Evaporating interface oscillation without nucleation ($m = 377.7$ kg/(m^2·s), $q'' = 5.1 \times 10^5$ W/m^2)

is periodic, accordingly its autocorrelation function is also periodic with the same period. Corresponding to the experimental measurement in Fig. 6.17(a) the autocorrelation from signal analysis is illustrated in Fig. 6.17(b). The source signal is dominated by a periodic component at a period around 0.8 s, forming regular oscillation throughout the time domain. A frequency domain analysis is further conducted using Fast Fourier Transform (FFT), and the result is shown in Fig. 6.17(c). The power spectrum density of the signal has a steep peak at 1.17 Hz, which is the principle component of the source.

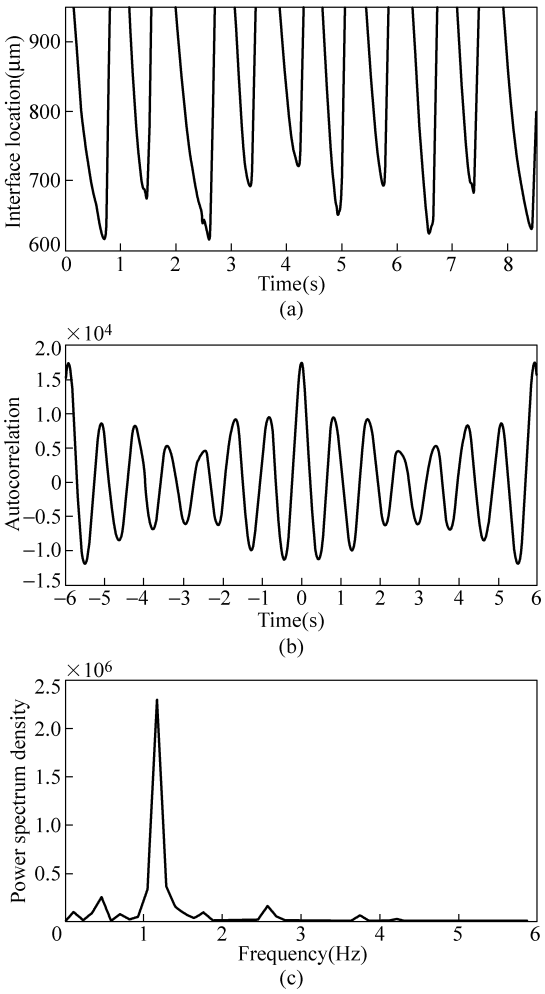

Figure 6.17 Signal analysis of an evaporating interface oscillation without nucleation ($m = 377.7$ kg/(m^2·s), $q'' = 5.1 \times 10^5$ W/m^2)

6.6.2 Evaporating Interface

The signal analysis has explored the composition and the dominant component of an interface oscillation. As shown in Fig. 6.16, no obvious sign of nucleation appeared near the evaporating interface of the bubble, i.e., the thin film evaporation is supposed to be the main mode of evaporation. This demonstrates that the thin film evaporation is capable to sustain a (quasi-)stable interface at averagely high mass and heat flux in microchannels.

Not all evaporation at the upstream bubble cap, on the other hand, was in the form of thin film evaporation. Even in the same run of an experiment at the same conditions, the evaporating interfaces in different channels could show a variety of behavior patterns. As shown in Fig. 6.18, occasional nucleation occured in the vicinity of the oscillating interface in a channel. When the interface was located upper far away from the heated region, the evaporation was insufficient and the interface was pushed downwards, as illustrated in Figs. 6.18(a) and (b). The liquid was then heated to a favorable temperature for nucleation (especially at the corner zone of the channel), and boiling happened locally (see Fig. 6.18(c)). Since the nucleation site was very close to the interface, a new bubble coalesced with the elongated bubble instantly. The process was too fast to be captured by the video system, and only the injected droplets on the downstream wall were recorded as the evidence of the locally explosive boiling. The droplet jet caused a lack of liquid to sustain evaporating thin film, and thus the interface was pushed further downwards by the incoming flow. The process from Figs. 6.18(b) to (d) recurred for many times until the upper bubble cap was far away from the equilibrium position where the evaporation rate exceeded the flow rate. Then the interface moved upwards (Fig. 6.18(e)) again and repeated the process from Figs. 6.18(a) to (e).

The variation of interface location with time is illustrated in Fig. 6.19(a). The time and frequency domain analysis of the interface location oscillation are depicted in Figs. 6.19(c) and (e), respectively. The characteristic frequency is then found to be around 0.47 Hz. Since the nucleation process induced notable droplet injection, the nucleation periodicity and intensity can be revealed by the droplet generation, whose volume is measured as the cube of droplet diameter, as shown in Fig. 6.19(b). From Figs. 6.19(a) and (b), the nucleation (droplet generation) signal is almost in phase with the interface oscillation, although the former one seems much more complicated than the latter one. This is further confirmed by its autocorrelation function, as shown in Fig. 6.19(d), noting that the peak at 0 s suggests strong random perturbation. The power spectrum chart in Fig. 6.19(f) indicates that the characteristic frequency of nucleation process is 0.47 Hz, the same as the interface oscillation frequency.

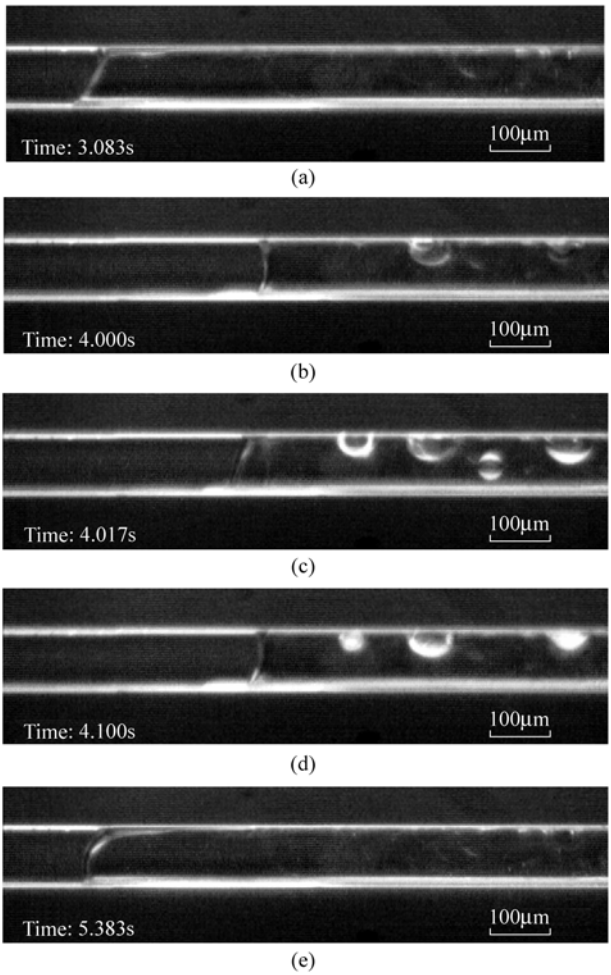

Figure 6.18 Evaporating interface oscillation with nucleation ($m = 377.7$ kg/(m^2·s), $q'' = 5.1 \times 10^5$ W/m^2)

The nucleation occurred at a further upstream location away from the interface when the flow rate increased, as shown in Fig. 6.20. The distance between the active site and the bubble cap was large enough for the CCD to capture the whole bubble growth process. When a new bubble grew to a comparable size with the channel width, as shown in Fig. 6.20(c), the liquid behind it was suddenly vented downwards to form a strong jet. At the same time the elongated bubble

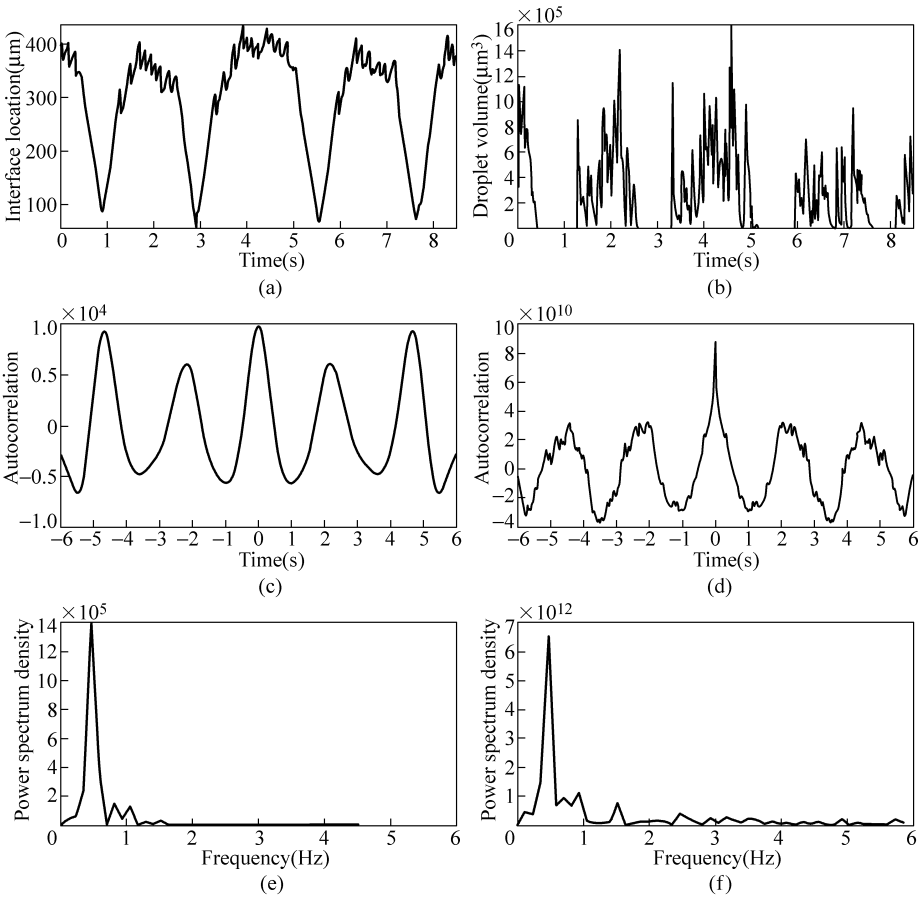

Figure 6.19 Signal analysis of evaporating interface oscillation with nucleation ($m = 377.7$ kg/(m^2·s), $q'' = 5.1 \times 10^5$ W/m^2)

moved upwards and coalesced with the bubble (see Fig. 6.20(d)). And then the newly formed interface was pushed back to the balance point downstream (see Fig. 6.20(e)). Similar signal analysis process is applied on the phenomena in Fig. 6.20. The slight difference lies in that the nucleation behavior is represented by recording the bubble growth history from the active site. Figures 6.20(a), (c) and (e) are the results of interface oscillation, while Figs. 6.21(b), (d) and (f) are due to the nucleation. Both signals are periodic with a characteristic frequency of 0.94 Hz.

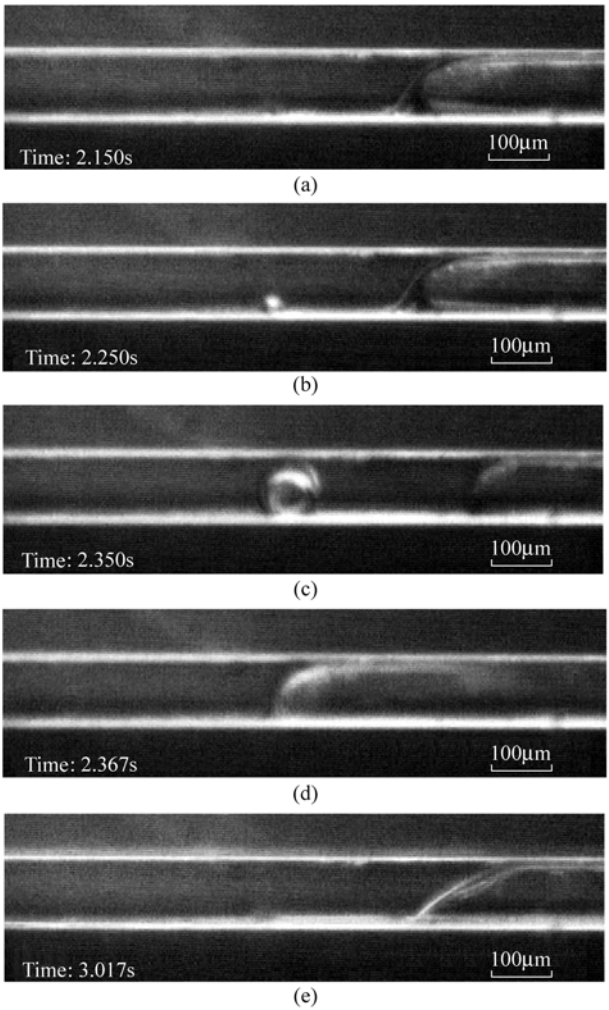

Figure 6.20 Evaporating interface oscillation with nucleation ($m = 453.2$ kg/(m^2·s), $q'' = 5.0 \times 10^5$ W/m^2)

It could be concluded from above discussion that the oscillating phase interface of an elongated bubble in an individual channel was mainly sustained by thin film evaporating, and was influenced by local nucleation. The highly diversified boiling behavior, especially the nucleation phenomenon, depended on the non-uniformly distributed flow and heat conditions between the parallel channels, as well as the various local wall conditions.

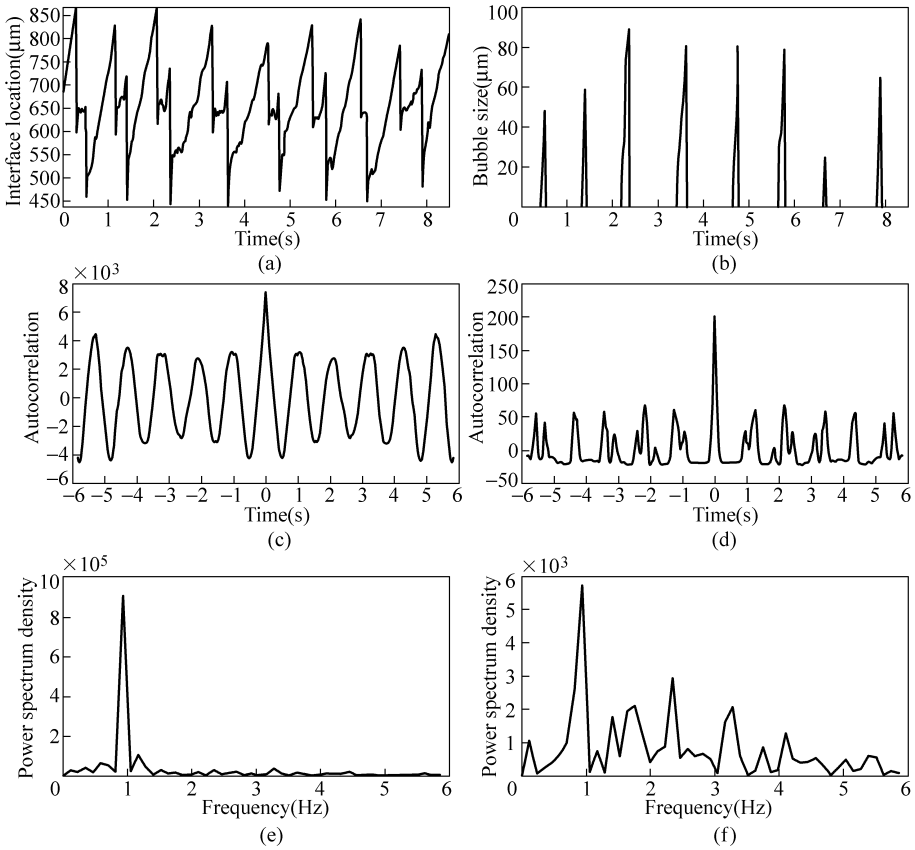

Figure 6.21 Signal analysis of evaporating interface oscillation with nucleation ($m = 453.2$ kg/(m^2·s), $q'' = 5.0 \times 10^5$ W/m^2)

6.6.3 Condensing Interface

Diversified phase change was also observed at the condensing interface of the downstream bubble cap. Figure 6.22 shows a typical condensation process starting from droplet formation. According to the heat transfer analysis in the cross section, dropwise condensation firstly appeared at the low-temperature top wall of a channel, i.e., the bottom of Pyrex glass layer (see Fig. 6.22(a)). And the droplets gradually coalesced to a liquid film around the corner formed by the channel walls (see Fig. 6.22(b)). As the condensation continued, the liquid film thickness increased, and the effective flow area was suppressed. Therefore high speed mist flow prevailed outside of the film, as shown in Figs. 6.22(c) and (d). When the liquid film grew to a critical thickness, the elongated bubble broke into

two bubbles (see Fig. 6.22(e)). The measured film thickness shows that, as depicted in Fig. 6.22(b), the critical thickness before the bubble breakup was always smaller than approximately 65% of the channel width. After the bubble breaking, the newly formed short vapor column vented downstream, whereas the upper elongated bubble remained stable with its interface periodically repeating the whole oscillation process.

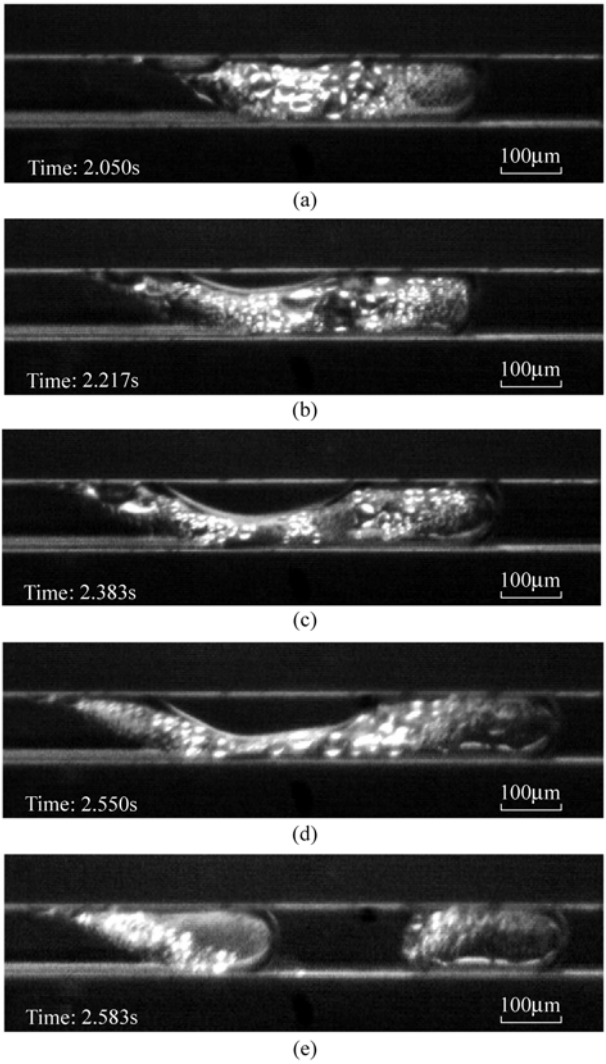

Figure 6.22 Condensing interface oscillation with dropwise condensation ($m = 453.2$ kg/(m^2·s), $q'' = 5.0 \times 10^5$ W/m^2)

Figure 6.23(a) records the location of the condensing interface changing with time, and Fig. 6.23(b) records the evolution of the liquid film thickness, which represents the intensity of the condensation. Figs. 6.23(c) and (e) show the results of time and frequency domain analyses for interface oscillation, respectively, while Figs. 6.23(d) and (f) show those for condensation cycle. The oscillation of the condensing interface behaved much more complicated than the evaporating interface. Its autocorrelation distribution (see Fig. 6.23(c)) reveals strong disturbance of random factors, as well as a sign of multiply periodic superposition. Figure 6.23(e) shows the complex frequency composition of the interface oscillation, which could be categorized into two groups at 0.9 Hz. For the peaks higher than 0.9 Hz, the frequencies are identical with the dominant frequencies (ranging from 0.94 to 1.70 Hz) in Fig. 6.23(f), which is the spectrum distribution

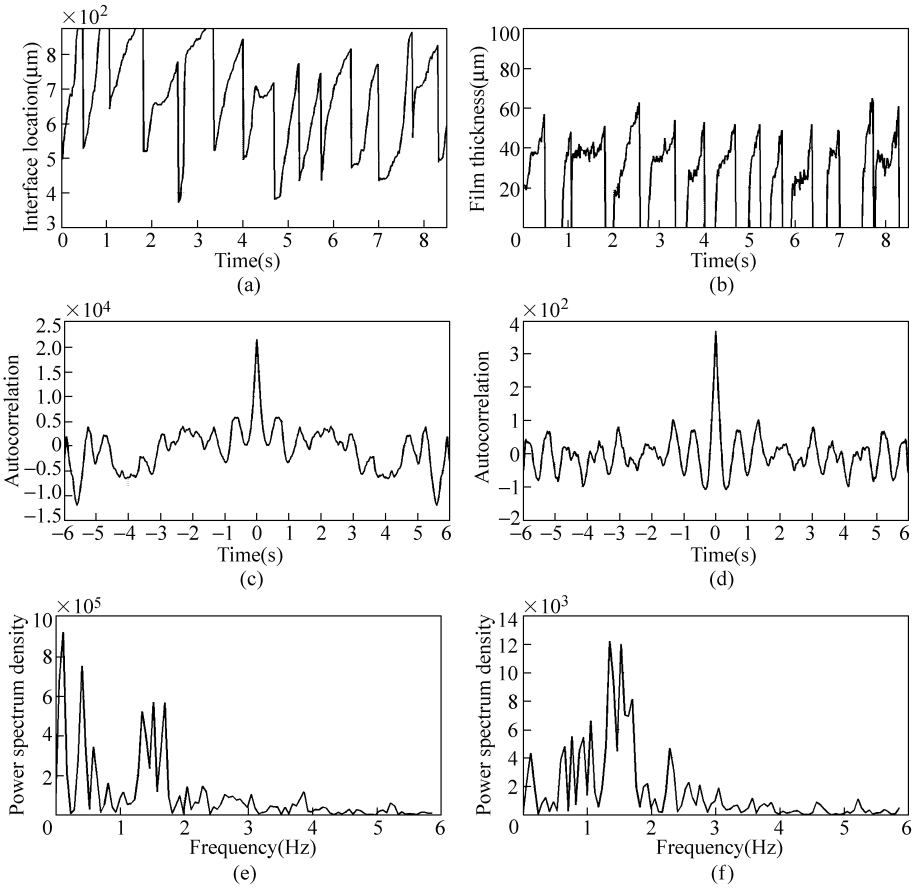

Figure 6.23 Signal analysis of condensing interface oscillation with dropwise condensation ($m = 453.2$ kg/(m^2·s), $q'' = 5.0 \times 10^5$ W/m^2)

of the liquid film thickness signal. These frequencies correspond to the process from dropwise condensation to film formation, and finally bubble breakup, as depicted in Fig. 6.22. Therefore this frequency group represents the intrinsic cycle of condensation. For the peaks lower than 0.9 Hz in Fig. 6.23(e), on the other hands, the low frequency periodic components impact the average interface location, which shows regular fluctuation during a longer time span.

It is worth noting that, both the evaporating cap in Fig. 6.20 and the condensing cap in Fig. 6.22 belonged to the same elongated bubble in an individual channel during one run of the experiment. Limited by the experimental facility, simultaneous visualization on both caps could not be realized. Thus the time zeros were not identical in Figs. 6.20 and 6.22. However, the connection between the two caps can still be discovered from the spectrum analysis results. The main oscillating component was 0.94 Hz for the nucleation-dominated evaporating cap (see Fig. 6.21(e)), which was quite close with the dominant frequency band (0.97 – 1.70 Hz in Fig. 6.23(e)) of condensing interface oscillation. And the low frequency component (0.12 Hz in Figs. 6.23(e) and (f)) of condensing cap also appeared in the nucleation spectrum (see Fig. 6.21(f)). The overlapping frequencies indicated complex internal relations between the oscillating behavior of the up- and downstream caps. The cyclic influence from phase change process (evaporation and condensation) was marked, especially in the higher frequency band. And the periodic components in the lower frequency band should be transported through the vapor flow within the bubble.

When an evaporation process is similar with the situation shown in Fig. 6.16, i.e., intensive thin film evaporation becomes the major mode of evaporation instead of nucleate boiling, then the large-amplitude and high-frequency oscillation of the upstream cap would cause the downstream cap to oscillate at similar amplitude and frequency, as depicted in Fig. 6.24. Since the interface was sweeping quickly with large amplitude, dropwise condensation was hardly formed. Alternatively, the vapor was condensed mostly on the side walls or directly at the phase interface (see Fig. 6.24(a)). High speed and pulsating vapor flow pushed the interface downwards, while the liquid film increment at the side walls formed a bottle neck near the cap of the bubble (see Figs. 6.24(b) and (c)). At the instant when the pulsating vapor flow reversed, the elongated bubble broke into two parts (see Fig. 6.24(d)). The downstream part of the bubble vented out, whereas the upstream part iterated the above cycle (see Fig. 6.24(e)). The signal analysis shows that this periodic process operated at a frequency as high as 4.15 Hz (see Fig. 6.25(c)). At the same time there was a small-amplitude additive component superimposing just at the double frequency of 4.15 Hz. The other major peaks on the spectrum were all located at the multiples of 4.15 Hz, which should be the harmonic components induced by the rectangular sampling wave.

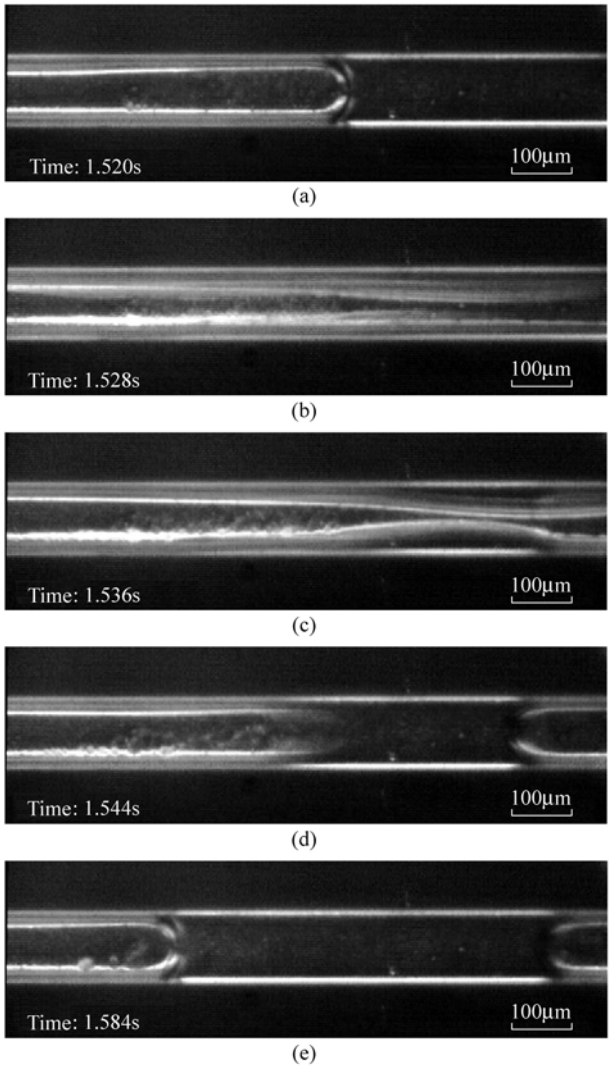

Figure 6.24 Condensing interface oscillation without dropwise condensation ($m = 453.2$ kg/(m^2·s), $q'' = 5.0 \times 10^5$ W/m^2)

A simple comparison shows that, the frequency of a film evaporation/condensation dominant interface oscillation was notably higher than that of a nucleation or dropwise condensation dominant interface oscillation. For an instance, the characteristic frequency in Fig. 6.16 (1.17 Hz, thin film evaporation driven) was approximately 2.5 times of that in Fig. 6.18 (0.47 Hz, nucleation driven), while the characteristic frequency in Fig. 6.24 (4.15 Hz, film condensation driven) was approximately 2.4 times of the upper limit of the dominant frequency band in Fig. 6.22 (0.94 – 1.70 Hz, dropwise condensation driven).

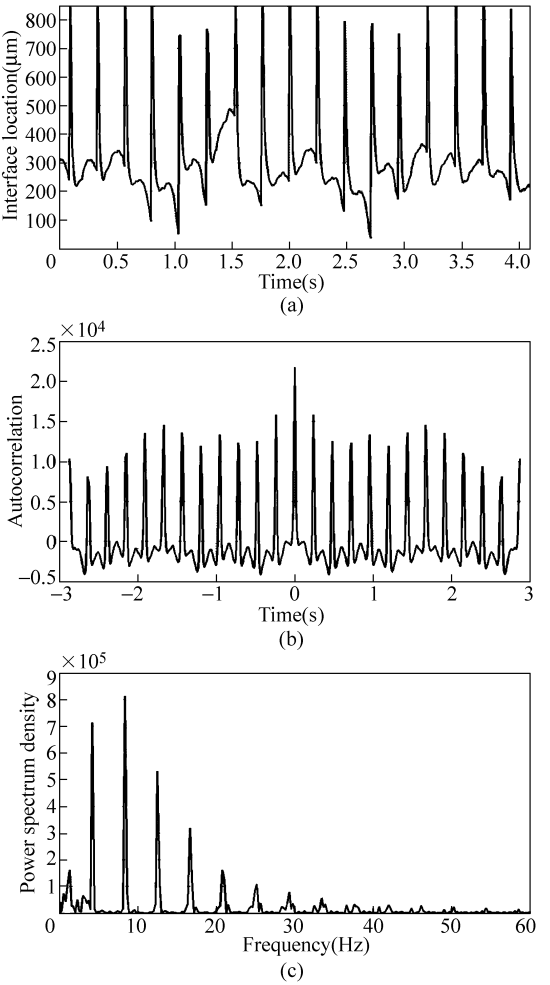

Figure 6.25 Signal analysis of condensing interface oscillation without droplet condensation ($m = 453.2$ kg/(m^2·s), $q'' = 5.0 \times 10^5$ W/m^2)

References

[1] D. B. Tuckermann, R. F. Pease. Ultrahigh thermal conductance microstructures for cooling integrated circuits. Proc. 32nd Electronics Components Conf., 145, 1981.

[2] M. B. Bowers, I. Mudawar. High flux boiling in low flow rate, low pressure drop mini-channel and microchannel heat sinks. Int. J. Heat Mass Transfer, 37: 321 – 332, 1994.

[3] L. Lin, A. P. Pisano. Bubble forming on a micro line heater. Micromechanical Sensors, Actuators, and Systems, ASME DSC, 32: 147 – 164, 1991.

[4] L. Lin, K. S. Udell, A. P. Pisano. Liquid-vapor phase transition and bubble formation in micro structures. Thermal Sci. Engng., 2: 52 – 59, 1994.

[5] W. Qu, I. Mudawar. Transport phenomena in two-phase micro-channel heat sinks. Journal of Electronic Packaging, Transactions of the ASME, 126: 213 – 224, 2004.
[6] H. Y. Wu, P. Cheng. Boiling instability in parallel silicon microchannels at different heat flux. Int. J. Heat Mass Transfer, 47: 3631 – 3641, 2004.
[7] B. Agostini, M. Fabbri, J. E. Park, et al. State of the art of high heat flux cooling technologies. Heat Transfer Engineering, 28: 258 – 281, 2007.
[8] J. Xu, J. Zhou, Y. Gan. Static and dynamic flow instability of a parallel microchannel heat sink at high heat fluxes. Energy Conversion and Management, 46: 313 – 334, 2005.
[9] G. Hetsroni, A. Mosyak, E. Pogrebnyak, et al. Periodic boiling in parallel micro-channels at low vapor quality. International Journal of Multiphase Flow, 32: 1141 – 1159, 2006.
[10] C. Huh, J. Kim, M. H. Kim. Flow pattern transition instability during flow boiling in a single Microchannel. Int. J. Heat Mass Transfer, 50: 1049 – 1060, 2007.
[11] K. H. Chang, C. Pan. Two-phase flow instability for boiling in a microchannel heat sink. Int. J. Heat Mass Transfer, 50: 2078 – 2088, 2007.
[12] S. G. Kandlikar, W. K. Kuan, D. A. Willistein, et al. Stabilization of flow boiling in microchannels using pressure drop elements and fabricated nucleation sites. J. Heat Transfer, 128: 389 – 396, 2006.
[13] A. Kosar, C. J. Kuo, Y. Peles. Suppression of boiling flow oscillations in parallel microchannels by inlet restrictors. J. Heat Transfer, 128: 251 – 260, 2006.
[14] R. Muwanga, I. Hassan, R. MacDonald. Characteristics of flow boiling oscillations in silicon microchannel heat sinks. J. Heat Transfer, 129: 1341 – 1351, 2007.
[15] X. F. Peng, B. X. Wang. Forced-flow convection and flow boiling heat transfer for liquid flowing through microchannels. Int. J. Heat Mass Transfer, 36: 3421 – 3427, 1993.
[16] X. F. Peng, B. X. Wang. Liquid flow and heat transfer in microchannels with/without phase change (Keynote Lecture). Proc. 10th Int. Heat Transfer, 1: 159 – 177, 1994.
[17] X. F. Peng, B. X. Wang. Evaporation space and fictitious boiling for internal evaporation of liquid. Science Foundation in China, 2: 55 – 59, 1994.
[18] X. F. Peng, G. P. Peterson. Flow boiling of binary mixtures in microchanneled plates. Int. J. Heat Mass Transfer, 39: 1257 – 1264, 1996.
[19] X. F. Peng, B. X. Wang. Forced-convection and boiling characteristics in microchannels (Keynote Lecture). Proc. 11th Int. Heat Transfer, 1: 371 – 390, 1998.
[20] X. F. Peng, H. Y. Hu, B. X. Wang. Boiling nucleation during liquid flowing in microchannels. Int. J. Heat Mass Transfer, 41: 101 – 106, 1998.
[21] X. F. Peng, H. Y. Hu, B. X. Wang. Flow boiling through V-shape microchannels. Experimental Heat Transfer, 11: 87 – 100, 1998.
[22] H. Y. Hu, G. P. Peterson, X. F. Peng, et al. Interface fluctuation propagation and superposition model for boiling nucleation. Int. J. Heat Mass Transfer, 41: 3483 – 3490, 1998.
[23] X. F. Peng, B. X. Wang. Nucleation and thermodynamic nonequilibrium for boiling in microchannels and microstructures. In: Annual Review of Heat Transfer (Tien C L, eds.). New York: Begell House Inc., 11: 307 – 350, 2000.
[24] X. F. Peng, D. Liu, D. J. Lee, et al. Cluster dynamics and fictitious boiling in microchannels. Int. J. Heat Mass Transfer, 43(23): 4259 – 4265, 2000.

[25] X. F. Peng, D. Liu, D. J. Lee. Dynamic characteristics of microscale boiling. Heat and Mass Transfer, 37(1): 81 – 86, 2001.

[26] X. F. Peng, Y. Tien, D. J. Lee. Nucleation in microchannels: statistical mechanics approach. International Journal of Heat and Mass Transfer, 44(15): 2957 – 2964, 2001.

[27] X. F. Peng, Y. Tien, D. J. Lee. Arguments on microscale boiling dynamics. Microscale Thermophysical Engineering, 6(1): 75 – 83, 2002.

[28] J. T. Liu, X. F. Peng. Interface oscillation of subcooled flow boiling in locally heated microchannels. Heat and Mass Transfer, 45: 459 – 469, 2009.

[29] V. P. Carey. Liquid-Vapor Phase-Change Phenomena: an Introduction to the Thermophysics of Vaporization and Condensation Processes in Heat Transfer Equipment. New York: Hemisphere Pub. Corp., 1992.

[30] H. Y. Kwak, Y. W. Kim. Homogeneous nucleation and macroscopic growth of gas bubble in organic solutions. Int. J. Heat Mass Transfer, 41: 757 – 767, 1998.

[31] J. H. Lienhard, Kanimi. Homogeneous nucleation and the spinodal line. ASME J. Heat Transfer, 103: 61 – 64, 1981.

[32] V. P. Skripov. Metastable Liquids. New York: John Wiley & Sons Press, 1974.

[33] J. F. Lu, X. F. Peng. Dynamical evolution of heterogeneous nucleation on surfaces with ideal cavities. Heat and Mass Transfer, 43: 659 – 667, 2007.

[34] R. K. Shah, A. L. London. Laminar flow forced convection in ducts: a source book for compact heat exchanger analytical data. New York: Academic Press, 1978.

7 Boiling in Droplets

Abstract An experimental investigation was conducted to describe the oscillation behavior of water droplets on solid surfaces as air flew through over the droplets, and the dynamical process was recorded by using a high-speed CCD. Two liquid drop oscillation modes, forward-backward and upward-downward, and their mutual conversion were visually observed. A numerical simulation was also conducted to investigate the inner flow in an oscillating liquid droplet. A 2D model was proposed to describe the interfacial movements and the flow in oscillating droplets with shear stress induced by outside air flow. The 2D inner flow field was reconstructed to explore the liquid flow velocity and pressure profile and better understand the oscillating mechanisms.

An experimental investigation was conducted to visually observe the dynamical characteristics of water droplets with evaporation and nucleation on stainless steel and polished silicon surfaces. The water droplet diameter, contacting area and spreading speed were measured at the surface temperature ranging from 110℃ to 190℃. The spreading of water droplets during evaporation and nucleate boiling had a close relationship with the dynamic bubble behavior in the droplet as well as the surface properties. A model was proposed to describe the dynamical behavior of droplet spreading. Particularly, bubble volume, bubble interaction, surface temperature and surface properties had very strong influence on droplet spreading. Water droplets were easiest to spread at the surface temperature of 130℃, and the spreading tendency increased with increasing surface roughness. Using a high-speed video imaging system, the dynamical process of the evaporation and boiling behavior of a droplet was recorded. Infrared ray temperature measurement technique was employed to investigate the instantaneous characteristics of heat transfer as the droplet was boiled. In the transition boiling regime, the phase change behavior of a droplet displayed a cyclical process. Restricted cyclical, sole-bubble cyclical and metastable cyclical styles were observed as the surface temperature increased.

Keywords liquid droplet, oscillation, spreading, restricted cyclical, single-bubble cyclical, metastable cyclical

Droplet boiling is of interest in various practical applications due to the high heat transfer coefficient and heat flux at a lower superheat. Droplet boiling is widely

X. Peng, *Micro Transport Phenomena During Boiling*

employed in many high technology applications, such as thermal control and management of space shuttles, nuclear reactor safety, fire suppression, cooling of turbine blades. In particular, it plays an important role in the liquid-fuel engine and the combustion technology. Recently, with rapid development of MEMS and microelectronic technology the thermal loads imposed on or generating from electronic devices and chips increasingly become large and exceed the cooling capabilities of the traditional single-phase forced convection. An urgent need for developing the new cooling technologies has strongly motivated the study on the evaporation of droplets.

Most available investigations on the transition boiling of a droplet focused on macroscopical heat transfer mechanism and evaporation rate [1 – 3]. The attention was addressed on the effect of initial wetted diameter, solid temperature, solid conductivity, etc. on the lifetime of a droplet evaporation and heat transfer rates. Few studies have stressed the dynamical phase change behavior of bubbles for this boiling regime.

7.1 Oscillation of Sessile Droplets

The dynamical behavior of liquid droplets on solid surfaces is of critical importance for theoretically understanding the interfacial transport phenomena and many practical applications, such as spray cooling, spray print, and fire suppression. Many investigators conducted a lot of comprehensive investigations on the oscillation of various droplets. Here, the droplet boiling characteristics are discussed to understand the fundamental mechanisms [4].

7.1.1 Experimental Observations

Figure 7.1 schematically illustrates the experimental setup, mainly including a wind tunnel, test section, droplet generator and imaging system. Droplets were generated using a scaled sprinkle injector and placed on the solid surface. The initial droplet volume was changed from 2 μL to 6 μL in the present experiments, corresponding droplet radius varying from 0.78 mm to 1.12 mm. Cu chips were employed as test solid surfaces and polished by five different sandpapers (320 to 1200 grid) to make different chips having different surface roughness. A bracket was fixed in the tunnel to hold the test surface.

The typical experimental phenomenon of forward-backward oscillation is illustrated in Fig. 7.2 for a water droplet on a Cu surface induced initially at an air flow 8.5 m/s. The oscillation was a result of the coupled action of the air flow, solid surface roughness, surface tension, and liquid properties. The droplet stayed stably on the surface without air flow, while the viscous effect drove the droplet to oscillate when the air flew through over the droplet. The shear force caused the

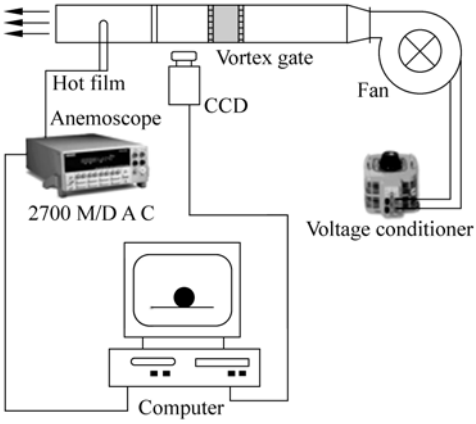

Figure 7.1 Experimental system

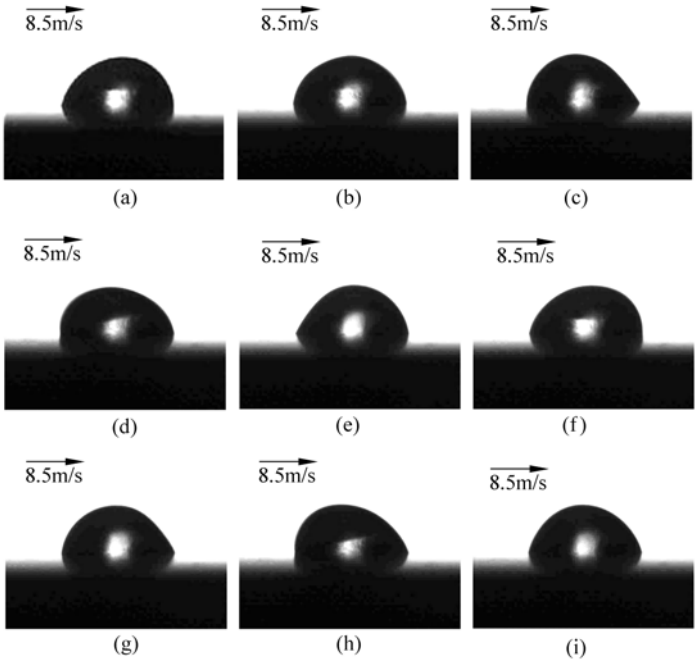

Figure 7.2 Forward-backward oscillations (2 μL droplet, surface polished with 320 grid sandpaper)
(a) 0 ms; (b) 2 ms; (c) 4 ms; (d) 6 ms; (e) 8 ms; (f) 10 ms; (g) 12 ms; (h) 14 ms; (i) 16 ms

inner flow and the droplet began to deform backward and both the kinetic and potential energy began to increase. There existed a critical position or dynamic equilibrium position at which the kinetic energy reached its maximum and the force was balanced. The kinetic energy decreased when the droplet continued to deform backward, and the potential energy continued to increase. Then the kinetic

energy was equal to zero and potential energy reached its maximum at a critical position or positive limitation, as shown in Fig. 7.2(f). The droplet began to deform inversely. The potential decreased and kinetic energy increased. There also existed a dynamic equilibrium position where the kinetic energy reached its maximum. Because of the inertia, the droplet continued to deform forward, accordingly decreasing the kinetic energy and increasing the potential. At the critical position or reverse limitation, as shown in Fig. 7.2(h), the deformation stopped and potential reached its maximum while kinetic energy was equal to zero. And the droplet began the next oscillation period.

The upward-downward model observed during the experiments is shown in Fig. 7.3. The air flow caused inner flow and induced the forward-backward oscillation first, and then might enforced the droplet to deform downward during the former mode process. When the droplet began to deform downward, both the kinetic energy and potential began to increase. There existed a critical position or dynamic equilibrium position at which the kinetic energy reached its maximum and the force was balanced. The kinetic energy decreased when the droplet continued to deform downward, and the potential continued to increase. As the kinetic energy was equal to zero and potential energy reached its maximum at the positive limitation, as illustrated in Fig. 7.3(b). The droplet began to deform inversely. The potential decreased and the kinetic energy increased. There also existed a dynamic equilibrium position where the kinetic energy reached its maximum. Because of the inertia, the droplet continued to deform upward, accordingly decreasing the kinetic energy and increasing the potential. At the critical position or reverse limitation, as shown in Fig. 7.3(c), the deformation stopped and potential energy reached its maximum while kinetic energy was equal to zero. And the droplet began the next oscillation period.

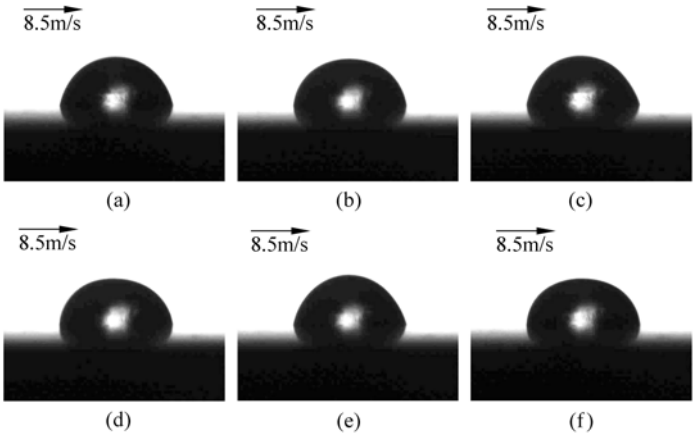

Figure 7.3 Upward-downward oscillations (2 μL droplet, surface polished by 320 grid sandpaper)
(a) 0 ms; (b) 2 ms; (c) 4 ms; (d) 6 ms; (e) 8 ms; (f) 10 ms

These two oscillatory models were observed to transition from one to the other for some conditions. The transition from forward-backward to upward-downward always happened when oscillating from back to front, while that from upward-downward to forward-backward happened when oscillating from bottom to top.

7.1.2 Oscillatory Behavior

The effect of air velocity and droplet size on the oscillations was investigated for different copper surfaces, and oscillatory period was obtained from the recorded images. In general, the period of forward-backward mode was twice of that of upward- downward. Here only the forward-backward mode is discussed.

Figure 7.4 presents the period for different cases. Very clearly, as air speed reached some values, the oscillatory period would be increased accordingly, and only small period change occurred. The transition air speeds were not the same for all cases. There must be a threshold value for the period varying with the air speed. Larger droplet size produced longer period, and the surface tension is expected to play an important role for this phenomenon. The surface tension would make the droplet to maintain its balance shape, and the larger size droplet with less effect of the surface tension has the larger transmutation which needs more time to recover. Further investigations are necessary to understand the mechanisms and to recognize the regularity of the period change.

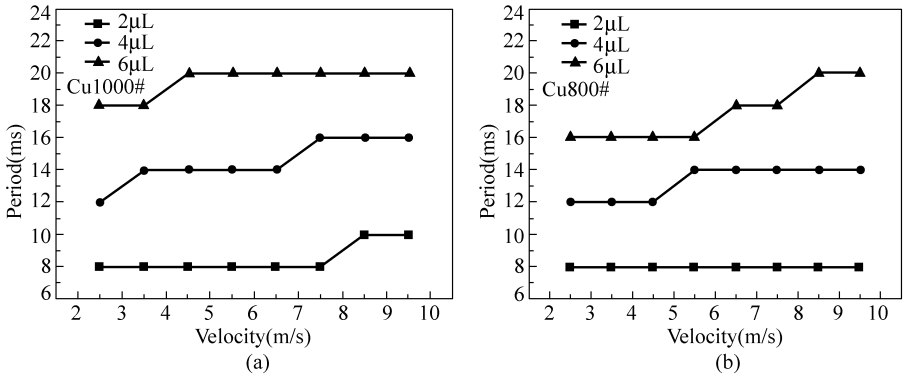

Figure 7.4 Oscillatory period on a copper surface
(a) Polished by 1000 grid sandpaper; (b) Polished by 800 grid sandpaper

Figures 7.5 and 7.6 show the droplet oscillatory periods for different rough copper surfaces. Horizontal ordinate 1 to 5 represent the surfaces polished by 1200 grid, 1000 grid, 800 grid, 600 grid and 200 grid sandpaper, respectively, and accordingly the surface roughness increases from 1 to 5. Surface roughness did not alter the period of 2 μL droplet when the air speed was lower than 8 m/s. When the air speed was higher than 8 m/s, the period increased to 10 ms only for

surface 2. Figure 7.6 illustrates the relationship between period and surface roughness for 4 μL droplet. The oscillatory periods remained 12 ms for all surfaces at the speed of 2.5 m/s with that for surface 2 increased to 14 ms at 3.5 m/s while other surfaces remained 10 ms. When the speed increased to 4.5 m/s, periods for both surface 1 and 2 were 14 ms and other surfaces still 12 ms. For the speed at 5.5 to 6.5 m/s, the period of surfaces 4 was 16 ms and all the others were 14 ms. The change became more significant when the speed was higher than 6.5 m/s, as shown in Fig. 7.6(b). The effect of surface tension was observed to become less important for larger droplets, and the roughness plays a more important role. Generally, the roughness would impede the transmutation, and the period would be longer. However, when the roughness was large enough compared with the contact scale, it could not affect the period any more, and the period decreased after the roughness reached a critical value, which was consistent with the experimental results.

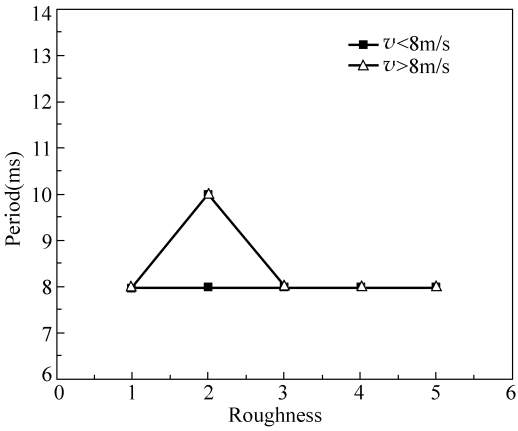

Figure 7.5 Period varies with the roughness for the 2 μL droplet

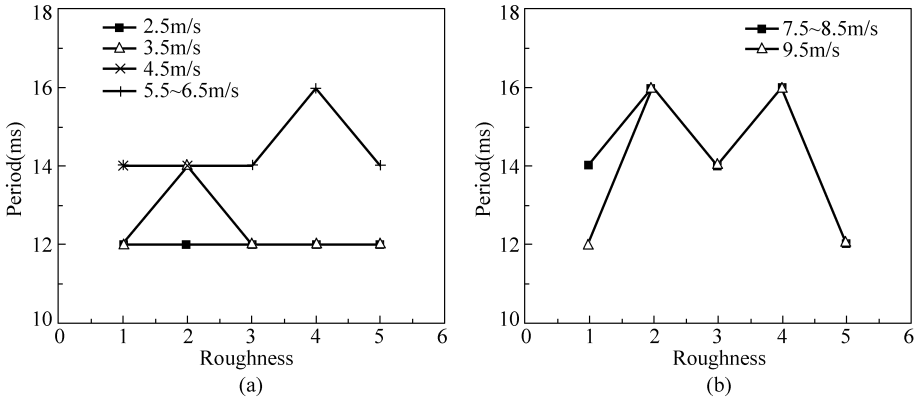

Figure 7.6 Effect of roughness on period for a 4 μL droplet
(a) Air speeds lower than 6.5 m/s; (b) Air speeds higher than 6.5 m/s

A droplet could be modeled as a control volume with vapor-liquid and solid-liquid interfaces. The shear force produced by the air flow drove the inner fluid to flow circularly. Though the oscillation was not apparent at very low speeds, it did exist and the phenomena observed in present investigation might arouse the recognition to the heat transfer mechanisms associated with droplet dynamics.

7.1.3 Physical Understanding

Figure 7.7 schematically illustrates the inner flow in a process of forward-backward oscillation. The air pressure makes the droplet to deform and increase the potential energy. As shown in Fig. 7.7(a), driven by the air flows along the front-side because of the shear, the inner liquid flows along the path 1 near the gas-liquid interface, and the back-side liquid begins to flow to front for maintaining the droplet. However, the front-side liquid flows faster than the back-side liquid since the drive force of the back-side is smaller. The liquid accumulates at the back-side and expands the back-side interface and draws the front-side interface, accordingly increasing the potential. The expansion could not infinitely increase because of the interfacial tension. When the potential reaches the critical value, back-side interface shrinks forward and the front-side interfaces begins to expand. The back-side liquid flows inversely because of the back-side elastic force, but the front-side liquid still maintains the flowing direction. Thus, two circular flows appear inside the droplet, as shown in Fig. 7.7(b). Flows 1 and 3 provide the main driving forces and make the liquid accumulating at the droplet top and increasing the potential there. When the potential is large enough to overcome the shear flow, the front-side liquid is driven to flow inversely, as shown in Fig. 7.7(c). Therefore, one circle is left inside the droplet. The liquid then accumulates at the front-side and expands the front-side interface and draws the back-side interface, as dispieted in Fig. 7.7(d). The potential begins to increase and makes the front- side flow inversely when it reaches a critical value, accordingly compelling the front-side interface to shrink backward. The back-side maintains the flowing direction due to the inertial, and two circles reappear in the droplet, as shown in Fig. 7.7(e). The front-side liquid flows along the path 1 near the interface to form a circle with path 2, while the back-side liquid flows along path 3 to form another circle with path 4. Both path 2 and 4 are from up to down, the same as shown in Fig. 7.7(b). Flows 1 and 3 provide the main driving forces and make the liquid accumulating at the droplet top, and the potential increases at the top. When the potential is able to overcome the inertial flow, the back-side liquid is driven to flow inversely, as shown in Fig. 7.7(f). Therefore, one circle is left inside the droplet. The flowing behaviour comes to (a) again and drives the next oscillation.

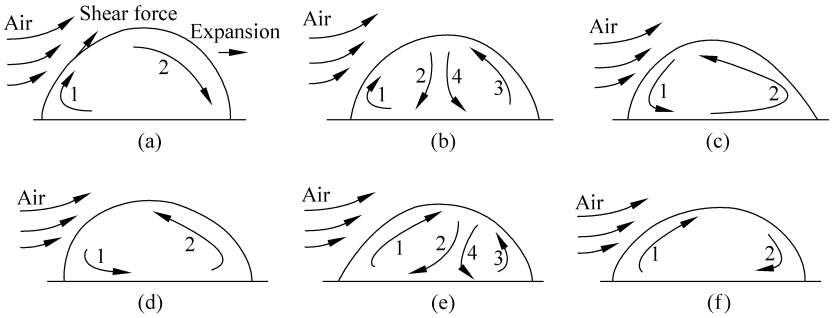

Figure 7.7 Forward-backward oscillation

Figure 7.8 schematically illustrates the inner flow in the process of upward-downward oscillation. The air pressure makes the droplet to deform and increases the potential energy. As shown in Fig. 7.8(a), the top liquid flows to the bottom along path 3 and the liquid of both the front-side and back-side flows to the top near the gas-liquid interface along paths 1 and 2, respectively. During this process, the middle flow provides the main driving force and causes the middle liquid to flow more quickly than the two sides, making the liquid accumulating at the bottom and expanding the two side interfaces outward, accordingly increasing the potential. The expansion could not infinitely increase because of the interfacial tension. When the potential reaches the critical value, the two side interfaces begin to shrink inward and the top interface begins to expand. The two side flows supply the main driving force and make the liquid at two sides flowing faster than in the middle, as shown Fig. 7.8(b). The liquid begins to accumulate and expands the top interface, accordingly increasing the potential at the top. When the potential reaches its critical value, the middle flow becomes the main driving flow and makes the liquid accumulating at the two sides. Therefore, the flowing behavior comes to that shown in Fig. 7.8(a) again and next oscillation begins.

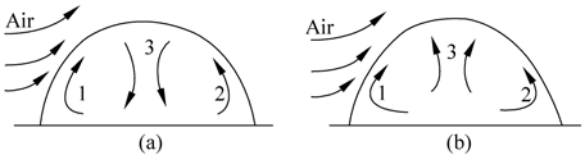

Figure 7.8 Upward-downward oscillation

There are two ways to transit from forward-backward mode to upward-downward mode, as shown in Figs. 7.7(b) and (e), respectively. The flow direction along path 1 along the frontside must be changed inversely to maintain the forward-backward oscillation as shown in Fig. 7.7(b). However, it is difficult to change the flow direction of path 1 because of its accordance with the shear force direction. If the accumulation at the top is not enough to overcome the shear flow

induced by the air shear, two circular flows will maintain and make the middle flow along paths 2 and 4 inside the droplet, thus inducing the upward-backward oscillation. And in Fig. 7.7(e), the flow direction along path 3 at the back-side must be changed inversely to maintain the forward-backward mode. It is easy to change the flow direction of path 3 because of the main force from the air shear flow along the front. Thus transition would not occur in this situation generally. So, the transition always occurs in the process of deforming from the back-side to front- side, accordingly in the process shown in Figs. 7.7(a) to (c), which is accordant with the experimental observation. And the transition process would be from Figs. 7.7(b) to 7.8(a).

Figure 7.8(a) illustrates the transportation of liquid from the top to the bottom. The middle flow along path 3 is the main flow while the shear flow increases the speed, and the circle is difficult to change. However, the side flows along paths 1 and 3 become the main flow as shown in Fig. 7.8(b). The flow 1 would be increased and drives the circle change to that shown in Fig. 7.8(a) and then to that shown in Fig. 7.9(b). Thus the transition occurs in the process of the liquid transportation from the bottom to the top, which is also accordant with the experimental observation.

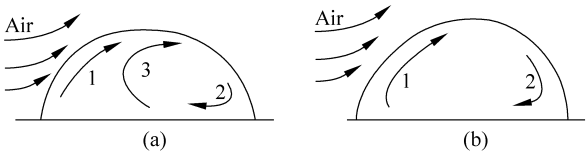

Figure 7.9 Transitions between two oscillation modes

In above discussions, the inner flow and its performance could be adopted to illustrate the oscillation maintainability and the transition. Also, the inner flow mode might be able to illustrate the relationship between period and the droplet size and surface roughness.

The inner flow and the oscillation are caused by the outer air flow. At a specified air speed, the surface tension plays a more important role as the droplet size is small, and the amplitude is small, accordingly the flow distance is short and need very short time to complete a circle. So the period is short. When increasing the droplet size, correspondingly the amplitude increases because of the decrease of the surface tension force, thus the flow distance will be longer and need more time to complete a circle, accordingly increasing the period.

Surface roughness affects the flow behaviour at the bottom of the droplet. When roughness increases, the resistant force on the surface increases and decreases the flow speed. When other conditions maintain unvaried, the low fluid speed will increase the time to complete a circle inside the droplet, and consequently the period increases. However, there is a critical value that the effect on fluid speed will decrease if the roughness exceeds it. Because of the roughness scale,

compared to the droplet contact characters with surface, is too large to affect the flowing liquid. So the period increases first and then decreases when the surface roughness increases.

7.2 Model of Droplet Oscillation

7.2.1 Physical Model

Although an actual oscillation occurs inside a three dimensional droplet (see Fig. 7.10(a)), two-dimensional model was constructed initially by using Fluent 6.0, since the main oscillation was irritated along the air flow. As shown in Fig. 7.10(b), air flow region is a rectangle with dimension of 20 mm by 20 mm. Inlet, outlet, symmetry and wall are specified. Cartesian coordinate was established on the wall where the droplet was located, as shown in Figs. 7.10(c) and (d). The boundary conditions and parameters were set and illustrated in Tables 7.1 and 7.2. To realize the oscillation, two different wall conditions were set upon whether the wall contacts with liquid or not. The region wetted by liquid (water) was wall 1 with contact angle of 10° while the region exposed to air directly was wall 2 with contact angle of 170°. In this case, the droplet does not spread out and contact line does not move. Temperature change was negligible during the oscillation. The laminar flow was used to describe the two-phase flow.

Volume-of-Fluid (VOF) was adopted for this two-phase flow simulation. The main phase was air while a droplet was patched out of the air region with wall 1 as shown in Fig. 7.10(b). The contact interface of a droplet reached the solid surface. In this two-phase model, air was the continual phase while liquid was the discrete phase specified by subscripts 1 and 2, respectively.

As mentioned above, the actual physical model was of three dimensions, as shown in Fig. 7.10(a). Flow in the z-plane was neglected in two-dimensional model to emphasize the flow in x-plane. This is acceptable to some extension to obtain the main flow behavior and interfacial characteristics.

7.2.2 Flow Characteristics

1. Inside Droplet

Velocity vector and pressure profile inside a droplet are schematically shown in Figs. 7.11 and 7.12, respectively. Two eddy patterns exist and move inside the droplet during the oscillation. The left eddy is clockwise, while the right one is counterclockwise driving liquid flow downward along the symmetrical axis of

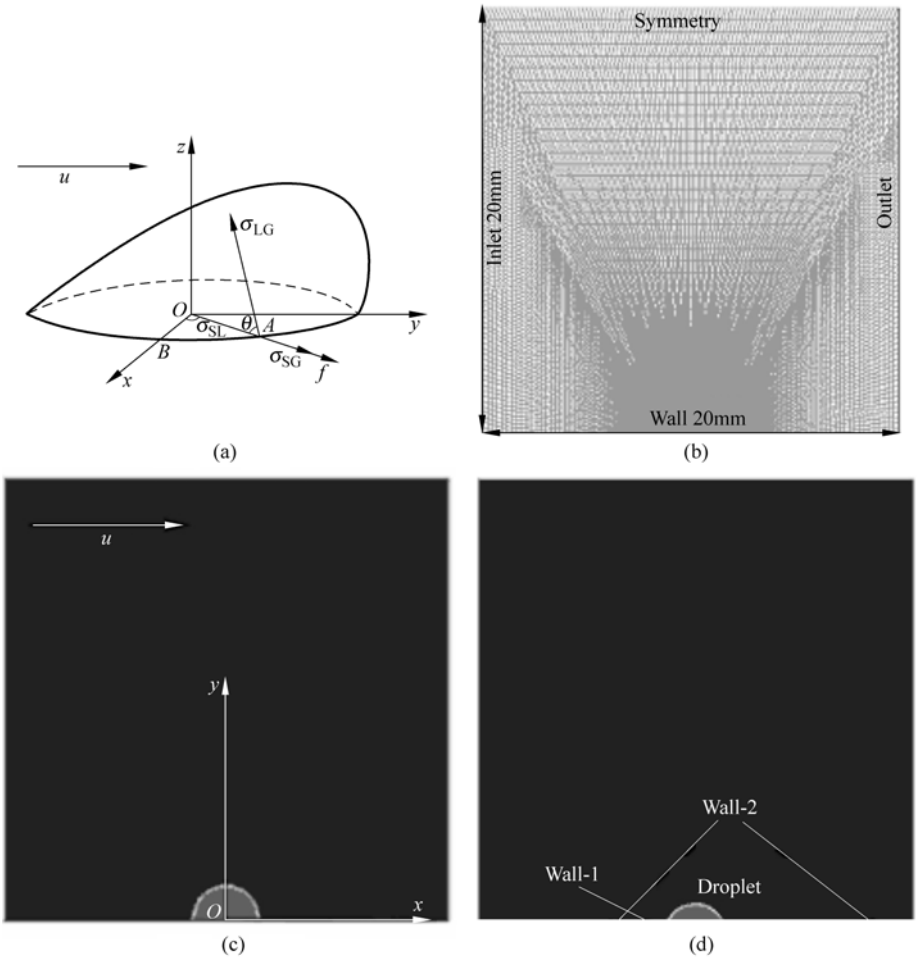

Figure 7.10 Analytical model
(a) 3-D model; (b) 2-D mesh; (c) Coordinate system; (d) Droplet patch

Table 7.1 Boundary Conditions

Inlet	Outlet	Symmetry	Wall 1	Wall 2
Velocity inlet	Pressure outlet	Symmetrical interface	Solid wall	Solid wall

Table 7.2 Simulation Parameters

Contact surface radius r (mm)	Air velocity u(m/s)	Surface tension σ(N/m)	Initial contact angle θ(°)
1.5	5	0.073	90

the two eddies. At the right limitation position, as shown in Fig. 7.11(a), the right eddy occupies a smaller region than the left one. When the droplet transited to the left limitation position, as shown in Fig. 7.11(c), the right eddy occupies a larger region than the left one. When the droplet reverses to the right limitation position, as shown in Fig. 7.11(e), the right eddy becomes smaller again. Figure 7.12 indicates that the pressure profile inside the droplet almost maintains. The core region of the eddy is the local low pressure region, while the stagnation region (the middle region of the bottom layer, edge and top region) is local high pressure region. During the oscillation, low pressure region of the right eddy is enlarged at first and then decreased when the droplet transited from the right limitation position shown in Fig. 7.12(a) to the left limitation position shown in Fig. 7.12(c), and to the right limitation position again shown in Fig. 7.12(e).

Velocity and pressure profiles are presented in Fig. 7.13 for the $y = 0.75$ mm plane which is located at the half height of the droplet. As shown in Fig. 7.13(a), the peaks at $x = \pm 0.5$ mm indicate the core locations of eddies on the cross-section. The peaks move to the negative x direction and then to the positive direction. Generally, the average velocity at the right side is larger than that of the left side. The same tendency is also presented in Fig. 7.13(b) except that the left pressure is larger than the right side.

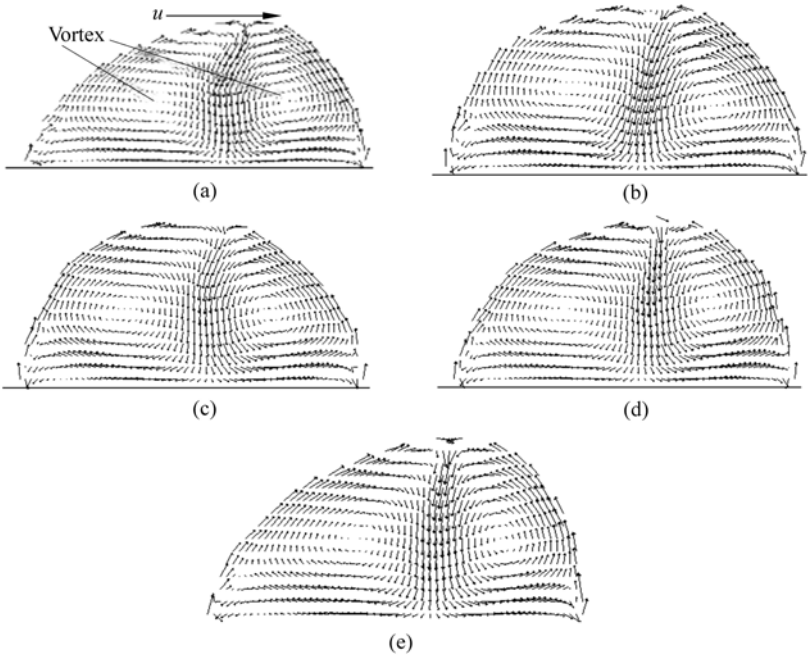

Figure 7.11 Inner flow
(a) 66 ms; (b) 71 ms; (c) 76 ms; (d) 80 ms; (e) 84 ms

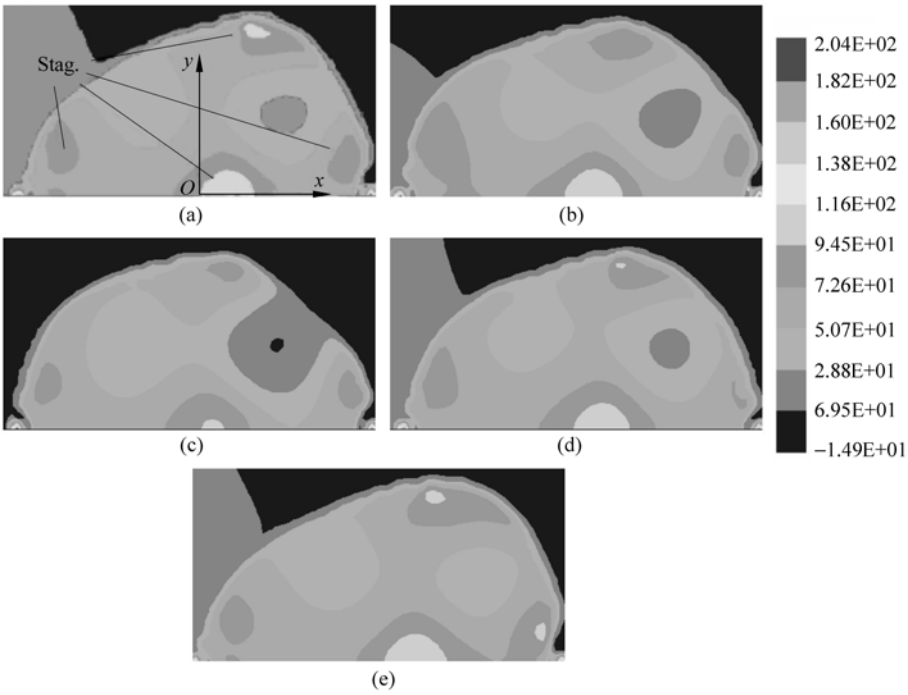

Figure 7.12 Inner pressure profile
(a) 66 ms; (b) 71 ms; (c) 76 ms; (d) 80 ms; (e) 84 ms

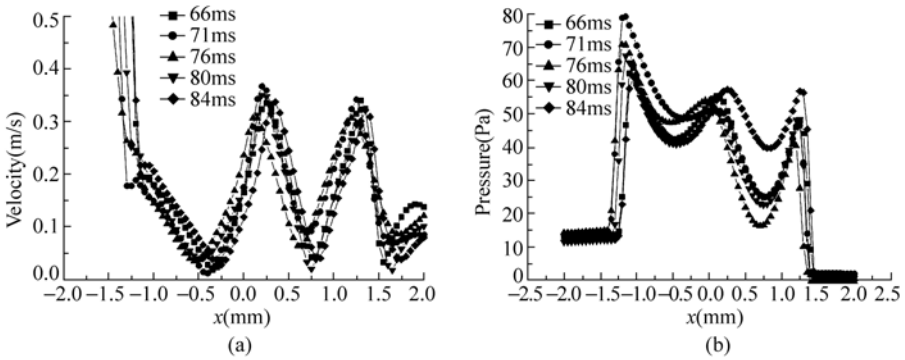

Figure 7.13 Velocity and Pressure at $y = 0.75$mm plane
(a) Velocity; (b) Pressure

2. Outside Droplet

Figure 7.14 presents the streamline inside and outside the droplet. The upstream flow pattern is not same, however the downstream flow pattern is affected by the droplet oscillation. During the oscillation, vortex is introduced from the droplet. This vortex develops on the downstream and finally detaches from the droplet.

Vortex appears, grows, and detaches right within one oscillating period, which indicates a close relation between oscillation and vortex characteristics.

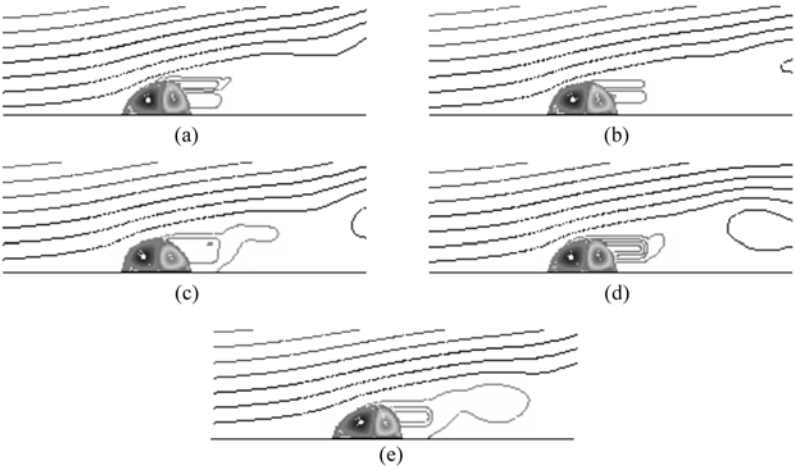

Figure 7.14 Streamline
(a) 66 ms; (b) 71 ms; (c) 76 ms; (d) 80 ms; (e) 84 ms

7.3 Transitional Boiling Behavior

7.3.1 Experimental Description

The experiments [5] were performed using the apparatus shown in Fig. 7.15, consisting of test section, temperature acquisition system, and video acquisition system. The test section included a horizontal platform, a heating assembly, a metal plate, and a glass enclosure. The stainless steel surfaces of 50 mm × 50 mm × 5 mm were maintained at constant temperatures ranging from 120℃ to 160℃, heated by a copper heater. Both a relay and a digital thermostat were used to control power supply making the surface temperature within ±0.25℃ prior to droplet deposition. The sides of the plate and heater were insulated, and a glass enclosure was employed to diminish the heat loss induced by natural convection. During the tests, the surface was maintained at a uniform temperature within the deviation of ±1% in a center area of 20 mm^2. Several T-type thermocouples of 0.3 mm in diameter were used to measure the surface temperatures, and a HP acquisition system was used to record temperature measurements. Infrared ray temperature measuring technique was employed to capture the temperature of solid surface and the free surface of the droplet. A Leica CLS fiber-optic system with a concentric ring lamp was used to illuminate the droplet, providing a uniform

background light. The light filter was used for decreasing the heating effect on the droplet. The deionized water was selected as working liquid.

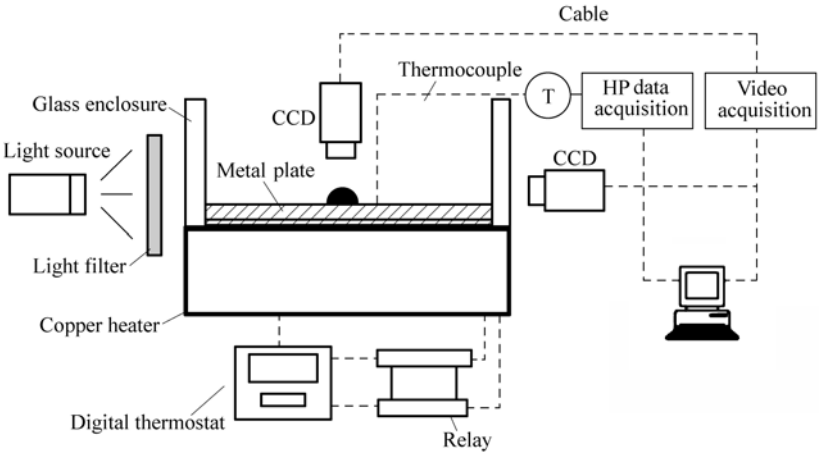

Figure 7.15 Experimental system

The video acquisition system included a high speed CCD camera and a Matrox Pulsar high-speed video imaging card with maximum rate of 16000 frames per second, zoom lens, and tripod. A Basler 504Ak CCD camera with zoom lens was used to continuously capture images of an evaporating droplet displayed on the computer using a matching software program. The magnification was 20 – 50 times, depending on the type of lens used.

The experiments were performed at atmospheric pressure and a room temperature of 25℃. When the plate was heated and reached a specified temperature, a 10 μL water droplet was gently deposited on the heated plate from a micro-syringe placed about 20 mm above the plate. The images were recorded from the time the droplet was generated on the end of the micro-syringe needle until it was completely evaporated. The experiments were repeated at least five times at a specified plate temperature. The heated plates would be cleaned with ethanol and acetone before the droplet was deposited every time, preventing the surface from oxidation while being heated.

The phase change behaviors of a transition boiling droplet turn out to be cyclical because of the intermittent contacts of liquid and vapor on the superheated surface within the droplet. When a subcooled droplet was dropped on the heated solid surface, it would experience a process of preheating. Nucleate boiling was observed at the bottom of the droplet. The diameters and the life time of the bubbles would decrease during the preheating period, with the surface temperature increasing. These characteristics were shown in Fig. 7.16 and Fig. 7.17.

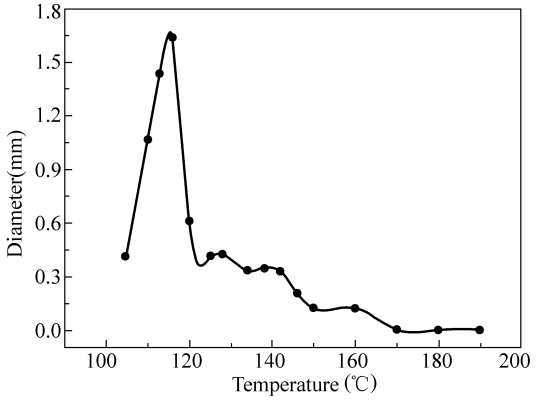

Figure 7.16 Bubble diameter during the initial boiling stage

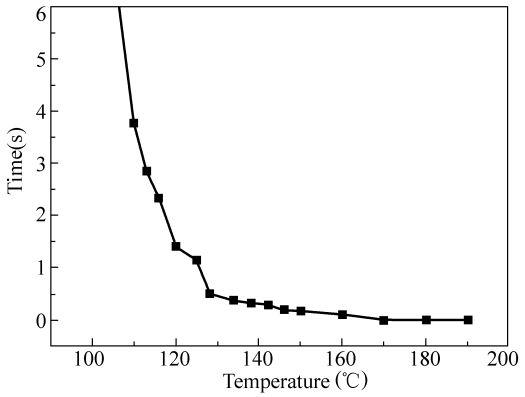

Figure 7.17 Duration of nucleate boiling during the initial boiling stage

7.3.2 Restricted Cyclical Phase Change

For a deionized water droplet on a stainless steel (SS) surface at 125℃, the restricted period behavior is shown in Fig. 7.18. Just as the droplet was placed on the surface, ultrafine bubbles immediately generated on the bottom surface. The bubbles would suddenly grow up and coalesce into several larger bubbles which would shrink to a certain size after expanding to a maximum value. Since the free surface of the droplet was subcooled, the dynamical bubble behavior was confined within the droplet. The repeated expansion-shrink of bubbles leaded to the cyclical phase change behavior of the droplet. Apparently, the upper liquid of the droplet still is subcooled, and when the bubble expanded to the maximum size, its top could enter the subcooled liquid region and the condensation would take place at the top of the bubble, resulting in the shrink of the bubble. Meanwhile, the response time of expansion or shrink of a bubble is much shorter than those of interfacial

temperatures of bubbles. Once the bubble shrunk to its minimum size, the evaporation rates at the bottom of the bubble should exceed the condensation rates at the top of the bubble, so that the bubble expanded again. The diameter evolution of a bubble marked in Fig. 7.18 was shown in Fig. 7.19. Very clearly, the cyclical phase change behavior was demonstrated by the sinusoid-liked diameter variation of bubbles within the droplet.

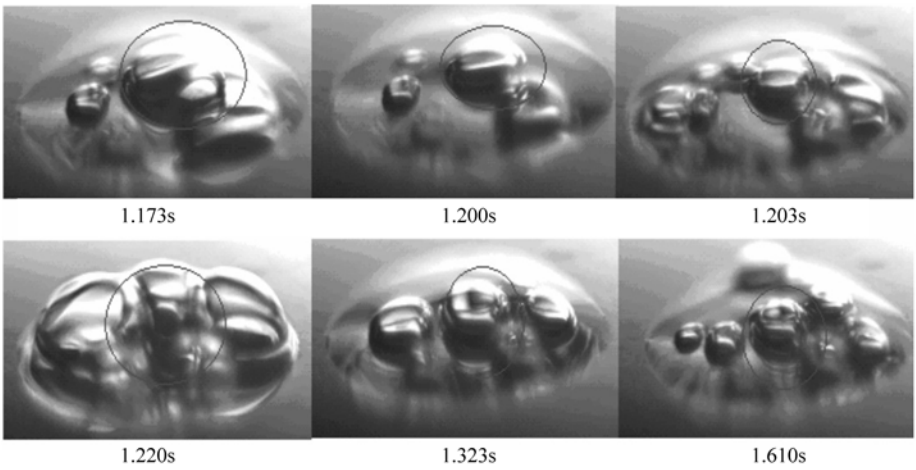

Figure 7.18 Restricted cyclical behavior

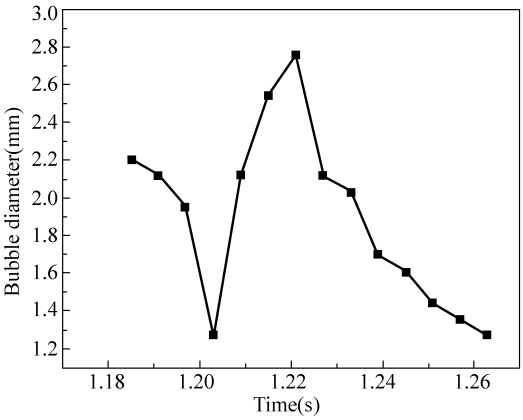

Figure 7.19 Diameter evolution for the bubble marked in Fig. 7.18

7.3.3 Single-Bubble Cyclical Phase Change

The phase change is shown in Fig. 7.20 for a deionized water droplet on a SS surface at 135℃. As surface temperature increased, the ultrafine bubbles would

shrink and coalesce into a large bubble immediately, instead of growing up and coalescing into several larger bubbles. Consequently, the evaporation of the droplet evolved into a cyclical process, with a big bubble repetitive activity of grow-collapse. Initially, ultrafine bubbles assembled into a large bubble which occupied about 90% of the droplet volume, extruding and changing the shape of the interface. And then, the big bubble broke. The space occupied by the bubble would be filled with the liquid around the contact line. After the collapsing of the bubble, the droplet would become very unstable. One more big bubble would grow upward immediately, and then broke again. The process repeated several times. It was so fast and violent that a jet flow was observed. At the last stage, the big bubble would shrink to a certain size after expanding to a maximum value, instead of breaking. As the bubble shrink to a minimum size, it would collapsed immediately. And this expansion shrink collapsing also repeated several times until the droplet dry out.

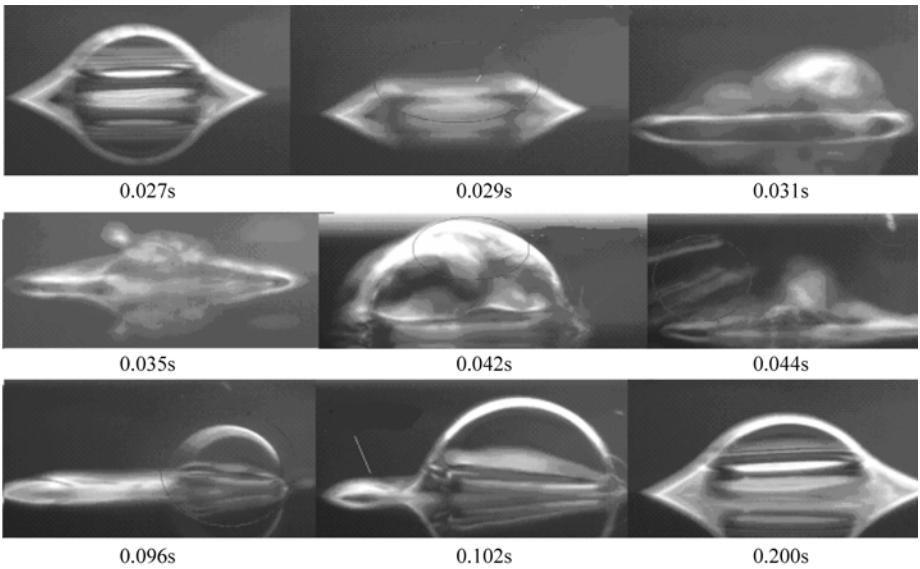

Figure 7.20 Single-bubble cyclical behavior

When the big bubble grew upward, a thin liquid film was formed at the bottom of the droplet, between the bubble and the solid surface, which was shown in Fig. 7.21. In the initial stage, the liquid film was thick enough to provide enough quantity of steam, and the liquid film had better performance on the heat transfer than that of the situation if the bubble contacted the heated surface directly. Therefore, the bubble would grow and break easily since the pressure inside the bubble was always higher than the circumstance pressure outside the bubble. In the last stage, the liquid film became ultrafine. It would tear at the contact line to shrink towards the center of the droplet when the bubble grew, leading to

decreasing liquid contact area. Consequently, the thermal resistance increased and the evaporation rates rapidly decreased. When the bubble expanded to the maximum size, its top could enter the subcooled circumstance region and the condensation should take place at the top, resulting in the shrink of the bubble. Meanwhile, the liquid film was so thin that it couldn't provide enough quantity of steam, and the vapor pressure inside the droplet was lower than the ambient pressure, which also made the bubble shrunk.

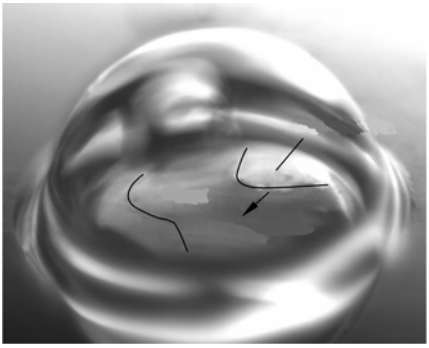

Figure 7.21 Liquid film under a bubble

7.3.4 Metastable Cyclical Phase Change

For a droplet on a SS surface at 160℃, metastable cyclical phase change is shown in Fig. 7.22. Even at a very high surface temperature, there were no bubbles on the bottom surface at all. Abnormally, the droplet stayed stably for a few milliseconds and was heated abruptly. Though the temperature at droplet bottom is approximately equal to surface temperature, the upper liquid is still subcooled. Energy was congregated within the droplet but could not be released effectively

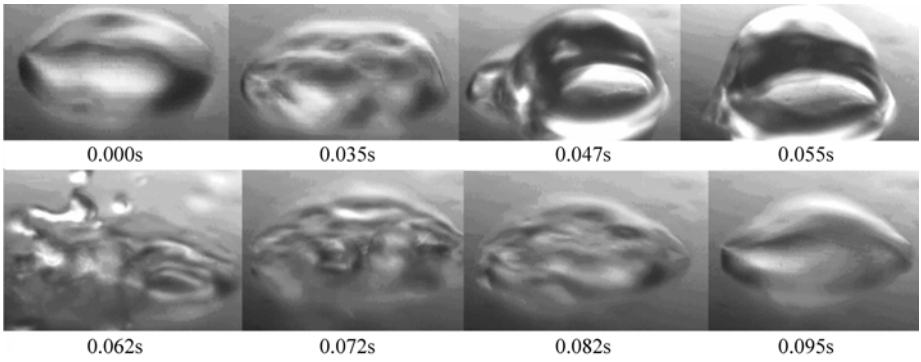

Figure 7.22 Metastable cyclical behavior

through the free surface. The droplet should be at the stage of metastability. And then, the free droplet surface suddenly surged and a big bubble grew up immediately, releasing the energy congregated. The whole process was so fast and violent that it lasted only 0.095 s. The droplet would come back to the quiet and peace state as initial stage after the energy being released. This process would repeat several times until the droplet was dryout.

7.4 Droplet Spreading During Evaporation and Nucleation

7.4.1 Phenomenon Observations

For a deionized water droplet on a SS surface with parallel strip nick surface at the temperature of 110℃, the dynamical evaporation is presented in Fig. 7.23. The droplet was evaporated with nucleate boiling in it. The lifetime of the droplet was 19 s. Very clearly, just as the droplet was deposited on the surface, several bubbles immediately generated at the bottom, having diameter of 0.1 – 0.2 mm. And bubble size would gradually increase and reach a diameter of 0.3 – 0.4 mm. Meanwhile, the height of the droplet would continuously decrease, however, the wetted diameter remained constant. When the bubbles expanded to the maximum size, their top entered the subcooled liquid region and the condensation took place at the top of the bubbles. The interaction between the bubbles was very strong and extruded the liquid. The contact line slightly outspreaded and remained droplet height remained unchanged. The bubbles gradually collapsed and disappeared as the droplet spread, and the droplet became a thin film without any bubbles at all. Finally, the contact line shrunk and the droplet was gradually

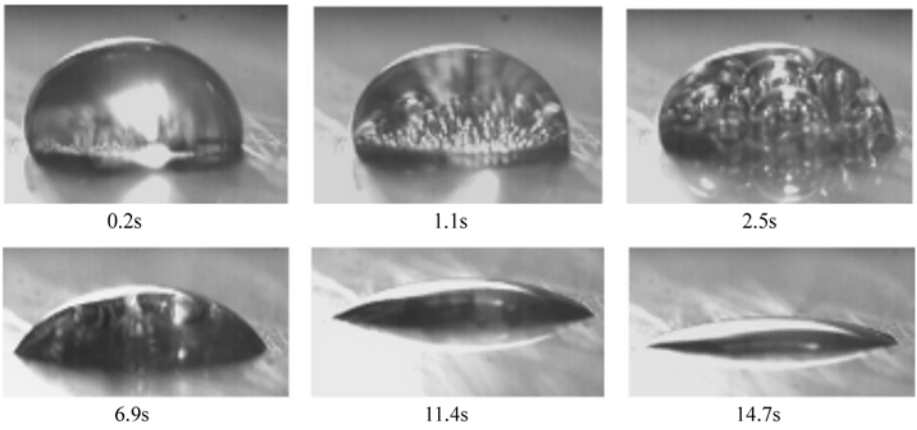

Figure 7.23 Spreading of a droplet with evaporation and nucleation

dryout. As the droplet became a thin film, the evaporation rates increased with decreasing in the height of the droplet [6], greatly enhancing the heat transfer. In film evaporation regime, the spreading of droplets was mainly due to the contact line motion [7], resulting in the dynamic spreading and wetting. However, in the case of the nucleate boiling regime, the interaction between the bubbles and the dynamic nucleation leaded to extruding the liquid. Apparently, the drive forces were different for these two cases.

7.4.2 Influencial Factors

Figure 7.24 illustrates the dynamical behavior of droplets on three surfaces at 130℃. The spreading of water droplets had a close relationship with the dynamic bubble behavior in droplets as long with the surface properties. The lifetime of a droplet on the parallel-strip nicked surface at 130℃ was 7.1 s, spreading just lasting only 0.8 s. As shown in Fig. 7.24(a), several bubbles of 0.2 – 0.3 mm in diameter immediately appeared and extruded each other as the droplet was deposited on the heated surface. However, the interaction of bubbles was not strong enough to break through the free interface at 130℃. The dynamic bubble behavior was confined within the droplet, leading to the contact line slightly outspreading and the wetted diameter increasing. Finally, the dynamical bubbles were strong enough to drive the whole droplet to wriggle on the surface.

The spreading and the dynamic bubble behavior on the stainless steel surface with reticulate nick were much more intense than that on the parallel-strip-nicked surface, as shown in Fig. 7.24(b). As the droplet was deposited on the heated surface, a lot of small bubbles immediately generated within the droplet, having diameter about 0.07 – 0.15 mm. Instead of congregating and coalescing into several large bubbles, the small bubbles drove the droplet to completely outspread to a large area. In this transient period the bubble kept stable size. When the droplet outspreaded completely, the bubbles suddenly grew up and coalesced into several larger bubbles which would shrink to a certain size after expanding to a maximum value. This process repeated several times until they coalesced into a large bubble. When one big bubble which occupied about 90% of the volume of a droplet formed, the spreading was terminated. Accordingly, the evaporation of the droplet turned into a repetitive process of expansion-shrink of bubbles, until the droplet dried out. The lifetime of the droplet was 8.2 s, and the process of spreading lasted only 360 ms. It was shown that the lifetime of a droplet of the same initial volume on the reticulate-nicked surface was longer than that of the parallel-strip-nicked surface at a specified temperature. The cooling performance was dependent upon the droplet spreading.

The spreading of a droplet on the polished silicon surface was shown in Fig. 7.24(c). Without the interaction between large bubbles, the evaporation did not experience the outspreading drove by the bubbles, but only free spreading

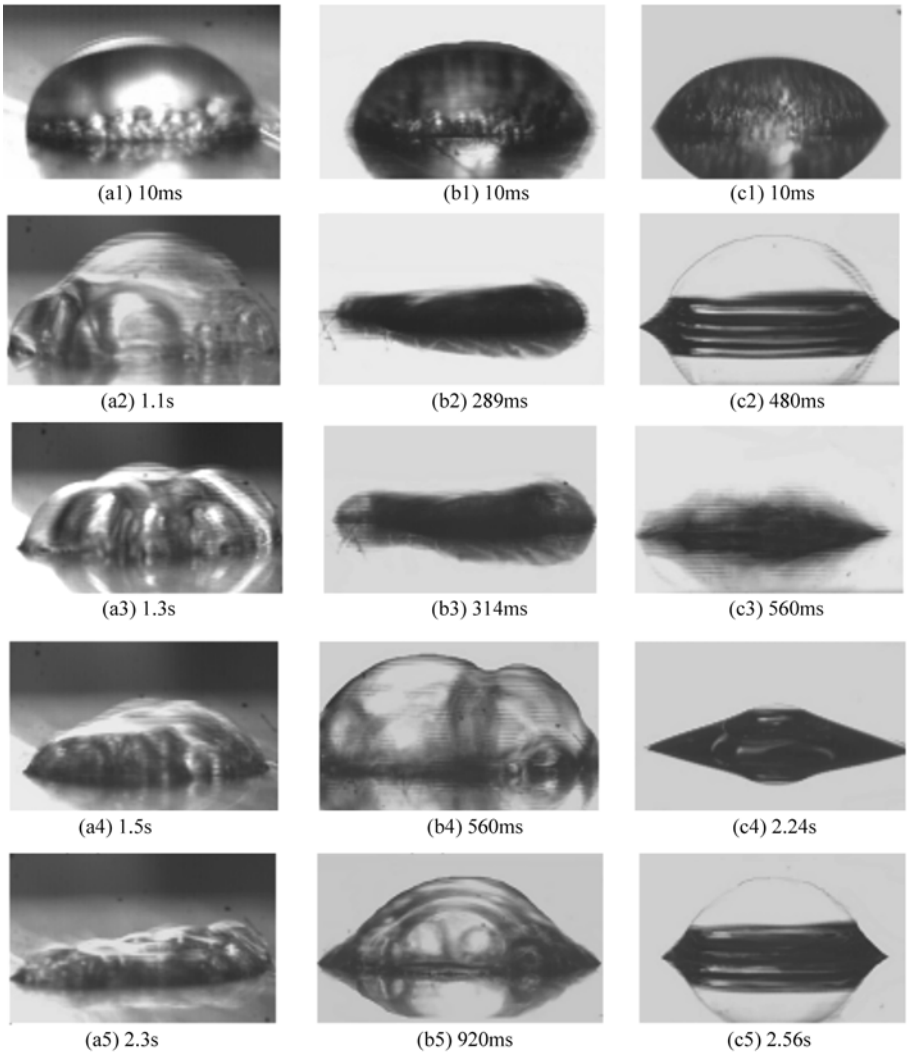

Figure 7.24 Droplte spreading on three surfaces at 130℃
(a) Strip SS plate; (b) Reticulate SS plate; (c) Polished silicon

being observed. The ultrafine bubbles would shrink and coalesce into a large bubble in about 0.8 s, and bubbles with stable size were hardly observed. And then the evaporation of the droplet turned into a seasonal process, with the bubble repetitive activity of grow-collapse. Or the periodic evaporation and nucleation of a droplet on the polished silicon surfaces was observed in the experiments. At the initial stage, ultrafine bubbles assembled into a large bubble which occupied about 90% of the droplet volume, extruding and changing the shape of the interface (see Fig. 7.24(c2)). And then, a big bubble formed (see Fig. 7.24(c3)). Thirdly, the contact line shrunk, and the ultrafine bubbles appeared and assembled

once again (see Fig. 7.24(c4)). In this case, the lifetime of a droplet was about 5.1 s, including 8 cycles of repetitive evaporation. The lifetime averaged over the first 5 cycles was about 0.84 s per cycle. The period would be shorter with the evaporation rate increasing at the last stage, about 0.36 s per cycle. The significant distinctness of evaporation behavior on the polished silicon surface was likely due to the lack of the nucleation sites on the relatively smooth surface.

At surface temperature ranging from 110℃ to 190℃, the existence of several large bubbles were observed in a droplet, and the bubbles extruded each other to drive the droplet to outspread. The droplet was easiest to spread at the surface temperature of 130℃, and the spreading tendency increased with increasing surface coarseness. Actually, the capillary effect of the coarse and nicked surface was propitious to induce a droplet spreading, and quite a number of nucleation sites uniformly distributed on nick surfaces. Obviously, the bubble distribution was quite uniform at relatively low heat fluxes, preventing the bubbles from assembling into a big bubble in an instant. When bubbles assembled into a big one, the spreading was terminated.

7.4.3 Spread Area and Spread Speed

The spread area of a deionized water droplet on three surfaces at different temperatures was illustrated in Fig. 7.25. Clearly, a droplet was easiest to spread at temperature of 130℃ on two rough surfaces. At this level of surface temperature, it was easy to form several bubbles having enough size to compete and extend with each other, which drove the droplet spreading. If the surface temperature was lower, the bubbles within a droplet were too small to overcome the interfacial forces and drive the droplet spreading. When the surface temperature was higher than 130℃, the bubbles would assembled into a big one in an instant, greatly restricting droplet spreading, particularly induced by nucleate boiling. It was found that the spreading tendency increased with increasing surface coarseness when the surface temperature was lower than 160℃. The droplet spreading shows quite different behavior on the polished silicon surface from that on other two surfaces. It did not obviously spread induced by nucleation or nucleate boiling beyond the temperature of 160℃ because of the lack of nucleation sites on it. With the surface temperature increasing, the spread area of a droplet on a polished silicon surface would increase as well, compared with other two stainless steel surfaces. For this case, a gas/vapor film was formed under the droplet. So the droplet would easily overcome the viscous force to spread.

The spread speed of deionized water droplets on the heated surfaces employed in present experiments at different temperatures was shown in Fig. 7.26. The spread speed of a droplet on the polished silicon surface was higher than that of the parallel-strip-nicked surface, although its spread area was smaller. Both the spread

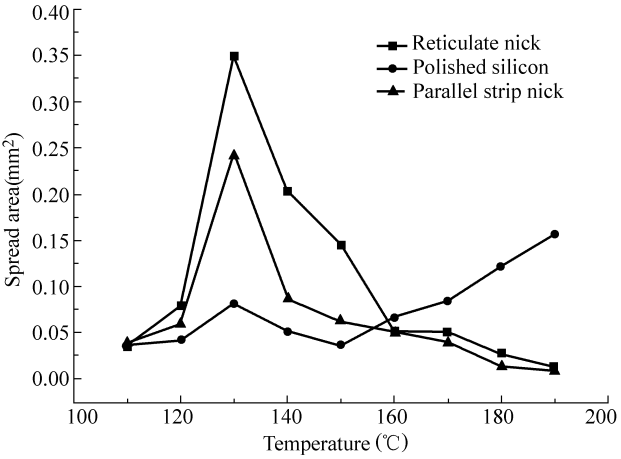

Figure 7.25 Variation of spread area

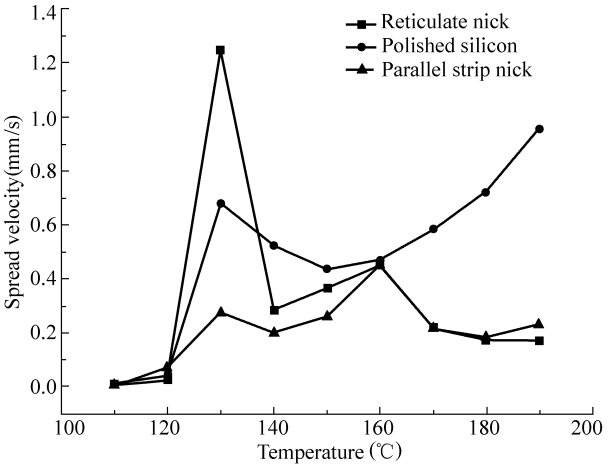

Figure 7.26 Variation of spread speed

area and the spread speed reached their maximum values at the temperature of 130℃. It was also found that both the spread area and the spread speed were almost the same with each other on different solid surfaces at 160℃. At this temperature, the phenomenon of Leidenfrost was observed and the formation of a vapor film under droplets made the spreading dependent of the surface properties.

The dynamic bubble behavior in the droplet at the temperature ranging from 110℃ to 190℃ could be divided into 3 stages. At the initial stage (with the temperature ranged from 110℃ to 130℃), ultrafine bubbles assembled into several large bubbles. The interaction between bubbles was strongest, extruding the droplet to completely outspread. During this period, the spread area and the spread speed curve increased sharply along with the size of bubbles increasing.

At the second stage (with the temperature ranged from 130℃ to 160℃), as the surface temperature increased, the bubbles assembled into a big bubble in an instant, the spreading was terminated. So the spread area and speed decreased. Then the evaporation of the droplet turned into a seasonal process, with the bubble repetitive activity of grow-collapse. The periodic process would be observed most obviously on the polished silicon surface. At the third stage (with the temperature ranged from 160℃ to 190℃), the bubble with stable size was hardly observed. The gas/vapor film was formed under droplet and the phenomenon of Leidenfrost was observed [8, 9].

7.4.4 Heat Fluxes

Figure 7.27 shows the heat fluxes averaged over the entire wetted area and the lifetime of the droplet. It is assumed that all heat transferred from the heated surface are used to evaporate the droplet. This assumption is particularly valid for small droplets, because the sensible heat required to heat the drop from the ambient temperature to the temperature of the heated surface is typically less than 10%.According to the curves, the average heat flux for water droplet on three kinds of heated surfaces all decreased at the temperature ranged from 110℃ to 130℃, and reached the bottom at 130℃. For at this temperature, a droplet was easiest to outspread, enhancing the cooling performance and reducing the average heat flux. And then the heat flux would increase sharply. For the polished silicon surface, the heat flux would approach its peak at 160℃, and then drop sharply when the surface temperature was higher. In that case, a gas/vapor film was formed under droplet. So the droplet would easily overcome the viscous force to outspread. At the same time, the gas/vapor film increased the thermal resistance due to decreasing in contact area between the wetted surface and the liquid, the heat flux rapidly decreased. However, for stainless steel of strip and reticulate nick surface, the heat

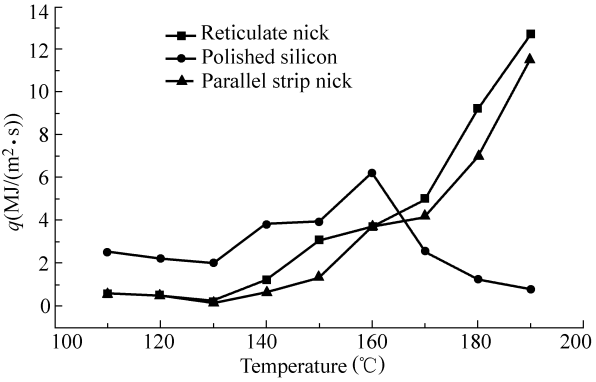

Figure 7.27 Average heat fluxes vs. wall temperature

flux increased along with increasing the temperature of the heated surfaces after 130℃. The heat flux of the two solid surfaces was almost the same with each other at 160℃, and then increased sharply.

According to Figs. 7.25 to 7.27, during nucleation boiling the spreading speed and area of a droplet played a substantial role for the heat flux. When the spreading area and speed increased, the average heat flux decreased. The cooling performance enhanced.

References

[1] M. di Marzo, D. Evans. Dropwise evaporative cooling of high thermal conductivity materials. International Journal of Heat and Technology, 5: 126 – 136, 1987.

[2] E. F. Crafton, W. Z. Black. Heat transfer and evaporation rates of small liquid droplets on heated horizontal surfaces. Int. J. Heat and Mass Transfer, 47: 1187 – 1200, 2004.

[3] K. Makino, I. Michiyoshi. Effects of the initial size of water droplet on its evaporation on heated surfaces. Int. J. Heat and Mass Transfer, 22: 979 – 981, 1979.

[4] Zhiyong Lin，Xiaofeng Peng. Inner flow behavior in an oscillating liquid droplet. Heat Transfer—Asian Research, 38 (8), 2009.

[5] G. Lu, X. D. Wang, X. F. Peng. Transitional boiling characteristics of an individual liquid droplet on heated solid surface, ASME-ICMN 2007 Conference, 2007.

[6] X. D. Wang, G. Lu, X. F. Peng, et al. Evaporation and nucleate boiling of an individual droplet on surfaces. Proceedings of the 2005 ASME Summer Heat Transfer Conference (San Francisco), 4: 703 – 710, 2005.

[7] Gui Lu, Xiaofeng Peng, Xiaodong Wang. An experimental investigation on spreading of droplets with evaporation and nucleation. Heat Transfer—Asian Research, 38 (1): 40 – 50, 2009.

[8] K. J. Baumeister, F. F. Simon. Leidenfrost temperature—its correlation for liquid metals, cryogens, hydrocarbons and water. ASME Journal of Heat Transfer, 95: 166 – 173, 1973.

[9] C. T. Avedisian, J. Koplik. Leidenfrost boiling of methanol droplets on hot porous/ceramic surfaces. Int. J. Heat and Mass Transfer, 30: 379 – 393, 1987.

8 Boiling in Micro-Structures and Porous Media

Abstract An experimental investigation was conducted to visually observe the boiling behavior in a 3D porous structure made of staggered glass beads, especially the bubble dynamics and pore-scale liquid flow around bubbles associated with the heat and mass transport at the bubble interface. The experiments show that the dynamic bubble behavior was significantly affected by the bead-packed structure, and several unique boiling phenomena caused by special pore geometry were observed and discussed. Intensive wetting of the liquid replenishment protected heated surface from full dryout. The bubble shape and primary bubble interface were described by using a force balance on the bubble. An introductory model was proposed to perform a theoretical analysis and explore the dryout process inside the pore structure. The theoretical results were compared with experimental data, and the present model provided a good explanation of the fundamental mechanisms and predicted the important influences of the bead-packed structure on dryout behavior.

Keywords interface, bubble dynamics, boiling, bead-packed structure, replenishment, dryout

Many efforts have been devoted to studying phase-change heat transfer in the porous structure with a horizontal heated surface in the past owing to their important technological applications [1]. In this work, an experimental investigation of boiling heat transfer in a porous structure, as shown in Fig. 8.1, was performed, and the efforts on this topic were driven by the development of the porous-wicked evaporator for capillary pumped loops (CPL) system. CPL is a high-performance heat transport device that is widely used for cooling of modern electronic devices [2, 3] as well as for the thermal management of advanced aerospace vehicles [4, 5]. As the key component of CPL system, the porous-wicked evaporator represents the heart of a CPL system and correspondingly determines the available capillary pumping head for heat transport of the overall loop. The contribution of interfacial effects on boiling heat transfer is extremely distinct in porous media, where unique phenomena, or problems, may arise because the dynamic behavior of the bubble interface is significantly affected by the porous structure during boiling [6].

X. Peng, *Micro Transport Phenomena During Boiling*

8.1 Experimental Observations

8.1.1 Test Apparatus

The experimental apparatus shown in Figs. 8.1 and 8.2 were used for visual observations and test measurements of boiling phenomena occurring in various porous structures and/or porous media. Normally, glass beads having different sizes are employed as porous materials or simulate porous structures. In the conducted experiments transparent test sections were packed with glass beads, having an average particle diameter of 0.5 – 7 mm. The phase-change behavior within the bead-packed structure could be observed through the front glass-pane. The bead-packed structure saturated with working fluid was heated from the vessel bottom by a heating assembly consisting of a labyrinth-type foil heater mounted on the bottom and a DC power supply. Wang et al. [6 – 8] described the experimental devices and test procedures in detail. Experiments were performed for different conditions, including various pore structures, fluids, and thermal boundary conditions.

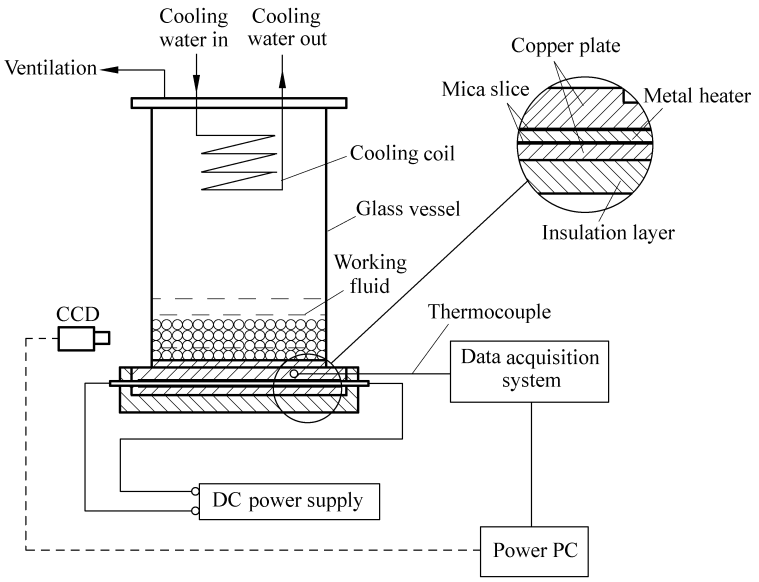

Figure 8.1 Schematic diagram of the experimental apparatus

The planform of the porous structure adjacent to the heated surface is shown in Fig. 8.3. For the purpose of studying the bubble behavior in the porous structure adjacent to the heated surface, the pore space adjacent to the heated surface is

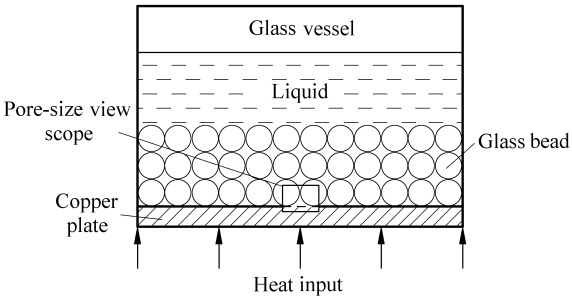

Figure 8.2 Pore-scale view scope of CCD camera

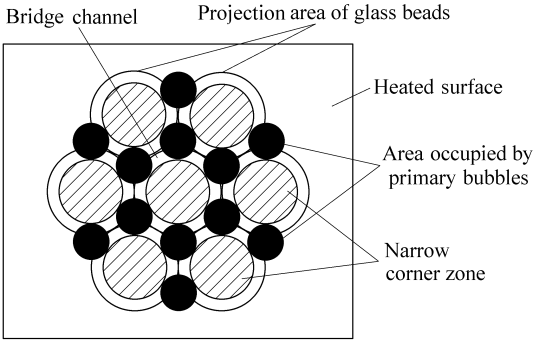

Figure 8.3 Planform of the porous structure adjacent to the heated surface

divide into three main areas, the cavity that is occupied by a primary bubble (the primary bubble is a bigger bubble which is merged by other little bubbles generated in the narrow corner or the bridge-channel in the pore immediately adjacent to the heated surface), the narrow corner zone between a glass bead and the heated surface, and the bridge channel connected two neighboring primary bubbles.

8.1.2 Low Applied Heat Flux

For subcooled boiling of water in a bead-packed porous structure at ambient pressure and temperature of 18.4℃, the bubble growth behavior at a low heat flux ($q'' = 16.1\,\mathrm{kW/m^2}$) is shown in Fig. 8.4. Under this condition, the active-site density on the heating surface and bubble release frequency was rather low, the bubble stayed for a long time on the wall before departure. The temperature of the liquid near the heating surface in the cavity was not high, and the condensation occurred on the top surface of the primary bubble while the mass balance was supported by the evaporation of the liquid in the narrow corner zone. The narrow corner zone was a very active area that would probably be influenced by the bubble growth behavior in the neighboring cavity and was occupied by the

replenished water due to the capillary action resulted by the pressure perturbation (see Fig. 8.4(c)). Consequently, the primary bubble would be wetted without the supply of the evaporation of the liquid in the narrow corner zone during its growing process (see Fig. 8.4(d)).

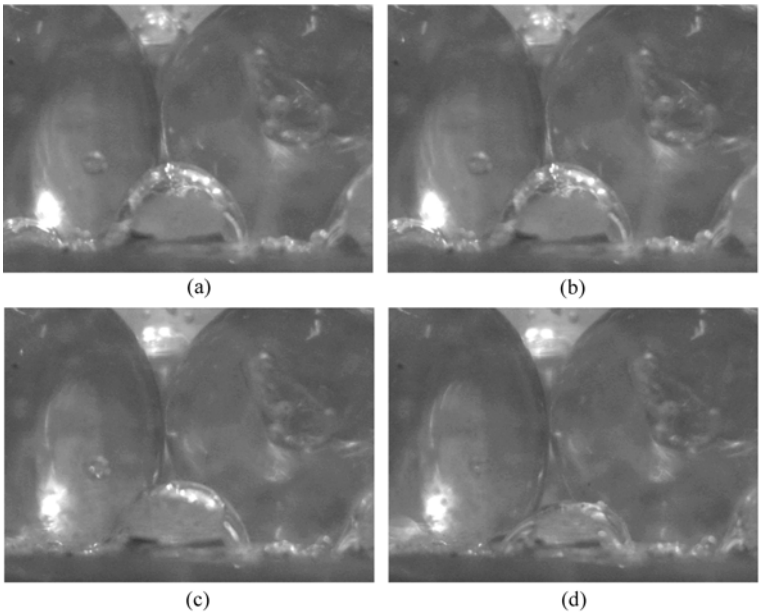

Figure 8.4 Bubble behavior in the bead-packed structure at $q'' = 16.1\,\mathrm{kW/m^2}$
(a) 0.00 s; (b) 7.02 s; (c) 19.11 s; (d) 23.66 s

Consecutive snapshots of a typical bubble lifetime during its growth-collapse cycle at a heat flux of 36.8 $\mathrm{kW/m^2}$ are presented in Fig. 8.5. As the applied heat flux was increased, the average wall temperature was maintained as before at the early beginning and bubble sites on the heating surface increased (see Fig. 8.5(a)). Bubble sites in the narrow corner were more than in other areas. Bubbles generated in the narrow corner expanded and penetrated into the cavity formed by the neighboring glass beads, and merged to a bigger bubble (primary bubble, see Figs. 8.5(b) and (c)). As the primary bubble grew, the pore size became the restriction of the bubble's further growth, and the primary bubble distorted and elongated (see Figs. 8.5(d) and (e)), subsequently the bubble would be truncated at the neck of the elongated bubble and quickly escaped from the pore (see Fig. 8.5(f)). Immediately following the primary bubble collapse, the pore space was re-occupied by replenished water due to the capillary action (see Fig. 8.5(g)), and another cycle of bubble growth-collapse was followed (see Fig. 8.5(h)). During this bubble cycle the wall temperature fluctuation was observed to be about $\pm 1 - 2℃$.

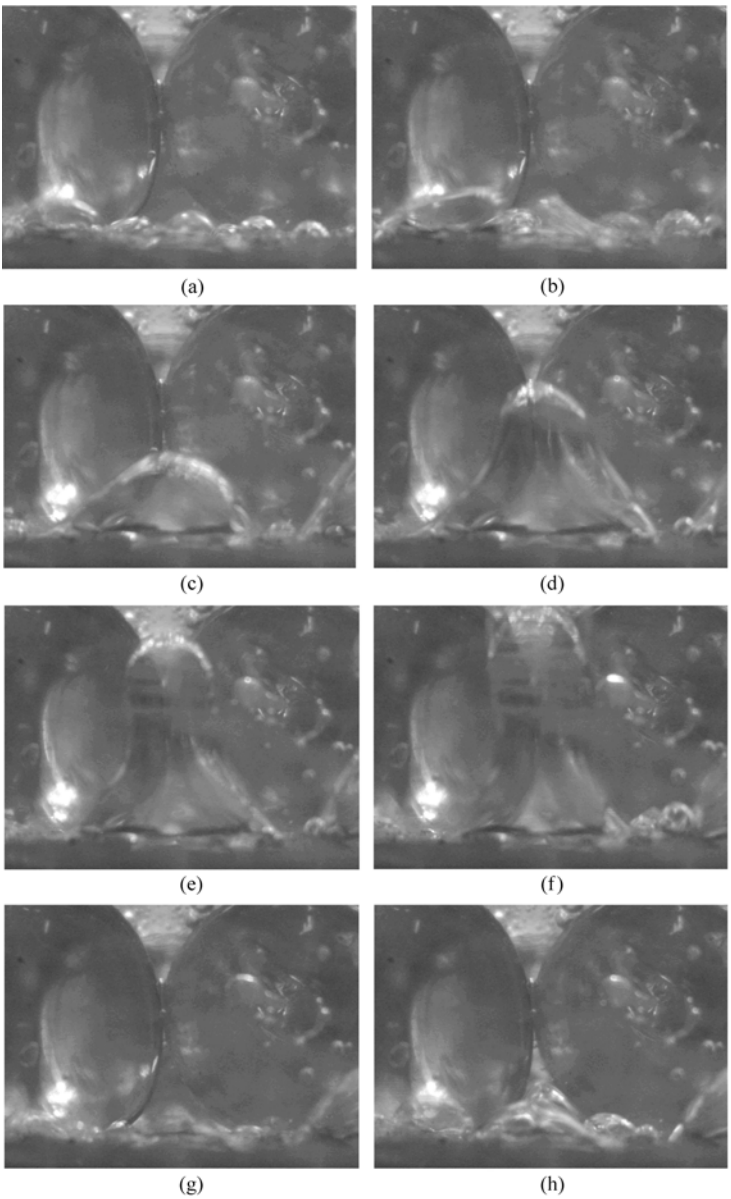

Figure 8.5 Bubble behavior in the bead-packed structure at $q'' = 36.8\ \text{kW/m}^2$
(a) $t = 0.00$ s; (b) $t = 0.15$ s; (c) $t = 0.36$ s; (d) $t = 0.82$ s; (e) $t = 1.12$ s;
(f) $t = 3.41$ s; (g) $t = 3.46$ s; (h) $t = 3.72$ s

It was observed that as the primary bubble grew, the subcooled water was pumped into the narrow corner and reduced this area's active-site density (see Fig. 8.5(e)), therefore the narrow corner is a dual-effect area which is a very active wetting area as well as an active bubble generation area.

In the pore-scale view, it was observed that the bubble distorted and elongated for the case when the pore size became the restriction of the bubble's further growth as the bubble grew. A concave section was shaped in the middle of the distorted bubble, as shown in Fig. 8.5(f), consequently a downward replenished-liquid flow was driven by the pressure difference that was caused by the special configuration of the distorted bubble. Replenishment that plays a very important role on the dry-out and rewetting process is a unique characteristic of the bead-packed structure, and also the liquid-supply for wetting effect of the narrow-gap corner zone.

As the applied heat flux changed (increased or decreased), the liquid-vapor interface adjacent to the bridge-channel zone moved (dry-out or rewetting) while the balance between the interfacial evaporation flux and the replenishment flux was broken. Two neighboring primary bubbles would probably coalesce at not very high heat flux ($q'' = 45.2\ \mathrm{kW/m^2}$) for the case when the bridge-channel between these two bubbles was dried out completely (see Figs. 8.6(a) and (b)). The coalesced bubble stayed on the heated wall just like a dryspot and was hard to collapse. However, the exsistence of the coalesced bubbles was just only a local phenomenon because of the low heat flux, and the coalesced bubble area would be wetted due to the wetting effect of the narrow corner (see Figs. 8.6(c) and (d)). Therefore, the heat transfer was not reduced by the occurrence of the coalesced bubble while the heat flux was not very high.

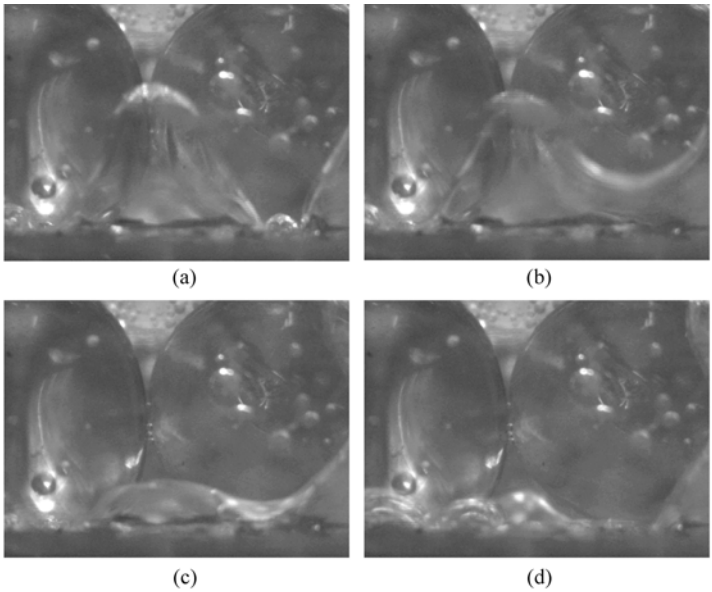

Figure 8.6 Bubble behavior in the bead-packed structure at $q'' = 45.2\ \mathrm{kW/m^2}$
(a) $t = 0.00$ s; (b) $t = 0.10$ s; (c) $t = 0.20$ s; (d) $t = 0.36$ s

8.1.3 Moderate Applied Heat Flux

When the applied heat flux was further increased to 67.6 kW/m^2, it can be seen from Fig. 8.7 that the bubble growth-collapse process became much faster. At higher heat flux, it was observed that for a single bubble, the bubble behavior was about the same as those for a lower heat flux presented in Fig. 8.5. However, Fig. 8.7 shows that at a higher heat flux the waiting period between two bubble growth-collapse processes became shorter, with the intensive pressure oscillations resulted from the departure of the bubble significantly affected the growth of the newly-generated bubble that may be distorted by the pressure oscillations as shown in Fig. 8.7(b). This also resulted in the flow turbulence and unsteady vapor-liquid interface in the pore. It can be demonstrated by larger wall temperature fluctuation of about $\pm 3-4$℃.

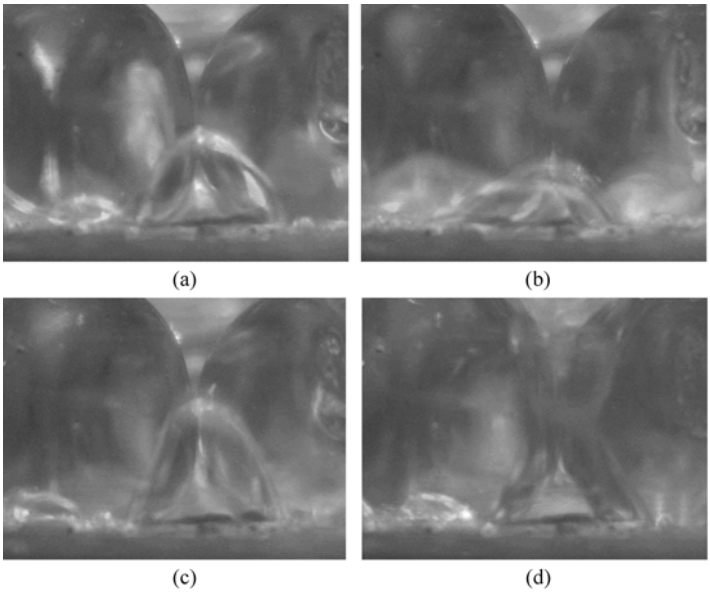

Figure 8.7 Bubble behavior in the bead-packed structure at $q'' = 67.6$ kW/m^2
(a) $t = 0.00$ s; (b) $t = 0.04$ s; (c) $t = 0.08$ s; (d) $t = 0.12$ s

8.1.4 High Applied Heat Flux

As the applied heat flux was increased to approach CHF, the bubble release frequency was very high, and the scene of pore-scale phase-change behavior was highly disordered, as shown in Fig. 8.8. Under this condition, the bridge-channel was occupied by the vapor at most of the time and the primary bubbles coalesced

immediately once they were generated. The wall temperature was highly unsteady and sometime could be as high as 200℃. However, actual dryout of whole surface of the wall could not be observed at even very high applied heat fluxes. It's seen from Fig. 8.8 that the existence of the coalesced bubbles on the heated surface was one of the main features of the bubble behaviors for high heat flux compared with the cases of low heat flux. As the heat flux increased, the wetting process in the narrow-gap corner became more intensive because of the intensive liquid-replenishment caused by the frequent bubble departure, and this area was very hard to be dried out. Consequently the drying out in the bridge-channel was rather unsteady because of the wetting effect of the narrow-gap corner.

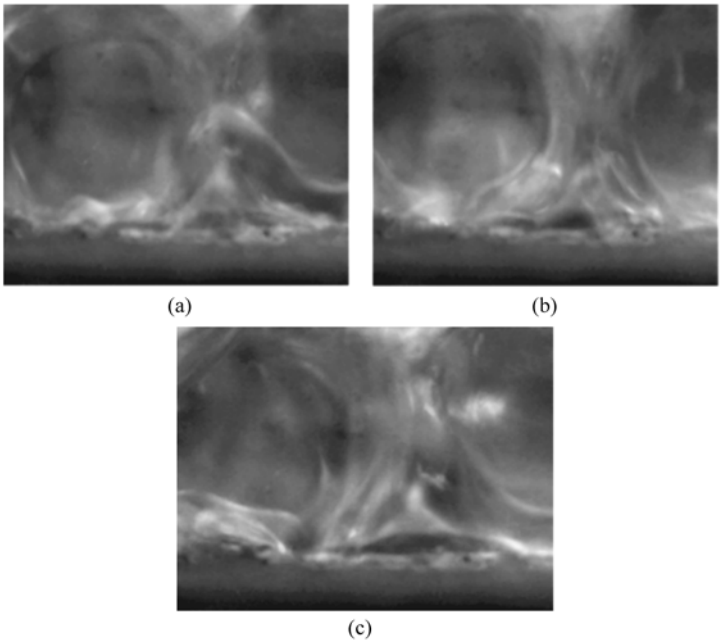

Figure 8.8 Dry spot formation and rewetting in gap-corner area at $q'' = 121.3\ \mathrm{kW/m^2}$ (a) $t = 0.00$ s; (b) $t = 0.04$ s; (c) $t = 0.12$ s

8.2 Bubble Behavior in Bead-Packed Structure

8.2.1 Boiling Process

Peng et al. [9] noted that the dynamic bubble behavior is significantly affected by the bead-packed structure, especially the pore structure adjacent to the heated surface. Special pore geometry changes the boiling process, especially the bubble

behavior, and thus influences the boiling heat transfer mechanism:

(1) Bubble generation: active sites for boiling on a plain surface are randomly distributed on the heated surface, however, bubble sites display regularly depending on pore geometry in the bead-packed structure. Active nucleation sites mainly exist in the narrow corner zone, where most vapor embryos initialize from this area. Small vapor embryos generating from the narrow corners grow up into the main cavity and merge into a primary bubble.

(2) Bubble growth: during the initial stage of bubble growth, the bubble is very small and the pore structure is not a limiting factor for bubble growth. For this inertia-controlled early stage of the bubble growth process, the bubble has nearly a hemispherical shape. With the restriction of pore size exerted on the growing bubble, the bubble grows into a converging-diverging shape and deforms while the vapor front of the growing bubble remains spherical due to surface tension. A typical fully-developed bubble is shown in Fig. 8.9(a). As illustrated in Fig. 8.9, the pore space near the heated surface is vapor-filled with liquid menisci in the narrow corners. For a fully-developed bubble, bubble growth is mainly controlled by the evaporative heat transfer on the liquid meniscus in the narrow-gap corner. The liquid meniscus becomes thinner with increasing heat flux but it dose not vanish even at very high heat fluxes. During evaporation on the liquid meniscus, the replenishing-liquid is pulled into the narrow corner by capillary pressure. Owing to the replenishment, the narrow corner zone maintains excellent wetting performance to protect the heated surface from full dryout. Consequently, the boiling heat transfer was enhanced by this evaporation-replenishment process.

(3) Bubble detachment: With the action of buoyancy, the concave section slims down as the bubble elongates gradually. Subsequently, the bubble is truncated at the neck of the elongated bubble and departs rapidly from the pore. This process was favorable for bubble release. In a very short period after bubble detachment, the liquid is sucked into the pore, which accelerates the forthcoming bubble nucleation process and the onset of next bubble cycle.

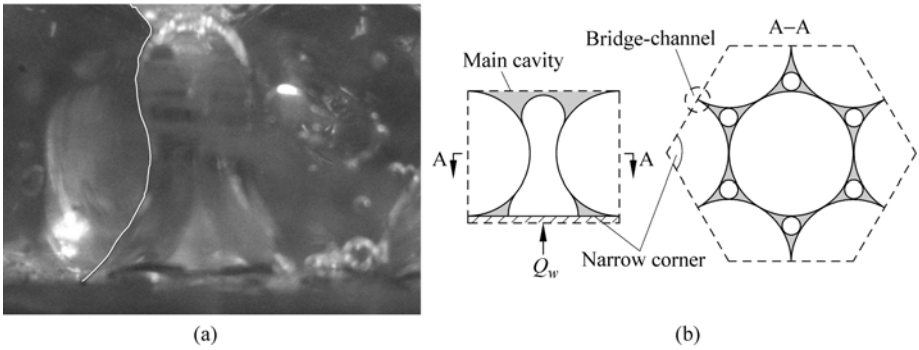

Figure 8.9 Pore geometry and bubble interface
(a) Full bubble configuration; (b) Pore geometry

8.2.2 Static Description of Primary Bubble Interface

Based on the observation of bubble dynamics in the bead-packed structure, the profile of primary bubble interface is modeled within the low-heat-flux regime, which is referred to as a static description compared with the dynamic behavior of bubble interface in the high-heat-flux regime. The interface of a fully-developed bubble is divided into three parts: Ⅰ-top section, Ⅱ-concave section, Ⅲ-base section, where each part will be described separately. As shown in Fig. 8.10, the top section interface is a spherical coronal, the base section interface is approximately a part of a hemisphere, and the concave section interface is assumed to touch the solid particle surface directly. Then, the bubble profile can be described by five primary configuration parameters as

$$R_2 = R_p(\sec 30^\circ - 1) \tag{8.1}$$

$$\tan\theta_1 = (R_2 + R_p)/R_p \tag{8.2}$$

$$R_3 = (\sec\theta_1 - 1)R_p \tag{8.3}$$

$$R_1 = (R_2 + R_p)\csc(\pi - \theta_2) - R_p \tag{8.4}$$

These four relations indicate that the bubble shape is determined by only one parameter, θ_2, if the particle diameter is specified.

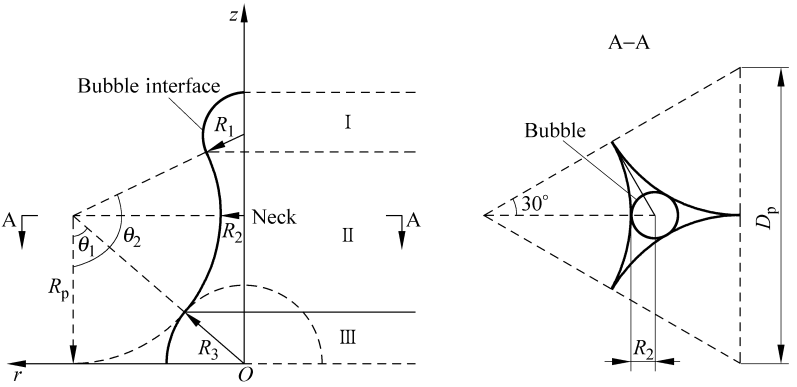

Figure 8.10 Bubble interface model

For a fully-developed bubble, it can be assumed that only the top section interface moves as the bubble grows (this is not valid at a very high heat flux and will be discussed in the later section). The position of the vapor front at the top is determined by θ_2. For a given working fluid, the departing bubble shape (bubble profile before departing) can be obtained from a force balance between the forces

retaining and detaching the bubble. Assuming the inertial effect is negligible during heat-transfer-controlled growth, interfacial tension tends to hold the bubble, while buoyancy acts to draw the bubble away, as shown in Fig. 8.11, or

$$F_\sigma = F_\mathrm{G} \tag{8.5}$$

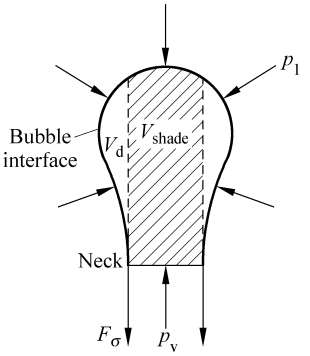

Figure 8.11 Forces acting on the bubble above its neck

Since the bubble is truncated at the neck, the interfacial force, F_σ, is

$$F_\sigma = 2\pi R_2 \sigma \tag{8.6}$$

And the buoyancy is expressed as

$$F_\mathrm{G} = \rho_\mathrm{l}(V_\mathrm{d} - V_\mathrm{shade})g - \rho_\mathrm{v} V_\mathrm{d} g + \pi R_2^2 (p_\mathrm{v} - p_\mathrm{l})_\mathrm{shade} \tag{8.7}$$

where V_d and V_shade are given in terms of primary configuration parameters as

$$\begin{aligned} V_\mathrm{d} = {} & \frac{\pi}{3}\{R_\mathrm{1d}[1+\cos(\pi-\theta_\mathrm{2d})]\}^2\{3R_\mathrm{1d} - R_\mathrm{1d}[1+\cos(\pi-\theta_\mathrm{2d})]\} \\ & + \int_{\frac{\pi}{2}}^{\theta_\mathrm{2d}} \pi[R_\mathrm{p} + R_2 - R_\mathrm{p}\sin(\pi-\theta)]^2 R_\mathrm{p}\sin\theta \mathrm{d}\theta \end{aligned} \tag{8.8}$$

$$V_\mathrm{shade} \cong \pi R_2^2[R_\mathrm{1d} - (R_\mathrm{1d} + R_\mathrm{p})\cos\theta_\mathrm{2d}] \tag{8.9}$$

The vapor pressure is assumed to be uniform inside the bubble, and the liquid pressure near the top section interface, p_l, is obtained from the Young-Laplace equation as

$$p_\mathrm{l} = p_\mathrm{v} - \frac{2\sigma}{R_\mathrm{1d}} \tag{8.10}$$

Combining Eqs. (8.5) – (8.10), the departing bubble profile corresponding to the departure angle θ_2d is determined by the following equation

$$\frac{(\rho_l - \rho_v)V_d g - \rho_l V_{shade} g}{2\pi R_2 \sigma} + \frac{R_2}{R_{ld}} = 1 \tag{8.11}$$

8.2.3 Comparison of Results

In Fig. 8.12, The theoretical prediction of the departing bubble profile is compared with experimental photographs of a growing bubble (see Fig. 8.12(a)) and a departing bubble (see Fig. 8.12(b)). The predicted bubble profile is in good agreement with the real interface of a departing bubble (see Fig. 8.12(b)). It can be also observed that there is a reasonable consistency between the prediction

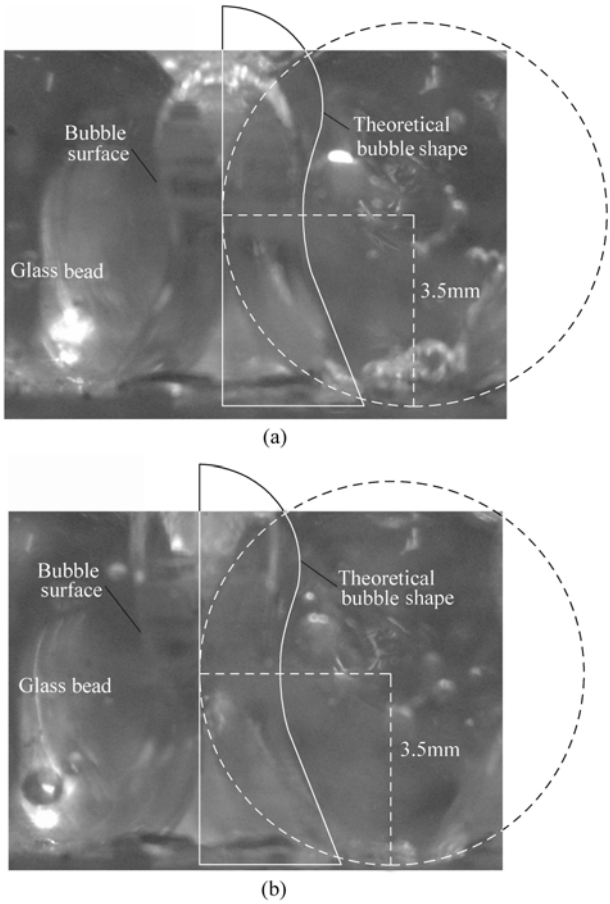

Figure 8.12 Comparison of bubble interfaces (D_p = 7 mm, water)
(a) Growing bubble; (b) Departing bubble

and the real shape at the bubble interface below the neck for a growing bubble as well as for a departing bubble. This supports the assumption that only the top section interface of a fully-developed bubble changes during bubble growth in the low-heat-flux regime.

As shown in Fig. 8.13, the departure angle, θ_{2d}, and the relative departure diameter, $2R_{1d}/D_p$, of the primary bubble, determined by Eqs. (8.11) and (8.4), increases with decreasing particle diameter, as a result of increasing capillary contribution compared with buoyancy. This implies that the narrowness of the pore

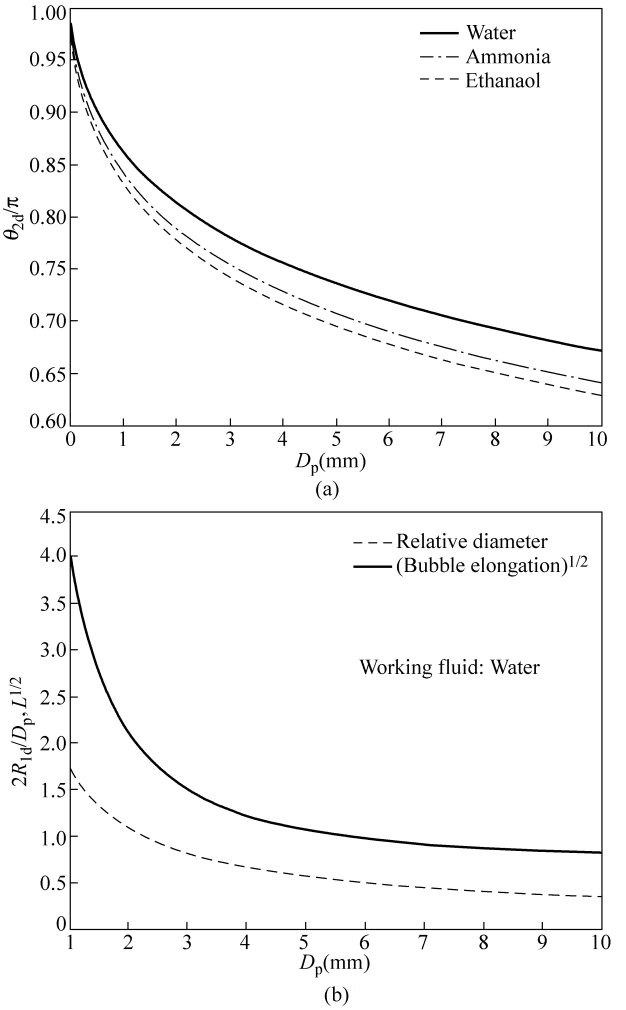

Figure 8.13 Departing bubble behavior
(a) Departure angle vs. particle diameter; (b) Departure diameter and bubble elongation vs. particle diameter

structure becomes more important for smaller particles. A configuration parameter, bubble elongation L, was presented to represent the distortion of the bubble due to the narrowness of pore space

$$L = \frac{h}{D_{\mathrm{p}}} \tag{8.12}$$

where h is the characteristic height of the primary bubble. For a departing bubble,

$$h_{\mathrm{d}} = \left(\frac{V_{\mathrm{d}}}{V_{\mathrm{pore}}} + 0.5 \right) D_{\mathrm{p}} \tag{8.13}$$

where the cavity volume $V_{\mathrm{pore}} = D_{\mathrm{p}}^3(\sqrt{3} - \pi/3)/4$. Apparently, bubble elongation represents the narrowness of the pore structure and increases quickly with decreasing particle diameter, as illustrated in Fig. 8.13(b). Additionally, the departure diameter, $2R_{\mathrm{ld}}$, is much larger than the cavity size for very small particles. For this condition, the pore space already has been fulfilled by the vapor before the bubble detachment. Therefore, smaller particles, and consequently smaller pore space, provides more possibilities for the occurrence of stable dryspots on the heated surface. Further study needs to be performed to fully understand the bubble detachment mechanism in a porous structure with very small particles.

8.3 Replenishment and Dynamic Behavior of Interface

For boiling in the bead-packed structure, a downward replenishing-liquid flow around the deformed bubble interface is driven by the capillary pressure gradient. The liquid flow around the bubble is induced virtually by the evaporation and condensation taking place at the bubble interface. The replenishment provides the necessary liquid supply required by evaporation at the bubble interface in the narrow corner area.

8.3.1 Replenishing Liquid Flow

As shown in Fig. 8.14, the curvature of the liquid-vapor interface in the narrow corner zone is usually much larger than that of a bubble interface at other locations. Accordingly, a negative capillary pressure gradient along the *z*-directional coordinate is found. Under the influence of this pressure gradient, the replenishing-liquid flows into the corner area.

With a view of the pores in the bead-packed structure as being a system of parallel, equilaterally-staggered capillary ducts, a preliminary analysis is conducted

to determine driving forces for the pore-scale replenishing liquid flow using the general concepts of porous media and Darcy's approximation, as shown in Fig. 8.14. Neglecting gravitational effects, the area-averaged mass flux of liquid (replenishment flux) and vapor (evaporation flux) flow inside the pore can be described as follows

$$\frac{\mathrm{d}p_\mathrm{l}}{\mathrm{d}z} = \frac{\dot{m}_\mathrm{r}\nu_\mathrm{l}}{KK_\mathrm{rl}} \tag{8.14}$$

$$\frac{\mathrm{d}p_\mathrm{v}}{\mathrm{d}z} = -\frac{\dot{m}_\mathrm{e}\nu_\mathrm{v}}{KK_\mathrm{rv}} \tag{8.15}$$

where the permeability of the porous structure $K = \dfrac{D_\mathrm{p}^2\phi^3}{150(1-\phi)^2}$, and relative permeabilities of liquid and vapor phases are represented as [10]

$$K_\mathrm{rl} = (1-\beta)^3 \tag{8.16}$$

$$K_\mathrm{rv} = \beta^3 \tag{8.17}$$

with β being the vapor fraction in the pore. Subtracting Eq. (8.14) from Eq. (8.15) and noting that the evaporation flux is balanced by the replenishment flux, i.e. $\dot{m}_\mathrm{r} = \dot{m}_\mathrm{e}$, results in the capillary pressure gradient

$$\frac{\mathrm{d}p_\mathrm{c}}{\mathrm{d}z} = -\frac{\dot{m}_\mathrm{r}}{K}\left(\frac{\nu_\mathrm{v}}{K_\mathrm{rv}} + \frac{\nu_\mathrm{l}}{K_\mathrm{rl}}\right) \tag{8.18}$$

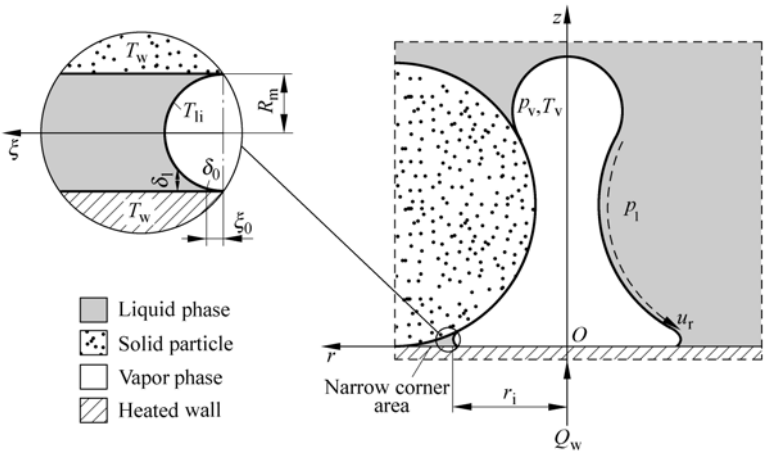

Figure 8.14 Replenishment flow and interface structure

The Eq. (8.18) is given in dimensionless form as

$$\frac{\mathrm{d}J(\beta)}{\mathrm{d}\eta} = -Ca\left(\frac{1}{K_{\mathrm{rv}}} + \frac{\gamma}{K_{\mathrm{rl}}}\right) \tag{8.19}$$

where

$$J(\beta) = \frac{p_{\mathrm{c}}(\beta)}{\sigma}\sqrt{\frac{K}{\phi}},\quad \eta = \frac{z}{\sqrt{K\phi}},\quad \gamma = \frac{\nu_{\mathrm{l}}}{\nu_{\mathrm{v}}},\ \text{and}\ \ Ca = \frac{\dot{m}_{\mathrm{r}}\nu_{\mathrm{v}}}{\sigma} = \frac{\dot{m}_{\mathrm{e}}\nu_{\mathrm{v}}}{\sigma}.$$

The Leverett function [11], $J(\beta)$, was correlated by Udell [12] as

$$J(\beta) = 1.417\beta - 2.120\beta^2 + 1.263\beta^3 \tag{8.20}$$

which is a function only of β, or

$$\frac{\mathrm{d}J(\beta)}{\mathrm{d}\eta} = \frac{\mathrm{d}J(\beta)}{\mathrm{d}\beta}\frac{\mathrm{d}\beta}{\mathrm{d}\eta} \tag{8.21}$$

Thus, the differential equation becomes

$$\frac{\mathrm{d}\beta}{\mathrm{d}\eta} = -\frac{Ca\left(\dfrac{1}{K_{\mathrm{rv}}} + \dfrac{\gamma}{K_{\mathrm{rl}}}\right)}{J'} \tag{8.22}$$

An equation similar to Eq. (8.22) also were obtained by Udell [12]. The appropriate boundary condition of Eq. (8.22) at the bubble top is

$$\beta = 0 \quad \text{at} \quad \eta = \frac{h_{\mathrm{d}}}{\sqrt{K\phi}} \tag{8.23}$$

Equation (8.22) can be integrated numerically to obtain the vapor fraction profile in the pore, or a dynamic description of the bubble interface.

8.3.2 Dynamic Behavior of Bubble Interface

At a high heat flux, the bubble interface profile, especially the interface in the narrow-gap corner, does vary with the applied heat flux. To balance the replenishment flux and the evaporation flux, the bubble interface is regulated by the evaporative heat transfer to establish an appropriate capillary pressure gradient for the replenishing liquid flow. As illustrated in Figs. 8.15 and 8.16, the vapor fraction increases continuously from the top of the bubble to the heated surface;

and correspondingly, a negative capillary pressure gradient, driving a downward replenishing liquid flow, exists along the η-directional coordinate. Figure 8.17 also shows that the vapor fraction profile (or the bubble interface profile) varies with the capillary number, Ca. As Ca increases, the vapor fraction enlarges; that is, the bubble interface expands horizontally, which is in agreement with the experimental observation shown in Fig. 8.18. Consequently, a larger capillary pressure gradient is established for a higher Ca in order to keep the mass balance between the replenishment and the evaporation, as seen in Fig. 8.17.

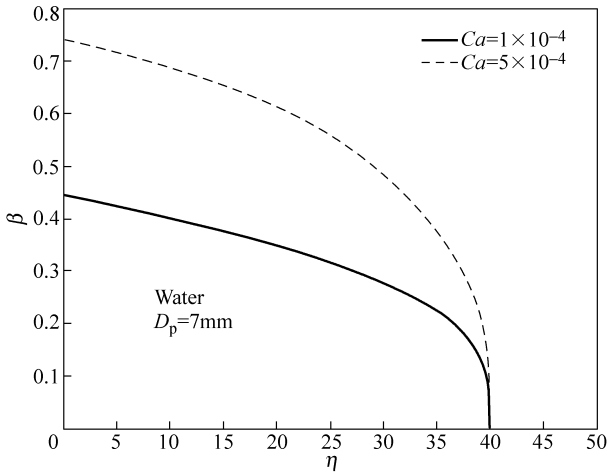

Figure 8.15 Vapor fraction profiles

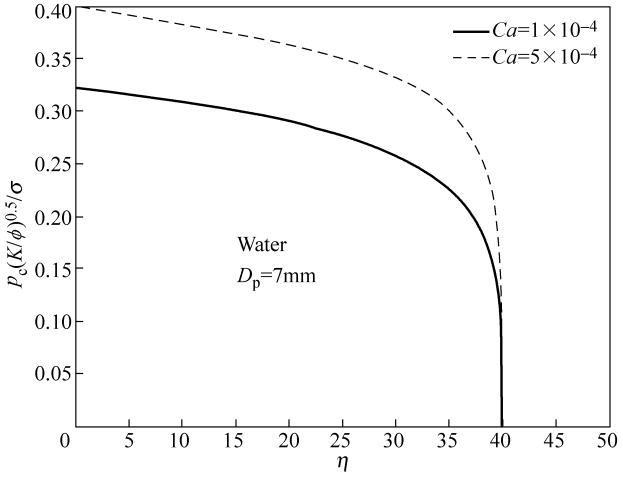

Figure 8.16 Capillary pressure profiles

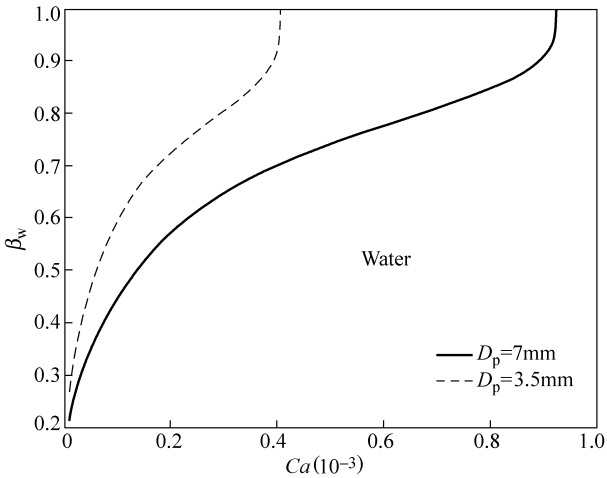

Figure 8.17 Vapor fraction on the heated surface vs. capillary number

The bubble interface, especially the interface adjacent to the heated surface, tends to expand horizontally with increasing applied heat flux. The relation between the vapor fraction on the heated surface, β_w , and the capillary number is illustrated in Fig. 8.18. The variation of β_w allows a qualitative description of the geometry of the liquid-vapor interface adjacent to the heated surface (see Fig. 8.13). As illustrated in Fig. 8.12, the liquid-vapor interface expands into the

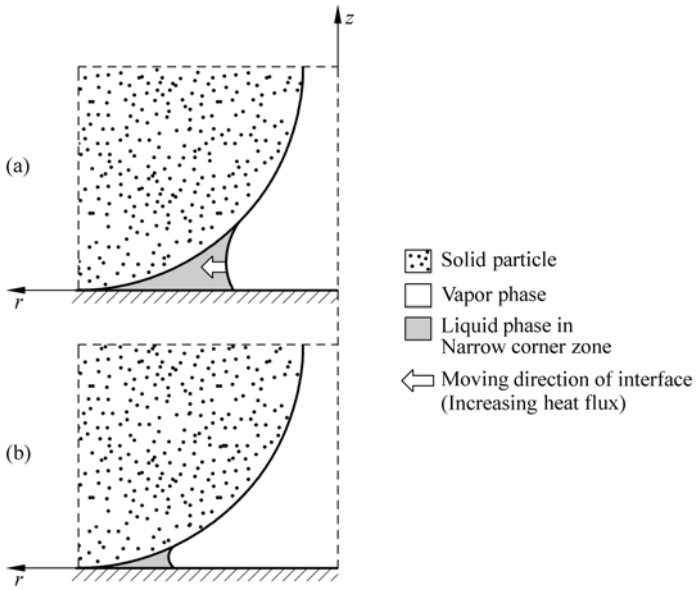

Figure 8.18 Liquid-vapor interface adjacent to the heated surface
(a) Low heat flux; (b) High heat flux

narrow corner area with increasing applied heat flux, and the effective meniscus radius continuously reduces as the liquid meniscus becomes thinner. As a result, the capillary pressure driving the replenishing-liquid flow increases with increasing heat flux. In conclusion, the bubble interface is regulated by interfacial heat and mass transport to provide sufficient driving force for the replenishment. This is also consistent with the observed experimental evidence (see Fig. 8.18).

8.3.3 Interfacial Heat and Mass Transfer at Pore-Level

The replenishment is highly involved with the interface and induced by the interfacial heat and mass transport. The boiling heat transfer is improved by this "evaporation-replenishment" mode in the bead-packed structure. Following the analysis of Chien and Webb [13], the pore-scale interfacial heat transfer can be idealized as a problem of evaporation on the liquid meniscus in the narrow corner by assuming that the evaporation mainly takes place at the bubble interface within the narrow corner zone, as shown in Fig. 8.14. Other important assumptions are introduced as

(1) The temperatures of both the heated wall and solid particle surface in the narrow corner are constant, T_w.

(2) The vapor phase inside the bubble is saturated.

(3) The curvature of the liquid meniscus varies with the applied heat flux, but is independent of ξ for very small meniscus in the narrow corner. Therefore, the radius of the liquid meniscus, R_m, can be expressed as (see Fig. 8.15)

$$R_m = \frac{1}{2}\left[R_p - \sqrt{R_p^2 - (R_p + R_2 - r_i)^2} \right] \tag{8.24}$$

(4) The temperature distribution is linear within the thin liquid film.

Assuming Eq. (8.24) implies a one-dimensional heat conduction across the liquid film and gives

$$q_l''(\xi) = k_l \frac{T_w - T_{li}}{\delta_l} \tag{8.25}$$

where the liquid film thickness, δ_l, can be geometrically obtained from Fig. 8.14 as

$$\delta_l = R_m - \sqrt{R_m^2 - \xi^2} \tag{8.26}$$

In Eq. (8.25), T_{li} is the local liquid temperature at the liquid-vapor interface. Accounting for the effect of capillary pressure and disjoining pressure on the

liquid meniscus, Chien and Webb [13] approximated T_{li} as

$$T_{\mathrm{li}} = T_{\mathrm{v}}\left(1 + \frac{p_{\mathrm{c}} - p_{\mathrm{d}}}{\rho_{\mathrm{l}} h_{\mathrm{fg}}}\right) \tag{8.27}$$

where the disjoining pressure p_{d} is given by [14]

$$p_{\mathrm{d}} = -\frac{\overline{A}}{\delta_{\mathrm{l}}^3} \tag{8.28}$$

and the Hamaker constant $\overline{A} = 3.11 \times 10^{-21}$(J) for water-glass system [15]. The Eqs. (8.25) and (8.27) can be combined to eliminate T_{li} in favor of T_{w}

$$q_{\mathrm{l}}''(\xi) = k_{\mathrm{l}} T_{\mathrm{v}} \frac{\Delta T_{\mathrm{w}}^* - \left(\dfrac{p_{\mathrm{c}} - p_{\mathrm{d}}}{\rho_{\mathrm{l}} h_{\mathrm{fg}}}\right)}{\delta_{\mathrm{l}}} \tag{8.29}$$

where $\Delta T_{\mathrm{w}}^* = (T_{\mathrm{w}} - T_{\mathrm{v}})/T_{\mathrm{v}}$. The total heat transfer rate through a single pore can be evaluated as

$$Q_{\mathrm{pore}} = 2\pi r_{\mathrm{i}}\left[2\int_{\xi_0}^{R_{\mathrm{m}}} q_{\mathrm{l}}''(\xi)\mathrm{d}\xi\right] = \dot{m}_{\mathrm{r}} h_{\mathrm{fg}} A_{\mathrm{pore}} \tag{8.30}$$

where $A_{\mathrm{pore}} = \sqrt{3}D_{\mathrm{p}}^2/4$. Assuming the meniscus is axisymmetric, the location of the liquid-vapor interface on the heated surface, r_{i}, is related to the vapor fraction on the heated surface, β_{w}, by the following equation

$$r_{\mathrm{i}} = \sqrt{\frac{\beta_{\mathrm{w}} A_{\mathrm{pore}}}{\pi}} \tag{8.31}$$

The length of liquid film along the coordinate, ξ_0, corresponds to the thickness of an equilibrium non-evaporating liquid film, δ_0, or

$$\xi_0 = \sqrt{R_{\mathrm{m}}^2 - (R_{\mathrm{m}} - \delta_0)^2} \tag{8.32}$$

where δ_0 is the film thickness at which no more evaporation takes place. The equilibrium non-evaporating thickness is expressed as [14]

$$\delta_0 \cong \left(\frac{\overline{A}}{\rho_{\mathrm{l}} h_{\mathrm{fg}} \Delta T_{\mathrm{w}}^*}\right)^{1/3} \tag{8.33}$$

Substituting Eq. (8.29) into Eq. (8.30) and rearranging gives

$$Ca = \frac{4\nu_v k_l T_v}{\sigma h_{fg}} \sqrt{\frac{\pi \beta_w}{A_{pore}}} \int_{\xi_0}^{R_m} \frac{\left[\Delta T_w^* - \left(\frac{p_c - p_d}{\rho_l h_{fg}} \right) \right]}{R_m - \sqrt{R_m^2 - \xi^2}} d\xi \tag{8.34}$$

Finally, the dimensionless evaporative heat transfer coefficient is defined as

$$h_e^* = \frac{Ca}{\Delta T_w^*} \tag{8.35}$$

Based on the equations outlined above, the procedures for predicting the evaporative heat transfer coefficient are summarized here. For a given Capillary number (applied heat load), β_w can be determined by Eq. (8.22) at $\eta = 0$. Then, the geometric parameters of the capillary meniscus can be determined from Eqs. (8.24), (8.26) and (8.31). Afterwards, ΔT_w^* is obtained by solving Eqs. (8.32) and (8.34) simultaneously. The dimensionless evaporative heat transfer coefficient, h_e^*, is finally calculated from Eq. (8.35).

The dimensionless evaporative heat transfer coefficient, h_e^*, was predicted as a function of the Capillary number, as shown in Fig. 8.19. With an increase of the Ca (or applied heat flux), h_e^* gradually increases, reaches a peak value (corresponding to Ca_{pk}), and drops rapidly afterwards. The increase of h_e^* during early stages of boiling ($Ca < Ca_{pk}$) may be partly attributed to the fact that the evaporating liquid film in the narrow corner area becomes thinner. Additionally, heat transfer is enhanced also by the violent, repeated dryout-rewetting process observed around the narrow corner, which results from unceasing interactions between the replenishment and interfacial evaporation. This dynamic process can accelerate the collapse of dry areas covering the heated surface, and accordingly intensify the fluid mixing. As the imposed heat flux increases further ($Ca > Ca_{pk}$), most area of the heated surface is covered by vapor (see Fig. 8.17), h_e^* begins to drop due to the loss of evaporating regions. Under this condition, the narrow corner may be surrounded by the vapor phase and the path for the replenishing-liquid flow into the narrow corner may be disconnected. Owing to the lack of liquid supply, the advancement and widespread areas of dryout may follow. If this trend continues, dryout of the heated surface may occur. As seen in Fig. 8.19, the higher heat transfer coefficients are exhibited for smaller pore sizes compared to larger pore sizes. This is due to the process of liquid replenishment being significantly intensified in smaller pore structures due to existing, strong capillary effects. But it can be also found that the Ca_{pk} of a 3.5 mm pore structure is much lower than that of a 7 mm pore structure. As mentioned previously, the problem of spatial limitation becomes more serious with decreasing pore size. Due to the extreme narrowness of the pore space, the vapor fraction on the heated surface increases rapidly with heat flux for smaller pore structure (see Fig. 8.17). Thus, dryout usually occurs much earlier in smaller pore structures.

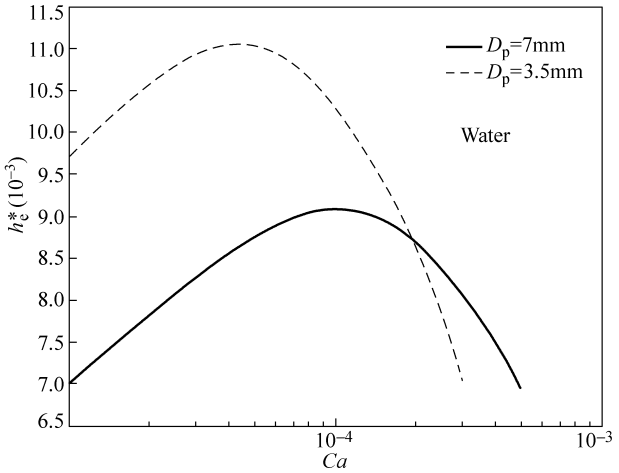

Figure 8.19 Dimensionless evaporative heat transfer coefficient vs. capillary number

8.4 Pore-Scale Bubble Dynamics

8.4.1 Introduction

For boiling on heated surfaces in bead-packed structures, the dryout limit is associated with the dynamic behavior of dry spots. Dry spots occurred simultaneously with the formation of vapor bubbles and were wetted by the replenishing-liquid. Usually, the evaporation occurring at the interface was balanced by the liquid replenishment for the bubble growth, which is a unique characteristic of the boiling on heated surface in bead-packed structures and plays a very important role in the dryout and rewetting process. For sufficiently high heat fluxes, it would occur at some local point on the heated surface where a dry area was not sufficiently wetted and suddenly started growing, sometimes leading to coalescence and widespread dry regions. This widespread growth of vapor patches, and correspondingly limited nucleate boiling activity, caused CHF or dryout of the heated surface.

Although most bubbles coalesced with each other to form large dry areas at a very high heat flux, some wetted regions existed around dry areas, especially in the narrow corner areas. The narrow corner has a very open area which is resistant to dryout even at extremely high heat fluxes due to its intensive capillary wetting effect. The wetting effect of the narrow corner originates from the interfacial evaporation occurring in this narrow corner. Driven by this interfacial mass transport, the replenishing liquid flow was supplied to the heated surface for rewetting. Hence, the entryway of the replenishing liquid must be cut

off for the formation of a stable dry spot on the heated surface. Generally, stable dryout of the heated surface required that the narrow corner was surrounded completely by vapor, i.e. only an isolated wetted region existed. Additionally, the experimental observation showed that the wetting effect also was enhanced by frequent bubble detachment. Dry spots on the heated surface can be completely extinguished by the replenishing liquid following the bubble detachment.

From the discussion above, some conclusions can be reached for the occurrence of stable dryout of the heated surface, described as the followings:

(1) The narrow corner was surrounded completely by vapor which prohibits the liquid replenishment caused by the interfacial mass transport.

(2) Intensive and fast interfacial evaporation was required for ensuring the enlargement and spreading of dry spots before collapse.

(3) The formation of dryout is mainly dependent upon the dynamical characteristics of pore-scale bubbles.

8.4.2 Discrete Rising Bubble

For nucleate boiling, the applied heat flux can be expressed as

$$q''_{\mathrm{w}} = (N_{\mathrm{b}} / A_{\mathrm{w}}) f \, h_{\mathrm{fg}} \rho_{\mathrm{v}} V_{\mathrm{d}} \tag{8.36}$$

where $N_{\mathrm{b}} / A_{\mathrm{w}}$ is bubble population density, f the bubble departure frequency, and V_{d} the volume of departure bubble. These parameters all increase with applied heat flux and will reach their critical values when the applied heat flux is sufficiently high.

The regime of discrete bubbles is characterized by the intermittent generation of single distinguishable bubbles, as sketched in Fig. 8.20(a), where bubbles do not interfere with each other. The center-to-center spacing between two consecutive bubbles with a rising velocity, $\overline{U}_{\mathrm{b}}$, can be derived as

$$L_{\mathrm{c}} = (\tau_{\mathrm{b}} + \tau_{\mathrm{w}}) \overline{U}_{\mathrm{b}} \tag{8.37}$$

where τ_{b} and τ_{w} denote the bubble growth period and waiting time, respectively. For spherical bubbles, L_{c} can be defined as

$$L_{\mathrm{c}} = m D_{\mathrm{d}} \tag{8.38}$$

where m is a multiplier and dependent on the applied heat flux, and D_{d} is the bubble detachment diameter. For boiling in the bead-packed structure, bubbles are deformed and elongated [6], such that

$$L_{\mathrm{c}} = m h_{\mathrm{d}} \tag{8.39}$$

where h_d is the characteristic height at release of the elongated bubble. From Eqs. (8.37) and (8.39) with bubble frequency, $f = \dfrac{1}{\tau_b + \tau_w}$, it follows that

$$f = \frac{\bar{U}_b}{m h_d} \tag{8.40}$$

The bubble release frequency increases with the applied heat flux. Obviously, $m > 1$ for the discrete bubble regime and approaches unity with increasing applied heat flux.

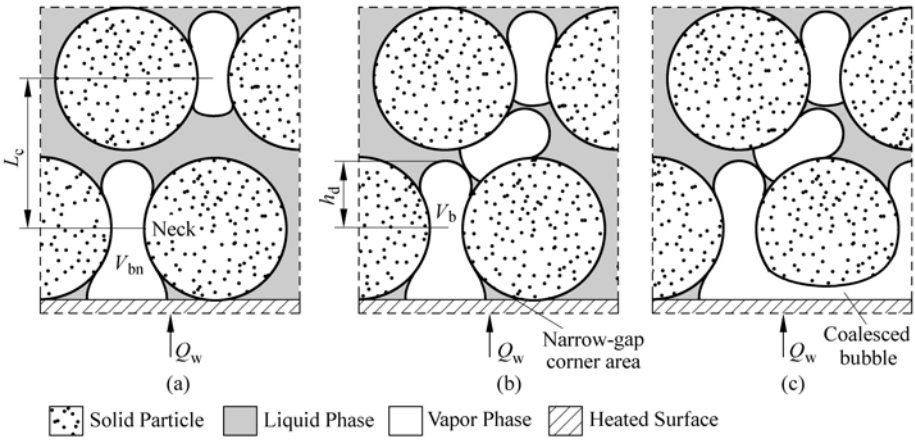

Figure 8.20 Boiling regime
(a) Discrete bubble; (b) Bubble interference; (c) Coalesced bubble

Usually, most small bubbles generated from the heated surface evolve into a primary bubble, where both the shape and departure diameter of the primary bubble were determined and nearly invariable for a given pore size. The departure volume, V_d, of the primary bubble is obtained from the following expression of force balance [9]

$$\Delta\rho g(V_d - V_{bn}) = \sigma\pi\left(\frac{2}{\sqrt{3}} - 1\right)D_p \tag{8.41}$$

where V_{bn} is the volume of the bubble part below the neck, which is nearly equal to half the volume of the cavity, or

$$V_{bn} \cong \frac{V_{cavity}}{2} = \frac{D_p^3}{8}\left(\sqrt{3} - \frac{\pi}{3}\right) \tag{8.42}$$

A pore where primary bubbles can be generated continuously is defined as an

active pore. At low heat fluxes corresponding to the discrete rising bubble regime, only a few pores are activated and randomly distributed on the heated surface, which is mostly covered by wetted regions. Dry spots on the heated surface do not grow and are extinguished easily.

8.4.3 Bubble Departure Interference

After detachment, a bubble will rise through the porous structure due to buoyancy. But the velocity of the rising bubble is restricted by the pore configuration. The existence of the bubble rising limitation means that the bubble frequency will reach a threshold as the heat flux increases. This will happen at a high heat flux condition when the bubble generation capacity exceeds the bubble escape frequency corresponding to the bubble rising behavior in the porous structure. Under this condition, consecutive bubbles interfere with each other (see Fig. 8.20(b)) and form continuous vapor columns, then $m \leqslant 1$. For the critical sitation or m=1, the critical bubble frequency is derived as

$$f_c = \frac{\bar{U}_b}{h_d} \tag{8.43}$$

where h_d can be approximately expressed as [9]

$$h_d \cong \frac{V_d - V_{bn}}{V_{cavity}} D_p \tag{8.44}$$

In a bead-packed structure, the real flow path for the rising bubble is a converging-diverging channel. To simplify the analysis, an elongated bubble was assumed to rise in a vertical triangular column-channel, as illustrated in Fig. 8.21. The rising behavior of a Taylor bubble (elongated bubble) was described as [16]

$$Ca = 5.8 \times 10^{-4} E\ddot{o}^{1.0226} + 2.223 \times 10^{-4} E\ddot{o}^{2.2203} \tag{8.45}$$

where the capillary number is defined as

$$Ca = \frac{\mu_l \bar{U}_b}{\sigma} \tag{8.46}$$

the Eötvös number as

$$E\ddot{o} = \frac{\Delta\rho g D_h^2}{\sigma} \tag{8.47}$$

and hydraulic diameter as

$$D_h = \frac{\sqrt{3}}{6} D_p \tag{8.48}$$

Substituting Eqs. (8.44) – (8.48) into Eq. (8.43) and rearranging yields

$$f_c = \left[1.608\times10^{-5}\left(\frac{\Delta\rho g D_p^2}{\sigma}\right)^{1.0226} + 3.144\times10^{-7}\left(\frac{\Delta\rho g D_p^2}{\sigma}\right)^{2.2203} \right] \frac{\Delta\rho g D_p}{\mu_l} \quad (8.49)$$

As expected, the bubble escape capability decreases with the decrease of pore size. After the bubble frequency reaches a threshold, consecutive bubbles will interfere with each other as heat flux is further increased. The interference between bubbles provides favorable conditions to the growth of dry spots. Under large vapor columns, or mushrooms, dry spots will grow and coalesce with each other.

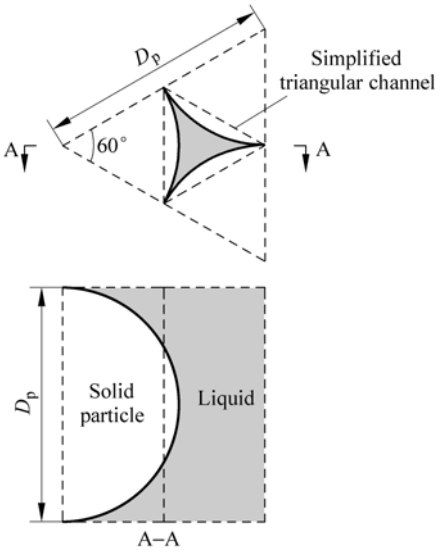

Figure 8.21 Simplified flow path of a rising bubble

8.5 Occurrence of Dryout

8.5.1 Lateral Bubble Coalescence and Local Vapor Patch Formation

For boiling nucleation in the present case, bubble sites showed rather high regularity depending upon the bead-packed structure—only one primary bubble can be formed in each cavity during a bubble cycle (see Fig. 8.14). When the heat flux is sufficiently high, nearly all pores can be activated. Consequently, every

pore can be treated as a fixed bubble site and the critical bubble population density $(N_b / A_w)_c$ is easily derived from pore geometry as

$$(N_b / A_w)_c = \frac{1}{\frac{\sqrt{3}}{4} D_p^2} \tag{8.50}$$

In the experiments with high heat flux, the interaction between neighboring bubbles became very active and significant bubble coalescence was observed on the heated surface. Coalescence of neighboring bubbles made narrow gap corner zones encompassed by vapor bubbles (see Fig. 8.20(c)). This indicated that the liquid replenishment and wetting effects of gap corner areas were greatly repressed, and the balance between evaporation and liquid replenishment was broken. The critical condition or heat flux corresponding to blocking liquid replenishment is the same as Eq. (8.36), that is

$$q_c'' = (N_b / A_w)_c f_c h_{fg} \rho_v V_d$$

Because of the lack of liquid replenishment, several large vapor patches were formed from the coalescence of isolated dry spots as the heat flux was increased. The resident time of these large vapor patches on the surface was greatly increased accordingly. The formation of large dry patches would evoke the occurrence of the complete dryout of the heated surface. Fortunately, intermittent rewetting of the heated surface can still be established repeatedly following the bubble detachment for this boiling regime. It is expected that more strict conditions are required for establishing stable dryout.

8.5.2 Dryout

As noted above, the collapse of local dry patches and transition rewetting follow the bubble detachment. As illustrated in Fig. 8.8, at a very high heat flux repeated alternations of dryout and rewetting invariably occurred during vigorous boiling. Steady dryout would be reached only if the local dry patch evolves into a more stable pattern and the liquid replenishment is hindered before its collapse. Without rewetting, dry areas enlarge quickly and evolve into a continuous vapor film covering the heated surface, where the surface temperature begins to rise and dryout occurs.

For convenience of analyzing problem, the bead-packed structure on the heating surface is simplified to be a regular structure, one bead with six beads surrounding, as shown in Fig. 8.14. The critical condition blocking liquid replenishment, as mentioned above, would be that the bubbles in the six neighboring primary pores are coalescing each other and liquid only exists in the narrow-gap corner. This is actually the most important precondition for dryout occurring on the heating surface.

It is assumed that dryout is complete evaporation of the liquid in a narrow-gap corner, as shown in Fig. 8.14, or the following relation holds if dryout occurs

$$(q_{\mathrm{d}}'' - q_{\mathrm{c}}'')A_{\mathrm{u}}\tau_{\mathrm{s}} = \rho_{\mathrm{v}}V_{\mathrm{gap}}h_{\mathrm{fg}} \tag{8.51}$$

where the unit heating area, A_{u}, is defined as,

$$A_{\mathrm{u}} = \frac{1}{(N_{\mathrm{b}}/A_{\mathrm{w}})_{\mathrm{c}}} \tag{8.52}$$

If the waiting time of bubble formation is negligible compared with the bubble growth period, referring to Fig. 8.14, the minimum time in which six neighboring bubbles coexist, τ_{s}, is

$$\tau_{\mathrm{s}} \cong \frac{1}{6}\tau_{\mathrm{b}} \cong \frac{1}{6f_{\mathrm{c}}} \tag{8.53}$$

Accounting for the movement of the bubble bottom interface, V_{gap} is obtained as

$$V_{\mathrm{gap}} = \frac{\sqrt{3}}{4}D_{\mathrm{p}}^2 h_{\mathrm{base}} - V_{\mathrm{base}} \tag{8.54}$$

where

$$h_{\mathrm{base}} = R\cos\theta \tag{8.55}$$

$$V_{\mathrm{base}} = \frac{2}{3}\pi R^3 - \frac{\pi}{3}(R - h_{\mathrm{base}})^2\left[3R - (R - h_{\mathrm{base}})\right] \tag{8.56}$$

8.5.3 Discussion and Comparison

With the analytical description above, numerical simulation of the dryout behavior was performed for boiling of water in pore structures. The thermal fluid conditions were taken from the experiments, and the properties of water used are listed in Table 8.1. Figure 8.22 illustrates the bubble frequency threshold, f_{c}, representing the capability of a bubble to escape from the pore structure, as a function of pore size. When the pore structure becomes narrower, both drag force and surface tension become strong and significantly restrict the rising of the bubble, and the bubble escape capability recedes with the decrease of pore size, as shown in Fig. 8.22. Apparently, small pore structures would easily induce dryout. This trend is reasonably consistence with current and previous experimental observation [6, 9, 17, 18]. It should be noted that the rewetting process actually is intensified for small pore structures, however, the predicted value of f_{c} is accordingly very small for small pores.

Table 8.1 Thermophysical properties of working fluid

Working fluid	Water
Saturation temperature, T_{sat}	373 (K)
Latent heat of liquid-vapor phase-change, h_{fg}	2260 (kJ/kg)
Density of liquid, ρ_l	958 (kg/m^3)
Density of vapor, ρ_v	0.6 (kg/m^3)
Surface tension, σ	0.0589(N/m)
Dynamical viscosity of liquid, μ_l	2.8×10^{-4} (N·s/ m^2)

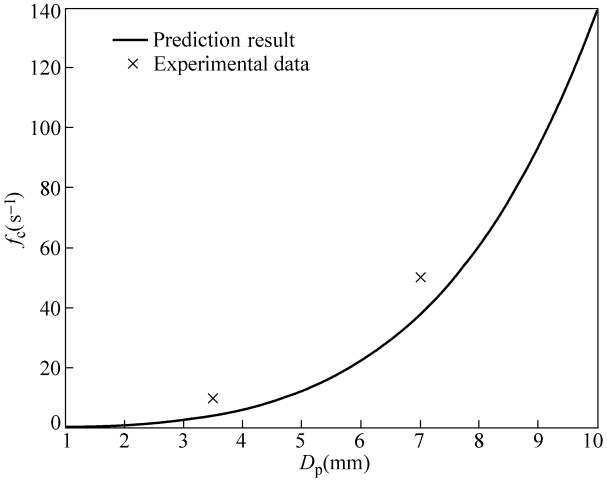

Figure 8.22 Bubble frequency threshold

Obviously, the liquid replenishment clogged due to the difficulty of vapor escape, or the rewetting effect induced by pore structure is repressed by the capability of liquid replenishment. This might also imply that some important factors, influencing the dryout and rewetting behavior in very small pore structures, are not included in present description. Further study is highly necessary to understand these complicated phenomena.

Due to low bubble escape capability and the narrowness of the passage, the interaction of bubbles and dry areas become more active in smaller pore structures. Consequently, large vapor patches surrounding the narrow corner areas easily occur in smaller pore structures compared with those in larger pore structures. The liquid replenishment is restricted when the narrow corner is encompassed with dry areas. The blockage of liquid replenishment emerges at lower applied heat flux for smaller pore structures than that for larger pore structures. A comparison of the critical heat flux blocking liquid replenishment based on the theoretical prediction and the experimental data is illustrated in Fig. 8.23. Though only two experimental data are available, the theoretical results show reasonably similar

trend. For larger pore scales both are likely coincident, but the theoretical analysis gives under predictions for smaller pore scale due to the sub-predicted value of f_c.

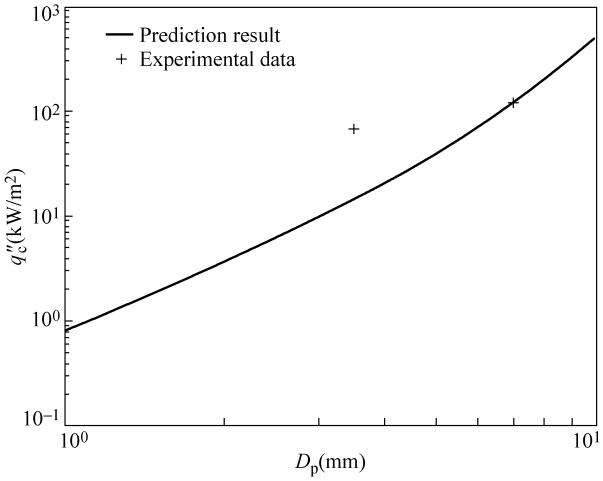

Figure 8.23 Heat flux blocking liquid replenishment

Also, the enlargement of local dry areas is easier and faster for smaller pore structures, and the variation of dryout heat flux with pore size is illustrated in Fig. 8.24. The experimental data from Dhir [19] was used for comparison. Very clearly, the predictions are reasonably consistent with the experimental data for larger bead-packed pore scale. However, the prediction is far from the available

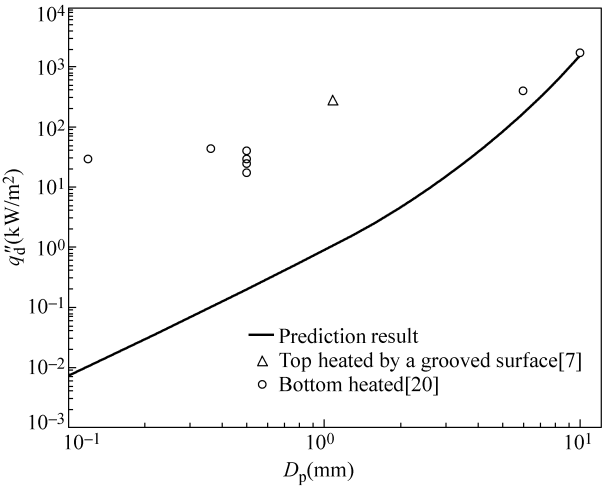

Figure 8.24 Comparison of predicted with measured dryout heat flux

experimental results for small pore sizes, and this trend is enlarged as the solid bead diameter becomes smaller. Apparently, although the bubble escape possibility is repressed by the extreme narrowness of the smaller pore scale, the rewetting effect is actually intensified for the smaller pore size. The theoretical predictions also were compared with the dryout heat flux in a porous structure heated from above using grooved surface reported by Zhao and Liao [20]. In this case owing to the existence of vapor channels near the heated surface, the capability for bubble venting from the heated surface was enhanced. Accordingly, the dryout heat flux of this system increased.

Although above-discussed comparisons truly indicate that the dryout and rewetting are very complicated to theoretically describe so far. The present work is only an attempt to preliminarily understand some important influences.

References

[1] C. Y. Wang, P. Cheng. Multiphase Flow and Heat Transfer in Porous Madia. In：J. P. Hartnet, T. F. Irvine, Y. I. Cho, et al.(Eds.). Advances in Heat Transfer, 30: 93-196. New York: Academic Press, 1997.

[2] G. P. Peterson. An Introduction to Heat Pipes: Modeling, Testing and Applications. New York: John Wiley & Sons Inc., 1994.

[3] A. Faghri. Heat Pipe Science and Technology. Washington DC: Taylor & Francis, 1995.

[4] Jentung Ku. Overview of Capillary Pumped Loop Technology, HTD-Vol.236, Heat Pipes and Capillary Pumped Loops. ASME, 1993.

[5] Jentung Ku. Recent advances in capillary pumped loop technology. 1997 National Heat Transfer Conference. Baltimore, MD, 1997.

[6] Z. Wang, X. F. Peng, T. Liu. Visualization of boiling phenomena in a bead-packed structure. Experimental Heat Transfer, 15(3): 177 – 189, 2002.

[7] Z. Wang, X. F. Peng, J. M. Ochterbeck. Dynamic bubble behavior during boiling in bead-packed Structures. Int. J. Heat and Mass Transfer, 47(22): 4771 – 4783, 2004.

[8] Z. Wang, J. M. Ochterbeck, X. F. Peng. Boiling dryout on flat surfaces covered with bead-packed structures. Heat and Mass Transfer, 43: 405 – 414, 2007.

[9] X. F. Peng, Z. Wang, D. J. Lee. Dynamic behavior of bubble interface during boiling. Journal of Thermal Science, 11(4): 308 – 319, 2002.

[10] I. Fatt, W. A. Klikoff. Effect of fractional wettability on multiphase flow through porous media. Transactions, AIME, 216: 426 – 432, 1959.

[11] M. C. Leverett Capillary behavior in porous solids. Transactions, AIME, 142: 152 – 169, 1941.

[12] K. S. Udell. Heat transfer in porous media heated from above with evaporation, condensation, and capillary effects. Journal of Heat Transfer, 105 (2): 485 – 492, 1983.

[13] L. H. Chien, R. L. Webb. A nucleate boiling model for structured enhanced surfaces. International Journal of Heat and Mass Transfer, 41 (14): 2183 – 2195, 1998.

[14] P. C. Wayner Jr., Y. K. Kao, L. V. Lacroix. The interline heat transfer coefficient of an evaporating wetting film. International Journal of Heat and Mass Transfer, 19 (5): 487 – 492, 1976.

[15] J. Gregory. The calculation of Hamaker constants. Advances in Colloid and Interface Science, 2: 396 – 417, 1969.

[16] Q. Liao, T. S. Zhao. Modeling of Taylor bubble rising in a vertical mini noncircular channel filled with a stagnant liquid. International Journal of Multiphase Flow, 29 (3): 411 – 434, 2003.

[17] Z. Wang, X. F. Peng, B. X. Wang. Experimental investigation of nucleate boiling in a bead-packed structure. Journal of Engineering Thermophysics, 23 (6): 742 – 744, 2002.

[18] Z. Wang, X. F. Peng, B. X. Wang. The effect of limited space on nucleate boiling: boiling characteristics in a bead-packed structure. In: Proceedings of 2002 Chinese National Heat Transfer Conference, Shanghai, China, 369 – 372, 2002.

[19] V. K. Dhir. Heat transfer from heat-generating pools and particulate beds. J. P. Hartnet, T. F. Irvine, Y. I. Cho, et al.(Eds.). Advances in Heat Transfer, 29: 1 – 57. New York: Academic Press, 1997.

[20] T. S. Zhao, Q. Liao. On capillary-driven flow and phase change heat transfer in a porous structure heated by a finned surface: measurements and modeling. International Journal of Heat and Mass Transfer, 43 (7): 1141 – 1155, 2000.

9 Explosive Boiling

Abstract With the rapid development of practical engineering applications in cooling of electronic device, LED and laser power source, thermal management of aerospace and other systems and devices, micro energy systems and micro-manufacturing have become a strong technique to understand the microscale transport phenomena and the notable shift of thermal science and heat transfer research from the macroscale to microscale. So far, very few experiments have been conducted to investigate the boiling of static liquid in microtubes and/or microchannels, which might be very helpful to analyze the nature of micro-boiling in microtubes and microstructures.

In this chapter, a series of experiments was conducted to visually observe boiling nucleation phenomena in mini/micro capillary tubes employing a high speed CCD. In some capillary tubes with inner diameter from 1.5 mm to 0.05 mm, the liquid was emitted instantaneously at a higher heat flux, rather than generating nucleate boiling, which is referred as liquid exploding emission. In mini tubes of $D_i = 1.5$ mm, violent jet flows with macro bubbles were formed, and the liquid was almost totally emitted out of the tube. While in micro tubes of $D_i = 50 - 200$ μm, the emission was much stronger, and only fog-like jet flow was observed consisted of extremely tiny bubbles, which indicates the mechanism of nucleation different from that in mini tubes. It is expected that the scale effects intensely influence not only the onset of emission, but also the strength and nature of emissions. Especially, for micro tubes, both critical emission heat flux and temperature corresponding to exploding emission were measured with different heating lengths and arrangements of two end sections. Boiling nucleation and liquid film evaporation played critical roles in different stages during exploding emission. Dimensionless critical emission volumetric heat was introduced to describe the conditions of the emission instead of heat flux, and theoretical discussions were conducted to explore the influences of thermal properties and geometrical configuration, particularly heating length and asymmetry of two end sections of tubes.

Keywords mini/micro capillary tubes, exploding emission, jet flows, fog-like jet flow

X. Peng, *Micro Transport Phenomena During Boiling*

9.1 Experimental Phenomena

Microscale boiling has been widely employed in many practical applications, particularly for heat removal and/or heat dissipation at very high energy fluxes/densities. Exploring complex phenomena, indecisive and mystical physical mechanisms of microscale boiling and associated heat transfer have already become one of the most attractive research topics in the world [1 – 6].

9.1.1 Visual Observation Test

Figure 9.1 schematically illustrates the experimental setup for mini tubes. The test section was a transparent mini capillary tube made of pyrex glass with inner diameter $D_i = 1.5$ mm and outer diameter $D_o = 3.5$ mm. Two sides of the test section were connected with the left and right vessels containing the ethanol liquid, respectively. High speed CCD with the highest speed of 16000 ft/s was utilized to capture the phenomena visibly by means of a microscope. Direct current power supply was employed as the source of the wire heater winded around the test section. Both the voltage and current applied to the heater were measured to calculate the heat supply.

Before experiments began, ethanol was infused into the vessels and mini tube connecting with two vessels. For escaping the possible air in the mini tube, the mini tube was preheated for a while. Then the power supply was turned on for starting the experiment and increased slowly. The whole nucleation process was recorded by high speed CCD.

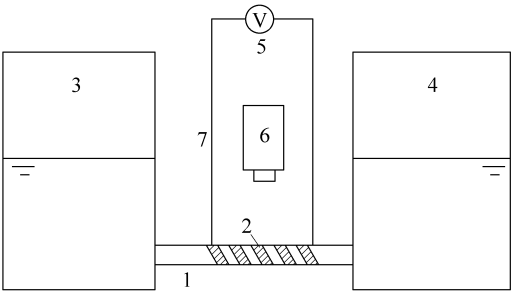

Figure 9.1 Experiment setup for mini tu bes
1–Test section of mini capillary tube; 2–Heater; 3–Left vessel; 4–Right vessel;
5–Power supply (DC); 6–CCD; 7–Electrical wires

The experimental system for micro tubes is shown in Fig. 9.2. An extremely small capillary tube filled with de-ionized water was located horizontally in the air, the transparent metal film was used as the heater connected to the direct electrical source. High speed CCD was employed to visually record the dynamical

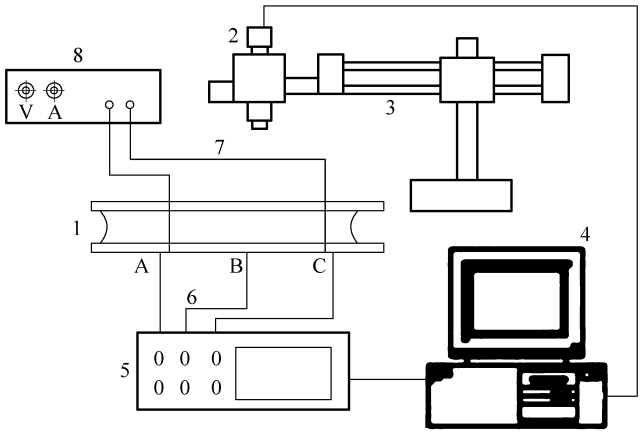

Figure 9.2 Experimental setup for micro tubes
1–Test Section: Extremely small tube; 2–CCD; 3–Microscope; 4–Computer; 5–Data collection equipment; 6–Thermocouple; 7–Electrical wires; 8–Power supply (DC/AC)

Table 9.1 Geometry parameters of tested micro tubes

Diameter (μm)	Length (μm)	Heating style	L_l^*	L_h^*	L_r^*	D_i^*	V_h^*
50	20	8-4-8	4.00E-01	2.00E-01	4.00E-01	2.50E-03	9.820E-07
		7-6-7	3.50E-01	3.00E-01	3.50E-01	2.50E-03	1.470E-06
		6-8-6	3.00E-01	4.00E-01	3.00E-01	2.50E-03	1.960E-06
		3.5-10.5-3.5	2.00E-01	6.00E-01	2.00E-01	2.50E-03	2.950E-06
100	20	9-2-9	4.50E-01	1.00E-01	4.50E-01	5.00E-03	1.960E-06
		8-4-8	4.00E-01	2.00E-01	4.00E-01	5.00E-03	3.930E-06
		6-8-6	3.00E-01	4.00E-01	3.00E-01	5.00E-03	7.850E-06
		5-10-5	2.50E-01	5.00E-01	2.50E-01	5.00E-03	9.820E-06
		2-16-2	1.00E-01	8.00E-01	1.00E-01	5.00E-03	1.570E-05
200	20	8-4-8	4.00E-01	2.00E-01	4.00E-01	1.00E-02	1.570E-05
		7.3-5.3-7.3	3.65E-01	2.65E-01	3.65E-01	1.00E-02	2.080E-05
		6-8-6	3.00E-01	4.00E-01	3.00E-01	1.00E-02	3.140E-05
	30	13-4-13	4.33E-01	1.33E-01	4.33E-01	1.00E-02	1.050E-05
		11-8-11	3.67E-01	2.67E-01	3.67E-01	1.00E-02	2.090E-05
		9-12-9	3.00E-01	4.00E-01	3.00E-01	1.00E-02	3.140E-05
		8-14-8	2.67E-01	4.67E-01	2.67E-01	1.00E-02	3.670E-05
		4-22-4	1.33E-01	7.33E-01	1.33E-01	1.00E-02	5.760E-05
		12-6-12	4.00E-01	2.00E-01	4.00E-01	1.00E-02	1.570E-05
		6-18-6	2.00E-01	6.00E-01	2.00E-01	1.00E-02	4.710E-05

process and images of the phenomena with a suitable microscope. Three thermocouples were installed on the outside tube wall, two exactly close to two electrodes connecting power wire to the film, and one located at the centre between two ends of the heating section, respectively, or three points A, B, C shown in Fig. 9.2.

The tested micro tubes have inner diameter (D_i) of 200, 100 and 50 μm, and outer diameter (D_o) of 320, 375 and 375 μm, respectively. In each test, the capillary tube was first filled with deionized water in the whole length (L). Then applied heat flux on heat section (L_h) was increased very slowly to reach a proper value. The voltage, current, water temperature and wall temperatures were all recorded and stored into the computer simultaneously. Finally turn off the electrical source.

In micro tube experiments an infrared scanner made by FLIR Corporation was employed to visually show the outside wall temperature of the micro tubes. The resolution of this scanner is 50 μm and the highest record frequency is 50 ft/s. The wall temperature during nucleation in micro tube could be instantaneously and clearly recorded to give the convenience of discovering the novel phenomena.

In present experiments, jet flows or very violent jet flows from mini tubes and liquid exploding emission from micro capillary tubes were visually observed, rather than normal nucleation and visible bubble generation as the liquid was heated to very high temperature or a high applied heat fluxes corresponding to normal boiling conditions for usual cases.

9.1.2 Jet Flow in/from Mini Tubes

The typical experimental observations are illustrated in Fig. 9.3 for mini tubes. For convenience to describe and discuss the phenomena, the test tube is divided to three regions, namely as left unheated region (LUR), heated region (HR), utilizing the heating wire winding around the tube and right unheated region (RUR). In the initial stage of heating, both temperature and heat flux in HR were increased by enlarging the input voltage of the heater. Before they reached a critical value, convective heat transfer occurred likely in a very small open closure, and no phase change was observed. As the tube was heated at a certain temperature or at a certain heat flux corresponding to Fig. 9.3(a) defined to be the moment of $t = 0$ ms, some phenomena associated with phase change would be initiated or emerge. After only 2 ms, a fog-like flow firstly emerged at the bottom of the heating region evolving into LUR and RUR in the tube, as shown in Fig. 9.3(b), which is the initial stage of the jet flow. Very clearly, there is an interface observed between the liquid and fog-like flow, in HR, RUR and LUR, from the modified images shown in Figs. 9.4(a) and (b), exactly corresponding to Figs. 9.3(a) and (b). At $t = 4$ ms, fully developed stage was reached and fog-like jet flow fully occupied the tube, or actually pushed the inside liquid out of the tube, as shown in Fig. 9.3(c). Another 2 ms later, the inside ethanol liquid was

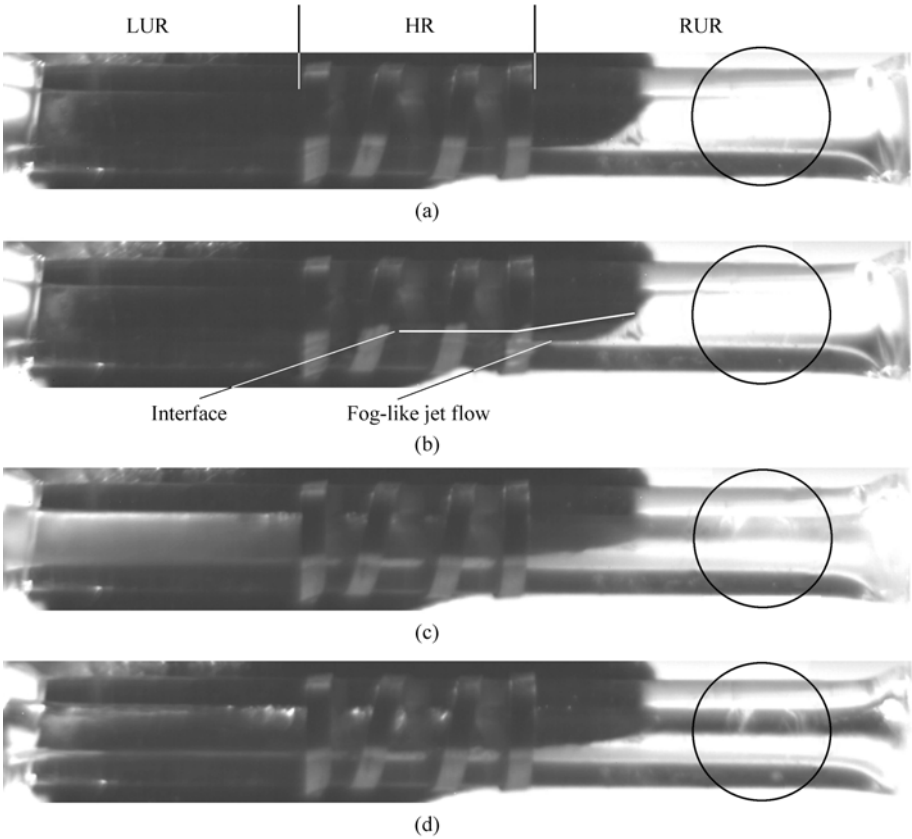

Figure 9.3 Evolution of fog-like jet flow in a mini tube
(a) $t = 0$ s, the moment before emission; (b) $t = 2$ ms, the initial stage of emission; (c) $t = 4$ ms, fully developed fog-like jet flow; (d) $t = 6$ ms, end of jet flow evolution

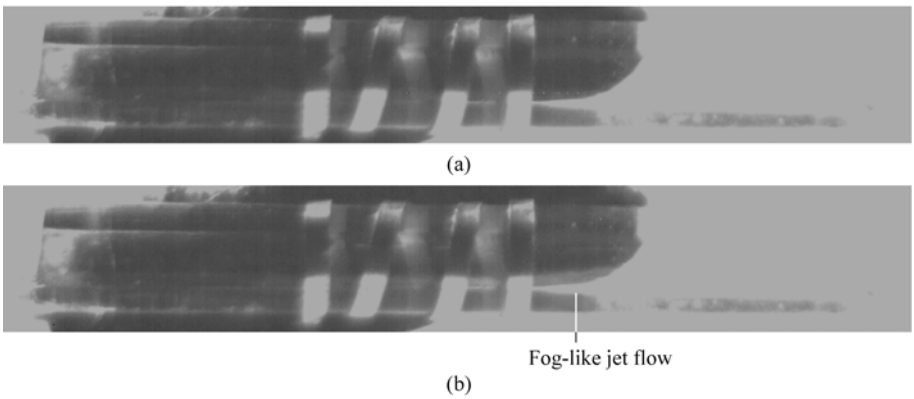

Figure 9.4 Modified images of fog-like jet flow in the tube
(a) $t = 0$ s, modified image of the moment before emission;
(b) $t = 2$ ms, modified image of the initial stage of emission

almost all pushed out of the tube. The whole emission process in mini tube was less than 6 ms, which is very short.

It is difficult to exactly identify what the fog-like jet flow is in Figs. 9.3(b) and (c). Wang et al. [7] observed several modes of jet flows, high-energy liquid jet, fog-like jet, cluster-like jet, bubble-forming jet, bubble-bunch jet and bubble-top jet during the subcooled nucleate boiling on a very fine wire at relatively higher heat fluxes. Figure 9.5 presents some images of high-energy liquid jets and fog-like jets without visible bubbles, very similar to the fog-like jet flow in Figs. 9.3(b) and (c). It may be expected that the jet flow should be one important boiling mode and different jet flows may also expected due to the scale effect (or diameter) of mini tubes. Actually, several modes of jet flows were observed and became much stronger as decreasing the diameter of the tube in recent experiments.

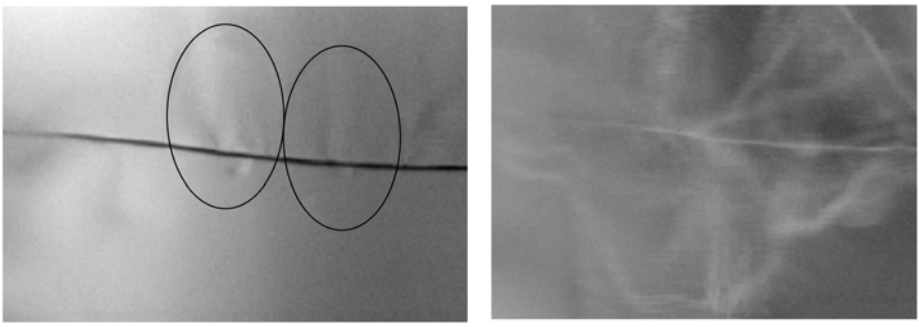

Figure 9.5 Jet flow phenomena during nucleate boiling on heated tiny wire [7]
(a) High-energy liquid jets; (b) Fog-like jets

Wang [8] reported the speed of the high-energy jets and fog-like jets are 10 – 15 mm/s. However, the speed of the fog-like jet flow in a mini tube is much larger and can reach 500 mm/s at least in the experiments. In the present experiments, subcooled nucleation occurred in mini tubes which was a highly confined space and the energy was hard to dissipate and easy to break out in a certain direction, just like the two sides of the tube. This is expected to enhance the jet flow and results in some different behavior from the jet flows on a wire in a liquid poor, as observed by Wang et al. [7].

Behavior of the liquid in the vessel, or the phenomenon at the end of the mini tube is illustrated in Figs. 9.6(a), (b) and (c), corresponding to the cases in Figs. 9.3(b), (c) and (d), respectively. At $t = 2$ ms, very steady state and peaceful interface between liquid and air was observed, as clearly shown in Fig. 9.6(a). At this moment, power of the initial stage of jet flow was not strong enough to break

the interface. While at 4 ms, since the fog-like jet flow fully developed in and extended to outside of the tube, the liquid at the exit was violently disturbed and the free surface was broken with the huge pushing power caused by the jet flow in the mini capillary tube. In the area near the exit of mini tube the liquid was burst out very high and the jet flow actually penetrated the free surface and burst into the air. This indicates the jet flow was very strong at this moment and is different from the jet flows observed by Wang et al. [7]. At $t = 6$ ms in Fig. 9.6(c), or after the liquid almost went out and jet flow disappeared in the tube, the liquid in the vessel was sprayed out very violently. This implies that the increase of wall temperature and heat flux would intensify the jet flow, and decreasing tube diameter would be expected to have the same effect.

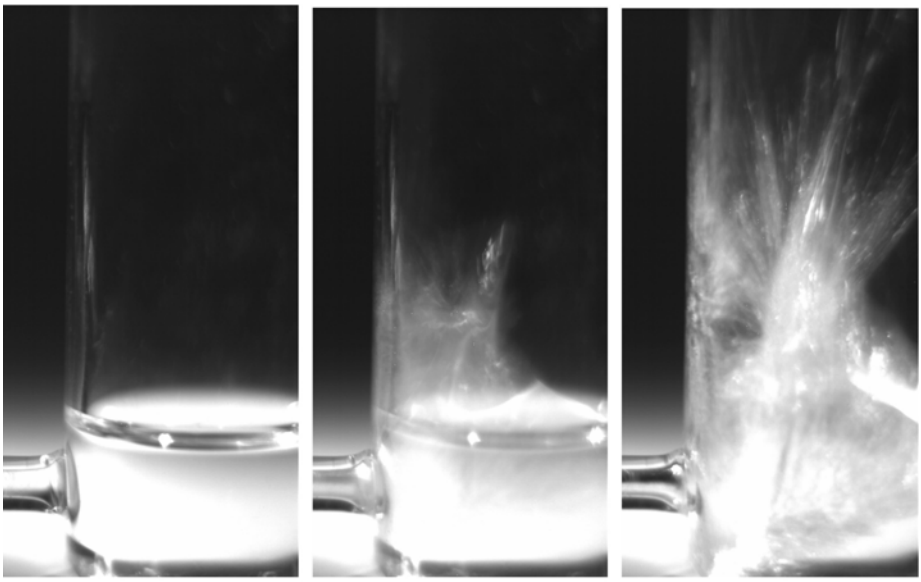

Figure 9.6 Behavior of liquid in vessel
(a) $t = 2$ ms; (b) $t = 4$ ms; (c) $t = 6$ ms

9.1.3 Exploding Emission from Micro Tubes

In the experiments of micro capillary tubes, the extremely fast liquid or vapor bursting was observed rather than clear jet flows. This is referred as exploding emission for distinguishing this from the jet flows discussed above and due to extremely fast nucleation of liquid in the tubes at very high wall temperature or heat flux. Before the exploding emission, nucleation and/or bubble generation

was not observed, meaning that normal nucleate boiling was very difficult in the very small tubes. Figure 9.7 presents the images of a whole process of liquid/vapor exploding emission recorded by the high camera at the speed of 5000 fps in a tube long 20 mm and inner diameter 200 μm, and the length distribution of three sections was 6-8-6. $t = 0$ ms refers to the moment just before the emission. Very clearly, water was emitted very fast out of the tube when the heat flux reached a critical value, and at 0.2 ms a very thin water film about 25 μm in thickness formed on the tube surface immediately after the emission, as shown in Fig. 9.7(b). At 0.4 ms there was no water film left in the tube, as shown in Fig. 9.7(c). This means that the film was shrunk to a water column somewhere in the tube after a very short time the power was shut down, which is also expected being caused by the temperature decrease of the tube.

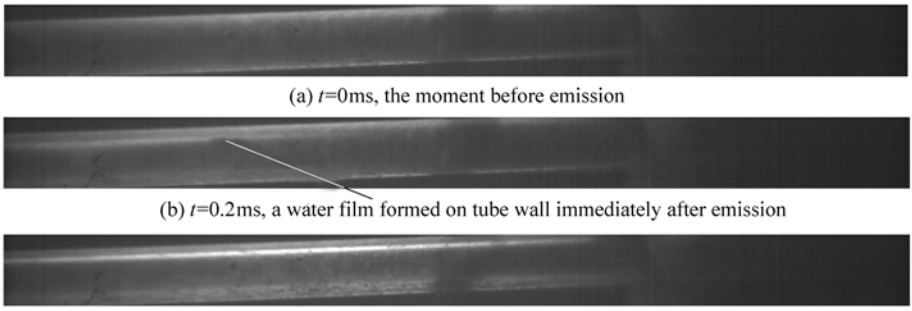

(a) t=0ms, the moment before emission

(b) t=0.2ms, a water film formed on tube wall immediately after emission

(c) t=0.4ms, film disappearance after power shut down

Figure 9.7 Water emission from the tube ($D_i = 200$ μm, $L = 20$ mm, 6-8-6)

Behavior of water exploding emission in the left section is shown in Fig. 9.8 for a micro capillary tube of $D_i = 200$ μm, $L = 20$ mm and '6-8-6' distribution. Figure 9.8(a) depicts the normal state before the emission with the clear interface between circumstance air and water in the tube. At 0.2 ms, the interface became blurred as shown in Fig. 9.8(b), and actually water was heated to a critical state ready to violent phase change, which is likely a metastable state of water to cause exploding emission. Figure 9.8(c) shows the strong emission was formed ($t = 0.4$ ms). At $t = 0.6$ ms, as shown in Fig. 9.8(d), the most water in the tube was emitted and a water film formed on the tube surface. In the later stage, Fig. 9.8(e), the water emission stopped and only a little vapor flew out of the tube, which might depend upon the evaporation of the water film due to further tube cooling or heating induced by the delay of power turnoff. In Fig. 9.8(f) the emission was totally stopped and the water film began to shrink to form column again driven by capillary force.

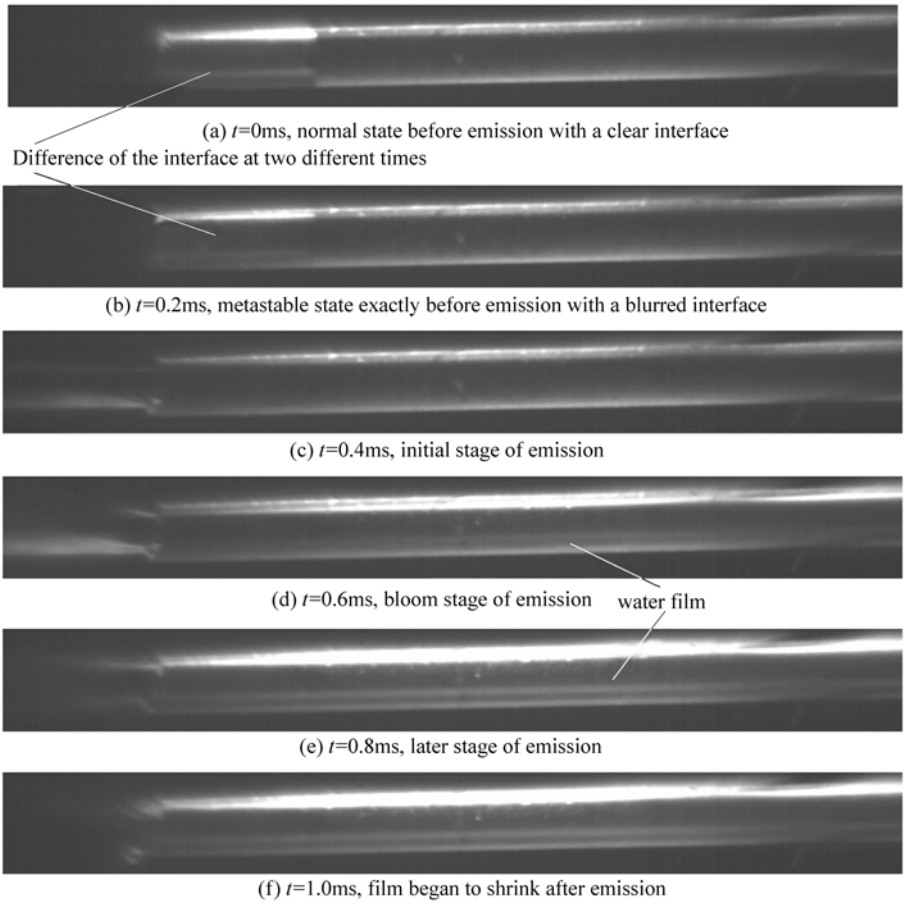

Figure 9.8 Behavior of left section during emission (D_i = 200 μm, L = 20 mm, '6-8-6')

9.2 Temperature Behavior During Emitting

Figure 9.9 presents instantaneous wall temperature of the tested micro tube during exploding emitting, showing high surface temperatures in heating section and lower temperature in LUR and RUR. Temperature variations of four locations, corresponding to LUR, HR-left, HR-right and RUR in Fig. 9.9, during the exploding emitting are plotted in Figs. 9.10 and 9.11 with a time interval 0.02 s.

Four different stages, corresponding to the four regions in Fig. 9.10, can be divided for the whole emitting as preheating, emitting, heating remain and unheating duration. Local magnified temperature feature of emitting and preheating stages is shown in Fig. 9.11. From Fig. 9.10 there was a smooth increase of temperatures at two heat locations during preheating as a result of enlarging

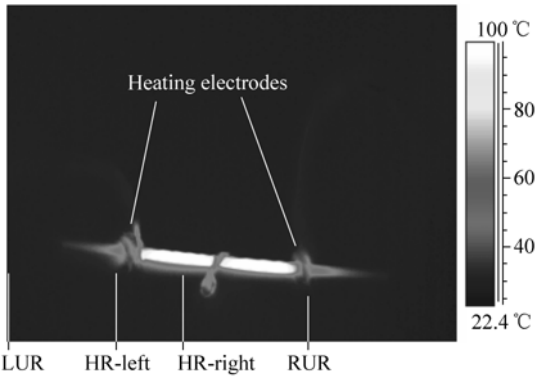

Figure 9.9 IR image of surface temperature during emitting

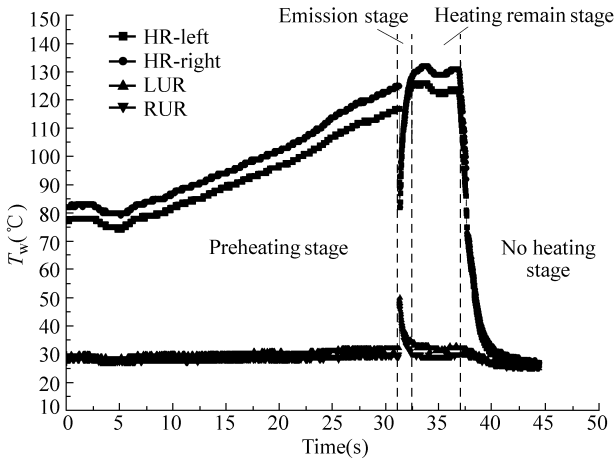

Figure 9.10 Temperature variations at four locations during exploding emitting

heating power, and there is nearly no temperature change in unheating regions, 30℃ in LUR and 32℃ in RUR. As soon as the critical heat flux or wall temperature was reached, exploding emission was triggered, with 117℃ at HR-left and 125℃ at HR-right. Then intense vaporization in heating section of the tube pushed out all the liquid in both sides immediately, as shown in Fig. 9.8(a) – (f). Meanwhile an ultra thin film formed on the tube wall, as shown in Fig. 9.7(b) and Fig. 9.8(d). This film would be rapidly evaporated and take huge heat from the wall. Accordingly, there was a rapid temperature drop to a minimum value of 82℃ at both left and right heating locations, causing a temperature difference of about 43℃, as clearly shown in Fig. 9.11. And then the temperature rebounds over 125℃ due to heating remain and decrease of liquid film thickness as evaporating. The time of reaching the minimum value was the exactly time when liquid film dried out. And the consequent temperature rebounding stage was induced by the remaining heating without liquid film. Very clearly, the spanning time during the

temperature drop was about 0.04 s, which represents the existence time of the liquid film on the tube wall, a very short time. Before the emission occurrence there is a temperature difference about 8℃ between HR-left and HR-right, which is may be induced by the heterogeneous heating. However, when dropping to the minimum temperature during emitting, they had the same value, which is expected to the homogeneous spreading of the liquid film happened and it had uniform heat transfer performance on the tube wall. Another characteristic of the heating curves during emitting is that the velocity of temperature drop is much larger than that of temperature rebounding up. This may be highly dependent of complicated and intense convection with thin film evaporation, which has a huge heat transfer coefficient.

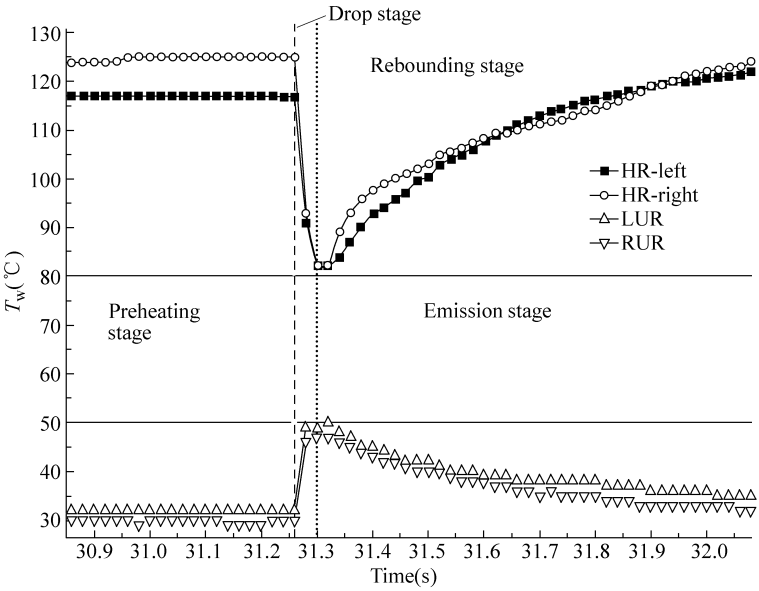

Figure 9.11 Local temperature behavior during preheating and emitting

Look back to the two curves at the two regions without heating. When the exploding emission occurred, the temperatures raised rapidly as a result of the hot liquid emitting out and contacted and heated the tube wall. From Fig. 9.11 it could be seen that 0.02 s was taken for the two end sections without heating to reach the maximum temperature, but for the heating section was 0.04 s to the minimum one. Apparently, when emission occurred, the liquid was emitted very fast and the liquid film formed and attached to the whole capillary tube wall including all sections with and without heating less than 0.8 ms, as shown in Fig. 9.8(e). Consequently, the heat transfer coefficient may be the same for all regions. It is worth to note that this resulted in a temperature difference about 90℃ for two regions without heating and only 40℃ for two regions with heating.

This may indicate that the emitted liquid and/vapor had/carried very high energy and very good heat transfer performance.

9.3 Theoretical Discussion

9.3.1 Geometrical Parameters

The observed experimental phenomena and some important parameters describing them, such as wall temperature and heat flux initiating exploding emission, are expected to be closely related to the geometrical parameters and configuration, including inner diameter and different section lengths of a test tube, L_l, L_h, L_r. The experiments show that the critical emitting heat flux $q''_{i,c}$ initiating the emission was greatly influenced by inner diameter (D_i), distribution of two end sections and their arrangement (equal arrangement $L_l = L_r$ or non-equal arrangement $L_l > L_r$), heating length (L_h) and whole length L of a test tube. An attempt was made to explore the relation between influencing factors and the critical emitting heat flux, or scaling analysis was introduced to correlate experimental data effectively and obtain correlations to describe and understand the emission and associated phenomena.

Some dimensionless geometrical parameters, dimensionless left, heating and right lengths, diameter and volume, are introduced as the followings, respectively.

$$L_l^* = L_l / L \tag{9.1}$$

$$L_h^* = L_h / L \tag{9.2}$$

$$L_r^* = L_r / L \tag{9.3}$$

$$D_i^* = D_i / L \tag{9.4}$$

$$V_h^* = L_h^* \cdot \frac{\pi}{4} D_i^{*2} \tag{9.5}$$

9.3.2 Critical Emitting Heat Flux

Heat fluxes and temperatures were experimentally measured for exploding emission occurring in different tested tubes. Here specific volumetric heat transfer, heat transferred into liquid per unit volume, is introduced instead of heat flux to describe the critical value of the emission.

In a microchannel or tube, the following relation was derived from thermodynamics aspects of phase transition to express the minimum heat transfer initiating boiling nucleation [9],

$$q''_{\mathrm{i,n}} = \frac{h_{\mathrm{lv}} a_{\mathrm{v}}}{c\pi(v''-v')D_{\mathrm{i}}} = \frac{h_{\mathrm{lv}}}{c\pi(v''-v')D_{\mathrm{i}}} \cdot \frac{k_{\mathrm{v}} v''}{c_{\mathrm{p,v}}} \tag{9.6}$$

where c is an empirical constant and is taken as unit in this paper for simplifying analysis without losing its generality. Using Eq. (9.6), dimensionless critical emitting heat flux is expressed as

$$q''_{\mathrm{i,c}}{}^{*} = q''_{\mathrm{i,c}} / q''_{\mathrm{i,n}} = q''_{\mathrm{i,c}} / \left(\frac{h_{\mathrm{lv}}}{c\pi(v''-v')D_{\mathrm{i}}} \cdot \frac{k_{\mathrm{v}} v''}{c_{\mathrm{p,v}}} \right) \tag{9.7}$$

Since emission occurred in a very narrow temperature range close to saturation one, 100℃ to 150℃, the properties of the working fluid are considered as constant, and average values are taken in this investigation. Then dimensionless specific volumetric heat q'''^{*}_{i} is derived as

$$q'''^{*}_{\mathrm{i,c}} = q''^{*}_{\mathrm{i,c}} / \left(\frac{\pi}{4} D^{*}_{\mathrm{i}} \right) \tag{9.8}$$

The experimental results of q'''^{*}_{i} are presented as the function of dimensionless volume, $V_{\mathrm{h}}{}^{*}$, in Fig. 9.12 for the tested tubes having two equal end sections or symmetrical arrangement of two end sides and different inner diameters of 50, 100 and 200 μm. Very clearly, the dimensionless specific volumetric heat rapidly decreases with the increase of dimensionless volume of heating section. By correlating the data in Fig. 9.12 (a) a semi-empirical correlation of q'''^{*}_{i} and $V_{\mathrm{h}}{}^{*}$ is obtained as.

$$q'''^{*}_{\mathrm{i,\,c},\varepsilon=0} = 0.0692 / V_{\mathrm{h}}{}^{*0.71} \tag{9.9}$$

In Fig. 9.12(b), the empirical correlation, from Eq. (9.9), is compared with experimental data, and they are within a deviation of $\pm 25\%$, showing a reasonable good agreement with each other.

Equation (9.9) can be rewritten in dimension form as,

$$q'''_{\mathrm{i,\,c}\,\varepsilon=0} = \frac{0.0262 h_{\mathrm{lv}} a_{\mathrm{v}}}{(v''-v')L_{\mathrm{h}}^{0.71} D_{\mathrm{i}}^{2.42}} L^{1.13} \tag{9.10}$$

$$q''_{\mathrm{i,\,c}\,\varepsilon=0} = \frac{0.0205 h_{\mathrm{lv}} a_{\mathrm{v}}}{(v''-v')L_{\mathrm{h}}^{0.71} D_{\mathrm{i}}^{1.42}} L^{1.13} \tag{9.11}$$

Equation (9.10) indicates that the critical emitting specific volumetric heat is reversely proportional to inner diameter, D_{i}, with an exponent of 2.42 and increases

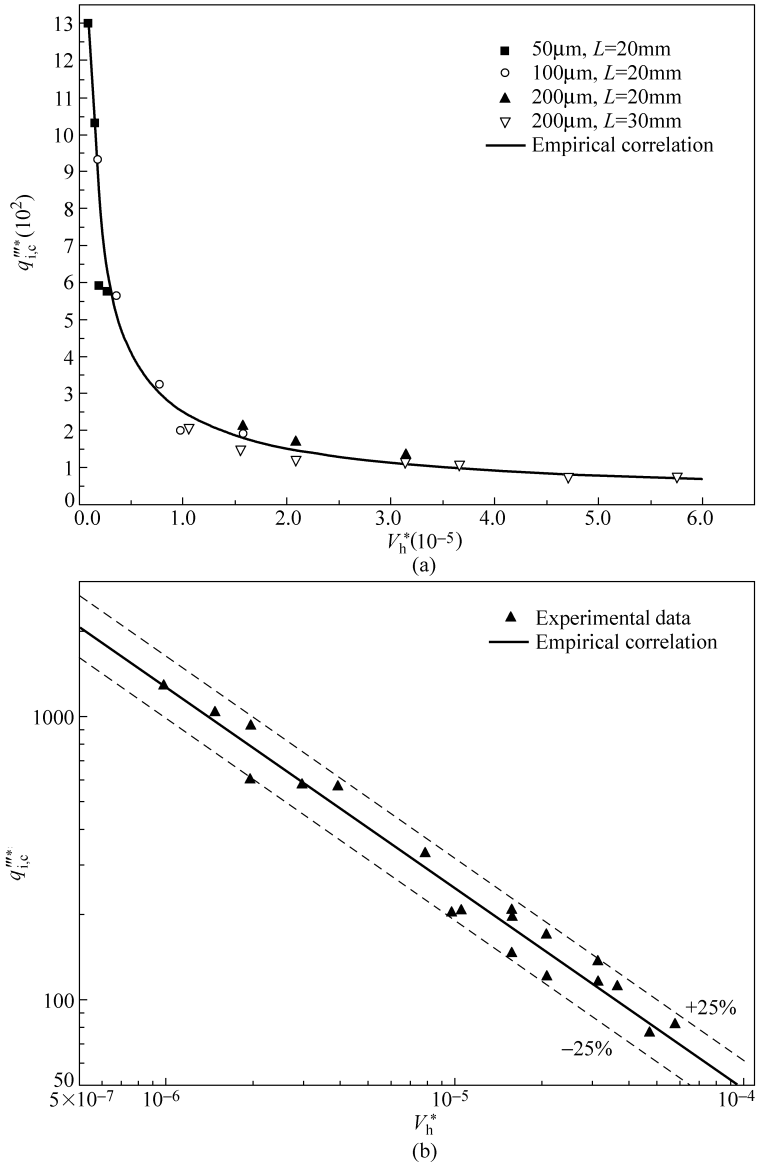

Figure 9.12 Change of $q_i'''^*$ with V_h^* for micro tubes having two equal end sections (a) Experimental results; (b) Comparison of semi-empirical correlation with experimental data

as an exponent function of tube length L. Obviously, for specified L_h and D_i the increase of tube length expands liquid volume in two end sections, and this accordingly increases the resistance of the emission at the both tube ends. For specified D_i and L increase of L_h decreases the critical emitting specific volumetric heat, which actually weakens the emitting resistance in the two end sections.

Equation (9.11) displays similar regularities for the critical emitting heat flux, except replacing the exponent of D_i, or 2.42 with 1.42. These discussions strongly indicate that smaller tubes require much higher specific volumetric heat to induce exploding emission, and exploding emitting phenomenon becomes much stronger as tube diameter is decreased.

And also, the semi-empirical correlation from Eq. (9.11), or experimentally obtained critical emitting heat flux is close to the critical nucleation heat flux in a microchannel and/or tube theoretically derived by Peng et al. [9]. This obviously implies that the exploding emission is mainly induced by confined nucleation in small capillary or micro tubes. On the other hand, the experimental observations and measured results provide some solid evidences to support the previous theoretical investigation by Peng et al. [9].

9.3.3 Asymmetrical Effect

If lengths of two end sections are not same, this asymmetry is certainly expected to have great influence on the nucleation and exploding emission in different capillary or micro tubes. The influence of the asymmetrical distribution is described as an asymmetrical function, $f(\varepsilon_1, \varepsilon_2)$, dependent upon two asymmetrical parameters, geometrical asymmetrical factor ε_1 and thermal sensitive factor ε_2. These parameters are defined as

$$\varepsilon_1 = \frac{L_l^* - L_r^*}{L_l^*} \tag{9.12}$$

$$\varepsilon_2 = \frac{L_r^*}{L_h^*} \tag{9.13}$$

$$f(\varepsilon_1, \varepsilon_2) = q_{i,c,\varepsilon_1 \neq 0}^{'''*} / q_{i,c,\varepsilon_1 = 0}^{'''*} \tag{9.14}$$

In fact, ε_1 represents geometrical asymmetry for different distributions of left and right end sections, indicating the possibility of direction selection of exploding emission. Obviously, for symmetrical distribution of two end sections and $L_l = L_r$ or $L_l^* = L_r^*, \varepsilon_1 = 0$. For an asymmetrical distribution of two end sections, i.e. $L_l > L_r$ or $L_l^* > L_r^*, \varepsilon_1 \neq 0$. The geometrical asymmetry is enlarged with the increasing ε_1, and reach $\varepsilon_1 = 1$ as extreme asymmetrical distribution. The thermal sensitive factor, ε_2, expresses relative driving capacity to cause exploding emission by heating for the shorter end section.

The experimental results of the function $f(\varepsilon_1, \varepsilon_2)$ are depicted in Fig. 9.13 as the function of ε_1 and ε_2 for different tested tubes. General speaking, values of $f(\varepsilon_1, \varepsilon_2)$ are about 1 or about 0.68 (only one data is about 0.62), indicating the existence of asymmetrical effect (or induced by both ε_1, ε_2) would decrease the

critical value of exploding emission. Very clearly, tube size or diameter would result in different effects on two parameters, ε_1 and ε_2. For capillary or micro tubes of 200 μm in inner diameter, when $\varepsilon_1 < 0.7$, no significant asymmetric effect is observed on the specific critical heat of exploding emission or $f(\varepsilon_1, \varepsilon_2) \approx 1$. While when $\varepsilon_1 > 0.7$, the specific critical heat of exploding emission is significantly altered by the asymmetric effect and $f(\varepsilon_1, \varepsilon_2) \approx 0.68$. This is to say, there is a transition asymmetric parameter, $\varepsilon_{1,c}$, to identify the asymmetric effect on the specific critical heat of exploding emission. Similar trend is observed for tubes having inner diameter of 100 μm from Fig. 9.13. However, the transition asymmetric parameter seems smaller and more complicated. These aspects are relative to the thermal sensitive parameter, ε_2.

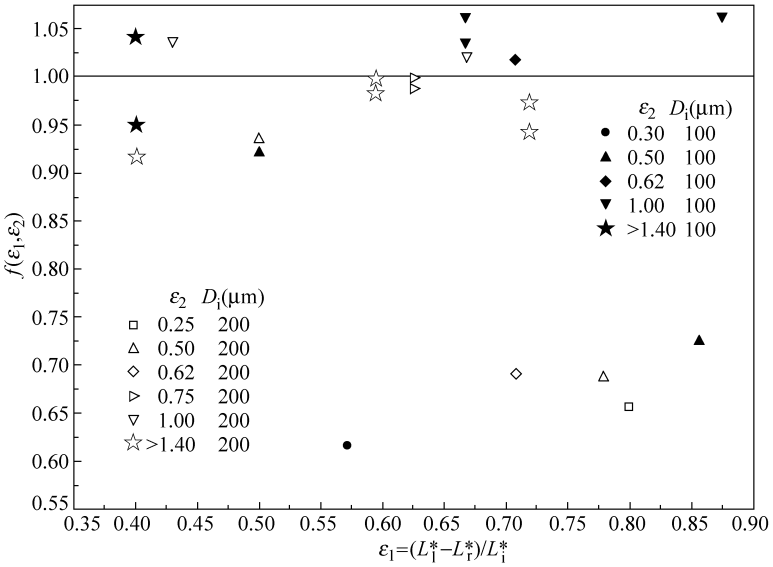

Figure 9.13 Effect of asymmetry on exploding emission

For both 100 and 200 μm tubes, if $\varepsilon_2 > 0.62$, the experimental results indicate that the thermal sensitive parameter would not have influence on the critical specific heat of exploding emission or extreme large $\varepsilon_{1,c}$ is required to trigger the asymmetrical effect. However, when $\varepsilon_2 < 0.5$, asymmetric function was affected significantly by geometrical asymmetrical factor, with the value smaller than 1 or in a range of 0.62 – 0.68 even for small value of $\varepsilon_{1,c}$. Furthermore, when $\varepsilon_2 = 0.62$ and $\varepsilon_1 = 0.71$, $f(\varepsilon_1, \varepsilon_2)$ is 1.02 for 100 μm tube and $f(\varepsilon_1, \varepsilon_2)$ is only 0.69 for 200 μm tube, indicating $\varepsilon_{1,c}$ is larger for 100 μm tube and smaller for 200 μm tube than 0.71. This may imply that both ε_2 and tube diameter affect the transition asymmetric parameter, $\varepsilon_{1,c}$. Obviously, the asymmetric effect on the exploding emission is very complicated and more comprehensive experimental and theoretical investigation is highly needed.

References

[1] D. B. Tuchkmann, R. F. W. Pease. Ultrahigh thermal conductance microstructures for cooling integrated circuits. Proc. 32nd Electronics Components Conf., 145, 1987.

[2] P. Y. Wu, W. A. Little. Measurement of the heat transfer characteristics of gas flow in fine channel heat exchanger used for microminiature refrigerators. Cryogenics, 24: 415 – 420, 1984.

[3] S. B. Choi, R. F. Barron, R. O. Warrington. Fluid flow and heat transfer in microtubes. Micromechanical Sensors, Actuators, and Systems, ASME DSC 32: 303 – 314, 1991.

[4] M. B. Bowers, I. Mudawar. High flux boiling in low flow rate, low pressure drop mini-channel and microchannel heat sinks. Int. J. Heat and Mass Transfer, 37 (2): 321 – 332, 1994.

[5] T. M. Adams, S. I. Khalik, S. M. Jeter, et al. An experimental investigation of single-phase forced convection in microchannels. Int. J. Heat Mass Transfer, 41: 851 – 857, 1998.

[6] P. Y. Wu, W. A. Little. Measurement of factors for the flow of gases in very fine channels used for microminiature Joule-Thomson refrigerators. Cryogenics, 23: 273 – 277, 1983.

[7] H. Wang, X. F. Peng, B. X. Wang, et al. Jet flow phenomena during nucleate boiling. International Journal of Heat and Mass Transfer, 45: 1359 – 1363, 2002.

[8] H. Wang. Multiplicity of nucleation and near-wall bubble dynamics of subcooled boiling on micro wires [Dissertation]. Beijing: Tsinghua University, 2004.

[9] X. F. Peng, H. Y. Hu, B. X. Wang. Boiling nucleation during liquid flow in microchannels. Int. J. Heat Mass Transfer, 41 (1): 101 – 106, 1998.

Index

Postscript

Prof. Xiaofeng Peng entered the Department of Thermal Engineering of Tsinghua University to study for his bachelor's degree in October, 1978. Later in 1983, under the supervision of Professor Buxuan Wang (Academician of the Chinese Academy of Sciences), he started his research on boiling heat transfer as a graduate student, and began to cultivate his research talent. While in the Department of Thermal Engineering, he grew from an undergraduate to a doctoral student, and then to a professor, with two thirds of his lifetime spent in Tsinghua University. He has been head of his research section and chair of the department.

Prof. Peng devoted all his passion and energy to fundamental heat transfer research and instructing students. He was extremely productive and gave us great wisdom until he passed away on September 10th, 2009.

This book is Peng's first academic monograph, an achievement based on his wide experience in the study of micro-scale boiling heat transfer. The content of the book systemizes his group's theses and papers. He had completed the first draft of the book before he passed away. According to the contract signed by Prof. Peng, Tsinghua University Press and Springer in March, 2007, this book should have been published by the end of 2009 and early in 2010. Prof. Peng finished his final revisions of Chapters 2, 3, and 4 before May, 2009, and planned to complete the remainder before September. However, he was stopped by his sudden and unexpected illness when visiting the U.S. during July.

After Prof. Peng passed away, Tsinghua University Press decided to continue the contract and publish his monograph. With the help and guidance of Prof. Buxuan Wang, Prof. Yuanyuan Duan and others, Prof. Peng's students continued revising the book. They carefully revised and supplemented the chapters that Prof. Peng had not finished, including reference numbering, content collation, editing, and index generation. Prof. Buxuan Wang then wrote the preface. This book may be different from what Prof. Peng had in mind, as he once mentioned that the content needed to be rearranged. However, I firmly believe that the joint work and passionate cooperation of friends, colleagues, and students, which have enabled publication of this book, have truly represent a pioneering, innovative academic work in the field of micro-scale heat transfer with phase change in China, which will certainly comfort and reassure the spirit of Prof. Peng.

At this moment, I am extremely grateful to the students who have offered their selfless help to the publication of this book: Zhanpeng Liang, Xiaodong Wang, Dong Liu, Qiming Li, Jianfeng Lu, Hao Wang, Yong Tian, Jiangtao Liu, Zhen Wang, Kejia Zhang, Zhiyong Lin, Gui Lu, Zheng Wang, Fen Wang, and Di Wu.

I also thank Prof. David Christopher for editing the English in the manuscript.

Prof. Peng's work had been supported by the National Natural Science (NSF) Foundation over many years. Many results published in this book were obtained in projects supported by NSF. In addition, this book has also been subsidized by the National Science and Technology Academic Writing Publishing Fund of 2009 from the Ministry of Science and Technology and the China Book Promotion Plan from General Administration of Press and Publication.

All the above are the words I want to put in, as one of his classmates and close friends.

Qiang Yao
Chairman，Department of Thermal Engineering
Tsinghua University
March 25, 2010